The Magnetopause : a quasi-tangential interface between the magnetosphere and the magnetosheath

Giulio Ballerini

Sorbonne Université

en cotutelle avec Università di Pisa

Ecole doctorale n° 127: Astronomie et Astrophysique d'Ile de France

Laboratoire de Physique des Plasmas

Équipe Plasmas Spatiaux

The Magnetopause: a quasi-tangential interface between the magnetosphere and the magnetosheath

Par **Giulio BALLERINI**

Thèse de doctorat d'Astronomie et Astrophysique

Dirigée par **Laurence REZEAU**, **Francesco CALIFANO** et **Gerard BELMONT**

Présentée et soutenue publiquement le 13 Septembre 2024

Devant un jury composé de :

President **Caterina RICONDA**	Professeur des universités	SU/LULI
Rapporteur : **Vincent GENOT**	Chercheur	CNRS/IRAP
Rapporteur : **Simone LANDI**	Professeur des universités	Università di Firenze
Examinateur : **Francesco PUCCI**	Chercheur	CNR/ISTP
Directeur : **Laurence REZEAU**	Professeur des universités	SU/LPP
Co-Directeur : **Francesco CALIFANO**	Professeur des universités	Università di Pisa
Invité : **Gerard BELMONT**	Émérite	LPP

Acknowledgments

Expressing my gratitude in this section is perhaps the hardest part of this thesis. Summing up these three (super intense) years in a few pages is not easy. For all the people who have been there for me over these years, please know that what I write here is but an infinitesimal portion of how thankful I am. It is mostly because of you, the presence, encouragement, and guidance that this work is what it is.

To that end, I begin with the three people who have inevitably been in close contact with me over the years: my supervisors. Laurence Rezeau, Francesco Califano, and Gerard Belmont. At least here in the acknowledgments, I will try not to be as redundant as I was in writing the thesis. To all three of them I am infinitely grateful in the first place for the great opportunity they have given me over these three years and for their constant presence, especially during the most stressful times. Laurence, thank you for everything you have taught me over these years and for all your wise words. Thank you also for your closeness when my inability to handle stress showed up. Francis, thank you for your availability, kind words, and continued presence. Thank you for always answering my doubts and constantly directing me even when I didn't know where to go. And finally, Gerard thank you (and sorry!) for the endless emails, doubts, and exchanges we had that were critical to the success of this work. To all three, thank you also for the encouragement and support and for making me feel part of a team rather than an individual PhD student.

I would also like to thank all the colleagues I have met over the years. Thank you to all the people I met at LPP and Pisa, who gave me an environment where I could discuss constructively and feel at home. Thanks also to all the colleagues who became more friends than simply colleagues and to the dinners and evenings we had together that always made me feel welcome.

Thanks also to the Menura team. Thank you all really for allowing me to work with such a promising code and for allowing me to participate and learn so much by working closely with you.

Finally, I would like to thank the Université Franco Italienne for the VINCI granting. Numerical simulations were conducted using high-performance computing resources on Leonardo and M100 (Cineca) and Jean Zay (IDRIS) for Menura, through Iscra C and Iscra B allocations, and on Irene (TGCC) for iPIC3D.

Also, I would like to thank my family. One of the few certainties I have in life is knowing that you will always be by my side at all times and for anything, and I can never be grateful enough. To Mom and Dad, thank you for your unconditional love and for being a reference point even in the most difficult times. Thank you also for all the sacrifices you have made, putting me and Alba first, and the constant encouragement without which I could not have experienced this beautiful journey. And to my sister Alba, Baba, thank you for always being there, even when we are on the opposite side of the world, and always believing in me, much more than I do myself. Thank you for being my fixed reference in a life of constant changes.

Finally, thank you also to all the friends who have allowed me to feel at home these past three years, despite the constant moving. I will not write a list here lest my carelessness cause me to forget someone but I hope I have pointed out how important you are to me outside of this acknowledgment. Last but not least, Lou. Thank you for coming into my life two years ago and embracing all the craziness since then.

Abstract

This thesis aims to study the Earth's magnetopause, defined as the boundary between the Earth's magnetosphere and the solar wind. Although considered in first approximation as a clear barrier between the two plasmas, the reality is more complex, as the solar wind plasma and the magnetosphere plasma mix with each other in the magnetopause in ways not yet fully understood. One example of this interaction is magnetic reconnection, which creates a flow of mass and magnetic field between the two media.
In this thesis, we focus on regions of the magnetopause away from areas of magnetic reconnection. In these regions, which make up most of the structure, the magnetopause often takes on a one-dimensional, stationary structure and is generally modeled as a discontinuity through the Classic Theory of Discontinuities (CTD). However, *in situ* data from recent space missions show how this theory does not adequately describe the magnetopause. In fact, at the magnetopause, both a rotation of the magnetic field in the plane tangent to the structure and compressive characteristics are observed. In order to describe these properties simultaneously, the magnetopause is described in CTD as a tangential discontinuity. However, this classification is a singularity in the theory that requires the normal component of the magnetic field to the structure to be zero. Instead, we observe from the data that this component is small but not zero, emphasizing the need to introduce a "quasi-tangential" description in order to describe the magnetopause.
In this thesis, therefore, the CTD is used as a starting point, exploiting its limitations in describing the magnetopause, in order to determine which terms are relevant in its equilibrium. To this end, we use *in situ* measurements from the Magnetospheric Multiscale Mission (MMS, NASA). The first part of the work aimed to develop an instrument, called GF2, that estimates the direction of the normal to the magnetopause more accurately than current instruments. Indeed, accurate estimation of the normal is of fundamental importance in order to determine which experimentally relevant terms are not included in the classical theory. This instrument was tested both on the MMS mission data, analyzing in detail a December 28, 2015 magnetopause crossing, and through a numerical simulation obtained through the hybrid-PIC code Menura, demonstrating good skill in determining the normal.
The same magnetopause crossing of MMS was also used to study the magnetopause equilibrium in detail. In particular, taking advantage of the normal obtained through the previously developed instrument, we show that the divergence of the pressure tensor plays a key role in this equilibrium, unlike the assumption in CTD. Specifically, we show that the effects of finite Larmor radius (FLR) play an important role in the quasi-tangential discontinuity when the Larmor radius of the ions is not completely negligible with respect to the thickness of the magnetopause. To generalize the result, a similar statistical study was also conducted on a database of MMS magnetopause crossings, which confirmed that these results are common in the magnetopause.
Finally, one part of the project focused on Mercury's magnetosphere, deviating slightly from the main objective of this thesis. In this analysis, full-kinetic simulations were used in order to analyze the generation of whistler waves in the reconnection region in the magnetotail. In this study, the small size of Mercury's magnetosphere compared with that of Earth is exploited in order to learn new insights about Earth's magnetosphere.

Résumé

Cette thèse vise à étudier la magnétopause terrestre, définie comme la limite entre la magnétosphère terrestre et le vent solaire. Bien que considérée en première approximation comme une barrière nette entre les deux plasmas, la réalité est plus complexe, car le plasma du vent solaire et celui de la magnétosphère se mélangent dans la magnétopause d'une manière qui n'est pas encore totalement comprise. Un exemple de cette interaction est la reconnexion magnétique, qui crée un flux de masse et un champ magnétique entre les deux milieux.
Dans cette thèse, nous nous concentrons sur les régions de la magnétopause éloignées des zones de reconnexion magnétique. Dans ces régions, qui constituent la majorité de la structure, la magnétopause prend souvent une structure unidimensionnelle et stationnaire et est généralement modélisée comme une discontinuité par la Théorie Classique des discontinuités (CTD). Cependant, des données *in situ* provenant de missions spatiales récentes montrent que cette théorie ne décrit pas correctement la magnétopause. En effet, à la magnétopause, on observe à la fois une rotation du champ magnétique dans le plan tangent à la structure et des caractéristiques de compression. Afin de décrire ces propriétés simultanément, la magnétopause est décrite dans le CTD comme une discontinuité tangentielle. Cependant, cette classification est une singularité dans la théorie qui exige que la composante normale du champ magnétique à la structure soit nulle. Au lieu de cela, nous observons à partir des données que cette composante est faible mais non nulle, ce qui souligne la nécessité d'introduire une description " quasi-tangentielle " pour décrire la magnétopause.
Dans cette thèse, le CTD est donc utilisé comme point de départ, en exploitant ses limites dans la description de la magnétopause, afin de déterminer quels termes sont pertinents dans son équilibre. À cette fin, nous utilisons des mesures *in situ* de la Magnetospheric Multiscale Mission (MMS, NASA). La première partie du travail visait à développer un instrument, appelé GF2, qui estime la direction de la normale à la magnétopause avec plus de précision que les instruments actuels. Une estimation précise de la normale est en effet d'une importance fondamentale pour déterminer quels termes expérimentalement pertinents ne sont pas inclus dans la théorie classique. Cet instrument a été testé à la fois sur les données de la mission MMS, analysant en détail une traversée de la magnétopause le 28 décembre 2015, et à travers une simulation numérique obtenue au moyen du code hybride-PIC Menura, démontrant une bonne compétence dans la détermination de la normale.
La même traversée de la magnétopause de MMS a également été utilisée pour étudier en détail l'équilibre de la magnétopause. En particulier, en exploitant la normale obtenue grce à l'instrument précédemment développé, nous avons montré que la divergence du tenseur de pression joue un rle clé dans cet équilibre, contrairement à l'hypothèse du CTD. Plus précisément, nous montrons que les effets du rayon de Larmor fini (FLR) jouent un rle important dans la discontinuité quasi-tangentielle, lorsque le rayon de Larmor des ions n'est pas complètement négligeable par rapport à l'épaisseur de la magnétopause. Pour généraliser ce résultat, une étude statistique similaire a également été menée sur une base de données de traversées de magnétopause MMS, qui a confirmé que ces résultats sont communs dans la magnétopause.
Enfin, une partie du projet s'est concentrée sur la magnétosphère de Mercure, s'écartant légèrement de l'objectif principal de cette thèse. Dans cette analyse, des simulations cinétiques complètes ont été utilisées afin d'analyser la génération d'ondes de sifflement dans la région de reconnexion de la queue magnétique. Dans cette étude, la petite taille de la magnétosphère de Mercure comparée à celle de la Terre est exploitée afin d'obtenir de nouvelles informations sur la magnétosphère de la Terre.

Riassunto

Questa tesi ha come obiettivo lo studio della magnetopausa terrestre, definita come il confine tra la magnetosfera terrestre e il vento solare. Sebbene considerata in prima approssimazione come una barriera netta tra i due plasmi, la realtà è più complessa, in quanto il plasma del vento solare e quello della magnetosfera si mescolano tra di loro nella magnetopausa in modi non ancora completamente compresi. Un esempio di questa interazione è la riconnessione magnetica, che crea un flusso di massa e campo magnetico tra i due mezzi.
In questa tesi, ci concentriamo sulle regioni della magnetopausa lontane dalle aree di riconnessione magnetica. In queste regioni, che costituiscono la maggior parte della struttura, la magnetopausa assume spesso una struttura unidimensionale e stazionaria e viene generalmente modellizzata come una discontinuità attraverso la Teoria Classica delle Discontinuità (CTD). Tuttavia, i dati *in situ* delle recenti missioni spaziali mostrano come questa teoria non descriva adeguatamente la magnetopausa. Infatti, nella magnetopausa si osservano sia una rotazione del campo magnetico nel piano tangente alla struttura che caratteristiche compressive. Al fine di descrivere queste proprietà contemporaneamente, la magnetopausa è descritta in CTD come una discontinuità tangenziale. Tuttavia, questa classificazione è una singolarità nella teoria che richiede che la componente normale del campo magnetico alla struttura sia nulla. Dai dati osserviamo invece che questa componente è piccola ma non nulla, sottolineando la necessità di introdurre una descrizione "quasi-tangenziale" al fine di descrivere la magnetopausa.
In questa tesi, dunque, la CTD è utilizzata come punto di partenza, sfruttando i suoi limiti nel descrivere la magnetopausa, al fine di determinare quali termini siano rilevanti nel suo equilibrio. A tale fine utilizziamo le misure *in situ* della missione Magnetospheric Multiscale (MMS, NASA). La prima parte del lavoro ha avuto lo scopo di sviluppare uno strumento, chiamato GF2, che stima con maggiore accuratezza rispetto agli strumenti attuali la direzione della normale della magnetopausa. Una stima accurata della normale risulta infatti di fondamentale importanza al fine di determinare quali termini rilevanti sperimentalmente non sono inclusi nella teoria classica. Questo strumento è stato testato sia sui dati della missione MMS, analizzando nel dettaglio un attraversamento della magnetopausa del 28 dicembre 2015, sia attraverso una simulazione numerica ottenuta attraverso il codice ibrido-PIC Menura, dimostrando una buona abilità nella determinazione della normale.
Lo stesso attraversamento della magnetopausa di MMS è stato inoltre utilizzato per studiare nel dettaglio l'equilibrio della magnetopausa. In particolare, sfruttando la normale ottenuta attraverso lo strumento sviluppato in precedenza, abbiamo dimostrato che la divergenza del tensore di pressione gioca un ruolo fondamentale in tale equilibrio, differentemente da quanto assunto in CTD. Nello specifico, dimostriamo che gli effetti del raggio di Larmor finito (FLR) giocano un ruolo importante nella discontinuità quasi-tangenziale, quando il raggio di Larmor degli ioni non è completamente trascurabile rispetto allo spessore della magnetopausa. Per generalizzare il risultato è stato inoltre condotto uno studio statistico analogo su un database di attraversamenti della magnetopausa di MMS, che ha confermato che questi risultati sono comuni nella magnetopausa.
Infine, una parte del progetto si è focalizzata sulla magnetosfera di Mercurio, discostandosi leggermente dall'obiettivo principale di questa tesi. In questa analisi, sono state utilizzate simulazioni full-kinetic al fine di analizzare la generazione di onde whistler nella regione di riconnessione nella magnetocoda. In questo studio, le dimensioni ridotte della magnetosfera di Mercurio rispetto a quella della Terra vengono sfruttate al fine di ottenere nuove informazioni sulla magnetosfera terrestre.

Résumé long en français

En physique de l'espace, le milieu a une tendance naturelle à s'auto-organiser en cellules distinctes, séparées par de fines couches. Ce comportement peut être observé à des échelles très différentes. Les magnétosphères planétaires, qui sont des bulles dans le flux du vent solaire et qui en sont séparées par des chocs d'étrave et des magnétopauses, et les interface entre le vent solaire et les corps non magnétisés en sont des exemples notables. Parmi toutes ces couches minces, la magnétopause terrestre joue un rôle particulier et constitue l'objet principal de cette étude. Cette structure est définie comme la frontière entre le plasma du vent solaire et le plasma planétaire, dominé par le champ magnétique.
L'importance de cette région vient du fait qu'elle a été explorée par un grand nombre de sondes spatiales depuis le début de l'ère spatiale, jusqu'aux missions multi-spatiales les plus récentes comme Cluster (ESA, Escoubet et al. (2001)) et Magnetospheric Multiscale (MMS, NASA, Burch and Phan (2016a)), ce qui a permis une description détaillée de ses propriétés. En outre, en raison d'une très faible composante normale du champ magnétique par rapport à la magnétopause, elle peut être identifiée comme une couche "quasi-tangentielle". Cette caractéristique est une conséquence directe de la propriété de gel qui prévaut aux grandes échelles, des deux côtés de la frontière, empêchant presque toute pénétration de flux magnétique et de matière entre le vent solaire et les milieux magnétosphériques (tous deux étant des plasmas magnétisés). Par grandes échelles, nous entendons ici les échelles de fluide où une loi d'Ohm idéale s'applique, comme dans le régime magnétohydrodynamique (MHD) idéal. Cependant, de petits écarts par rapport à une séparation stricte entre les deux plasmas existent, au moins localement et pour un intervalle de temps donné, et on sait qu'ils ont des conséquences importantes pour toute la dynamique de la magnétosphère : sous-orages, aurores, etc. Le consensus le plus large considère actuellement l'état d'équilibre de la frontière, valable sur la majeure partie de sa surface, comme une discontinuité tangentielle, avec une valeur strictement nulle, tandis que l'injection de plasma n'est autorisée qu'autour de quelques régions de reconnexion, où les gradients caractérisant la couche présentent des caractéristiques bidimensionnelles. Dans cette étude, nous remettons en question la nécessité d'utiliser une description de la magnétopause par une discontinuité strictement tangentielle en utilisant les données de la mission MMS.

Afin d'analyser correctement l'équilibre à la magnétopause, nous nous sommes concentrés sur les régions où la magnétopause présente des caractéristiques unidimensionnelles et stationnaires (représentant la majorité de la structure). Ces régions sont en effet celles où la magnétopause peut être modélisée comme une discontinuité. Ces régions sont généralement modélisées à l'aide de la théorie classique des discontinuités (CTD, Belmont et al. (2019)). Dans cette théorie, qui est utilisée à la fois pour les milieux neutres et les plasmas (magnétisés), les quantités physiques en aval et en amont sont liées par les lois fondamentales de conservation : masse, quantité de mouvement, énergie et flux magnétique, et elle est caractérisée par les hypothèses simplificatrices suivantes : une couche stationnaire, des variations 1D et une pression isotrope de part et d'autre. Pour les plasmas, l'hypothèse supplémentaire d'une loi d'Ohm idéale des deux côtés est prise en compte.
Dans la CTD, les lois de conservation fournissent un système d'équations de saut entre les quantités physiques en amont et en aval, à savoir les conditions de Rankine-Hugoniot dans les milieux neutres et les conditions de Rankine-Hugoniot généralisées dans les plasmas. La CTD amène à distinguer les discontinuités de compression et de rotation. Une caractéristique importante de ces solutions est que les solutions compressives et rotationnelles sont mutuellement exclusives: les solutions de choc sont purement compressives, sans aucune rotation du champ magnétique tangentiel (c'est ce qu'on appelle la "propriété de coplanarité"), tandis que la discontinuité rotationnelle implique une telle rotation, mais sans aucune variation de l'amplitude du champ magnétique et sans aucune compression de la densité des particules. Cette distinction persiste quels que soient les flux le long de la normale de la discontinuité, même lorsque les composantes

normales de la vitesse et du champ magnétique par rapport à la structure sont arbitrairement petites. La seule exception est la "discontinuité tangentielle", celle utilisée en général pour décrire la magnétopause, lorsque les deux flux normaux sont strictement nuls. Cette solution correspondrait, pour la magnétopause, au cas où il n'y a pas de connexion entre le vent solaire et la magnétosphère. Elle apparaît comme un cas singulier puisque la discontinuité tangentielle, avec une composante normale du champ magnétique strictement égale à zéro, n'est la limite d'aucune des solutions générales avec une petite valeur de cette composante normale.

Comme prévu, grâce aux observations *in situ*, la magnétopause de la Terre joue un rôle central dans la vérification des théories de discontinuité. En effet, la magnétopause terrestre présente, sur toute sa surface, à la fois une rotation du champ magnétique et une variation de densité puisqu'elle est la jonction de deux milieux, le vent solaire et la magnétosphère, où le champ magnétique et la densité sont différents. Cependant, d'un point de vue expérimental, les observations peuvent difficilement distinguer les petites composantes des composantes strictement égales à zéro en raison des incertitudes dues aux fluctuations et de la précision limitée de la détermination de la direction normale. Cela souligne donc la nécessité de résoudre la limite singulière pour les petites composantes normales du champ magnétique. Dans cette thèse, la CTD est utilisée comme point de départ pour améliorer notre compréhension de la magnétopause. La principale question abordée est la suivante : pourquoi la CTD ne parvient-elle pas à décrire les observations *in situ* ? Pour répondre à cette question, nous avons analysé des données complémentaires provenant de la mission MMS et de simulations numériques. Pour cette étude, l'utilisation d'une mesure multi-satellites est d'une valeur fondamentale. En effet, lorsqu'on utilise les mesures d'un seul engin spatial, il est impossible de distinguer si les quantités mesurées ont des dépendances temporelles ou spatiales (ou les deux). En mesurant un changement d'orientation du champ magnétique, par exemple, nous ne disposons d'aucune autre information pour déterminer s'il s'agit d'un changement d'état du plasma ou si le vaisseau spatial pénètre dans un plasma différent. En outre, la possibilité que plusieurs engins spatiaux sondent simultanément la magnétopause est d'une importance fondamentale pour le calcul des gradients sans dépendre d'hypothèses fortes sur les propriétés de la magnétopause.

La première partie de cette thèse se concentre sur le développement d'un nouvel outil nous permettant d'obtenir une détermination précise de la direction normale de la magnétopause à partir de mesures *in situ*. Une estimation précise du vecteur normal est en effet cruciale pour cette étude puisqu'elle nous permet de séparer les composantes normales et tangentielles de toute quantité physique à la frontière. Théoriquement, nous avons montré que le transport normal à travers la magnétopause est d'une importance fondamentale pour comprendre les propriétés de la frontière, en particulier les variations magnétiques dans le plan tangentiel. Comme ce transport normal est beaucoup plus petit que les valeurs tangentielles correspondantes, une trop grande incertitude sur la direction normale fausserait leur estimation. Au contraire, une bonne estimation de cette quantité permettra d'établir quels termes, dans l'expression générale des flux transportés, sont pertinents et non inclus dans les modèles classiques.
Au fil des ans, plusieurs méthodes ont été développées dans le but de déterminer avec précision la direction normale. La plus courante est la méthode de la variance minimale ("Minimum Variance Analysis", MVA, Sonnerup and Cahill (1967); Sonnerup and Scheible (1998)) introduite avec les premières mesures du champ magnétique dans l'espace. Cette méthode, qui nécessite des mesures effectuées par un seul engin spatial, fournit une normale globale, c'est-à-dire un vecteur normal unique pour chaque série temporelle entière à travers la frontière. L'outil repose sur l'hypothèse que la frontière est une couche parfaitement unidimensionnelle et stationnaire traversant l'engin spatial. La méthode "Minimum Directional Derivative" (MDD, Shi et al. (2005)) est un exemple notable d'outil multi-spatial. Cet outil utilise généralement les données du champ magnétique, mais il faut garder à l'esprit qu'il n'est pas basé sur les propriétés spécifiques de ce champ. La

technique MDD est une méthode dite “basée sur le gradient” puisque le calcul de la normale est basé sur l'estimation expérimentale de la matrice du gradient du champ magnétique, qui peut être obtenue à partir de mesures effectuées par plusieurs engins spatiaux à l'aide de la méthode des vecteurs réciproques. En outre, la matrice de gradient peut également être utilisée pour estimer la dimensionnalité de la frontière à partir du rapport entre les valeurs propres (Rezeau et al., 2018). L'outil développé dans le cadre de cette thèse, appelé “Gradient matrix Fitting” (GF2), est dérivé de la MDD. Ces deux outils fournissent une estimation de la direction normale locale, permettant d'étudier la variation de ce vecteur à chaque pas de temps. L'outil GF2 incorpore une procédure d'ajustement, en utilisant un modèle 2D, permettant d'imposer des contraintes physiques directement dans l'algorithme, comme la loi de Gauss dans le cas des mesures de champ magnétique. Cette fonctionnalité est différente de ce qui est fait dans le MDD, où les contraintes physiques sont vérifiées a posteriori. L'outil GF2 a été testé sur une traversée de magnétopause MMS le 28 décembre 2015, montrant des résultats comparables la méthode MDD standard. Cependant, un test plus précis de cet outil ne peut être réalisé qu'avec des données de simulation numérique.

À cette fin, en complément de l'analyse des données *in situ*, nous avons réalisé une étude numérique de la magnétopause. Il existe deux approches principales pour simuler la magnétopause : les simulations locales et les simulations globales. Les modèles globaux incluent l'ensemble de la magnétosphère 2D ou 3D dans le domaine de calcul, tandis que les modèles locaux se concentrent sur des sous-régions spécifiques plus petites (1D, 2D ou 3D en fonction du degré de réalisme attendu), telles que des parties de la queue d'une comète ou de la magnétopause. Bien que les simulations globales offrent une résolution plus faible de la magnétopause que les simulations locales, elles offrent un degré de réalisme plus élevé, nécessaire à notre étude. Pour cette raison, nous avons effectué une simulation globale en utilisant le solveur Menura (Behar et al., 2022), un code hybride-PIC, simulant une magnétosphère semblable à celle de la Terre. Cette simulation a été exploitée pour tester l'outil GF2 en le comparant au MDD, comme pour les données *in situ*. Alors qu'une étude quantitative nécessiterait une comparaison avec un calcul exact du vecteur normal pour déterminer la précision, plusieurs facteurs empêchent le calcul d'une direction normale “réelle”. Les principales sont la nature bidimensionnelle inévitable à petite échelle et les incertitudes dans le calcul du gradient de la matrice à partir des différences finies qui affectent la fiabilité du calcul de la direction normale. Ce test montre que, si les deux méthodes donnent le même résultat dans les régions où la magnétopause est unidimensionnelle, l'outil GF2, contrairement à MDD, permet effectivement de séparer les directions majeure et mineure des gradients dans les régions où la magnétopause présente des caractéristiques bidimensionnelles, les trop petites échelles étant filtrées dans les deux directions. Cependant, des simulations à plus haute résolution sont nécessaires pour une quantification exacte des performances de l'outil GF2. Cela nécessite des ressources informatiques considérables, ce qui rend une telle étude actuellement irréalisable avec une approche de simulation globale. Une analyse possible pourrait être effectuée avec des simulations locales (moins réalistes). Une telle étude est laissée en suspens pour l'avenir.

L'outil GF2 a ensuite été appliqué à l'étude de la structure de la magnétopause en utilisant la traversée MMS du 28 décembre 2015, utilisée précédemment pour tester l'outil GF2. Plus précisément, cette traversée a révélé des propriétés non décrites par le CTD, telles que la compression et la rotation simultanées. Pour étudier cette traversée, nous pouvons exploiter l'hodogramme du champ magnétique dans le plan tangentiel à la discontinuité, qui peut être facilement obtenu à partir des données *in situ*. Cette analyse nous permet de déterminer si la magnétopause présente des caractéristiques de rotation, de compression ou les deux. Si l'on considère une magnétopause traversée à partir des données *in situ*, et si le CTD était valide pour toutes les traversées, la forme de l'hodogramme dépendrait de la classe de discontinuité. Pour une discontinuité rotationnelle, l'hodogramme correspondrait à un arc de cercle de rayon

constant, tandis que pour un choc, l'hodogramme correspondrait à une ligne radiale. Pour la traversée du MMS analysée ici, l'hodogramme présente des caractéristiques linéaires (et non radiales). Pour étudier cette caractéristique, nous avons analysé les deux équations responsables de la séparation des discontinuités rotationnelles et compressives dans la CTD : la loi d'Ohm et l'équation d'impulsion (leurs projections dans le plan tangentiel de la magnétopause). L'analyse a montré que la divergence du tenseur de pression ionique joue un rôle clé dans l'équilibre de la magnétopause, violant l'hypothèse d'isotropie de la CTD. Nous montrons que cela est dû à des Effets de Rayon de Larmor fini (FLR) qui rendent le tenseur de pression non-gyrotrope. Pour tester cette caractéristique, deux indices de non-gyrotropie ont été exploités, l'une introduite dans cette étude et l'autre définie dans Aunai et al. (2013a). Cette étude confirme une non-gyrotropie significative, bien que faible, dans le tenseur de pression ionique. Nous avons également étudié la direction de la non-gyrotropie, montrant qu'elle diffère de celle du champ magnétique pour cette traversée, contrairement à ce que l'on suppose généralement. Plus précisément, pour cette traversée, cette direction est quasi-orthogonale à la fois au champ magnétique et à la direction normale de la magnétopause.

Bien que ces résultats soient très intéressants, il était donc nécessaire de déterminer s'il s'agissait d'une particularité de la traversée analysée ou d'une condition générale à la magnétopause. A cette fin, une étude statistique a été menée parallèlement à l'étude de cas. Nous avons sélectionné un ensemble de données de 146 traversées de la magnétopause présentant des caractéristiques unidimensionnelles et stationnaires afin d'établir une base statistique solide. Pour chacune de ces traversées, nous avons étudié l'hodogramme du champ magnétique dans le plan tangentiel en classant sa forme. Cette analyse a révélé que plus d'un tiers des traversées sélectionnés sont en désaccord avec la CTD, montrant une forme linéaire, ce qui indique que les FLR à la magnétopause sont significatifs, même s'ils ne sont pas prédominants. Il est bien connu que la version linéaire de la discontinuité rotationnelle est l'onde de cisaillement MHD d'Alfvén. Il semble ici que les discontinuités "quasi-tangentielles" de la magnétopause correspondent de la même manière aux "ondes cinétiques d'Alfvén" quasi-perpendiculaires. Plusieurs articles ont étudié les changements dans les discontinuités rotationnelles lorsque divers effets non idéaux sont introduits en utilisant différentes hypothèses. Cependant, ces différents articles aboutissent à des conclusions différentes, notamment en ce qui concerne le rôle de l'inertie des électrons dans l'équilibre de la couche. Même si l'étude statistique confirme le résultat obtenu par l'étude de cas, une analyse plus complète bénéficierait de l'étude du tenseur de pression calculé dans les simulations numériques. En particulier, nous pourrions exploiter la même simulation que celle utilisée pour tester l'outil GF2. Cependant, par manque de temps, nous n'avons pas pu réaliser cette analyse dans le cadre de cette thèse. Cette étude est laissée pour de futures recherches. Dans l'ensemble, cette étude souligne la pertinence des effets FLR à la magnétopause, en fournissant un cadre pour les recherches futures. Ces efforts amélioreront notre compréhension de la dynamique complexe à la magnétopause, contribuant au domaine plus large de la physique des plasmas spatiaux.

En outre, GF2 a été utilisé pour comparer les propriétés géométriques des structures magnétiques et ioniques à la magnétopause. Plus précisément, nous avons exploité le jeu de données des traversées sélectionnées pour l'analyse statistique et comparé les normales obtenues à partir des mesures du champ magnétique et du flux d'ions. Cette analyse a montré que la plupart des traversées présentent des structures similaires, avec 56,2 % des traversées dont les normales diffèrent de moins de 20 degrés, tandis qu'une partie de l'ensemble de données présente des différences significatives. À cette fin, nous avons également analysé les propriétés des mesures de flux d'ions. Plus précisément, nous nous sommes concentrés sur la dimensionnalité et la stationnarité de ces mesures. En outre, pour certaines traversées, la normale obtenue à partir du flux d'ions présente de fortes variations locales par rapport à la valeur moyenne. En ex-

cluant toutes les traversées ne respectant pas les bonnes propriétés, nous observons que seuls quelques traversées sont en dehors de la diagonale, avec seulement deux de ces traversées (sur 77, équivalent à 2.6%) ayant des angles supérieurs à 40^o. Une fois de plus, les simulations numériques sont cruciales pour contextualiser ces résultats. À cette fin, la simulation numérique Menura a été exploitée et a donné des résultats comparables : dans les régions présentant des structures de flux d'ions unidimensionnelles, les normales obtenues à partir du champ magnétique et du flux d'ions sont proches (avec des différences de l'ordre de 10 degrés). La partie prédominante de la structure présente des caractéristiques bidimensionnelles pour le flux de masse d'ions, montrant des normales de flux d'ions jusqu'à 90 degrés par rapport aux normales magnétiques. Une étude plus précise, s'étendant à un plus grand nombre de régions de magnétopause, devrait permettre de quantifier ce résultat et de mieux comprendre les résultats obtenus par l'étude statistique.

Outre l'étude de la magnétopause terrestre, une étude numérique de la magnétosphère de Mercure a été menée à l'aide du solveur iPIC3D (Markidis et al., 2010), un code PIC cinétique complet. L'étude s'est concentrée sur la magnétosphère de Mercure pour deux raisons principales : *i*) préparer l'arrivée de la mission JAXA/ESA BepiColombo sur Mercure (Benkhoff et al., 2021) et *ii*) exploiter la description cinétique complète de la mini-magnétosphère de Mercure pour mieux comprendre les caractéristiques globales de la magnétosphère terrestre. En effet, en raison des contraintes de calcul actuelles, la simulation de la magnétosphère de la Terre tout en capturant les échelles cinétiques n'est pas réalisable sur le plan du calcul sans changement d'échelle.
La simulation iPIC3D a été exploitée pour étudier la région de reconnexion dans la queue magnétique, en se concentrant sur l'influence de la topologie du champ magnétique sur la distribution des particules énergétiques. Cette analyse s'est principalement concentrée sur les ondes whistler à bande étroite qui ont été observées autour de la région de reconnexion du côté nuit. Ce résultat est remarquable puisque des ondes chorus en mode whistler ont été détectées lors des deux survols de Mercure effectués par BepiColombo (Ozaki et al., 2023). Néanmoins, les observations n'ont pas encore permis de connaître la distribution de ces ondes dans la magnétosphère de Mercure. Alors que ces ondes sont observées dans le secteur localisé de l'aube, les mesures dans la queue magnétique manquent encore. Notre analyse apporte une réponse à cette question. Cependant, un champ magnétique du vent solaire complètement orienté vers le sud a été utilisé dans la simulation effectuée. Pour comprendre comment cette hypothèse affecte la distribution des ondes, d'autres simulations numériques avec des orientations variables du champ magnétique du vent solaire sont nécessaires et prévues pour les travaux futurs. En outre, d'autres simulations numériques sont nécessaires pour tester l'influence du changement d'échelle du rayon appliqué dans cette simulation sur les caractéristiques de l'onde et la relation de dispersion. En résumé, cette recherche a permis une première analyse des ondes en mode whistler dans le cadre d'une simulation globale, préparant le terrain pour les études futures et les observations à venir de la mission BepiColombo. Une étude plus approfondie avec différents paramètres de simulation sera cruciale pour faire progresser notre connaissance de la magnétosphère de Mercure.

Les résultats discutés dans cette thèse sont présentés dans deux articles : "Role of FLR effects in magnetopause equilibrium", accepté par Journal of Plasma Physics, et "Whistler-mode waves in the tail of Mercury's magnetosphere : a numerical study", accepté par Astronomy & Astrophysics. En outre, j'ai participé activement avec l'équipe Menura à l'exécution et à l'analyse de la toute première simulation visant à étudier les conséquences de la turbulence du vent solaire sur une planète semblable à la Terre. Ceci est possible grâce à la particularité du code Menura qui résout les équations dans le repère du vent solaire, ce qui nous permet d'éliminer les contraintes sur les variations du champ magnétique alignées sur le flux et nous permet d'effectuer des simulations numériques incluant une plus large gamme d'événements du vent solaire (Behar, E. and Henri, P., 2023). Bien que plusieurs simulations numériques globales aient été réalisées

de nos jours pour étudier l'environnement de Mercure, en utilisant des modèles allant de la magnétohydrodynamique, multifluide, hybride à cinétique, aucun d'entre eux ne tient compte de la dynamique du vent solaire turbulent. Cette analyse est résumée dans un article intitulé "Impact of solar wind turbulence on the Earth's bow shock" que j'ai co-écrit et qui devrait être soumis dans les prochains mois à Astronomy & Astrophysics.

Contents

List of acronyms

- **AMR:** Adaptive Mesh Refinement
- **AU:** Astronomical unit (equal to 149 597 870 700 m);
- **CAM:** Charge Assignment Method;
- **CIR:** Co-rotational Interaction Region
- **CME:** Coronal Mass Ejections;
- **CPU:** Central Processing Unit;
- **CTD:** Classic Theory of Discontinuities;
- **CTA:** Constant Thickness Approach;
- **CVA:** Constant Velocity Approach;
- **EDR:** Electron Diffusion Region;
- **FLR:** Finite Larmor Radius effects;
- **GF2:** Gradient matrix Fitting;
- **GPU:** Graphics Processing Unit;
- **GRA:** Generic Residue Analysis;
- **GSE:** Geocentric Solar Ecliptic coordinate system;
- **IDR:** Ion Diffusion Region;
- **IMF:** Interplanetary Magnetic Field;
- **IMP 8:** International Monitoring Platform 8;
- **ISEE:** International Sun-Earth Explorer;
- **JUICE:** JUpiter ICy moons Explorer
- **MESSENGER:** MErcury Surface, Space ENvironment, GEochemistry and Ranging;
- **KHI:** Kelvin-Helmholtz instability;
- **MDD:** Minimum Directional Derivative;
- **MHD:** Magneto-Hydrodynamics;
- **MMS:** Magnetospheric Multiscale Mission;
- **MPI:** Message Passing Interface;
- **MSO:** Mercury Solar Orbital;
- **MVA:** Minimum Variance Analysis;
- **PIC:** Particle-in-Cell;
- **SITL:** Scientist-in-the-Loop;
- R_E**:** Mean Radius of the Earth (equal to 6378 km);
- **VDF:** Velocity Distribution Function;

Introduction

This thesis investigates the Earth's magnetopause, the structure defined as the boundary separating the interplanetary plasma, dominated by the solar wind, and the planetary plasma, dominated by the planetary magnetic field. A central question in magnetospheric physics is to understand how mass, momentum, and energy can penetrate from one medium to the other through this thin (with respect to the magnetosphere size) current layer. Within the scientific community, this structure is considered to be an impenetrable structure, not allowing for any flux of mass or magnetic field, except for some regions, where the layer is not planar, involving generally magnetic X lines, and where magnetic reconnection takes place thanks to non-ideal effects.

In this study, we focus on the regions of the magnetopause far from magnetic reconnection sites, representing the majority of the structure. Within these regions, the magnetopause exhibits a one-dimensional structure and can generally be considered stationary. It therefore meets the two main hypotheses defining a physical "discontinuity". However, as observed by *in situ* data from space missions such as Cluster (ESA) and Magnetospheric Multiscale Mission (MMS, NASA), the terrestrial magnetopause seems to escape the conventional discontinuity classification, which relies on several simplifying assumptions such as one-dimensionality, stationarity and isotropic conditions and ideal Ohm's law on both sides of the discontinuity. *In situ* data exhibit properties that mix features of shocks and rotational discontinuities. In the Classic Theory framework, such mixing is precluded except if the magnetopause is described as a tangential discontinuity, requiring the structure to be completely impermeable to mass flow and magnetic field.

In this thesis, we challenge this paradigm by questioning the description of the magnetopause as a tangential discontinuity and studying the limitations of the hypothesis of the state-of-the-art theory. Here we summarize the eight chapters composing this manuscript.

Thesis Overview

In Chapter 1, we provide a brief introduction to plasma physics, focusing on the definition of plasmas, their characteristic (temporal and spatial) scales, and the most important models used to describe plasma dynamics.

Chapter 2 delves into the interaction between the solar wind and the Earth's magnetosphere, introducing the notions required to understand the thesis work. Here, we discuss the similarities and differences between the different planetary magnetospheres. Chapter 2 also gives a detailed description of the structure of the Earth's magnetopause and a brief introduction to magnetic reconnection.

Chapter 3 focuses on the study of the Earth's magnetopause through *in situ* measurements, introducing the main space missions that have sampled the structure, with a particular focus on MMS, whose data are exploited in this study. In this Chapter, we highlight the importance of an accurate determination of the magnetopause's normal vector and discuss the most relevant state-of-the-art tools employed in contemporary research to estimate this vector. Finally, a new tool developed during this thesis, the Gradient matrix Fitting (GF2) tool, is presented and tested using a magnetopause crossing from MMS.

In Chapter 4, we analyze the magnetopause from a discontinuity perspective, presenting what we call the "Classic Theory of Discontinuities" and analyzing its limitations in modeling the magnetopause. Specifically, here we use the MMS crossing analyzed previously to illustrate the

theory's constraints and demonstrate how the full pressure tensor, and in particular its non-gyrotropy, has a fundamental role at the magnetopause equilibrium.

Chapter 5 generalizes the results discussed in Chapter 4 through a statistical study. In particular, we describe the characteristics of magnetopause crossings observed by MMS in order to explain the selection process exploited to select the database used to perform the statistical study. Finally, the results of this study are discussed, showing that what was observed in the previous chapter is rather typical at the magnetopause.

Beginning in Chapter 6, the manuscript shifts the focus to numerical simulations, complementing the study of the magnetopause from the *in situ* data analysis. In this Chapter, we introduce the most common numerical models used to simulate plasma dynamics, focusing in particular on the Menura and iPIC3D solvers employed during this work. Finally, this chapter introduces both global and local simulation approaches for simulating the magnetopause.

In Chapter 7, we present a global simulation of the interaction between the solar wind and the magnetosphere of an Earth-like planet, performed using the Menura solver. This simulation is then used to validate the GF2 tool, presented in Chapter 3, by comparing its results with a state-of-the-art tool.

Finally, in Chapter 8 we study Mercury's magnetosphere through a numerical simulation using the iPIC3D solver. The study discussed here slightly deviates from this thesis's main focus, exploiting Mercury's magnetosphere's smaller size (with respect to the Earth) allowing for the use of fully kinetic codes to simulate its dynamics. This "mini-magnetosphere" is therefore used to provide insights into Earth's magnetosphere. Here, we first highlight the relevance of the study of Mercury's magnetosphere and the major missions that have investigated it *in situ*. Additionally, we focus on the study of the generation of whistler-mode waves near the reconnection region observed in the simulation.

1 Fundamental concepts of plasma physics

Contents

A plasma is defined as an ensemble of a huge number of charged particles, globally neutral and dominated by electromagnetic forces. Plasmas are characterized by unique properties that distinguish them from other states of matter. A key feature of plasmas is the presence of charged particles that can respond collectively to electromagnetic fields, leading to phenomena such as plasma oscillations and various instabilities. Due to the differences with solids, liquids, and gases, plasma is also known as the "$4th$ state of matter".
Plasma dynamics is driven by the long-range coupling between the external and self-consistently generated electromagnetic fields (EMFs) and the global response of charged particles. Indeed, on one side, the local values of the electric and magnetic fields drive the dynamics of the particles via the Lorentz force. On the other, the position and velocity of the charged particles give the local values of charge density ρ and the current density $\mathbf{J}$ (after averaging in a small volume), which are the source terms in the Maxwell equations. In this context, the $\mathbf{E}$ and $\mathbf{B}$ fields must be considered as averaged fields within the framework of a statistical approach, known as mean-field theory (for a more detailed description see for instance plasma physics monographs such as Krall et al. (1973) or Belmont et al. (2014)). A sketch simplifying the loop of plasma physics is shown in Figure 1.1. Here it is easy to distinguish the plasma and gas dynamics. Indeed, for gases with no ionization, the red lines connecting the particles and electromagnetic sides disappear, decoupling the two.

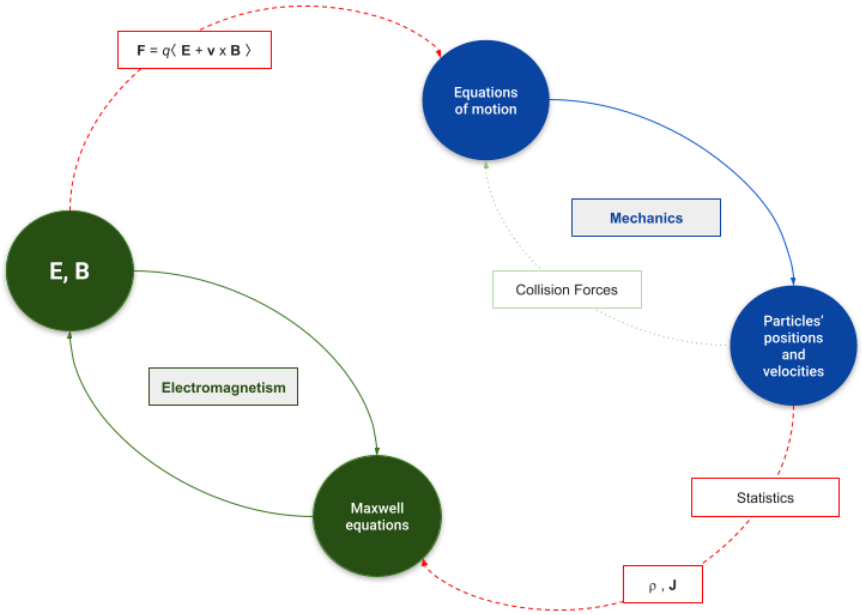

Figure 1.1: Schematic representation of The plasma loop. Credits: adapted from Belmont et al. (2019).

A further distinction between plasmas and non-ionized gases comes from collisions. Indeed, the notion of collisions is qualitatively and quantitatively different in these two media. In both cases, the mean free path due to collisions is defined as the characteristic scale length required for a particle to change its velocity significantly due to the other particles. In a neutral gas, this change only involves the close ("binary") interactions between two particles, so justifying the use of the word "collisions" in its usual sense. In contrast, in plasma, the deviation of a particles path involves interactions with numerous other particles, most of them being distant from it. The difference between the mean free path in plasmas and neutral gas and their collision regimes is sketched in Figure 1.2. In a neutral gas, the collision frequency is often much higher than any dynamical frequency. The so-called "perfect gas limit" refers to the cases where the collisions are perfectly elastic, neglecting any other interaction between the particles. Plasmas exhibit different collision regimes depending on their density and temperature. In all regimes, collective effects and electromagnetic interactions are far more significant than individual collisions. The weakly-coupled regime, which prevails in all space plasmas, is the equivalent for plasmas of gas for neutrals: the mean free path is much larger than the inter-particle distance. In this case, the kinetic energy of a single particle is also much greater than the potential interaction energy at the mean interparticle distance.

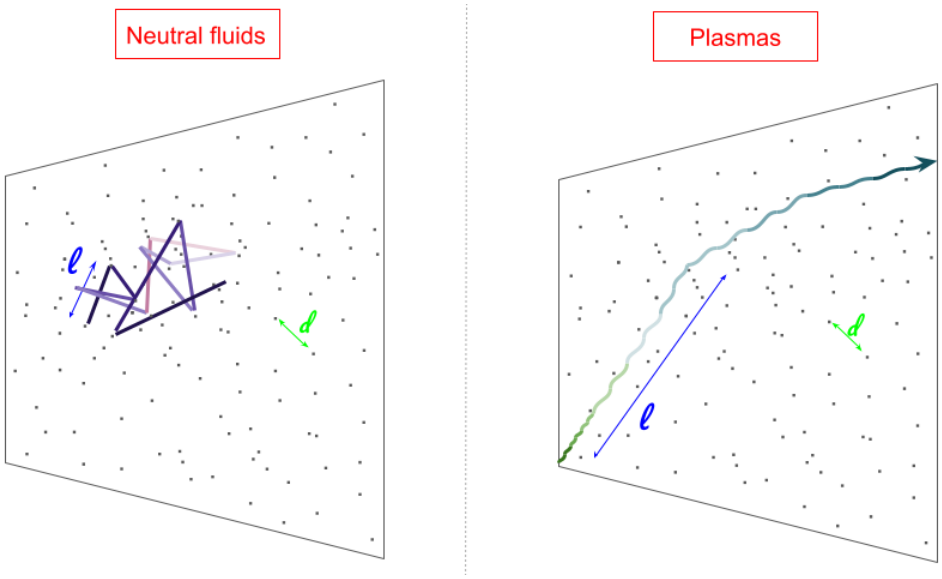

Figure 1.2: Sketch describing the reciprocal influence of charged matter and electromagnetic field in plasmas. Credits: adapted from Belmont et al. (2019).

Despite their rarity on Earth, it is estimated that more than 99% of all known matter in the Universe is in a plasma state (Baumjohann and Treumann, 1996). In general, the plasma state groups very different media, spanning several orders of magnitude in both temperature and density. Figure 1.3 shows the order of magnitude of some plasmas in the $n - T$ plane to fix ideas of how variable the nature of plasmas can be. Moreover, plasmas can also be distinguished between magnetized and non-magnetized ones. Due to this vast complexity and differences, there is no universal method (either analytical or numerical) that can be generally and easily used for describing the vast array of phenomena that occur in plasma. Plasma must therefore be studied within limited regimes that allow simplification of the equations involved. From Figure 1.3 we observe that the solar wind and magnetospheric plasmas are very tenuous plasmas, almost collisionless, and dominated by collective effects.
In this Chapter, we introduce the theoretical description of plasmas to include this work in a broader plasma physics context. In particular, in Section 1.1 we present the typical temporal

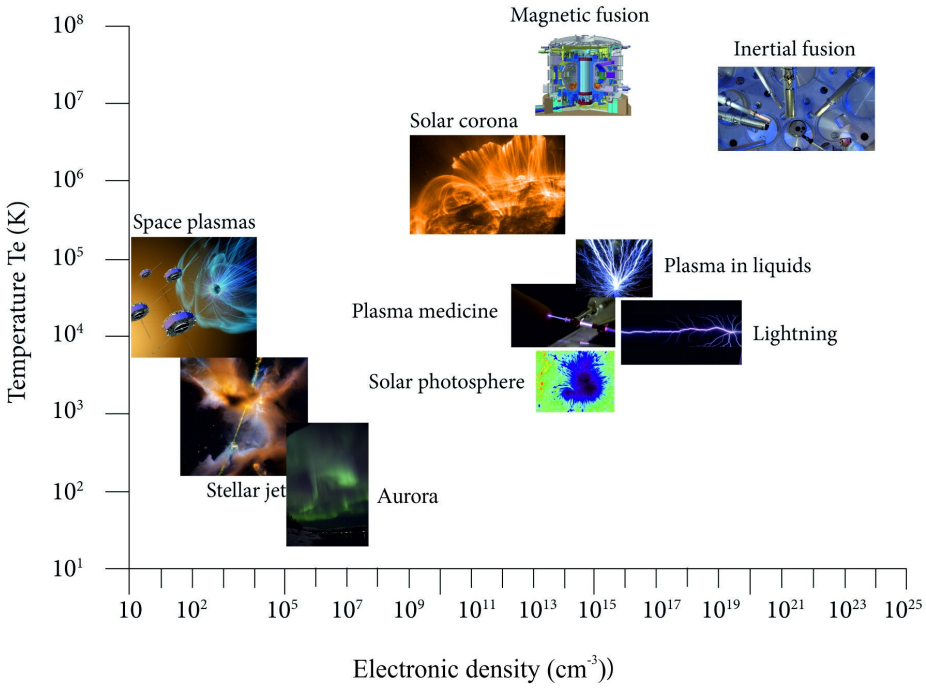

Figure 1.3: Several examples of plasmas as a function of their densities and temperatures. Credits: Fédération de recherche PLAS@PAR

and length scales in plasma physics. Then, in Section 1.2, a brief introduction to plasma models (kinetic, two-fluid, and single-fluid MHD) is discussed.

1.1 Characteristic time and length scales in plasma

In vacuum, the electrostatic potential of an isolated macroscopic charge q, supposed spherical is $\Phi(r) = \frac{q}{4\pi\epsilon_0 r}$. In a plasma, electrons are drawn toward it or away from it, depending on the sign of q, effectively shielding the electrostatic field for the rest of the plasma. This shielding effect modifies the effective potential in the proximity of the charge q, which is expressed as:

$$\Phi(r) = \frac{q}{4\pi\epsilon_0 r} e^{-r/\lambda_{De}} \tag{1.1}$$

where we defined the Debye length as follows

$$\lambda_{De} \simeq \sqrt{\frac{\epsilon_0 k_B T_e}{n_e e^2}} \tag{1.2}$$

Here, ϵ_0 is the electric permittivity of the free space, $-e$ is the electron charge, n_e the electron number density, T_e the electron temperature, and k_B the Boltzmann constant. The Debye length can be interpreted as the scale over which charged particles screen out the electrostatic field of an external "test" charge and so as the characteristic length beyond which the system behaves as a plasma, i.e. collectively. This parameter, of fundamental importance in plasmas, can be determined by balancing the electrostatic energy of the test charge with the thermal energy of the plasma particles. From this scale, we define the Debye Sphere as the spherical region surrounding a test charge within a plasma where the electric field is influenced by it.
The collective behavior of a plasma is featured by the plasma frequency, a frequency at which the plasma oscillates at all wavelengths in the presence of a charge unbalance:

$$\omega_{pe} = \sqrt{\frac{n_e e^2}{m_e \epsilon_0}} \tag{1.3}$$

Here, m_e is the electron mass. In the electromagnetic regime, the characteristic scale length of the dynamics is called the skin depth d_e:

$$d_e = \frac{c}{\omega_{pe}} \tag{1.4}$$

In the magnetized case, *i.e.* a plasma embedded in an external magnetic field $\mathbf{B}$, the electron characteristic scales are the gyroradius r_{Le} (or the Larmor radius) and the gyrofrequency ω_{ce}:

$$\omega_{ce} = \frac{eB}{m_e}, \quad r_{Le} = \frac{v_{the}}{\omega_{ce}} \tag{1.5}$$

Here, B is the magnetic field and v_{the} the electron thermal velocity, defined as follows:

$$v_{the} = \sqrt{\frac{3k_B T_e}{m_e}} \tag{1.6}$$

The characteristic scales associated with the ion dynamics derive from similar definitions where the indices e are replaced by indices i.

1.2 Different descriptions of plasmas

As previously discussed, there is no computationally manageable (and general) method to model a plasma as an N-body system of charged particles out of equilibrium. Indeed, this description would correspond to solving huge numbers (equal to N) of 3-dimensional vectorial equations of motion, with all particles being coupled one each other via the long-range electromagnetic interactions. Such a calculation is not achievable even on the more powerful supercomputers of the last generation. Thus, it is necessary to reduce the dimensionality of the problem. By taking several assumptions starting from the N-body system, one obtains different *plasma models*, whose spatial and temporal validity limits depend on the assumption. First of all, we find the collisionless Vlasov model valid at all scales, which can be further simplified to get reduced model equations aiming at studying plasma dynamics. In this section, we present the main plasma models and discuss their validity regimes.

1.2.1 The Vlasov-Maxwell equations

To rule out the deterministic N-body description of a plasma, a statistical description is needed (see Klimontovich (1982) for instance). For that purpose, we can start by using a distribution function F for the ensemble of N particles in a 6N-dimensional configuration space (plus time):

$$F = F(t, \mathbf{x}_1, \mathbf{x}_2, ..., \mathbf{x}_N, \mathbf{v}_1, \mathbf{v}_2, ..., \mathbf{v}_N) \tag{1.7}$$

To describe the evolution of the system, a conservation law can be used (the distribution function is conserved as known from Liouville's theorem). We have $d_t F = 0$, where $d_t = d/dt$ is the total derivative along the system trajectory $\{\mathbf{x_i}(t), \mathbf{v_i}(t)\}_{i=1,...,N}$ and involving the electromagnetic terms in the acceleration terms. However, we still need to reduce the dimensionality. To have a statistical description in lower dimensions, we must reduce the number of dynamical variables in phase space. From F, we can define the s-*particles* distribution function, $F^{(s)}$, as follows:

$$F^{(s)}(t, \mathbf{x}_1, \mathbf{x}_2, ..., \mathbf{x}_s, \mathbf{v}_1, \mathbf{v}_2, ..., \mathbf{v}_s) = \int^{(N-s)\times 6} \int F \prod_{i=s+1}^{N} d^3\mathbf{x}_i d^3\mathbf{v}_i \tag{1.8}$$

where $1 \leq s < N$. This function indicates the probability of finding each of the s particles in the $(\mathbf{x}_s, \mathbf{v}_s)$ position in the phase space and has a reduced dimensionality, equal to $6s$ dimensions. Specifically, our goal here is to obtain a mathematical description of plasma dynamics in terms

of the single-particle distribution function ($s = 1$) $F^{(1)}(t, \mathbf{x}_1, \mathbf{v}_1)$, evolving in a six-dimensional phase-space. Nevertheless, by integrating Liouville's equation, the resulting equation for $F^{(s)}$ still contains terms that depend upon the higher-order distribution function $F^{(s+1)}$ and so on, because of correlations between particles. This means that the equation for one particle $F^{(1)}$ will also contain the two particles $F^{(2)}$ (and so on). This infinite set of coupled equations is known as the Bogoliubov-Born-Green-Kirkwood-Yvon (BBGKY) hierarchy. To reduce the dimensionality, one has to truncate the chain by performing a so-called *closure problem*.

In Vlasov theory, we assume that the potential interaction energy is so low with respect to the particle kinetic energy that "collisions" can be neglected. As a result, the particle dynamics is dominated by the average field collectively generated by all particles, rather than by binary particle interactions. In summary, particle correlation can be totally neglected, breaking the hierarchy chain starting from the equation for the $F^{(1)}$ where we put $F^{(2)} = 0$.
Hereafter, we will omit the single-particle index and identify $F^{(1)}(t, \mathbf{x}_1, \mathbf{v}_1)$ with $f_\alpha(t, \mathbf{x}, \mathbf{v})$. In particular, the plasma species α is described by the following distribution function:

$$f_\alpha(t, \mathbf{x}, \mathbf{v}) = \sum_i \delta(\mathbf{x} - \mathbf{x}_{\alpha,i}(t))\delta(\mathbf{v} - \mathbf{v}_{\alpha,i}(t)) \tag{1.9}$$

The resulting equation for a given plasma species α (either ions or electrons) is the Vlasov equation (Vlasov, 1968):

$$\frac{\partial f_\alpha}{\partial t}(\mathbf{x}, \mathbf{v}, t) + \mathbf{v} \cdot \nabla f_\alpha(\mathbf{x}, \mathbf{v}, t) + \frac{q_\alpha}{m_\alpha}\Big(\mathbf{E}(\mathbf{x}, t) + \mathbf{v}\ \mathbf{B}\Big) \cdot \nabla_{\mathbf{v}} f_\alpha(\mathbf{x}, \mathbf{v}, t) = 0 \tag{1.10}$$

where q_α is the charge, m_α is the mass of the particle species and c is the speed of light.
The complete plasma dynamics description is then obtained by the non-linear coupling of the Vlasov equation with the Maxwell equations to self-consistently calculate the electromagnetic fields:

$$\nabla \cdot \mathbf{E} = \frac{\rho_c}{\epsilon_0} \tag{1.11}$$

$$\nabla \cdot \mathbf{B} = 0 \tag{1.12}$$

$$\nabla \times \mathbf{E} = -\frac{\partial \mathbf{B}}{\partial t} \tag{1.13}$$

$$\nabla \times \mathbf{B} = \frac{1}{c^2}\frac{\partial \mathbf{E}}{\partial t} + \mu_0 \mathbf{J} \tag{1.14}$$

where the electric charge density ρ_c and the current density $\mathbf{J}$ are obtained from the particle's distribution function. Here μ_0 is the vacuum magnetic permeability.

Collision operators: closures on the plasma description

In the case when collisions cannot be completely ignored, Equation 1.10 can be generalized by modeling the (previously neglected) integral term involving the $F^{(2)}$ on the right-hand side with a collision operator for population α, S_α. Depending on the closure of collisions, this equation is known by different names such as Boltzmann or Fokker-Planck, depending on whether the collisions are modeled as hard-sphere binary interactions or if the source term has the form of a diffusion operator.
For instance, in the case of the Boltzmann equation, it assumes that the interactions between particles are all binary and elastic (particles see a field which is either zero or due to a single other particle) and molecular chaos (collisions are considered as random and independent events). With these assumptions:

$$S_\alpha = (\partial_t f_\alpha)_c = \int\int d^3\mathbf{v}_2 d^\Omega \sigma |\mathbf{v}_2 - \mathbf{v}| [f(\mathbf{v}')f(\mathbf{v}'_2) - f(\mathbf{v})f(\mathbf{v}_2)] \tag{1.15}$$

where σ is the differential collisions cross-section.

1.2.2 The Fluid description

The kinetic approach is often too complicated and the plasma dynamics must be described by a fluid approach, still taking into account the role of the electromagnetic fields. These equations are obtained by integrating the Vlasov equation moments over the velocity coordinates for each species in the plasma. To do so, we define the lowest-rank fluid moments as follows:

- *Density:*

$$n_\alpha = \int f_\alpha \, d^3v \tag{1.16}$$

- *Fluid Velocity:*

$$\mathbf{u}_\alpha = \frac{1}{n_\alpha} \int \mathbf{v} f_\alpha \, d^3v \tag{1.17}$$

- *Pressure Tensor (second rank tensor):*

$$\mathbf{p}_\alpha = m_\alpha \int (\mathbf{v} - \mathbf{u}_\alpha)(\mathbf{v} - \mathbf{u}_\alpha) f_\alpha \, d^3v \tag{1.18}$$

- *Heat flux (third rank tensor):*

$$\mathbf{Q}_\alpha = m_\alpha \int (\mathbf{v} - \mathbf{u}_\alpha)(\mathbf{v} - \mathbf{u}_\alpha)(\mathbf{v} - \mathbf{u}_\alpha) f_\alpha, d^3v \tag{1.19}$$

where we have omitted the tensor product notation ($\mathbf{u} \otimes \mathbf{u} \equiv \mathbf{uu}$, $(\mathbf{uu})_{ij} \equiv u_i u_j$). By increasing the fluid moment order, its rank increases. Higher-order fluid moments are defined correspondingly. Directly from these definitions, it is obvious that all fluid tensors must be symmetric in all of their indices.

Skipping the algebra (see for instance Krall et al. (1973) or Goldston and Rutherford (2003)) the first three moments of the fluid equations are given by:

$$\partial_t n_\alpha + \nabla \cdot (n_\alpha \mathbf{u}_\alpha) = 0 \tag{1.20}$$

$$\partial_t (n_\alpha m_\alpha \mathbf{u}_\alpha) + \nabla \cdot (n_\alpha m_\alpha \mathbf{u}_\alpha \mathbf{u}_\alpha + \mathbf{p}_\alpha) - m_\alpha q_\alpha \mathbf{E} + \mathbf{u}_\alpha \times \mathbf{B} = 0 \tag{1.21}$$

$$\partial_t \mathbf{p}_\alpha + \nabla \cdot (\mathbf{u}_\alpha \mathbf{p}_\alpha + \mathbf{q}_\alpha) + \mathbf{p}_\alpha \cdot \nabla \mathbf{u}_\alpha + (\mathbf{p}_\alpha \cdot \nabla \mathbf{u}_\alpha)^{\mathrm{T}} + \frac{q_\alpha}{m_\alpha c} \left[\mathbf{B} \times \mathbf{p}_\alpha + (\mathbf{B} \times \mathbf{p}_\alpha)^{\mathrm{T}} \right] = 0 \tag{1.22}$$

The fluid description of plasma is formally composed of an infinite chain of differential equations, one for each fluid moment, such as the ones defined in Equations 1.16 to 1.19 (and subsequent equations higher-order descriptions). Each fluid moment (i) equation, Eq. 1.20 to 1.22, implies the higher (i+1) fluid moment. This infinite chain of fluid equations self-consistently coupled with Maxwell's equations, represents the equivalent of the Vlasov-Maxwell system of equations. To be able to describe the plasma with a finite set of equations one must imperatively make a hypothesis (defined as *a closure*) about a moment that allows one to describe the (i)th moment using only lower order moments. Closures are chosen depending on the dynamics of interest of the system at study and are justified only for a range of parameters and for a chosen regime of the dynamics. The easiest example of closure is the polytropic closure. In this closure, the pressure is linked to the density through the relation $pn^{-\gamma} = const$ [1]. Several examples of the most common closures used for the study of collisionless plasma are presented in Chust and Belmont (2006).

[1] Here γ is the polytropic index. This closure includes the adiabatic and the isothermal (when $\gamma = 1$) limits.

1.2.3 The ideal Magneto-Hydrodynamics (MHD) equations

Starting from the multi-fluid description above (*i.e.* fluid equations for each species) we can derive a single fluid description, valid at characteristic scale L and velocity U. It is known as the ideal-MHD theory and it is adopted to describe the low-frequency and large-scale dynamics of a quasi-neutral plasma composed of ions and massless electrons. This theory is based on the following assumptions:

- The dynamics is limited to large scales, $L \gg \rho_i, d_i$ and low frequencies, $\omega \ll \Omega_{ci}$ [2];
- The pressure is supposed isotropic (diagonal tensor);
- The characteristic velocity is much lower than the light speed, $U \equiv L/\tau \ll c$ (where l and τ are the characteristic length and time scales of the dynamics, respectively). Fast variations and sharp boundaries can therefore not be described by the model;
- Furthermore, one typically also assumes zero electron mass ratio limit, $m_e/m_i \to 0$.

In MHD, the fluid density and velocity are defined as follows:

$$\rho = \sum_\alpha n_\alpha m_\alpha \tag{1.23}$$

$$\mathbf{u} = \frac{\sum_\alpha n_\alpha m_\alpha \mathbf{u}_\alpha}{\sum_\alpha n_\alpha m_\alpha} \tag{1.24}$$

$$p + \rho u^2/2 = \sum_\alpha p_\alpha + \rho_\alpha u_\alpha^2/2 \tag{1.25}$$

Here, the sum over the different populations is limited to the ion populations (in case different ion populations are found in the plasma) since the electron mass is neglected. Under these conditions, we can sum Equations 1.20-1.22 for the different species and after some algebraic ordering and simplification we get the following system:

$$\begin{cases} \partial_t n + (\mathbf{u}\cdot\nabla)n = -n(\nabla\cdot\mathbf{u}) & (1.26) \\ \partial_t \mathbf{u} = -(\mathbf{u}\cdot\nabla)\mathbf{u} - \nabla p + \dfrac{(\nabla\times\mathbf{B})\times\mathbf{B}}{\mu_0} & (1.27) \end{cases}$$

As for the fluid theory, a closure, typically the polytropic relation discussed above, is needed. For a more generic closure, the tensorial description of the pressure tensor may be included in this model. However, this case corresponds to a generalization of MHD rather than the standard description. The system is completed with the Faraday equation (Equation 1.13) and Ohm's law (see e.g. Krall et al. (1973) or Belmont et al. (2014)), which for an ideal plasma (i.e. no collisions) is as follows:

$$\mathbf{E} + mathbfu \times \mathbf{B} = 0 \tag{1.28}$$

The generalized Ohm's law

For a non-ideal plasma, however, the generalized Ohm's law is used to obtain the electric field. In a collisionless plasma, this equation reads:

$$\mathbf{E} + \mathbf{u}\times\mathbf{B} = \frac{1}{ne}\mathbf{J}\times\mathbf{B} - \frac{1}{ne}\nabla\cdot\mathbf{P}_e + \frac{m_e}{ne^2}\left[\frac{\partial\mathbf{J}}{\partial t} + \nabla\cdot\left(\mathbf{uJ} + \mathbf{Ju} - \frac{\mathbf{JJ}}{ne}\right)\right] \tag{1.29}$$

[2] A consequence of this slow variation hypothesis is the so-called quasi-neutrality approximation. In in this limit the space charge is much lower than the charge densities of each species. Therefore, in MHD the plasma is assumed locally neutral, $n \simeq n_i \simeq n_e$.

The right-side terms are the so-called (in order) "Hall", "electron pressure", "electron inertia" and "resistive" terms. These terms come into play as soon as the dynamics approach the characteristic ion scale and have an important role in the description of plasma instabilities such as magnetic reconnection. In particular for the first two, while the Hall term is responsible for ion demagnetization, the electron pressure term is responsible for breaking the magnetic topology.

2 The Sun-Earth interaction and the magnetopause

Contents

While on Earth plasmas are rare, they are found ubiquitously in the universe, *e.g.* in interstellar and intergalactic space, stars, accretion disks, astrophysical jets, and around black holes. Plasmas are also common in the entire Solar System, from the solar atmosphere to the near-Earth environment and other planetary magnetospheres.
In this chapter, we present the solar system plasmas. In particular, we introduce the Sun-Earth's magnetosphere interaction (and, generalizing, the interaction of the solar wind with other planetary environments in the Solar system). Later, we focus on the so-called Earth's magnetopause, the boundary that separates the solar wind and the planetary magnetosphere.

2.1 The Sun-Earth interaction

The interaction between the Sun and the Earth's magnetosphere gives rise to a very complex time-evolving structure, which is the primary focus of the study in this manuscript. This chapter aims to familiarize the readers with this structure and outline the main themes explored in the manuscript. For a more comprehensive description, the main reviews used as a basis of the following discussion will be included for each topic.

2.1.1 The solar wind

The solar wind consists of a flow of charged particles, globally neutral, that escapes from the Solar corona outwardly and is embedded in the solar magnetic field. Its existence was first hypothesized based on its interaction with planetary bodies in the solar system. Ever since the nineteenth century it has been established that there is a connection between solar activity and disturbances in the Earth's magnetic field (Sabine, 1851, 1852; Hodgson, 1859; Stewart, 1861). However, the association of these phenomena with a flow of particles escaping the Sun began at the beginning of the 20th century (Birkeland, 1901; Chapman, 1917; Stormer, 1918). Later on, the momentum transfer from the solar wind to cometary ions, and the estimation of solar wind

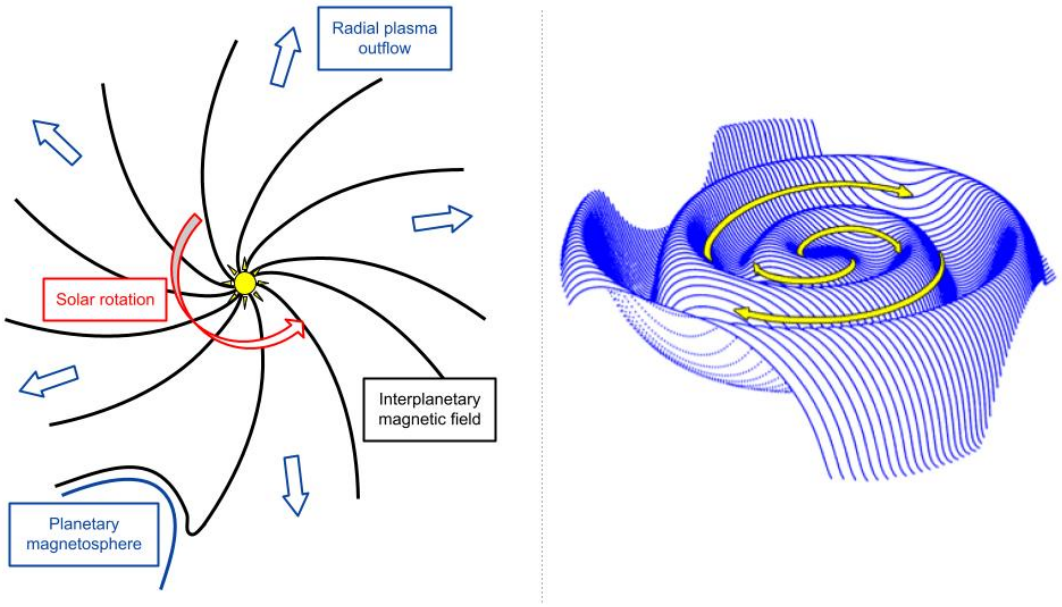

Figure 2.1: Left: Northward view of the Sun and the solar wind. The solar wind bending trajectories are underlined by the curves departing outwardly from the Sun. During its travel, the solar wind can impact magnetized objects (bottom left corner), forming a cavity(the magnetospheres). Credits: Modified from https://www-istp.gsfc.nasa.gov/istp/outreach/windandweather.html. Right: 3D visualization of the magnetic field lines in the solar wind (in yellow the Parker spiral). Credits: J. Jokipii, U Arizona.

velocity ranging between 500 and 1500 km s^{-1}, were quantified for the first time by Biermann and Schluter (1951) based on observations of comets' second tails systematically pointing away from the Sun. Since then, the solar wind has been a central topic in the community.

The origin of this flow of particles remained unclear until the first theoretical model of the solar wind, which was presented in Parker (1958). In this paper, E. Parker showed that the plasma in the Solar Corona, with a temperature of the order of millions of degrees Kelvin, has enough energy to overcome the gravitational potential energy of the Sun and to escape. According to Parker's model, the solar wind has a subsonic flow velocity at the base of the corona that increases monotonically as the logarithm of the distance. In this model, the solar wind becomes supersonic at about 5 solar radii from the Sun. Parker therefore found a solution with a radial flow with a velocity of the order of 500 km s^{-1} at the Earths orbit point is found, which is consistent with the observations.

A year after Parker's article, the Soviet spacecraft Luna 1 detected solar wind particles in space, and three years after, the observations were confirmed by NASA's Mariner 2 spacecraft[1]. Ever since rapid progress in solar wind physics has been made both in modeling and instrumentation (see the reviews for Viall and Borovsky (2020); Verscharen et al. (2019); Cranmer et al. (2017); Schrijver and Siscoe (2009); Schwenn and Marsch (1990, 1991), for instance)
The solar wind consists mainly of electrons, protons, and alpha particles. However, trace amounts of heavier ions such as oxygen, and iron are found. *In situ* measurements across the years also showed that the raw probability distribution of its speed in the ecliptic is usually single-peaked around 400 km s^{-1}, with a sharp cutoff below 250 km s^{-1}. Moreover, a negative correlation between the densities and the speed is observed for both protons and electrons. Furthermore, the solar wind plasma is almost collisionless, the mean free path being almost as large as the sun-earth distance. Therefore the magnetic field is "frozen-in" the plasma flow (non-ideal

[1]It is notable to mention that solar wind measurements were conducted by Explorer 10 (Bridge et al., 1962) However, it is currently understood that the spacecraft never reached the undisturbed interplanetary medium.

effects such as resistivity can be neglected, see Section 2.3.1.) Thus, to have a more realistic description of the solar wind we have to take into account the rotation of the Sun. As the solar wind magnetic field lines are anchored in the rotating Sun, their shape is an Archimedes'spiral, known as Parkers spiral, first proposed in Parker (1958), as sketched in Figure 2.1.

The Heliosphere

The region where the solar wind flows and where the Sun's magnetic field plays a very important and active role, is called the *Heliosphere*. It can be seen as a bubble in the flow of the local interstellar medium containing the entire Solar System ($R \sim 120$ a.u.) sustained by the pressure of the supersonic solar wind. At the edge of the Heliosphere, several discontinuities occur.

Firstly, the solar wind undergoes a sharp transition to subsonic flow in the so-called termination shock. Then, we found a region called Heliosheath where the plasma is slower, denser, hotter, and also the Suns magnetic field is compressed where the flow becomes even more turbulent. In this region, magnetic bubbles with sizes comparable to the Earth's orbit were observed by the Voyager mission (Opher et al., 2011). Finally, the last boundary called Heliopause is found, where the solar wind and the interstellar medium pressures eventually reach balance. The observed structure is similar to the structure formed from the interaction between the solar wind and planetary magnetosphere, which is analyzed in the following Section.

2.1.2 The Earth's magnetosphere and its interaction with the solar wind

The first to use the word magnetosphere was T. Gold in 1949 to describe the *region above the ionosphere in which the magnetic field of the [Earth] has a dominant control over the motions of gas and fast charged particles.* Quickly the word acquired the connotation it has today: the region of space dominated by a specific celestial body's magnetic field. The Earth's magnetosphere is continuously impacted by the solar wind dragging and shaping the magnetosphere plasma (including the frozen-in magnetic field) in the form of an elongated bubble around the planet. As a result, the magnetic field differs greatly from how it would have been if the planet was in a void environment. At the Earth, the dynamo sustains a quasi dipolar magnetic field with a magnetic moment $\mathcal{M} = 8.1 \cdot 10^{15} T m^{-3}$, corresponding to a magnetic field at ground level at the magnetic equator $B_{eq} = 0.31 \cdot 10^{-4} T$ [2].
The structure that develops from this interaction supports a very complex dynamics, presenting phenomena with a wide range of timescales and spatial lengths. We observe phenomena with timescales of a few seconds, as for the auroral pulsations (Yamamoto, 1988), together with phenomena lasting several days, such as the intensification of the electron radiation belt (Balikhin et al., 2011). Concerning spatial scales, we find phenomena with characteristic lengths between 0.4 cm (Debye length in the ionosphere) to $=10^6$ km for those concerning the whole magnetosphere, with thin layers of the order of the ion Larmor radius (typically about 1000 km).
As the solar wind reaches the terrestrial magnetic environment, it compresses the dayside and draws the nightside out into a magnetotail. The structure created with the interaction is divided into several sub-regions, as shown in Figure 2.2. Here we show a duskward view of the XZ plane in the GSE[3] frame with the solar wind flowing from the left.

[2] Similar magnetospheres are also found in other planetary objects within the Solar system, as discussed in Section 2.2

[3] The **Geocentric Solar Ecliptic (GSE)** coordinate system is an orthogonal system defined as follows:

- The **x** axis lies in the Earth-Sun direction and points toward the Sun;
- The **z** axis is perpendicular (pointing northward) to the ecliptic plane, defined as the plane of Earth's orbit around the Sun.;
- The **y** is defined subsequently.

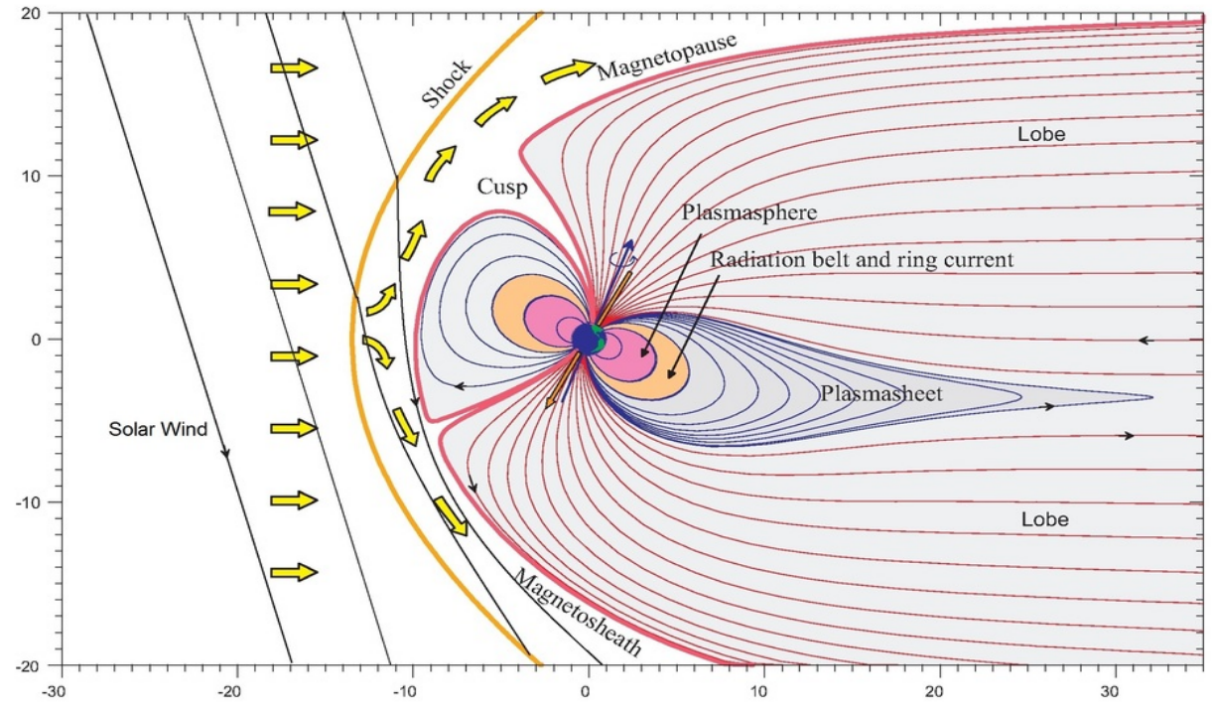

Figure 2.2: Dusk-ward view of the Earths magnetosphere. The main sub-regions are shown. The magnetospheric magnetic field is computed with the Tsyganenko statistical model (Tsyganenko, 1989). The units of the axes are in Earths Radii and the frame used is the Geocentric Solar Ecliptic (GSE) frame. Credits: P. Robert (CETP/CNRS)

At the Earth, the solar wind flows faster than both the magnetosonic and the Alfvén speeds[4]. As a result, a collisionless shock, the so-called bow shock, is formed. At the bow shock, the supersonic flow jumps down into a subsonic flow with a strong increase in plasma density, temperature, and magnetic field strength. The characteristic width of the bow shock is usually comparable to the local ion Larmor radius while it is located between 13 and 15 Earth's radii from the planet. Moreover, the bow shock can be classified either as quasi-parallel or quasi-perpendicular depending on the value of the angle between the shock normal and the upstream magnetic field's direction (with 45° being the threshold between the two). The existence of these two shock geometries leads to different, intrinsically kinetic, dynamics both along and across the bow shock (Burgess and Scholer, 2015).

Downstream of the bow shock, the *magnetosheath* is found first. The magnetosheath is a turbulent region where the shocked solar wind plasma is wrapped around the magnetosphere. Its shape and size vary depending on the strength of the solar wind and the orientation of the interplanetary magnetic field. Then, we find the *magnetopause*. It can be defined as the proper boundary between the Solar wind and magnetospheric magnetic fields. The magnetopause is characterized by a current sheet due to the difference between the (variable) solar wind magnetic field and the magnetospheric one, directed northward. The boundary is also characterized by a transition in plasma density. The magnetopause is the structure over which this work is focused and is described further in Section 2.3.

On the nightside of the Earth planet, the *magnetotail* is found. The magnetotail is a long, up to $\sim 200 R_E$, cylindrical-like structure where magnetic-field lines are connected to the Earth. However, the tail is not limited by boundaries as clear as its sunward side. The magnetotail is a

[4]Here the Alfvén velocity is defined $v_A = \sqrt{B^2/(2\mu_0\rho)}$, where B is the modulus of the magnetic field, μ_0 is the magnetic permeability of void and ρ is the plasma density.

reservoir of magnetic energy that powers several magnetospheric processes. The magnetotail is subject to global instabilities, in particular, those that produce substorms. Other geographical regions localized in the magnetosphere are:

- The *polar cusps*, defined as the regions where Earth's dipolar magnetic field diverges from the magnetic poles of the Earth.
- The *lobes*, characterized by open magnetic field lines that emerge from the Earths surface at one end while extending into interplanetary space at the other. They are characterized by low plasma density and magnetic field magnitude.
- The *plasma sheet*, a current sheet composed of highly energized plasma within Earth's magnetotail.
- The *plasmasphere*, a region composed of dense and cold plasma located just outside the ionosphere.
- The *Van Allen radiation belts* are concentric zones where energetic particles are trapped by the planetary closed magnetic field lines. The inner belt, closer to Earth, consists mostly of energetic protons, while the outer, extending further out, presents both protons and electrons.

A more detailed discussion of these regions, not treated in this manuscript, can be found for instance in Borovsky and Valdivia (2018)).

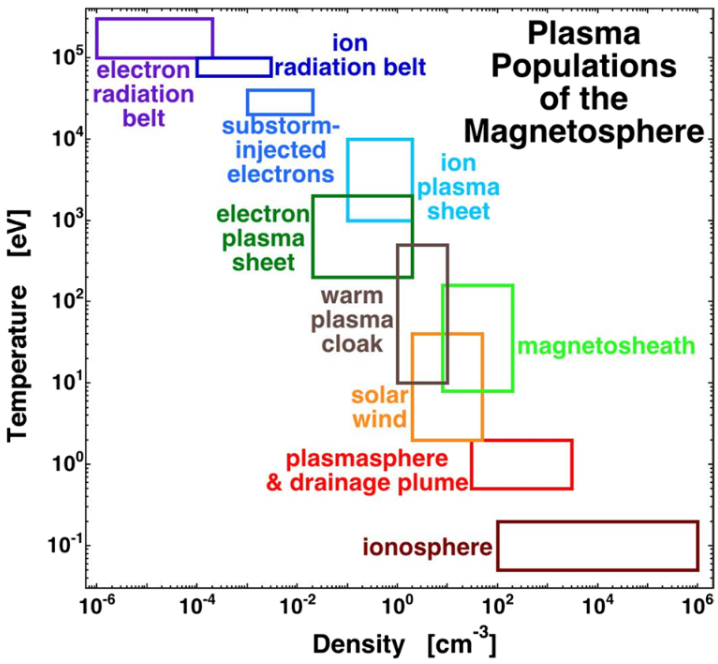

Figure 2.3: Plasma populations that populate the magnetosphere as a function of their temperature and density. Credits (Borovsky and Valdivia, 2018).

Furthermore, at the magnetosphere the different sub-regions present multiple plasma populations. Typical orders of magnitude of the density and temperature of these populations are shown in Figure 2.3. These plasmas are connected with each other via different types of electromagnetic plasma waves and instabilities that characterize the magnetosphere dynamics.

2.2 Planetary magnetospheres in the Solar System

In the previous section, we described the Earth's magnetosphere which was the first to be discovered. However, a similar structure surrounding other planetary objects interacting with a plasma flow has been discovered. The first *in situ* observations of planetary magnetospheres and their distinction from Earth's one date back to 1974 when the Jovian and the Hermean magnetospheres were observed through Pioneer 10 (Wolfe et al., 1974) and Mariner 10 missions (Ness et al., 1974), respectively. It is therefore worthwhile to compare these planetary magnetospheres with the Earth. Although they have not been investigated to the same extent due to their distances, past missions (such as Galileo, Cassini, or MESSENGER) as well as in progress or future missions (BepiColombo[5] and JUICE) have been undertaken or planned. The structure, dimension and typical dynamics of a planetary magnetosphere differ greatly depending on both the planetary body and the local solar wind properties. The size of a magnetosphere depends on the planet's magnetic field, radius, and the ambient solar wind density. Therefore, large magnetospheres are observed in planets with strong magnetic fields and those with weak magnetic fields surrounded by a more tenuous solar wind (farther from the Sun). Consequently, each magnetosphere exhibits unique and intriguing features that warrant thorough investigation. In the following, we discuss the main differences between these magnetospheres while a more complete discussion can be found in Bagenal (2013).

2.2.1 Solar wind parameters at different planets

As the distances between the planets in the Solar System and the Sun span over two orders of magnitude, the solar wind properties observed at these planets are widely different. The density of particles (mainly electrons and protons) decreases as the inverse square of the distance from the Sun. Moreover, the IMF varies with the distance, with its magnitude decreasing roughly as $r^{3/2}$. An overview of the solar wind parameters at the Solar System planets is shown in Table 2.1.

	a_p[au]	SW density [cm^{-3}]	IMF strength [nT]	IMF azimuth angle
Mercury	0.39	53	41	23^o
Venus	0.72	14	14	38^o
Earth	1.	7	8	45^o
Mars	1.52	3	5	57^o
Jupiter	5.2	0.2	1	80^o
Saturn	9.5	0.07	0.6	84^o
Uranus	19	0.02	0.3	87^o
Neptune	30	0.006	0.2	88^o
Pluto	40	0.003	0.1	88^o

Table 2.1: Properties of the solar wind at different planet locations. a_p is the distance between the planet and the Sun and it is computed at the semimajor axis of the orbit (1 au $=1.5\cdot10^8$km). The density indicated is the mean value (it fluctuates a factor of 5 about typical values, *i.e.* $n_{sw} \sim 7/a_p^2$ with a_p the distance of the planet in A.U.). IMF azimuth angle is $\tan^{-1}(B_\phi/B_r)$. Credit: Bagenal (2013)

	R_p [km]	Surface magnetic field [nT]	R_{mp} [R_p]	Magnetosphere size [R_p]
Mercury	2 439	195	1.4-1.6	1.5
Venus	6 051	-	-	-
Earth	6 373	30 600	10	8-12
Mars	3 390	-	-	-
Jupiter	71 398	430 000	46	63-93
Saturn	60 330	21 400	20	22-27
Uranus	25 559	22 800	25	18
Neptune	24 764	13 200	24	23-26
Pluto	1 153	Not known	Not known	Not known

Table 2.2: Scales of Planetary magnetospheres. R_p is the planetary radius while R_{mp} is the magnetopause nose distance, estimated from a theoretical formula (see Eq. 2.4) for typical solar wind conditions of the solar wind density (given in Table 2.1) and a velocity of 400 km s^{-1}. For outer planet magnetospheres, this underestimates the actual distance Kivelson and Russell (1995). R_{mp} and the magnetospheric sizes are expressed in the unit of planetary radius. Credit: Kivelson and Bagenal (2014).

2.2.2 Planetary differences

Other than the solar wind parameters, the intrinsic characteristics of individual planets strongly influence the structure and characteristic scales of their magnetospheres. On one hand, not all planets are magnetized: Venus and Mars have null or very small (remnant) magnetic fields. On the other hand, the magnetic fields of the magnetized planets vary by several orders of magnitude. Since the distance of the magnetopause from a planet can be estimated from a balance between the dynamic pressure of the solar wind and the planetary magnetic field pressure (as discussed in Section 2.3), the dimension of the magnetosphere can vary a lot depending on the internal magnetic field strength. Table 2.2 lists key parameters for the different planets, including the magnetic field at the surface and the characteristic scale of these magnetospheres. Moreover, also planetary satellites can present magnetospheres. As for planets, some of them have an intrinsic magnetic field (such as Ganymede) while some others (such as Titan, Io, Enceladus, Europa, and the Earth's Moon) do not. The peculiarity of these magnetospheres is that they can be completely contained within the planet's magnetosphere, not interacting with the pristine solar wind and enhancing the differentiation of magnetospheres in planetary objects. Furthermore, asteroids (small bodies with a radius below 1000 km) and comets may be characterized by a region surrounding them resembling the planetary ones. However, these magnetospheres are not analyzed here. A more detailed description can be found in Bagenal (2013) and Kivelson and Bagenal (2014).

Non-magnetized planets

The two non-magnetised planets are Mars and Venus. The former presents an extremely small planetary magnetic field while the latter is nonexistent. The electrical conductivity of the body determines the interaction between these unmagnetized planets and the supersonic solar wind. In general, the interaction with the plasma flow occurs via the remnant magnetization of the crust and/or currents associated with local ionization or induced in an electrically conductive ionosphere. This interaction forms a region similar to a planetary magnetosphere, causing the magnetic field of the solar wind to drape around the planets. For Mars and Venus (and also for Titan, Io, Enceladus, and Europa) this process is driven by their ionospheres. A schematic

[5]Described in detail in Section 8.2

illustration of this interaction is shown in Fig. 2.4.

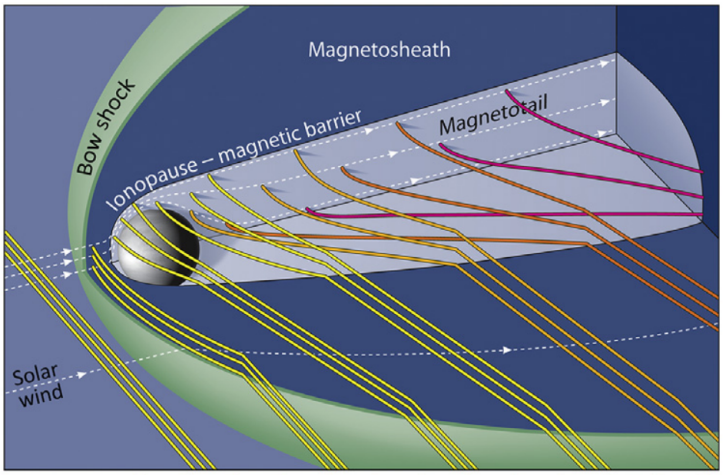

Figure 2.4: Schematic illustration of the interaction between the solar wind and an unmagnetized planet like Mars or Venus. Credit Kivelson and Bagenal (2014).

A different condition is found at the Earth's Moon, due to a very low surface conductivity and the absence of an ionosphere. In this case, there is no deflection of the solar wind which runs directly on the surface, where it is absorbed. As a result, the region immediately downstream of the Moon is left partially devoid of plasma.

Magnetized planets

As shown in Table 2.2, six planets in the solar system present an internally generated magnetic field: Mercury, Earth, Jupiter, Saturn, Uranus and Neptune. To possess a magnetic dynamo, a planet must have a large fluid, electrically conductive region undergoing convective motion. While the terrestrial planets have differentiated cores consisting of liquid iron alloys, in the high-pressure environments within the gas giants like Jupiter and Saturn, hydrogen exhibits metallic (liquid metal-like) properties. Uranus and Neptune, instead, have a mixture of water, ammonia, and methane forming a deep conducting "ocean". Even if planetary magnetic fields are usually simplified as dipoles, it is worth noticing that almost all planets exhibit non-dipolar contributions. In this sense, an excellent indicator is the ratio of the minimum to the maximum magnetic field at the planetary surface (equal to 2 for a dipole). This value is 2.8 at Earth, 4.5 at Jupiter, 12 at Uranus, and 9 at Neptune, demonstrating strong non-dipolar components, especially in the two latter.

While the size of a planet's magnetosphere depends on the strength of its magnetic field, the internal dynamic is determined by the offset of the dipole from the planet's center and by two angles, the one between the dipolar moment and the planet's spin axis (tilt angle), and the one between the planet spin axis and the solar wind direction. Both angles can be considered as constant to describe the magnetospheric configuration during a most of the plasma phenomena under study. This is because the angle between the spin axis and the solar wind direction varies significantly only over a planetary year and the planets magnetic field is assumed to vary only on geological timescales. Therefore, those magnetospheres of planets with dipole tilts below $\sim 10^{\circ}$ (i.e. Mercury, Earth, Jupiter, and Saturn) are reasonably symmetric and quasi-stationary. In the case of large dipole tilt angles, instead, a great variation of the relative direction between the orientation of the magnetic fields and the interplanetary flow direction is observed over a planetary rotation period. Therefore, highly asymmetric magnetospheres varying at the period of planetary rotation are observed. This is the case of Uranus and Neptune (having a tilt angle

of 59 and 47° respectively). A more accurate description of the differences between planetary magnetospheres can be found in Bagenal (2013).

Since the four terrestrial planets have far weaker magnetic fields generated in their interiors than the giant planets, as shown in Table 2.2, the difference in scale of the magnetospheres is huge. This difference in scales is schematized in Figure 2.5, comparing the magnetosphere structures of Mercury, the Earth, Jupiter and Saturn.

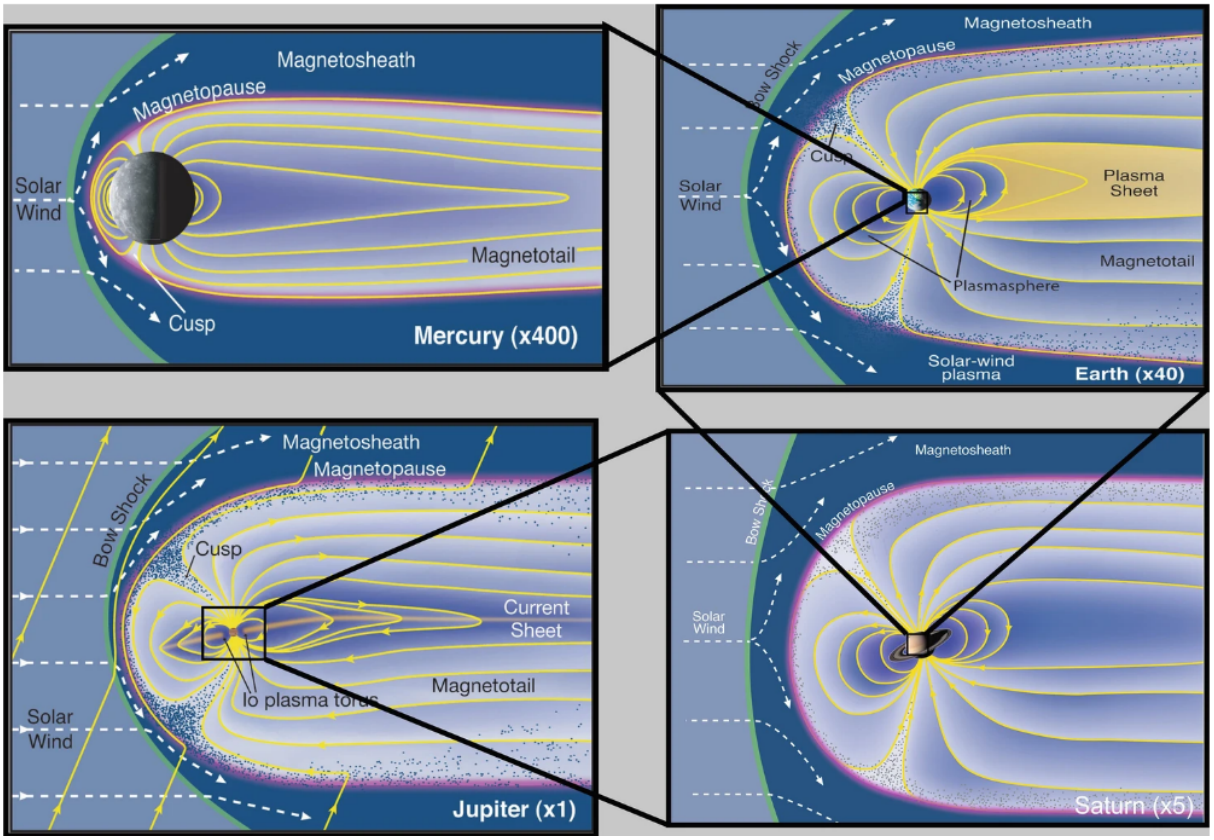

Figure 2.5: Scaling of the magnetospheres from Mercury, Earth, Saturn, to Jupiter. Credit Bagenal (2013).

2.3 The Earth's magnetopause

As discussed above, the magnetopause can be defined as the proper boundary between the solar wind and the magnetospheric plasma. In particular, the magnetopause separates the solar wind plasma, slowed down by the *bow shock*, and the magnetospheric one. The magnetopause is characterized by a transition in both the magnetic field direction and its magnitude. It is therefore a current sheet, which is usually referred to as the Chapman-Ferraro current.This boundary is also characterized by a transition in plasma parameters: density and temperature, and more generally distribution functions. This section aims at introducing the Earth's magnetopause, the main focus of this manuscript, in detail.

2.3.1 A large scale explication of the existence of the magnetopause

The existence of the magnetopause boundary can be explained as a consequence of the frozen-in property, which prevails at large scales. Let us first briefly recall this property and its demonstration.

The frozen-in flux theorem

The frozen-in-flux theorem, also known as the Alfvén theorem, describes the behavior of the magnetic field in a plasma. This theorem states that in an ideal plasma, as long as the ideal Ohm's law

$$\mathbf{E} + \mathbf{u} \times \mathbf{B} = 0 \tag{2.1}$$

is valid, the magnetic field lines are "frozen" into the fluid motion of the plasma. In other words, as the plasma moves and evolves, the magnetic field lines move with it, maintaining their topology. From this theorem it follows that the plasma and the magnetic field move anchored to each other at the so-called frozen-in velocity, given by $v_m = \mathbf{E} \times \mathbf{B}/B^2$.
This theorem can be demonstrated by considering the temporal variation of magnetic flux ψ through a loop C, moving with the plasma and spanning a surface called S. We have:

$$\frac{d\psi}{dt} = \int_C \frac{\partial}{\partial t}(\mathbf{B} \cdot d\mathbf{S}) \tag{2.2}$$

In this equation, both the magnetic field and the surface are varying. Concerning the magnetic field variation, we can use the $\partial \mathbf{B} \partial t = -\nabla \times \mathbf{E}$ equation. The variation of the surface S, instead, causes a change of magnetic flux per unit equal to $\mathbf{B} \cdot \mathbf{u} \times d\mathbf{r}$. By using the cross theorem on this term, we can rewrite Equation 2.2 as follows:

$$\frac{d\psi}{dt} = \int_C \nabla \times (\mathbf{E} + \mathbf{u} \times \mathbf{B}) \cdot d\mathbf{S} \tag{2.3}$$

which is equal to zero as long as the ideal Ohm's equation is valid.
The broader condition for the frozen-in property extends beyond the ideal Ohm's law, as it holds true wherever there is an absence of parallel electric fields, or even more broadly when the curl of the parallel electric field is zero (Belmont et al., 2012). This constraint arises directly from the electromagnetic properties described by Maxwell's equations and is solely contingent on plasma characteristics through the existence -or not- of the ideal Ohms law, which has the capability to nullify the parallel electric field.

Boundary between two colliding magnetized plasmas

In first approximation, we can consider the solar wind and the magnetospheric plasma as two plasmas pushed against each other. Due to the frozen-in flux condition, a thin discontinuity (*i.e.* the magnetopause) separating the two mediums is created. Therefore the magnetospheric and solar wind plasmas have to remain separated wherever the frozen-in condition is respected. Nevertheless, this simple view of the behavior of the two plasmas is in reality more complex since the frozen-in condition is valid only on ideal-MHD scale lengths. The two plasmas can indeed reconnect (occurring at the so-called "reconnection layer") around some regions where the condition is broken, as detailed in Section 2.3.4. In the following chapters, however, we will demonstrate how other kinetic effects may be taking place within the magnetopause allowing for the two media to interact. Consequently, this idea of the magnetopause as a discontinuity strictly separating two independent media except in some places may be inaccurate.

2.3.2 Magnetopause global features

The structure of the magnetopause has long been studied thanks to many space missions that have made enormous progress in understanding this barrier over the past seventy years[6]. In particular, measurements made by the Cluster (Escoubet et al., 1997) and the Magnetospheric Multiscale (MMS) Mission (Burch et al., 2016) allowed to characterize the boundary global

[6] An introduction of the timeline of the magnetopause *in-situ* exploration is discussed in Section 3.1

features in detail. They have shown that the magnetopause's position and shape vary dynamically in response to changes in solar wind conditions, such as fluctuations in solar wind velocity, density, and magnetic field orientation. Figure 2.6 illustrates an example of a magnetopause crossing, as observed by one of the Magnetospheric Multiscale (MMS) mission satellites. The mission is introduced in Chapter 3. Significant changes are evident in all visible parameters: the magnetic field reverses, plasma density increases sharply, and ion temperature decreases.

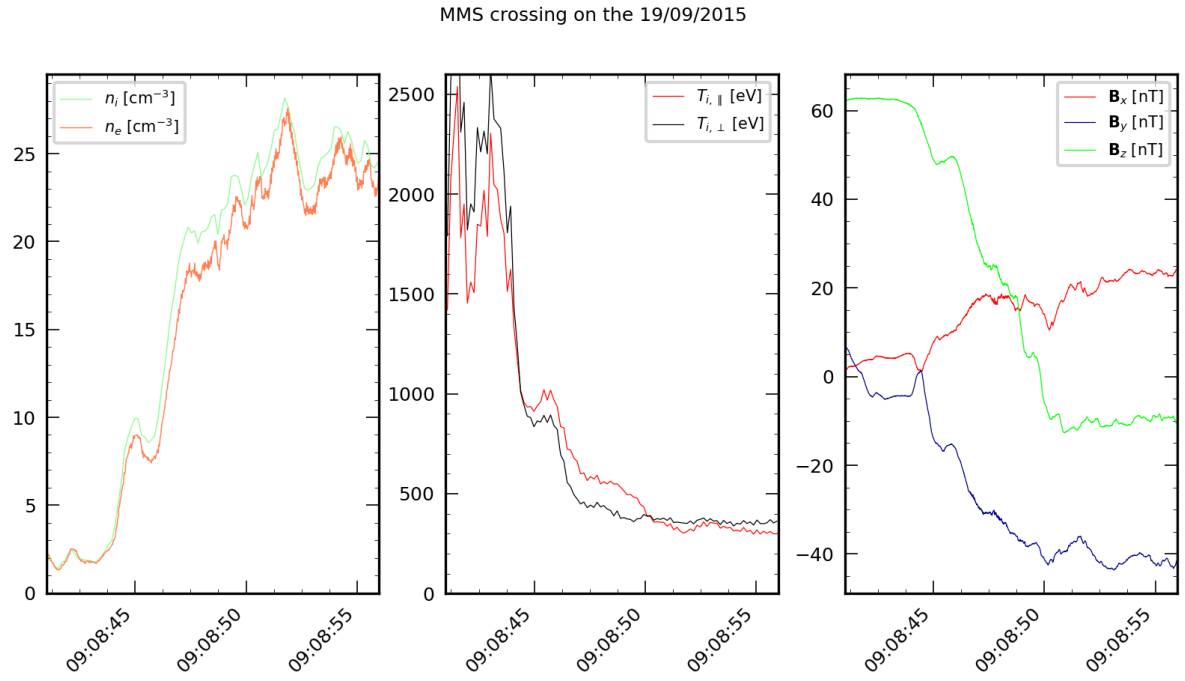

Figure 2.6: Crossing of the magnetopause as observed from MMS1. Here the ion and electron densities (left), the ion parallel and perpendicular temperature (centre) and magnetic field (right) are shown. The spacecraft is going from the magnetosphere to the magnetosheath.

By performing a statistical study on almost 3000 MMS magnetopause crossings, Haaland et al. (2020) estimated the mean value of the magnetopause thickness to be 734 km on the dayside (corresponding to around 12.5 d_i). This result is in line with earlier results, estimating the thickness to be in the (700 ± 300) km interval (Berchem and Russell, 1982a; Phan and Paschmann, 1996; Paschmann et al., 2005a). Moreover, the magnetopause is observed to be thicker at the flanks (approximately $15 - 20\%$) than at the dayside, either if the thickness is estimated in kilometers or reduced units of the upstream ion gyroradius or upstream ion inertial length. The boundary displacement velocities vary from a few tens of $km.s^{-1}$ to extreme values of several hundred $km.s^{-1}$. Finally, the acceleration of the boundary is far from negligible, reaching values on the order of 10 $km.s^{-2}$. Other mean values of the main physical parameter at the Earth's magnetopause can be found in (Haaland et al., 2020).

An interesting feature of the magnetopause is that the width of this structure is much smaller than the scale of the whole magnetosphere (of about $\sim 10R_E$, where $R_E = 6371$ km is the Earth's radius). For this reason, the magnetopause is usually viewed as a nearly two-dimensional thin boundary. Despite representing only a fraction of the overall structure, the internal structure of the magnetopause plays a pivotal role in regulating the exchange of plasmas between the solar wind and the magnetosphere.

2.3.3 How to model the magnetopause global structure

Although never mentioning the word "magnetopause", one of the first descriptions of this boundary was suggested by Chapman and Ferraro (1930). Theoretical calculations of the location of the magnetopause were obtained by using a hydrodynamic description (including the magnetic field) of the medium (as, for instance, in Spreiter et al. (1966a)). In this approximation, the shape of the structure can determined by the balance between the three pressures that exist in the plasma state: the dynamic (mnV^2), the thermal (nK_BT) and the magnetic ones ($\mathbf{B}^2/(2\mu_0)$). Here we defined $\mathbf{B}$ as the magnetic field and m, n, T, V as the ion mass, density, temperature and velocity. In the solar wind, the main pressure is the dynamic one. In the magnetospheric plasma instead, the magnetic pressure is the dominant one. Therefore, the balance between these two defines the location of the magnetopause (Tsyganenko, 1989; Baumjohann and Treumann, 1996).

By assuming for simplicity a dipolar magnetic field, from the force balance we can estimate the distance r_{mp} of the nose of the magnetopause (namely the *subsolar point*) with respect to the center of the planet:

$$\frac{r_{mp}}{R_E} = 2^{1/3}\left(\frac{B_{eq}^2}{2\mu_0\rho_{sw}u_{sw}^2}\right)^{1/6} \tag{2.4}$$

Here we defined ρ_{sw} the solar wind mass density and u_{sw} the solar wind flow speed, both upstream the *bow shock* and assumed that the strength of the magnetic field is $B(r) = B_{eq}(R_E/r)^3$, where B_{eq} is the magnetic field at the equator at the Earth's surface. The factor $2^{1/3}$ comes from the fact that, in reality, the magnetopause current produces a distortion on the dipole magnetic field due to the compression on the day-side. Therefore, the magnetic field within the magnetopause is approximately twice as large as that of a dipole. This approximation offers a valuable estimate of the magnetopause position, however, with limited precision. This limitation arises since the plasma beta (β) on both media typically approaches unity, and also because it overestimate the effects of the bow shock and the magnetosheath in altering solar wind properties. Furthermore, due to the deflection of the flow, the ram pressure at the magnetopause is reduced from the one far from the magnetopause by a factor $k \sim 0.88$ (Spreiter, 1976).

A theoretical model linking properly the position of the magnetopause and the solar wind parameters (as a function of the relative angle to the Sun-Earth axis) has been of strong interest inside the community over the years. Due to the complex interaction between the solar wind and the planetary magnetic field (over which the dynamics of the turbulent solar wind must be considered), many empirical models have been developed based on *in situ* observations. Understanding the influence of the solar wind and the interplanetary magnetic field (IMF) on the magnetopause requires the identification of the location of the magnetopause under a large variety of conditions. For this reason, many authors have developed statistical models to link the location of the magnetopause to the solar wind characteristics, employing different functional forms. It is worth noticing that one notable difficulty in this approach lies in the fact that the thickness of the magnetopause can vary, depending both on the location and solar wind conditions. In addition, depending on the satellite's trajectory relative to the magnetopause, numerous crossings can be observed in succession over long periods. Notable examples of these statistical models include Sibeck et al. (1991); Shue et al. (1997); Case and Wild (2013); Hasegawa (2012); Nmeek et al. (2020) and Nguyen et al. (2022b).

The Shue et al. (1997) model, along with its improved version presented in (Shue et al., 1998) following the validation with a magnetic cloud event in 1997, stands out as one of the most widely used analytical models. This model was derived as an empirical best fit to data from several magnetospheric satellites, including ISEE 1 and 2 and IMP 8, and will be used in this study to provide the relationship between the magnetopause radial distance r as a function

of the IMF z component, and the solar wind dynamic pressure. The distance turns out to be:

$$r = r_0 \left(\frac{2}{1 + \cos\theta} \right)^{\alpha} \tag{2.5}$$

where θ is the zenith angle and r_0 and α are parameters depending on the solar wind parameters. This model assumes axisymmetry around the Sun-Earth axis (an hypothesis questioned by the observations of Boardsen et al. (2000) and Safrankova et al. (2002)) and does not account for magnetospheric cusp regions. However, despite its limitations, it remains a valuable tool for our study. Its combination of accuracy and simplicity makes it well-suited for our purposes.

2.3.4 The magnetopause: a far-from-ideal boundary

The simplified concept of the magnetopause as a stationary discontinuity with one-dimensional gradients, everywhere and at all times, does not capture the complexity of its structure. In reality, the magnetopause exhibits a dynamic and multidimensional structure where plasma instabilities do play a key role.

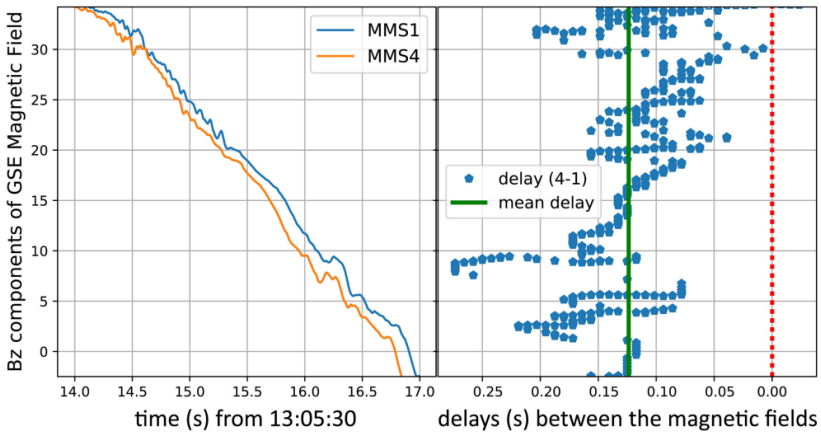

Figure 2.7: *Left:* the magnetic field component with the largest variation across the magnetopause (B_z), for two of the four MMS satellites. *Right:* Time delays occurring between measurements of the same magnetic field component for the same two satellites. (Credit: (Rezeau et al., 2018))

Regarding the routinely adopted assumption of a stationary magnetopause, recent missions such as Cluster and MMS (presented in detail in Chapter 3) have demonstrated that this assumption is not always valid (Paschmann et al., 2005b). The fact that the motion of the magnetopause can be different from being constant is evident from Figure 2.7showing a result from Rezeau et al. (2018). On the left panel, the most variable component of the magnetic field recorded by two of the four MMS satellites is shown. On the right, the time delay between measurements of the same B_z value is depicted. For a one-dimensional structure (such as the one here analyzed) moving at a constant normal velocity, such time delay should remain constant, even for spacecraft with different tangential positions. However, the delay between records of the same magnetic component value varies with time, exhibiting secular variation superimposed on large fluctuating components. The secular variation suggests that the magnetopause is not moving at a constant velocity but is instead decelerating in the considered crossing.

Furthermore, the magnetopause is characterized by a variety of transfer processes, each playing a distinct role in plasma dynamics, which can cause mass and magnetic flux transfer between the magnetospheric and magnetosheath plasmas. A compelling piece of evidence indicating plasma transfer at the magnetopause is the presence of boundary layers of magnetosheath plasma located earthward of the magnetopause, as noted by Eastman et al. (1976).

This boundary layer is referred to as low-latitude boundary layer or high-latitude boundary layer, depending on the location where it is observed. Processes allowing for mass and magnetic flux transfer include finite gyroradius scattering, diffusion, wave-induced diffusion, impulsive penetration, Kelvin-Helmholtz instability (KHI), and magnetic reconnection[7] (Fuselier, 2021). Notably, magnetic reconnection can be instigated by primary MHD instabilities, leading to it acting as a secondary instability. A meaningful phenomenon in this context is "Doubled mid-latitude Reconnection," as described by Faganello et al. (2014). This phenomenon serves as a clear example of the intricate interplay between the KHI and magnetic reconnection, where the latter is induced by the former.

2.3.5 The magnetopause as a space laboratory

As delineated in this chapter, the magnetopause turns out to be a very complex structure in which the flow of mass and magnetic field between the solar wind and magnetosphere is regulated. The magnetopause plays so a role of fundamental interest in so-called *Space Weather*, which encompasses the study of variations in conditions within the Solar System and heliosphere and their implications for human activities and life. Occurring almost periodically, on an 11-year cycle, the frequency and magnitude of phenomena on the surface of the Sun, such as Coronal Mass Ejections (CMEs) and solar flares, peak, releasing substantial quantities of energetic particles. These particles can be dangerous to life on Earth, altering to the magnetosphere and exposing the planet's surface to high-energy particles. Therefore, it is essential to comprehend the behavior of the magnetopause and its response to those events in order to predict and mitigate their possible effects on Earth.

The interest in the magnetopause extends beyond merely its relevance to space weather. Among the features that make the magnetopause of interest to the scientific community, we note the two following:

- Earth's magnetopause is the closest boundary between two astrophysical plasmas, allowing us to have precise in situ measurements. While data for other planets have been acquired during the years of space exploration, none match the resolution available at Earth and the amount of such measurements is by far lower than what we have of the Earth's. Furthermore, all these measurements come from single-satellite missions. At Earth, as discussed in Chapter 3, we have a large number of crossings available through multi-satellite missions, allowing to calculate gradients of the measured quantities.

- At the magnetopause, characteristic length scales are significantly larger than the dimensions of the probes. Indeed, spacecraft typically have dimensions in the order of a few meters. Contrary, the finest phenomena, such as magnetic reconnection, have a typical scale of around 10 km. Hence, within the magnetopause, it is possible to probe the plasma at length scales that cannot be achieved, even after re-scaling, using laboratory setups.

For these reasons, the Earth's magnetopause serves as a natural laboratory. Firstly, the study of this complex structure can help us improve our understanding of plasma physics and of all the physical processes outlined in the previous section, with a particular emphasis on magnetic reconnection. Secondly, studying the terrestrial magnetopause is valuable for comprehending planetary magnetopauses throughout the Solar System. This can also be helpful in designing and planning future space missions aimed at investigating these environments. Finally, as for the study reported in this manuscript, magnetopause can be used to study discontinuities between plasmas of different origins. Indeed, in space physics, the medium naturally self-organizes into distinct cells separated by thin layers, modeled as discontinuities. Notable examples of these

[7] A brief introduction of magnetic reconnection and its consequences at the magnetopause can be found in Section 2.4

layers, other than the Earth's magnetopause, are the heliopause and the region of interaction of the solar wind with non-magnetized bodies, such as comets. Thin layers can also form spontaneously, far from any boundary conditions, in the context of a turbulent medium.
In particular, by focusing on those purely one-dimensional regions of the magnetopause away from X-points and X-lines, the boundary can be studied as a discontinuity between the magnetospheric and the magnetosheath media. In this regard, we will show in Chapter 4 that the Classic theory of Discontinuities (CTD) is insufficient for describing it properly and investigate how it has to be completed.

2.3.6 How to study the magnetopause

As discussed above, the magnetopause serves as a valuable natural laboratory. To explore this frontier, comprehensively understanding its features and the limitations of existing models, the following two distinct approaches can be exploited:

- Analysis of space mission data: *in situ* data play a pivotal role in exploiting the magnetopause to investigate the boundary from a discontinuity perspective. In this regard, the vast amount of data accumulated over the years, coupled with the high precision and resolution of recent measurements, enables us to conduct studies of the local features of the magnetopause with great precision while also examining magnetopause characteristics statistically. A focal point of our manuscript (and in the study of the magnetopause from *in situ* measurements) is the investigation of the structure's normal component. The accurate determination of a normal direction is of fundamental importance, allowing us to determine which terms are experimentally relevant but not included or wrongly assumed in current theories. Moreover, having a good knowledge of the normal direction is also necessary to determine the speed of the structure and its thickness.

- Modeling the structure through numerical simulations: Despite the significant role of spacecraft observations in probing magnetospheric dynamics, their inherent limitation lies in their difficulty at capturing phenomena that are spatially and temporally confined. Consequently, relying solely on *in situ* spacecraft data poses a significant challenge in achieving a complete temporal sequence and global perspective of magnetospheric dynamics. Numerical simulations offer another avenue for this investigation, allowing for a global perspective and the study of temporally localized phenomena. A wide range of models and initialization techniques, tailored to the specific requirements and physical scales targeted by the study, can be used for this purpose. Simulations enable the interpretation of *in-situ* measurements within a three-dimensional framework, allowing differentiation between temporal and spatial fluctuations and thereby enhancing the understanding of magnetospheric dynamics. In this particular investigation, global simulations are employed to reconstruct the magnetosphere (and, therefore, the magnetopause)'s overall perspective, possibly using kinetic models.

Both of these methodologies will be extensively detailed in the following chapters. These sections will delve into the current State-of-the-art approaches from the standpoint of the thesis study, followed by a comparison with the results of the research related to this thesis project.

2.4 Magnetic reconnection in planetary magnetospheres

Magnetic reconnection is a fundamental plasma process in which magnetic field energy is released through the reconfiguration of the field topology[8]. A schematization of the change in magnetic

[8]The role of the magnetic reconnection in the magnetopause dynamics is not the primary focus of the study detailed in the following chapters. Indeed, the study discussed in this manuscript focuses on the magnetopause regions showing stationary and one-dimensional features, which are situated at a considerable distance from re-

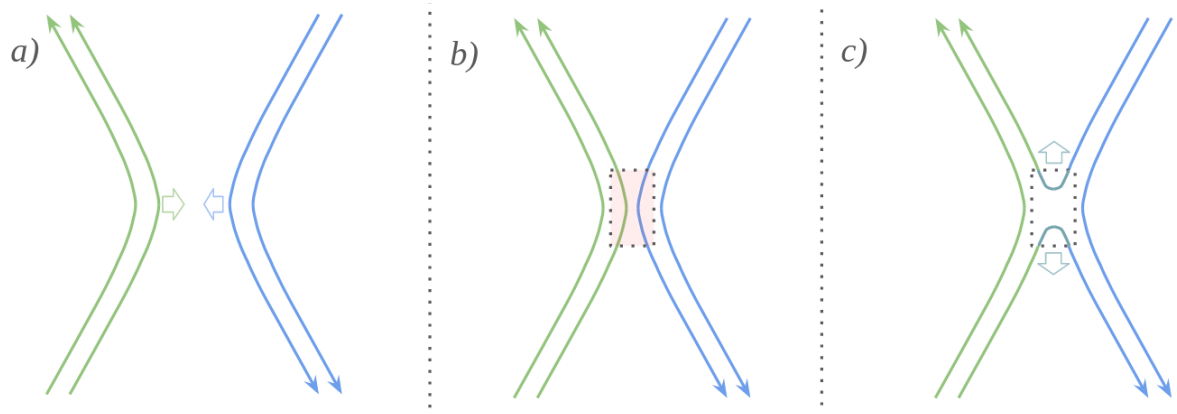

Figure 2.8: Change of topology of magnetic field lines during a magnetic reconnection event.(a): two magnetic field lines, belonging to two different plasma domains, approach each other transported by the flow. (b): the ideal Ohms Law (Equation 2.1) becomes invalid close to an "X point", inside the shadowed region (corresponding to the diffusion region). (c): the different plasmas are linked by the re-connected field lines while the energy magnetic energy is released as kinetic energy and heat.

topology resulting from reconnection is shown in Fig. 2.8. Magnetic reconnection is observed in a wide variety of magnetic environments such as the solar corona, planetary magnetospheres, and the heliopause. Its fundamental importance lies in its ability to transfer matter, momentum, and energy between different plasma environments while converting magnetic energy into thermal and bulk kinetic energy.
Magnetic reconnection is based on the formation of a two-layered diffusion region in which the magnetic field lines seem to break down and reconnect: the electron diffusion region (hereafter EDR), in which the frozen-in condition is broken for electrons that are demagnetized, and a broader ion diffusion region (IDR), which includes the EDR, in which ions are demagnetized. Here, demagnetized refers to the breakdown of the ideal Ohm's law (Eq. 2.1), due to the inclusion of nonideal processes not accounted for in MHD. Theory and modeling have shown that the thickness of the scattering region is approximately the inertial length of the corresponding particle (Drake and Kleva, 1991; Mandt et al., 1994; Biskamp et al., 1997; Fujimoto et al., 2011; Khotyaintsev et al., 2019), while its width is of the order of ten inertial lengths (Fuselier et al., 2017). A schematization of the standard two-dimensional magnetic reconnection figure is shown in Fig. 2.9. Three-dimensional effects of magnetic reconnection are not included in this section. For more information see (Yamada et al., 2010; Hesse and Cassak, 2020).

2.4.1 Location of magnetic reconnection in planetary magnetospheres

The significant importance of magnetic reconnection in planetary magnetospheres lies in its ability to allow solar wind particles to penetrate the magnetosphere. Furthermore, magnetic reconnection drives particle acceleration and their trajectories. In general, the location of magnetic reconnection depends on the solar wind orientation. For a southward IMF, magnetic reconnection occurs at the dayside magnetopause, specifically at the subsolar point in front of the planet. In these conditions, the solar wind stretches the magnetosphere toward the night side, resulting in the formation of a current sheet. Subsequently, magnetotail reconnection occurs, closing terrestrial field lines. This cyclic process, which couples the solar wind and the magnetosphere,

connection sites. The brief overview of this phenomenon provided in this section aims to establish a foundational context for the study outlined in Chapter 8. In Chapter 8, we use numerical simulations to investigate magnetic reconnection within Mercury's magnetotail, thereby extending beyond the scope of the main focus of this manuscript. For a more comprehensive treatment of magnetic reconnection, the reader is referred to the relevant literature.

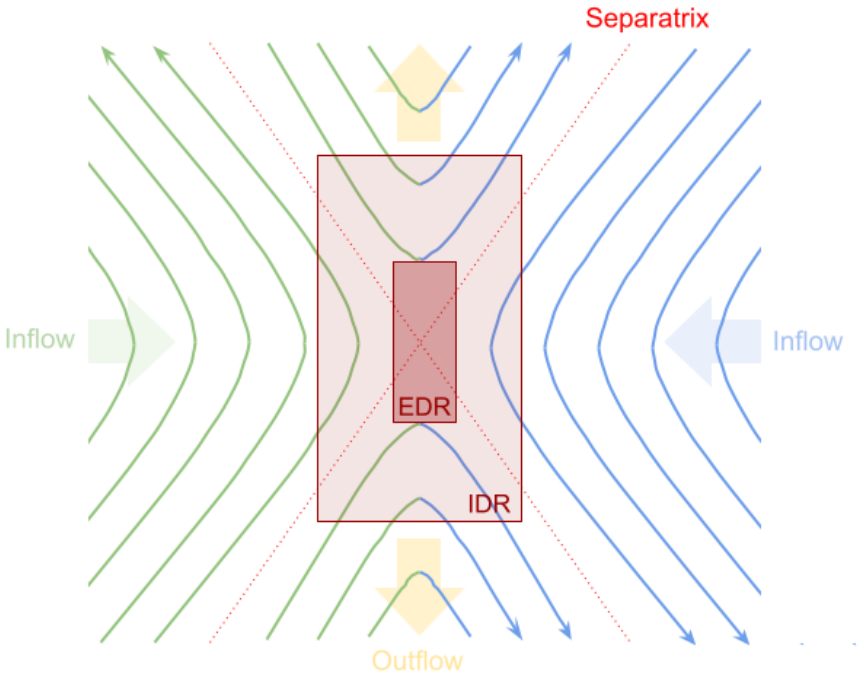

Figure 2.9: Sketch of magnetic reconnection in the 2D limit. The blue and green magnetic field lines are inflowing from the sides while the reconnected field lines, shown in double colors, are outflowing. The dotted red lines are called *separatrices* and divide the magnetic topology into four regions.

is known as the Dungey cycle (Dungey, 1961). Furthermore, magnetic reconnection plays a significant role in the magnetotail by causing the transfer of energy and momentum into the planet's inner tail region. This transfer allows for converting magnetic energy stored in the lobes into kinetic energy within the plasma sheet. Conversely, for a northward IMF, magnetic field inversion is usually observed at the cusps, which are regions near the poles of the Earth's dipole where solar wind plasma penetrates deep into the magnetosphere along magnetic field lines (and can be observed in Figure 2.10. For this configuration, magnetotail reconnection is significantly inhibited due to the absence of a current sheet in the magnetotail.
An example of how the impact of a solar wind magnetic field line can result in a modification of the magnetosphere topology is sketched in Figure 2.10. In this Figure, corresponding to the case of almost southward IMF conditions, it is evident that a localized magnetic reconnection event occurs within the green box in panel (c) in the dayside magnetopause, resulting in a significant modification of the topology of the magnetic field lines (d).

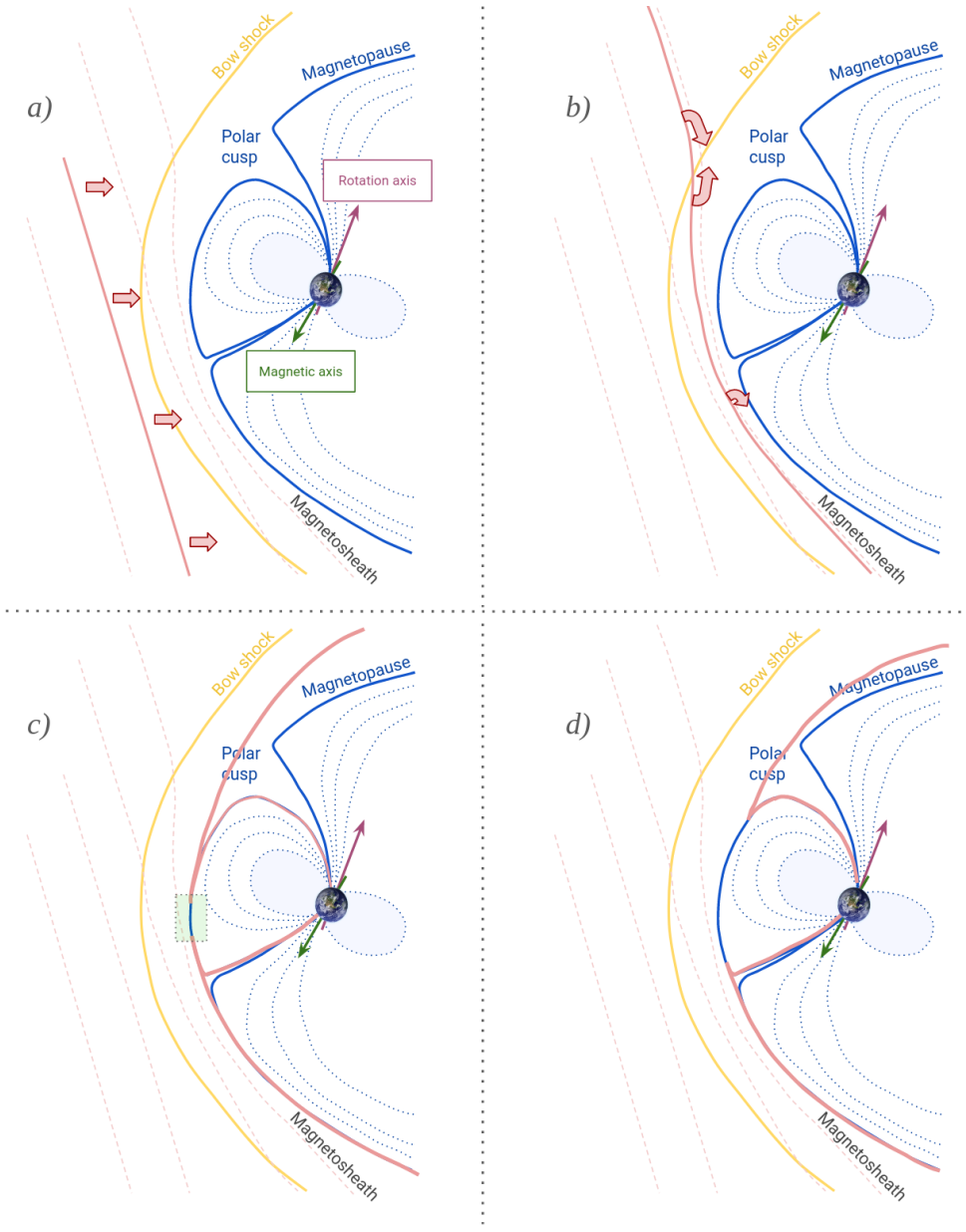

Figure 2.10: Schematization of the impact of a solar wind magnetic field line (pink) on the magnetosphere, resulting in a reconnection event at the sub-solar magnetospheric point. (a) : A solar wind magnetic field line originates from the left and is dragged by the solar wind; (b) : as it passes the bow shock, the magnetic field maintains its direction and starts to bend (as shown by the pink arrows) due to accumulation at the forefront of the magnetopause; (c) : at the magnetopause, reconnection takes place in the EDR, (d) : The magnetic field topology of both solar wind and magnetosphere magnetic fields up to global scales undergoes modifications on a global scale.

3 The study of the magnetopause from in situ data

Contents

In the previous chapter, we have discussed the main features of Earth's magnetopause. As discussed, the study of the magnetopause (and magnetospheres in general) is complementarily carried out through the analysis of *in situ* data and the exploitation of numerical models. We start focusing on *the analysis of satellite data*. Specifically, we concentrate on how to determine the normal direction of the magnetopause, emphasizing the importance of an accurate determination. We will present a new method developed during this PhD thesis and we will compare it to the main existing methods used to estimate the magnetopause normal direction.

3.1 From Pioneer 1 to the Magnetospheric Multiscale mission: probing the Earth's magnetopause

The concept of a sharp current sheet separating the solar wind and the magnetospheric plasma was first proposed by Chapman and Ferraro (1930), although never using the word magnetopause. This study was then followed by other theoretical studies (Chapman and Ferraro, 1933, 1940; Ferraro, 1952; Dungey, 1955; Parker, 1956) and indirect observations (Biermann, 1957) for the following twenty years. However, it was not until the late '50s and early '60s, with the advent of the space age, that *in situ* observations became possible allowing a new era of space research to begin. *In situ* investigations concerning the solar wind-magnetosphere interaction can be traced back to the launch of the Pioneer 1 spacecraft, launched in 1958. Analysis of data collected by the onboard magnetometer (Sonett et al., 1959, 1960) yielded indications of

"anomalous" behavior in the magnetic field approximately 13 R_E (with R_E the Earth radius) sun-ward from Earth. In particular, the decrease in magnetic field magnitude was explained in Sonett et al. (1960) as a consequence of the spacecraft penetrating the magnetopause in the direction of the sun. Subsequent evidence of a complex current structure, even on the night-ward side of Earth, emerged with NASA's Explorer missions 6 (Smith et al., 1960) and 10 (Smith, 1962; Heppner et al., 1963). Finally, the first unambiguous *in situ* observations were reported in Cahill and Amazeen (1963), through observations from the Explorer 12 spacecraft. As shown in Figure 3.1, the magnetopause crossing was observed to be characterized by both a rotation and a variation of the magnitude of the magnetic field. The crossing was also confirmed by the rapid changes observed in the energetic particle flux (Davis and Williamson, 1962; Freeman et al., 1963)

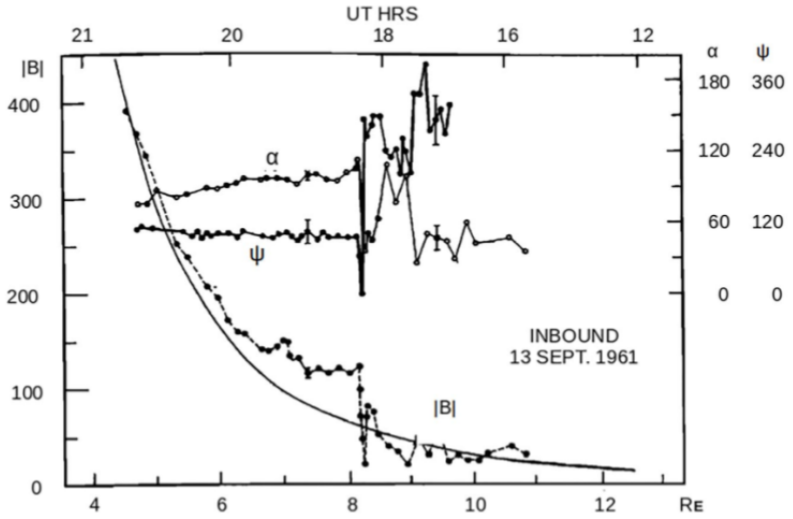

Figure 3.1: Magnetopause crossing observed by the Explorer 12 spacecraft providing the first unambiguous evidence of this boundary. Credit: Cahill and Amazeen (1963).

Another step forward in the comprehension of the Earth's magnetopause was achieved at the beginning of the multi-spacecraft space missions era. Using single spacecraft measurements it is impossible to distinguish whether measured quantities have either *temporal or spatial (or both) dependencies*. By measuring a change in orientation of the magnetic field, for instance, we have no further information to state whether it is a change of the plasma state or if it is the spacecraft penetrating a different plasma. The first estimation of the thickness and kinematic of the magnetopause was obtained by using the data from the two spacecraft ISEE-1 and 2 (Russell and Elphic, 1978), even though making strong assumptions about the magnetopause structure (planar and with stationary current sheets crossed at constant velocity). By performing a statistical study, Berchem and Russell (1982a,b) have estimated a magnetopause thickness between 200 and 1800 km, corresponding to about 10 ion gyro radii. The research also unveiled a highly dynamic magnetopause, characterized by fluctuating velocities spanning from a few kilometers per second to several hundred kilometers per second. The back-and-forth motion is presumably due to the response to changes in the solar wind pressure. Having an inter-spacecraft distance of less than 1000 km, the ISEE-1 and ISEE-2 spacecraft reduced enough the spatiotemporal ambiguity and allowed for the first time to compute, even though under some assumptions, one-dimensional spatial gradients. These two spacecraft had also a fundamental role in detecting the occurrence of magnetic reconnection at the magnetopause. The first unambiguous *in situ* observations were reported by Paschmann et al. (1979). Here, by analyzing the ion and electron distributions, they found higher flow speed in the magnetopause layer than in the adjacent re-

gions, correlated with the Alfvén velocity. The fast Alfvénic flows, nowadays often referred to as jets, are now the most frequently used signature to identify reconnection events.

3.1.1 The Cluster mission

After the ISEE-1 and 2 spacecraft, multi-point missions became the prevailing approach in designing space missions aimed at studying the Earth's magnetosphere. Another step forward a more accurate calculation of the magnetopause normal was achieved by the ESA Cluster mission Escoubet et al. (1997). This mission is composed of four spacecraft orbiting around the Earth assuming most of the time when crossing the magnetopause, a tetrahedron configuration (with an averaged inter-spacecraft distance spanning from 10 to 10,000 km, and allowing for the first time to compute three-dimensional gradients. Moreover, thanks to a new data analysis technique designed to exploit Cluster measurements, the mission made it possible to determine gradients under less strong hypotheses than that assumed for previous studies and to use 3D triangulation for the determination of both the orientation and motion of the magnetopause. Cluster was launched in 2000 [1] and started science operations in early 2001 and it is still operating at the time this manuscript is being written[2]. Thanks to an orbital period of about 57 hours, each Cluster spacecraft has flown through the region of the magnetopause more than 2.500 times. However, since the magnetopause motion is oscillatory, the real number of crossings is far higher. A comprehensive review of all the main results obtained thanks to the Cluster mission can be found in Haaland et al. (2021).

3.1.2 The Magnetospheric Multiscale mission

Cluster inter-spacecraft distance of the order of the ion's scale allowed researchers to investigate in detail the properties of the magnetopause from large scales down to the ion gyro-radius. However, to investigate the dynamics of the magnetopause sub-structures at the electron scale (*i.e.* around 10 km), a smaller inter-spacecraft distance was required. Also for this reason, the Magnetospheric Multiscale mission (MMS) (see Burch and Phan (2016a)) was launched in 2015, building on the success of the Cluster mission[3]. MMS primary objective was the study of magnetic reconnection, focusing in particular on the kinetic processes and the electron diffusion region (Phan et al., 2016; Torbert et al., 2018; Webster et al., 2018). MMS consists of four satellites, namely MMS1 to MMS4, have flown in different formations throughout their lifespan and maintained inter-spacecraft distances ranging from 7-10 km (the order of few electron inertial length at the magnetopause) to 100 km (few electron inertial lengths at the magnetotail around apogee).

Instrumentation onboard

To properly study the electron diffusion region, the MMS on-board instruments have unprecedentedly seen probing rates, allowing to resolve both spatially and temporally the magnetopause structures. Each MMS satellite is identical and equipped with the same instruments. Here we report the main characteristics of the instruments that were used for this study.

- **Fluxgate Magnetometer (FGM)**, used for magnetic field measurements. It consists of the Digital Fluxgate (DFG) and Analog Fluxgate (AFG), both mounted at the end of a

[1] The initial Cluster I mission was initially launched in 1996. However, due to the explosion of the Ariane 5 rocket, it never became operative. Therefore, Cluster II (nowadays called Cluster) took its place in 2000.

[2] The mission was originally planned for a 27 months-period. However, its exploitation phase has been extended for over two decades and is now expected to conclude in September 2024.

[3] Between Cluster and MMS, the THEMIS (NASA) mission was launched in 2007. This mission, consisting of five identical, aimed to investigate magnetic reconnection and the dynamics of mass and energy transfer in the near-Earth space environment.

five meters boom. The sampling frequency is 128 Hz in burst mode and 8 Hz in survey mode and its accuracy is about 0.1 nT for DC fields (Russell et al., 2016). Later in this section, the measurement modes concerning the FGM will be discussed further.

- **Electric field Double Probe (EDP)**, the instrument measuring the 3D electric field in the DC-100 kHz range. It is formed by the Axial Double Probes (ADP, Ergun et al. (2016)) and the Spin-plane Double Probes (SDP, Lindqvist et al. (2016)), which measure the electric field parallel and perpendicular to the spin axis, respectively. It is worth pointing out that one distinguishing feature of MMS with respect to previous missions is its 20-second spin period, which allowed for the implementation of long antennas along the spin axis allowing to measure the 3D electric field.

- **Fast Plasma Investigation (FPI)**, measuring the 3D velocity distribution functions (VDFs) of ions and electrons in the energy range of 10 to 30 keV. Each FPI consists of four Dual Ion Spectrometers (DIS) and four Dual Electron Spectrometers (DES). The time resolution is 150 ms and 30 ms for ions and electrons, respectively (Pollock et al., 2016). Compared to previous missions such as Cluster and THEMIS, a notable advancement of this instrument is that it allows for full azimuthal sampling of the VDFs without relying on spacecraft spin. This is achieved by using eight top-hat spectrometers (or equivalently 4 dual heads) positioned at 90^o angles onboard the spacecraft.

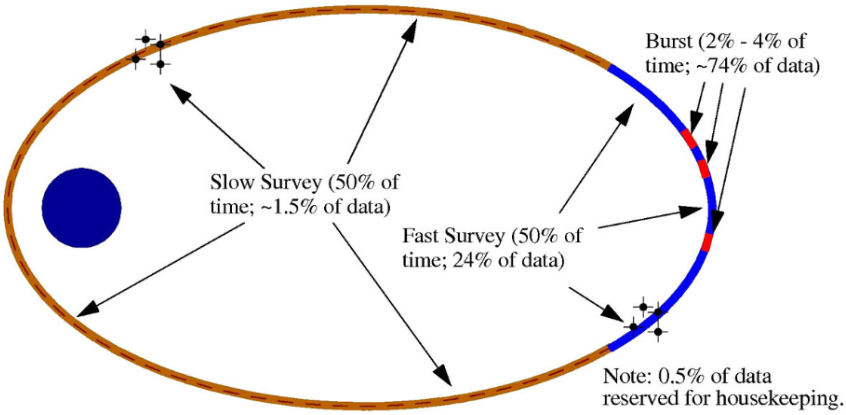

Figure 3.2: Schematic view of the sampling rates used by MMS as a function on the location of the spacecraft along its orbit. The blue circle on the right is the Earth. The four black crossed points superposed twice to the orbit are the four MMS spacecraft. Orbit intervals of high, medium and low interest are drawn respectively in red, blue and brown. Credits: Burch and Phan (2016b)

The instrumentation onboard primarily operates with three data acquisition rates, known as fast, slow, and burst survey. Within the regions of interest (corresponding to the orbital part located around the apogee, with the highest probability of observing the magnetic reconnection process at the magnetopause or in the magnetotail), all instruments gather burst data. However, owing to constraints on the daily data transmission capacity for each spacecraft, a significant portion of burst-mode data needs to be averaged down to a fast-survey rate before transmission. While all slow and fast rate data are transferred to the ground, only a small percentage of burst data is selected for transmission to the ground (Baker et al., 2016). A schematic view of the sampling rates as a function of the location is shown in Figure 3.2. The selection of the burst data intervals is performed by using a semi-automated data selection process complemented by ground-based scientists. The measurements are daily ranked based on a Figure of Merit (FOM). The Scientist-in-the-Loop (SITL) adjusts the FOM, prioritizing data for downlink, investigation,

or deletion, and provides detailed reports on selected data and observed phenomena [4]. A more detailed discussion of the SITL and data selection can be found in Baker et al. (2016). The role of SITL rotates among the teams involved in the mission. As Olivier Le Contel in LPP is responsible for the SCM instrument of the FIELDS consortium experiment I had the opportunity to be SITL for one week.

MMS Scientific Phases

To thoroughly investigate the localized EDR, MMS was designed to traverse the most possible reconnection sites in the Earth's magnetotail and dayside magnetopause. To accomplish this, two phases were programmed before the mission launch in 2015, each focusing on different regions. Phase 1 targeted the low-latitude dayside magnetopause, while Phase 2 aimed at looking at reconnection within the nightside magnetotail. These phases had an equatorial elliptical orbit with a perigee of 1.2 Earth radii (R_E) and a varying apogee from 12 R_E (Phase 1) to 25 R_E (Phase 2). The orbits of MMS during these two phases are shown in Fig 3.3, alongside those of Phase 3. Since plasma density and the magnetic field strength are larger at the dayside magnetopause than in the mid-magnetotail, corresponding to lower ion and electron inertial length and Larmor radius, the spacecraft distance for the tetrahedron varied between 10 and 400 km (estimated between 10 and 160km on the dayside and between 30 and 400 km on the nightside of the magnetosphere) to better sample the spatial structures.

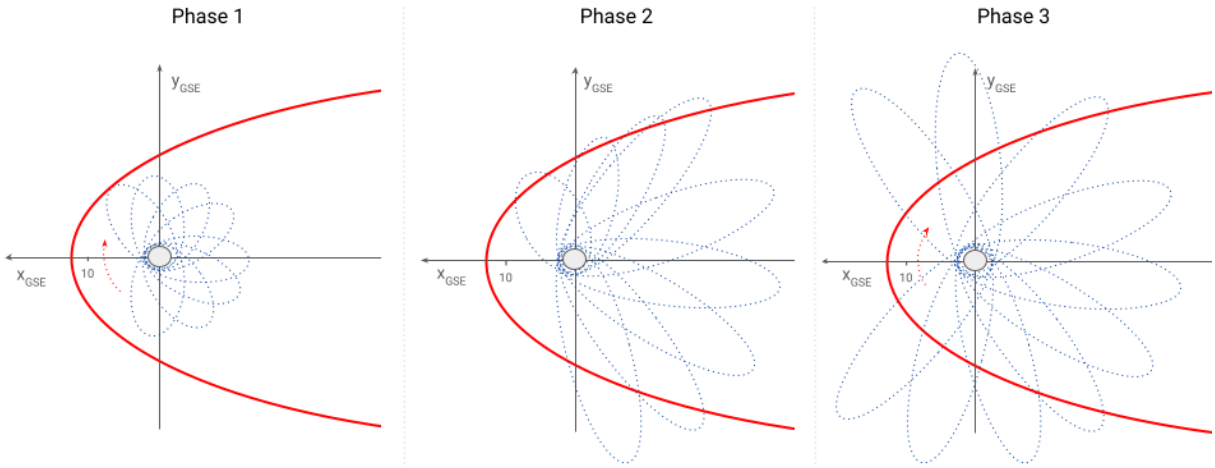

Figure 3.3: Simplified sketch of the MMS orbits in the ecliptic plane for Phases 1 to 3. The Sun is on the left and the red line is the magnetopause.

After completing the nominal mission, MMS was extended and at the time this manuscript is written, MMS is in its scientific Phase 9. For the study presented in this manuscript, data concerning Phases 1-3 are used. In Phase 3, from Sep. 2017 to Sep. 2018, MMS preserved the same apogee and perigee. Therefore during Phase 3, MMS spent more time in the dayside solar wind. Data from Phase 4 onwards are not included in this study because, since July 2018, four of the eighth FPI electron spectrometers of MMS4 have ceased operations. This prevents obtaining electron Velocity Distribution Functions (VDFs) measurements at high sampling times simultaneously on four satellites, thereby making it impossible to compute spatial gradients for particles. A more detailed description of the mission's objectives can be found in Burch and Phan

[4]Data with a higher FOM and is prioritized for downlinking. The SITL categorizes time intervals into four groups: Category 1 (FOM 150-199) for significant magnetic reconnection events, with MMS close or whithin the electron diffusion region, or active dipolarisation fronts in the magnetotail, Category 2 (FOM 100-149) for events such as exhaust region magnetic reconnection or shocks/foreshock, Category 3 (FOM 60-90) for secondary objectives like high-speed jets in the magnetospheath or solar wind turbulence, and Category 4 for less critical events, which may be overwritten and not downlinked.

(2016b) and Fuselier et al. (2014), while comprehensive descriptions of orbits for each scientific Phases can be found on the LASP site: https://lasp.colorado.edu/galaxy/display/mms.

3.2 Magnetopause crossings from *in situ* data

The primary aim of this study is to investigate the internal structure and equilibrium of the Earth's magnetopause. Therefore, it is pertinent to provide a concise overview of the fundamental characteristics associated with the magnetopause crossings as seen from spacecraft data. We begin with the very definition of this boundary, which delineates the interface between two different magnetized plasmas. For this reason, a magnetopause crossing is expected to present: 1) a transition in the magnetic field from that of the magnetosphere to that of the magnetosheath, leading to an observed current within the magnetopause; and 2) different plasma populations on both sides, with different energies, densities and, possibly, composition.
This section presents the key features of these crossings. We initiate with a comparison between Cluster and MMS measurements to underline the relevance of MMS data to this study. Additionally, typical values at both ends of the magnetopause will be discussed to present the complexity of the magnetopause itself. Finally, a brief overview of how the magnetopause dynamics are observed from the perspective of satellites will be provided.

3.2.1 Evolution of the magnetopause measurements: typical magnetopause crossings in the multi-spacecraft era

The step forward from Cluster to MMS is crucial for understanding the magnetopause. As already mentioned, while Cluster primarily focuses on ion scales, MMS targets electron scales. This difference and its impact on studying the internal magnetopause structure is evident in Fig. 3.4, comparing a Cluster crossing from July 5, 2002, to an MMS crossing from December 28, 2015. Here we show the measurements of ion and electron density, ion velocity, and magnetic field. We first observe the typical features of a magnetopause crossing: density variation, magnetic field rotation and compression, and bulk velocity alterations. However, we note that the values of these quantities both at the magnetosphere (left, beginning of the crossings) and magnetosheath (right) vary for each crossing. Specific values for main physical quantities are discussed in the following subsection.
Two noteworthy differences between the measurements of the two missions that can be extrapolated from this figure are:

- **Inter-spacecraft distances:** Because of the different distances, a major difference between the two missions in the time delay between the magnetopause crossing from one satellite to the other is observed. For Cluster, the distance between satellites for the crossing shown is on the order of 2000km, while for MMS it is about 50km. For MMS, Figure 3.4 shows a substantial portion of the magnetopause with four satellites simultaneously inside. With Cluster on the contrary, two spacecraft (Cluster 1 and 4) cross the magnetopause about 30 seconds before the two others (Cluster 2 and 3). This is a typical configuration, even if it is worth pointing out that there are orbits during which the Cluster inter-spacecraft distance has been as low as 10 km.

- **Sampling frequency:** There's a remarkable difference in sampling frequencies. Cluster measures the magnetic field at 22.4 Hz in normal mode, while MMS measures at 128 Hz in burst mode (the two modes shown in Figure 3.4, allowing five more times measurements within the same structure. The most significant difference is, however, in particle measurements (and in the electric field, as mentioned in the previous section but not shown here), where Cluster takes measurements every 4 and 2 seconds for ions and electrons, respectively. MMS measures ions every 0.15 seconds and electrons every 0.03 seconds. This frequency difference allows MMS to provide more measurements of particle distribu-

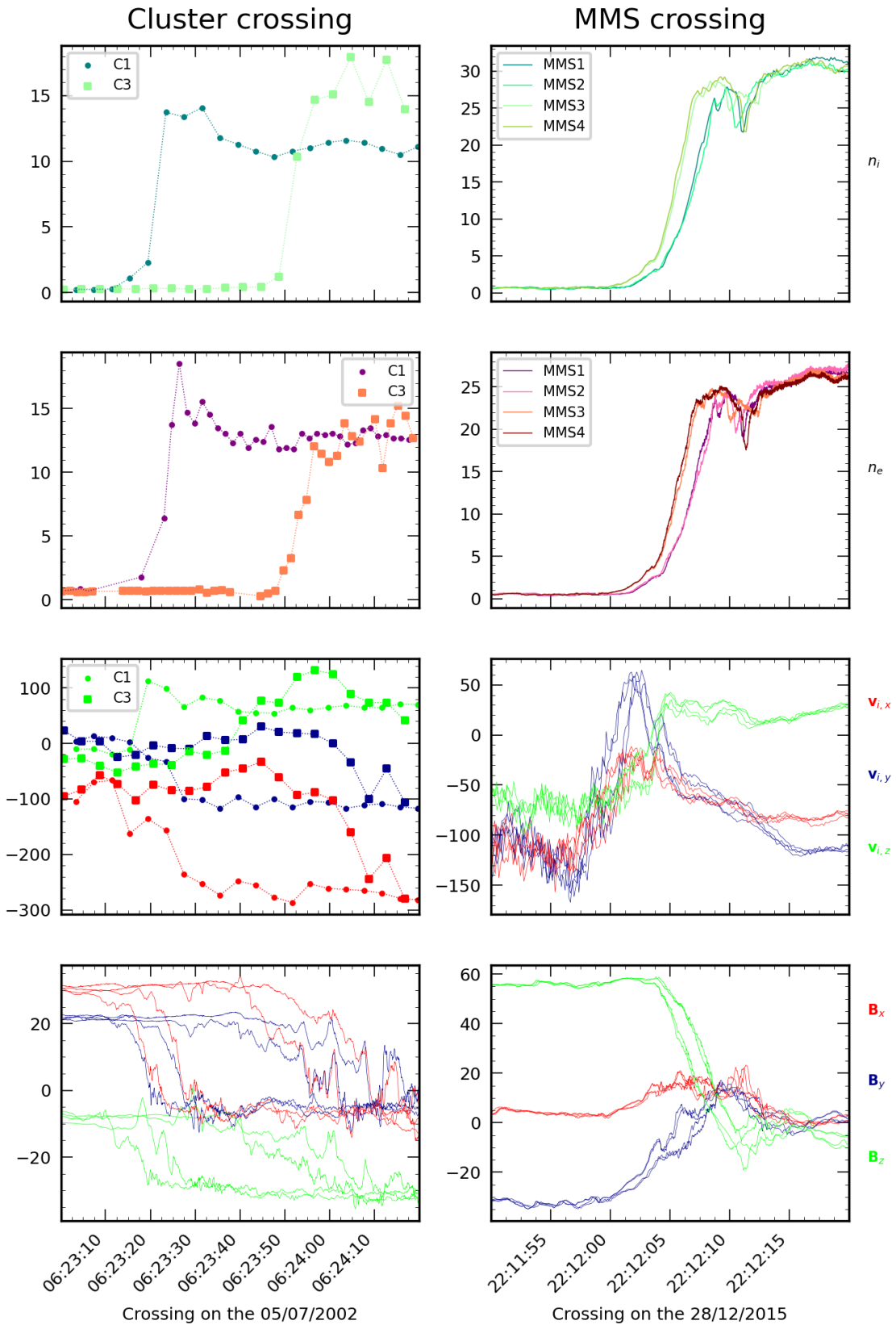

Figure 3.4: Typical crossing using the Cluster (left) and MMS (right) data. From top to bottom: ion density, electron density, ion velocity and magnetic field.

tion functions within the magnetopause, as the typical time length of a wave-unperturbed magnetopause crossing is of the order of ten seconds.

Additionally, it is important to note that ion velocity distribution measurements, and consequently their fluid properties, have been non-functional on Cluster 2 and 4 since the beginning of operations. For Cluster 3, they stopped working in 2009. Thus, Cluster didn't allow a multi-point measurement of these values.

Although Cluster was a fundamental mission for understanding the Earth's magnetosphere, MMS high resolution, highly accurate data with four-point measurements enabled the kind of study reported in this manuscript.

3.2.2 Magnetopause crossings: typical values of the magnetospheric and magnetosheath plasmas

To examine the internal properties of the magnetopause, it is pertinent to define the typical physical quantities of the two distinct regions it separates: the magnetosphere and the magnetosheath. Values discussed here are those relative to the dayside magnetosphere. On one side, the magnetopause exhibits a strong magnetic field, relatively close to the dipolar one, and very low densities. Moreover, the plasma within this region tends to be approximately stagnant. Typical values of magnetospheric plasma are provided in Table 3.1, as reported by Cassak and Fuselier (2016). In general, these values stay constant between different measurements, although there are instances where colder material from the plasmasphere infiltrates this region, thereby altering its density.

Parameter	Typical value
n_{msph} [cm^{-3}]	0.1
$\mathbf{B}_{msph}$ [nT]	56
$T_{i,msph}$ [$\times 10^5$ K]	2.4×10^3
$\mathbf{v}_{A,msph}$ [km s^{-1}]	3.9×10^3
β_{msph}	0.27

Table 3.1: Typical values of magnetospheric parameters at Earth's magnetopause, on the dayside. The parameters are: n the density, $\mathbf{B}$ the magnetic field, T_i the ion temperature, $\mathbf{v}_A$ the Alfvn velocity and β the plasma beta parameter. Electron temperature is usually around five times smaller than ion temperature, therefore not included.

On the other side, magnetosheath plasma originates from the solar wind. This plasma undergoes compression and heating at the bow shock. Due to the variability of solar wind quantities and the turbulent nature of the magnetosheath, the values in this region are much more variable compared to those in the magnetosphere. Table 3.2 presents typical values as reported by Cassak and Fuselier (2016). The algorithm used to estimate these values from average solar wind parameters is found in the cited book. In the solar wind, density and magnetic field are out of phase, meaning low densities correspond to high magnetic fields and vice versa. Finally, it's important to highlight how the typical plasma energies vary between the two plasma populations due to their differences. On the magnetosphere side, ionic energies are typically on the order of 10 keV, whereas on the magnetosheath side, they are one order of magnitude lower.

3.3 Investigating the magnetopause: The normal vector

When studying the magnetopause using *in situ* data, one of the most fundamental geometric characteristics to determine is the normal to its surface. Accurately determining the magnetopause normal is crucial for two main reasons: i) it allows tracking fundamental parameters at the magnetopause, such as its normal velocity with respect to the spacecraft and its dimension-

Parameter (derived)	Mean	Most probable	Median	Start of 5-95% range	End of 5-95% range
n_{msh} [cm^{-3}]	34.8	20	27.6	12	80
$\mathbf{B}_{msh}$ [nT]	24.8	20.4	22.4	8.8	39.6
$T_{i,msh}$ [$\times 10^5$ K]	12	5	9.5	1	30
$\mathbf{v}_{A,msh}$ [km s^{-1}]	92	99	93	55	97
β_{msh}	2.4	0.8	1.8	0.5	5.3

Table 3.2: Typical values of magnetosheath parameters at Earth's subsolar magnetopause (same as in Table 3.1).

ality, and ii) it enables to determine reliable estimates of the normal and tangential fluxes, the normal ones, which cross the magnetopause boundary, being much smaller than the tangential ones (so that their estimation is very sensitive to the normal accuracy). This becomes particularly important for understanding the equilibrium of the magnetopause and the limitations of the current theoretical description of the boundary, a topic examined in Chapter 4.[5]

In this context, determining the value of the magnetic field component normal to the structure is also of fundamental importance. Current models, as we will describe more precisely in the following chapter, distinguish between cases where $B_n = 0$ and B_n different from zero, even if very small. Hence, even a slight variation in this value corresponds to a significant variation in theoretical framework, which warrants investigation. At the magnetopause, this value is typically small, but due to experimental uncertainty, it is impossible to determine precisely whether it is exactly zero or not. Therefore, increasing the accuracy of the normal determination is very important. Quantitatively speaking, to determine the normal component of the magnetic field sufficiently well (assuming that $B_n/|\mathbf{B}| \sim 2\%$), a good enough accuracy of the normal should be of the order of $\delta\theta < 1°$. However, achieving such accuracy from *in situ* data is nearly impossible. Indeed, small-scale waves and turbulence are always superimposed on the laminar magnetopause profiles, bringing strong limitations in the normal direction accuracy for all methods due to the difficulty of filtering them out from the crossing itself. In recent literature, good accuracy in determining the normal direction is estimated to be around 5% (Denton et al., 2018). The first goal of this work is to develop a new tool to obtain a good enough accurate estimate of the normal. Specifically, in this section, we present some of the important state-of-the-art tools for obtaining normals and the evolution that led to our latest tool described here.

An important distinction that will be used in the following manuscript is between *global* and *local normals*, a distinction related to the extension of the time interval exploited to estimate the normal (with respect to the full magnetopause crossing time). With *global normal* we refer to a single normal vector for the full crossing of the structure, whereas *local normal* refers to the value per single measurement (or, to decrease the error due to the superimposed turbulence, averaged over a small time window). The difference between these two types of normals has particular relevance in the analysis of the internal structure of the magnetopause. A local normal determination allows, indeed, for the observation of local variations of the vector that are entirely lost with a global determination. A striking example is the case of a magnetopause crossing close to a reconnection event. In this scenario, a local normal allows us to observe a reversal of the vector within the magnetopause, which would be missed with a global normal.

Since the beginning of space exploration, several methods have been developed to determine

[5]Beyond the determination of the normal direction, the so-called "reconstruction methods" have also been introduced to analyze data at the magnetopause. These models are used to provide a more comprehensive view of the large-scale structure around the spacecraft. Although they have shown remarkable results (De Keyser, 2008; Hasegawa et al., 2005), they will not be used and further discussed in this manuscript since they assume the Grad-Shafranov equations to be valid (stationary MHD), and are therefore not suitable for investigating non-MHD effects such as the FLR effects.

the normal direction (see e.g., (Haaland et al., 2004; Shi et al., 2019)). The most common one is the Minimum Variance Analysis (MVA) method, introduced with the first measurements of the magnetic field in space (Sonnerup and Cahill, 1967; Sonnerup and Scheible, 1998). This method, which only requires single spacecraft measurements, provides a global normal and is based on the assumption that the boundary is a perfectly one-dimensional and stationary layer crossing the spacecraft. Other notable single-spacecraft methods include the Generic Residue Analysis (GRA) technique (Sonnerup et al., 2006), a generalization of MVA to other parameters than **B**, and the BV method (Dorville et al., 2014), which combines magnetic field and velocity data. Although these methods can provide an accurate determination of the normal (Dorville et al., 2015b), like MVA, they provide a global normal and thus cannot provide the necessary basis for investigating variations of the magnetopause normal within the structure and testing possible departures from mono-dimensionality. It is important to note that waves and turbulence limit the accuracy of the normal direction in particular for global ones. The main state-of-the-art tools developed to estimate the magnetopause normal will be presented in the following.

3.3.1 Multi-spacecraft tools for analyzing the magnetopause

The possibility of having more than one spacecraft simultaneously probing the magnetopause or, concerning Cluster, in close vicinity of it, is of fundamental importance for calculating gradients without relying on strong assumptions about the magnetopause properties. This progress is clearly reflected in the development of tools designed to study the magnetopause normal. Depending on the underlying principles used for determining the normal, these tools can be separated into two big groups.

- **Timing methods:** These tools focus on the temporal delay between the four satellites in crossing the magnetopause. As observed in Fig. 3.4, data profiles of the magnetopause are fairly identical but delayed at the magnetopause. Assuming a purely 1D boundary, these delays depend upon the positions of the four spacecraft along the normal direction and the velocity along this direction. They can therefore be exploited to estimate the direction of the magnetopause motion with respect to the spacecraft, which is a proxy for the normal. The displacement of the magnetopause in each spacecraft frame i can be written as:

$$\mathbf{R}_i \cdot \mathbf{n} = \int_{t_{0i}}^{t_i} V_n(t) dt \tag{3.1}$$

  Here, the integration limits refer to the magnetopause crossing interval while $V_n(t)$ is the magnetopause normal velocity and **n** is the magnetopause normal direction. To estimate the normal, it is necessary to make assumptions on the magnetopause properties to solve the system in Eq. 3.1. Depending on the assumption, several tools have been defined over the years. Among these, the two most popular approaches are the **Constant Velocity Approach** (CVA, (Russell et al., 1983)), which assumes that the magnetopause crossing velocity is constant, and the **Constant Thickness Approach** (CTA, (Haaland et al., 2004)), assuming that the magnetopause thickness is the same for the four satellites. In both cases, the assumptions are hard to verify for each crossing and therefore the main limitation lies in making a rather strong assumption whose validity must be checked afterward.

- **Gradient-based methods:** These methods rely on the possibility of computing spatial gradients at each time without assuming too strong hypotheses. Consequently, spatial gradients can be determined even on scales smaller than the thickness of the magnetopause itself, offering much broader possibilities not allowed by single-satellite measurements. However, computing gradients through multipoint measurements requires assumptions, which should be kept in mind as the analyses in this study heavily rely on gradient computations. The most common technique used to compute gradients is the *reciprocal vector*

method. This tool relies on the use of the reciprocal vectors, a well-established concept in various scientific fields such as solid state physics, that have been introduced in space plasma physics by Chanteur (1998). In the context of a tetrahedron configuration, the reciprocal vector with respect to a spacecraft is defined as a vector perpendicular to the face of the tetrahedron opposing the spacecraft, with a magnitude equal to the inverse of the distance from the spacecraft to the opposing face. Mathematically, this reads (using MMS1 as an example):

$$\mathbf{k}_1 = \frac{(\mathbf{r}_2 - \mathbf{r}_3) \times (\mathbf{r}_2 - \mathbf{r}_4)}{|(\mathbf{r}_2 - \mathbf{r}_1) \times ((\mathbf{r}_2 - \mathbf{r}_3) \times (\mathbf{r}_2 - \mathbf{r}_4))|} \tag{3.2}$$

Here, r_i is defined as the position of the i-th spacecraft. A schematic representation of the tetrahedron having at its vertex the four MMS spacecraft and the reciprocal vector corresponding to MMS1 is shown in Fig. 3.5.

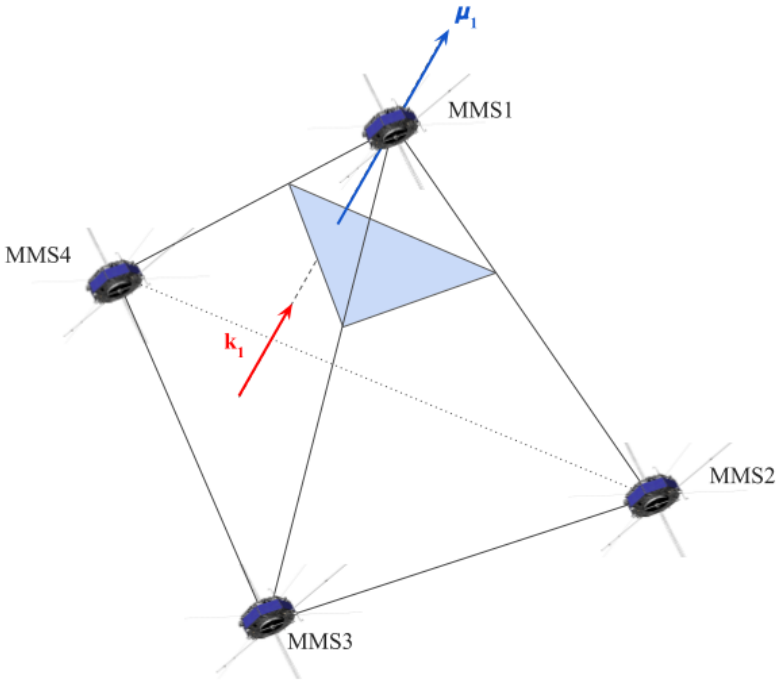

Figure 3.5: Schematic representation of the tetrahedron geometry for MMS. The reciprocal vector k_1 (Eq. 3.2) points toward MMS1 and corresponds to the gradient of the barycentric coordinate μ_1 which remains constant on any plane parallel to the surface that includes the other MMS spacecraft. Credits: adapted from Chanteur and Mottez (1993).

Gradients are calculated by a linear estimator which is the gradient of the barycentric coordinates of the multi-spacecraft cluster. Therefore, the accuracy of the results improves when the spacecraft configuration is reasonably regular and when there are no significant gradients at scales smaller than the inter-spacecraft distance. The situation is similar to the limited expansion of a function which is valid at order 1 if the order 2 term is negligible.

According to this tool, the gradient of a generic vector quantity $\mathbf{Q}$ is expressed as [6]:

$$\nabla \mathbf{Q} = \frac{\partial \mathbf{Q}_j}{\partial x_i} = \sum_{\alpha=1}^{4} (\mathbf{k}_\alpha \mathbf{Q}_\alpha)_{ij} = \sum_{\alpha=1}^{4} k_{\alpha i} Q_{\alpha j} \tag{3.6}$$

The estimation of gradients from multi-point measurements lies at the core of recent techniques capable of locally computing a local normal to the magnetopause structure. Observing the spatial variation of the normal direction within the magnetopause enables us to examine the sub-structural details of the layer and check the 1D hypothesis at the crossing scale. Other notable tools used to obtain the gradient matrix include the least squares methods (Harvey, 1998) and the Taylor expansion method (Pu and Kivelson, 1983). The most common gradient-based tool, the **Minimum Directional Derivative** (MDD, Shi et al. (2005)), is presented below (along with the most common recent tool to obtain the magnetopause normal).

3.3.2 State-of-the-art: the Minimum Directional Derivative (MDD) method

The Minimum Directional Derivative, hereafter referred to as MDD, is the multipoint tool the most widely used in the scientific community for studying the normal of magnetopause, as MVA was for single spacecraft analyses. The tool was first introduced by Shi et al. (2005). For the vector $\mathbf{B}$, the MDD method makes use only of the spatial derivatives $\partial_i \mathbf{B}$ (*i.e.* $\partial \mathbf{B}/\partial x_i$, with i referring to the three spatial directions), which are accessible at each time step thanks to the 4-point measurements. In this sense, it is the opposite of the MVA method, only relying on the temporal variances of the $\mathbf{B}$ components. Therefore, the MDD allows for an instantaneous determination of a *local* normal at any point inside the layer. In addition, contrary to MVA where the $\nabla \cdot \mathbf{B} = 0$ condition is exploited, MDD does not make any assumption about the geometry of the layer and the physical properties of the vector used. Therefore, while this tool is generally used on magnetic field measurements, it is important to remember that this tool is not based on specific properties of the magnetic field and can be used with any data set (such as ion and electron mass fluxes, the electric field, etc). This aspect is really important since it allows one to compare the magnetic structure with the geometry of any other set of data (in particular, the ion flux).
By exploiting the experimental estimation of the dyadic tensor $\mathbf{G} = \nabla \mathbf{B}$, the MDD method consists in diagonalizing the matrix $\mathbf{L}$ defined as follows (here T denotes the transposed):

$$\mathbf{L} = \mathbf{G} \cdot \mathbf{G}^T \tag{3.7}$$

This matrix is symmetrical; hence, the eigenvalues are real and the corresponding eigenvectors are orthogonal. In particular, it can be shown that the three eigenvalues λ_i ($i = 1, 2, 3$) represent the maximum, intermediate and minimum values of $(\mathbf{n}_i \cdot \nabla \mathbf{B})^2$, with $\mathbf{n}_i$ being their respective eigenvector (Shi et al., 2019). The normal direction is determined from the $\mathbf{L}$ matrix as the eigenvector corresponding to the maximum eigenvalue.

[6] The same tool can be used also to compute other space derivatives, such as (where g is a scalar quantity):

$$\nabla g = \sum_{\alpha=1}^{4} \mathbf{k}_\alpha g_\alpha \tag{3.3}$$

$$\nabla \cdot \mathbf{Q} = \sum_{\alpha=1}^{4} \mathbf{k}_\alpha \cdot \mathbf{Q}_\alpha \tag{3.4}$$

$$\nabla \times \mathbf{Q} = \sum_{\alpha=1}^{4} \mathbf{k}_\alpha \times \mathbf{Q}_\alpha \tag{3.5}$$

For purely 1D variations, it is clear that two eigenvalues are zero and that the third eigenvector does indicate the normal direction. When 2D and 3D variations are present, the eigenvector corresponding to the maximum eigenvalue can still be defined as a "normal" direction, but this definition is then more arbitrary. Nevertheless, the values of the two smaller eigenvalues still give a precious indication for the dimensionality of the variations. If only one eigenvalue is small, the result indicates the plane where the 2D variations occur. By defining λ_n, λ_m, λ_l the maximum, intermediate and minimum eigenvalues of $\mathbf{L}$, the following conditions can be found at the magnetopause (by defining $\mathbf{n}$, $\mathbf{m}$ and $\mathbf{l}$ as the respective eigenvectors):

- $\lambda_n \gg \lambda_m \sim \lambda_l$; Mathematically, it follows that $|\partial\mathbf{B}/\partial\mathbf{n}| \gg |\partial\mathbf{B}/\partial\mathbf{m}| \sim |\partial\mathbf{B}/\partial\mathbf{l}|$. Therefore, in this case, the plasma structure can be considered as "quasi-1D" since the magnetic field varies along (almost-)only the normal direction;
- $\lambda_n \sim \lambda_m \gg \lambda_l$, corresponding to a "quasi-2D" structure;
- $\lambda_n \sim \lambda_m \sim \lambda_l$, corresponding to a three-dimensional structure since variations of magnetic field are comparable in all three directions.

Based on this classification, the most common way of finding a quantitative determination of the dimensionality was proposed in Rezeau et al. (2018). This method relies on the definition of three parameters as a ratio of the eigenvalues, defined as:

$$\begin{cases} D_1 = \dfrac{\lambda_n - \lambda_m}{\lambda_n} \\ D_2 = \dfrac{\lambda_m - \lambda_l}{\lambda_n} \\ D_3 = \dfrac{\lambda_l}{\lambda_n} \end{cases} \tag{3.8}$$

By definition, these parameters have values between 0 and 1 and have a total sum equal to 1. By observing their values we can therefore distinguish whether the the local variations are one-dimensional ($D_1 = 1$), two-dimensional ($D_2 = 1$), or three-dimensional ($D_3 = 1$).

Advantages and limitations

The main advantage of using MDD, compared to single-spacecraft tools, is its capability to determine an instantaneous normal at any point within the layer, enabling a local study of the magnetopause rather than a global one. However, the accuracy of MDD is limited by the uncertainty of the spatial gradients it employs. Specifically, the assumption of linear variations used to compute the local gradient matrix through the reciprocal vector method cannot be fully satisfied due to the presence of small-scale waves and turbulence that are always superimposed on the magnetopause profiles. To address this issue, a filtering of the data is necessary. This procedure, however, leads to a loss of part of the temporal information on the variation but it still allows to keep local information whenever the filtered scales are sufficiently smaller than those associated with the full crossing. The quality of the filtering is therefore the biggest challenge in achieving accurate results. For instance, simple Gaussian filters done independently on the four spacecraft would provide insufficient accuracy since the relation $\nabla \cdot \mathbf{B} = 0$ is then violated in the result.

The attempt to answer these limitations to achieve an accurate determination of the magnetopause normal, despite the presence of local two-dimensional features, has been one of the primary objectives of this project. The focus has been on the development of a tool, derived from MDD but based on a fitting procedure, that guarantees that the condition $\nabla \cdot \mathbf{B} = 0$ is not violated. Imposing $\nabla \cdot \mathbf{B} = 0$ as a constraint in the model (or another condition when other vectors are used) allows improving the four spacecraft data filtering and therefore the result

accuracy. It is worth mentioning however that this relation is not the basis on the normal determination as it was in MVA. The development of this tool is discussed in the following section where the **Gradient matrix Fitting (GF2)** tool, representing the final developed version, is introduced and tested on a case crossing.

3.3.3 The *Denton et al (2016)* tool

Before delving into the presentation of GF2, it's worth briefly introducing the hybrid model developed by Denton et al. (2016, 2018). This model serves as an example of the ongoing pursuit of a more precise estimation of the magnetopause normal. It is obtained through a combination of MDD and MVA. The underlying idea is to achieve an accurate determination of the LMN system[7]. The hybrid tool relies on two observations (both validated from data over the years):

i) MDD generally provides a good determination of the normal direction, while it often fails at well characterizing the tangential plane, due to a possible degeneracy of its **L-M** eigenvalues.

ii) MVA generally provides a good determination of **L** while it often fails to give acceptable results of the **M-N** plane, due to a possible degeneracy of the corresponding eigenvalues.

By rotating these two reference systems by an angle proportional to that between the MDD and MVA normal vectors, the hybrid model gives a new normal. The estimated statistical uncertainty error for this tool is around 5 degrees. The accuracy of this determination is supported by the close proximity of the normals obtained through other state-of-the-art tools. However, while allowing for a good determination of the normal, this tool gives a global normal averaged on the whole crossing, and not a local one. Using the same algorithm on a shorter interval would provide a doubtful result since the variance calculated in MVA would not then be statistically significant.

3.4 A new tool: Gradient matrix Fitting

In this section, we introduce the Gradient matrix Fitting (hereafter **GF2**[8]) tool. It aims at achieving a more accurate determination of the magnetopause normal. The goal is to retain the advantages of state-of-the-art techniques, particularly MDD, which allows for the observation of local variations in the normal direction within the magnetopause, while overcoming its limitations, specifically the assumption of linear variations at inter-spacecraft scales. These approximations lead to neglect the effects of waves and turbulence at small scales and therefore do not allow one to make a complete study of the average magnetopause boundary. Ultimately, the aim is also to develop a tool capable of determining the normal from most of physical quantities, not limited to magnetic field measurements (such as with MVA, for example) to be able to make comparisons. Additionally, it was essential for the tool to be neither overly complex nor computationally too slow to ensure accessibility and, most importantly, to allow for statistical analysis.

This new tool was derived from MDD and can be classified as a gradient-based tool. Specifically, the tool involves developing a parametric model of the gradient matrix, valid for each time step inside the magnetopause. By fitting the gradient matrix estimated from data with this model, it is possible to obtain the best-fit parameters. The fitted matrix can be considered as the averaged gradient matrix, *i.e.* the matrix when the major contributions of waves and turbulence are filtered out, providing the laminar profile of the magnetopause. By using

[7] The **LMN** coordinates system is used to describe the orientation of the magnetopause boundary relative to the local magnetic field and it is widely used when studying magnetic reconnection. By definition, **L** represents the direction of maximum variance for the magnetic field, **N** is the normal vector perpendicular to the magnetopause, while pointing away from the Earth, and **M** completes the coordinate system, perpendicular to both **L** and **N**.

[8] The digit 2 indicates that in the version of the tool that we use here, the data are fitted with a 2D model.

this matrix, errors in determining the normal vector can be reduced and the departures from mono-dimensionality reliably estimated.

Throughout the project, various attempts were made to develop a reliable algorithm. In particular, the development focused on two main aspects: *i*) the parameterization of the gradient matrix and *ii*) the minimization process between the model and data to obtain the best-fit gradient matrix. Concerning the model, early versions assumed it was purely one-dimensional, presenting gradients only along the normal direction. However, it was observed that the presence of gradients, albeit minor, parallel to the magnetopause plane made two-dimensional modeling more effective, leading to its implementation. Furthermore, it can be shown that fitting with a 1D model is mathematically equivalent to the standard MDD technique used with smoothed data. As for the minimization process, early versions employed algorithms that computed each best-fit parameter through numerical minimization. However, this approach presented two main limitations: bigger computational time and a higher probability of converging to incorrect local minima, making it less suitable for statistical analysis. Therefore, analytical minimization was adopted, allowing for faster and more accurate determination of the modeled gradient matrix. In this section, only the final version is reported. This tool is also presented and discussed further in detail in Ballerini et al. (2024b), accepted in the Journal o Plasma Physics at the time of manuscript writing and included in Chapter 9.

3.4.1 The Gradient matrix Fitting (GF2) tool

The primary assumption of this method is that the structure under consideration can be locally fitted by a two-dimensional model. This does not imply that the magnetopause is assumed to be globally two-dimensional, but rather that local gradients are so, with the fit being carried out in short sliding windows within the global crossing. Based on this assumption, the parametric model of the gradient matrix $\mathbf{G}_{fit}$ reads as follows (for magnetic field measurements; generalizations are provided later):

$$\mathbf{G}_{fit} = \mathbf{e}_0\, \mathbf{B}'_{e0} + \mathbf{e}_1\, \mathbf{B}'_{e1} \tag{3.9}$$

where we define $\mathbf{e}_0$ and $\mathbf{e}_1$ as two unit vectors in the plane perpendicular to the direction of invariance and $\mathbf{B}'_{e0}$ and $\mathbf{B}'_{e1}$ as the variation of the magnetic field along these two directions, respectively. For simplicity, $\mathbf{e}_0$ and $\mathbf{e}_1$ are chosen as an arbitrary orthonormal basis for the plane of variance. Before minimizing the difference between this parametric matrix and the gradient matrix from data, one has first to choose the invariance direction[9] in order to determine the ($\mathbf{e}_0$, $\mathbf{e}_1$) plane. We have observed that the choice of the direction of invariance has no major influence on determining the normal direction, nor the estimation of the 2D effects. Several options can be chosen to estimate this direction. Whenever the boundary is strongly two-dimensional, the direction can be estimated as the minimum variance one obtained by directly applying the standard MDD method to the data. However, for the nearly 1D cases analyzed in this manuscript, the spatial derivatives in the tangential directions are dominated by noise, which makes the estimation not reliable. Therefore, for these cases, we choose to use the constant direction $\mathbf{M}$ given by MVA, generally interpreted as the X-line direction in the context of 2D magnetic reconnection models (*cf.* for instance Phan et al. (2013) for typical use of this choice and Aunai et al. (2016); Liu et al. (2018); Denton et al. (2018) for discussions).

The best-fit parameters are then chosen by minimizing the difference between $\mathbf{G}$ and the model $\mathbf{G}_{fit}$. To do that, we choose to minimize the following quantity:

$$\begin{aligned} D_{GF2} &= \mathrm{Tr}\big[(\mathbf{G}_{fit} - \mathbf{G}).(\mathbf{G}_{fit} - \mathbf{G})^T\big] \\ &= \mathbf{B}'^2_{e0} - 2\mathbf{e}_0.\mathbf{G}.\mathbf{B}'_{e0} + \mathbf{B}'^2_{e1} - 2\mathbf{e}_1.\mathbf{G}.\mathbf{B}'_{e1} + \mathrm{Tr}\big(\mathbf{G}\mathbf{G}^T\big) \end{aligned} \tag{3.10}$$

[9]The invariance direction here discussed is referred to the magnetic field measurements. Analogously, in Section 3.4.2, the invariance direction is referred to the $\mathbf{\Gamma}$ measurements.

Here Tr[] indicates the trace of the tensor. Here the last term can be disregarded as being independent of the fit parameters. To better exploit the magnetic field properties we impose $\nabla \cdot \mathbf{B} = 0$, as used in MVA but ignored in standard MDD. In the model, this condition can be written as:

$$\mathbf{e}_0 \cdot \mathbf{B}'_{e0} + \mathbf{e}_1 \cdot \mathbf{B}'_{e1} = 0 \tag{3.11}$$

This constraint is imposed on Eq. 3.10 by using Lagrange multipliers[10], leading to:

$$\begin{aligned} D_{GF2} =& \mathbf{B}'^2_{e0} - 2\mathbf{e}_0.\mathbf{G}.\mathbf{B}'_{e0} + \mathbf{B}'^2_{e1} - 2\mathbf{e}_1.\mathbf{G}.\mathbf{B}'_{e1} + 2\lambda(\mathbf{e}_0 \cdot \mathbf{B}'_{e0} + \mathbf{e}_1 \cdot \mathbf{B}'_{e1}) \\ =& \mathbf{B}'^2_{e0} - 2\mathbf{e}_0.(\mathbf{G} - \lambda\mathbf{I}).\mathbf{B}'_{e0} + \mathbf{B}'^2_{e1} - 2\mathbf{e}_1.(\mathbf{G} - \lambda\mathbf{I}).\mathbf{B}'_{e1} \end{aligned} \tag{3.12}$$

To conclude the minimization, the derivatives with respect to $\mathbf{B}'_{e0}$, $\mathbf{B}'_{e1}$ and λ must be imposed equal to zero, obtaining:

$$\begin{cases} \mathbf{B}'_{e0} = \mathbf{e}_0.(\mathbf{G} - \lambda\mathbf{I}) \\ \mathbf{B}'_{e1} = \mathbf{e}_1.(\mathbf{G} - \lambda\mathbf{I}) \\ \mathbf{e}_0 \cdot \mathbf{B}'_{e0} + \mathbf{e}_1 \cdot \mathbf{B}'_{e1} = 0 \end{cases} \tag{3.13}$$

This system is easily solved, obtaining:

$$\lambda = \frac{G_{00} + G_{11}}{2}, \tag{3.14}$$

From λ we obtain $\mathbf{B}'_{e0}$ and $\mathbf{B}'_{e1}$ and, therefore, finally determine the fitted gradient matrix $\mathbf{G}_{fit}$. From this matrix, the normal $\mathbf{n}$ and the tangential direction $\mathbf{t}_1$ (*i.e.* the one orthogonal to the direction of invariance) are easily obtained performing the nominal MDD technique. A simplified diagram outlining the procedure for estimating the normal is presented in Fig. 3.6.

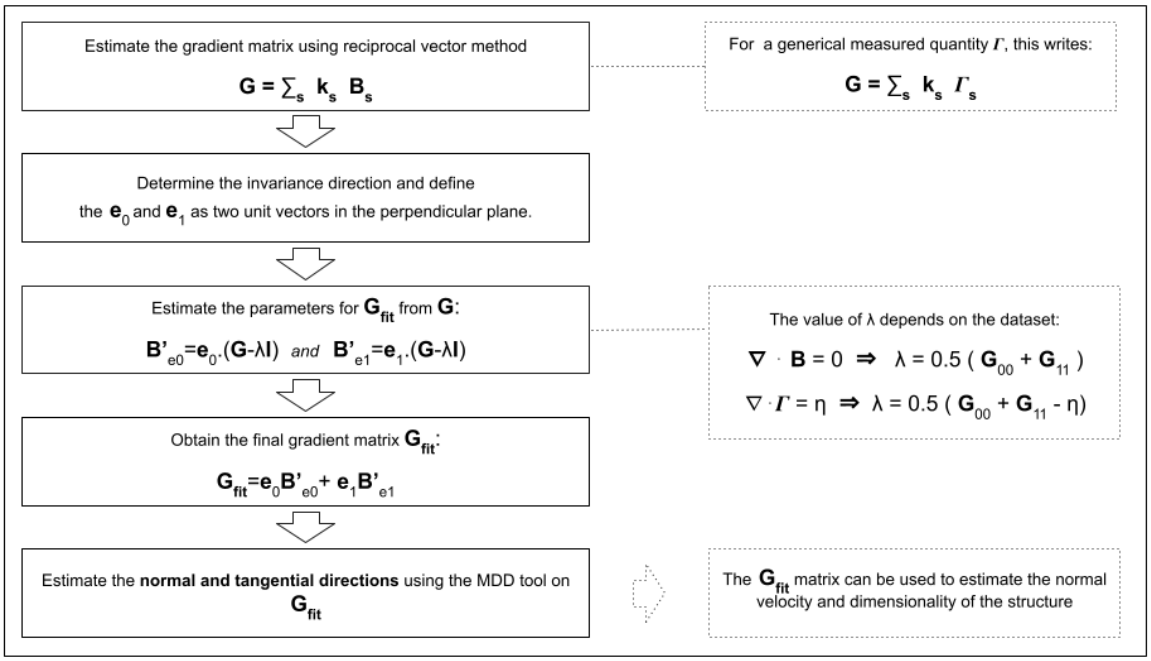

Figure 3.6: Scheme of the **GF2** algorithm.

[10]The Lagrange multiplier method is used to find the stationary points (local minimums or maximums, including extrema) of a real function $f(x, y, \ldots)$ subject to one or more constraints $g(x, y, \ldots) = 0$. In this method, further discussed in Goldstein (1950), the minima are found from the so-called Lagrange function, defined as $\mathcal{L}(x, y, \ldots, \lambda) = f(x, y, \ldots) + \lambda \cdot g(x, y, \ldots)$, where λ is a new variable defined as the Lagrange multiplier. In order to find the minima, this method consists in solving the system of equations formed by setting the partial derivatives of $\mathcal{L}$ with respect to all variables (including λ) equal to zero.

3.4.2 The magnetopause normal using other sets of data

This tool can be easily adapted to any other vector measurement by just changing the physical constraint. In particular, considering a generic vector $\mathbf{\Gamma}$ respecting a generic physical constraint $\nabla \cdot \mathbf{\Gamma} = \eta$[11]. In this case, the same algorithm as above can be used since no conditions on the structure were assumed. Therefore, the minimization leads to:

$$\begin{cases} \mathbf{\Gamma}'_{e0} = \mathbf{e}_0.(\mathbf{G} - \lambda \mathbf{I}) \\ \mathbf{\Gamma}'_{e1} = \mathbf{e}_1.(\mathbf{G} - \lambda \mathbf{I}) \\ \mathbf{e}_0 \cdot \mathbf{\Gamma}'_{e0} + \mathbf{e}_1 \cdot \mathbf{\Gamma}'_{e1} = \eta \end{cases} \tag{3.15}$$

Again the last equation corresponds to the physical constraint. This system is again easily solved, leading to:

$$\lambda = \frac{G_{00} + G_{11} - \eta}{2} \tag{3.16}$$

In conclusion, the **GF2** can be easily adapted to any set of data by changing the value of λ to the corresponding physical constraint. However, while theoretically any data can be used, the tool's effectiveness can be limited and possibly lead to less realistic results when large uncertainties exist, in the vector data set or in the scalar constraint.

3.4.3 Dimensionality index

From the filtered gradient matrix, we can also derive an indicator of the local dimensionality of the structure profiles, after filtering out any parasitic noise effects. Specifically, we can estimate the importance of two-dimensional effects in the structure profile. We achieve this by estimating the variation of the magnetic field (or any physical quantity of interest) along the normal and tangential directions obtained through the GF2 tool by projecting the $\mathbf{G}_{fit}$ matrix along them. By defining $\text{var}_n = |\partial_{\mathbf{n}}\mathbf{B}| = |\mathbf{G}_{fit}.\mathbf{n}|$ (and equivalently var_t along $\mathbf{t}_1$, i.e. the tangential direction obtained using GF2 and defined in Section 3.4.1), we can introduce a new dimensionality index:

$$\mathcal{D}_{GF2} = \frac{\text{var}_n - \text{var}_t}{\text{var}_n} \tag{3.17}$$

This parameter indicates the relative importance of the gradients along the tangential direction compared to those along the normal. Its values range between zero and one. In particular, one corresponds to the strict one-dimensional limit, and zero corresponds to the two-dimensional scenario where gradients are equivalent in module along both directions. This index is used together with the instantaneous index D_1, presented in Eq. 3.8, as a complementary measure of the dimensionality of the magnetopause.

3.4.4 The normal velocity

Finally, another useful by-product of the GF2 method is the ability to have a determination of the components of the velocity of the structure V_n and V_{t1} with respect to the spacecraft. However, the motion along the invariant direction remains unknown. Again, we write here the algorithm for magnetic field measurements while it is general for any set of data.
These components can be obtained by comparing the spatial derivatives and the temporal ones. Specifically, in the two-dimensional local limit there are no variations along the invariant direction. Therefore, we can write:

$$\partial_t \mathbf{B} = V_n \partial_{\mathbf{n}} \mathbf{B} + V_{t1} \partial_{\mathbf{t}_1} \mathbf{B} \tag{3.18}$$

[11] In the case of the ions mass flux, $\mathbf{\Gamma} = n_i \mathbf{u}_i$, the corresponding physical constraint is the mass conservation $\nabla \cdot (n_i \mathbf{u}_i) = -\partial_t n_i$. Therefore, in this case, $\eta = -\partial_t n_i$.

(Warning: the term $\partial_{\mathbf{t}_1}\mathbf{B}$, which is a spatial derivative along $\mathbf{t}_1$, obtained from G_{fit}, must not be confused with the temporal derivative $\partial_t\mathbf{B}$). By doing the scalar product between this equation and both $\partial_{\mathbf{n}}\mathbf{B}$ and $\partial_{\mathbf{t}_1}\mathbf{B}$, we find a system of two equations from which we find both velocities as follows:

$$\begin{bmatrix} V_n \\ V_{t1} \end{bmatrix} = \mathcal{M}^{-1} \begin{bmatrix} \partial_t\mathbf{B}.\partial_{\mathbf{n}}\mathbf{B} \\ \partial_t\mathbf{B}.\partial_{\mathbf{t}_1}\mathbf{B} \end{bmatrix} \tag{3.19}$$

Here, Specifically, $\mathcal{M}$ is the spatial variation matrix in the $\mathbf{n}-\mathbf{t}_1$ plane, defined by using the quantities var_n and var_t defined above and $\text{var}_{n,t} = \partial_{\mathbf{n}}\mathbf{B}.\partial_{\mathbf{t}_1}\mathbf{B}$, as follows:

$$\mathcal{M} = \begin{bmatrix} \text{var}_n^2 & \text{var}_{n,t} \\ \text{var}_{n,t} & \text{var}_t^2 \end{bmatrix} \tag{3.20}$$

3.5 Testing GF2 on *in-situ* data

A preliminary analysis to validate this tool was obtained by comparing the results with those obtained from other State-of-the-Art methods (specifically, MDD and, for the magnetic field, MVA). This analysis is carried out using data from a MMS crossing that occurred on December 28, 2015, at approximately 22:12 (the crossing shown in the panel on the right in Fig. 3.4). For this event, the spacecraft are located at [7.6, -6.7, -0.8] R_E in GSE coordinates (where R_E is the Earth's radius). The crossing shows one-dimensional features. The values of the two dimensional indices discussed above (Eq. 3.8 and 3.10), computed from the magnetic field and averaged on the crossing interval between 22:12:02 and 22:12:10, are $D_{1,mean} = 0.97 \pm 0.03$ and $\mathcal{D}_{GF2,mean} = 0.89 \pm 0.06$. The two values close to 1 highlight that the crossing can be considered as one-dimensional throughout the time interval. Finally, we remind here that the sampling frequencies of the magnetic field, and ion and electron measurements differ. Throughout this manuscript, these quantities are compared and/or used at the same instant of time. Therefore, to conduct this study it is necessary to interpolate all measurements at the same sampling times. To do that, we tested the two sampling frequencies: of the magnetic field, the highest, and of the ions, the lowest. The results obtained are consistent with the two methods. All figures shown in this manuscript use the sampling times of the MMS1 magnetic field.

3.5.1 Comparison with MDD

As a first test, GF2 was evaluated by comparing the magnetopause normals obtained using GF2 with those from MDD (and MVA for the magnetic field). The test discussed below is part of the study also presented in Ballerini et al. (2024b) and discussed in Chapter 9. The normals, along with the measurements, are shown in Fig. 3.7, for the magnetic field and ion and electron mass fluxes. Vertical lines delimit the time interval during which all the satellites are inside the magnetopause structure, showing that the crossing lasts about 5 seconds for particles and 8 seconds for the magnetic field. This crossing is chosen as a case study since the duration is long enough to allow for high resolution for all data. In this figure, we observe that, while the ion and magnetic field measurements show crossing which is dominated by the mean magnetopause profile, the electron mass flux is more characterized by fluctuations, with larger differences between the four spacecraft measurements. All normals shown here are obtained using sliding time windows of 0.31 seconds to filter out waves and turbulence at small scales. The role of this smoothing is further discussed in the following section.

The first striking result from Fig. 3.7 is the consistency of all these normals. For the magnetic field and ions, almost all the directions are less than ten degrees apart from each other, with an average difference of about five degrees. The major exception concerns the comparison between MVA and the two local normals during the last second of the interval for the magnetic field measurements. This discrepancy can be explained by the fact that the local

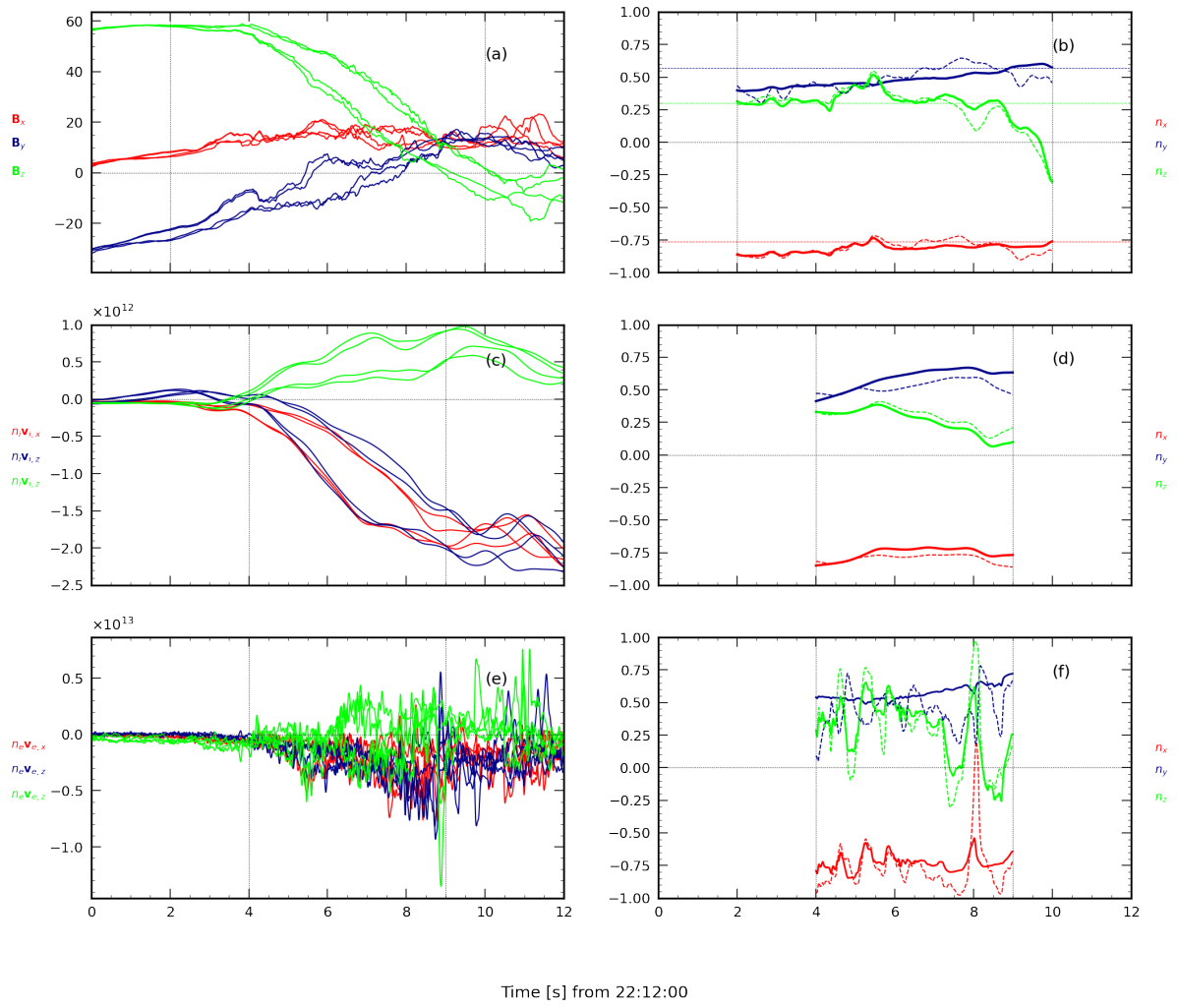

Figure 3.7: Comparison for the normals obtained with GF2 and MDD. From top to bottom the magnetic field, ion and electron mass flux (left), and their respective normals (right). The continuous (resp. dashed) line indicates the components of GF2 (resp. MDD) normal. Horizontal dotted lines in top panel indicate the MVA normal obtained over the whole interval, averaging the magnetic field measurements on the four spacecraft. Vertical dashed lines delimit the time interval of the crossing, different for the magnetic field and the particle mass flux.

normals differ noticeably in this part from their value averaged within the crossing, while MVA only returns a global normal, not allowing to detect such a change. The normals derived from ion measurements and magnetic field do not differ much within the common temporal interval, showing that the particle and magnetic structures are approximately identical. A different and interesting result is obtained however when observing the normal obtained using the electron flux data. While its average value is compatible with the normals obtained with the ion and magnetic field measurement (differentiating with the latter by about 15 degrees on average), we observe that this normal fluctuates a lot within the magnetopause, especially in the z direction. This feature is observed both in MDD and GF2. Furthermore, while these two approaches give compatible normals, the differences between these two are bigger than the ones observed for the magnetic field and ion mass flux, showing local differences of up to 40 degrees. While the normal obtained using GF2 seems to oscillate less than the MDD one, probably due to the fitting procedure, the significant fluctuations around the average cause the electron normal to be much more influenced by the smoothing procedure and therefore not reliable enough to be used in the

rest of the work.

To further interpret these results, the dimensionality of the magnetopause structure is analyzed using the $\mathcal{D}_{GF2}$ and D_1 parameters defined in Eq. 3.8 and 3.10. Both indices are shown in Fig. 3.8 for the three sets of measurements analyzed above. We observe that the values of $\mathcal{D}_{GF2}$ and D_1 are slightly different from each other in all three cases, especially for the electrons. Despite these differences, both indices indicate that the magnetopause is close to 1D both for magnetic field and ions: both have values always larger than 0.8 (and D_1 larger than 0.9), indicating bigger gradients along the normal direction with respect to the tangential ones. Specifically regarding the magnetic field, there is a slight decrease of $\mathcal{D}_{GF2}$ and D_1 observed in the last second of the crossing, which may account for the slight difference between the normal with respect to the average within the last part of the crossing. Additionally, both indices confirm that the electron structure is more complex with respect to the magnetic field and ions, showing characteristics significantly diverging from one-dimensionality for most of the interval, with values dropping below 0.7 for the entire last second of the crossing. This analysis thereby validates the earlier conclusions drawn solely from normal vector analysis.

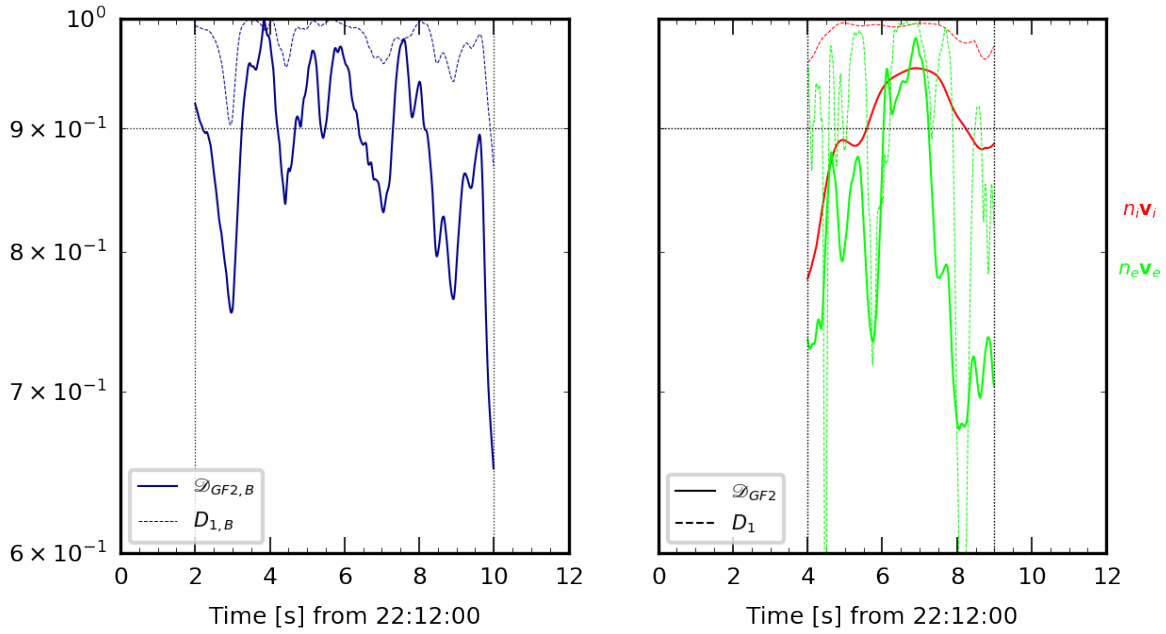

Figure 3.8: Dimensionality indices from the magnetic field (left) and particles (right, in red for ion and green for electron mass fluxes). Continuous line is the $\mathcal{D}_{GF2}$, dashed line the D_1.

In conclusion, this initial test demonstrates a satisfactory agreement between the GF2 estimation of the normal and other state-of-the-art tools, validating its capability to reliably determine the normal vector using at least the three sets of data used above. However, it's important to note that this study does not enable us to assert that GF2 is more accurate than MDD. Such a determination requires a comparison of results within a global simulation incorporating realistic turbulence. A similar analysis has been conducted in the past in Rezeau et al. (2018) on a two-dimensional numerical simulation performed by Dargent et al. (2017) using a particle-in-cell model[12]. In this study, they pointed out however how a 3D simulation is required to properly address this study. This kind of analysis has been performed also in this work on numerical simulation data, comparing the results of the MDD and GF2. The results of this study are discussed in Chapter 7.

[12]Numerical models for describing the plasma are discussed in Chapter 6.

3.5.2 The importance of smoothing

As mentioned above, a 0.31-second sliding window average was used to compute the normal at each time. The length of the window was selected to ensure that at least three data measurements, before interpolation, are included within the smoothing (the ion measurements are every 0.150 s). This averaging is designed to filter out waves and turbulence at small scales while retaining relevant information related to the magnetopause laminar profile and, therefore, to observe the local variations in the magnetopause normal. The influence of this filtering on the normal is shown in Fig. 3.9, where the normals are computed using different windows. We observe that increasing the length of the averaging interval results in the loss of fluctuations in the normal directions. Such short fluctuations are typically wave-dependent and subject to experimental uncertainty, thus not significant in the study of the magnetopause. Nonetheless, these fluctuations are up to around 8 degrees from the normal average on the 0.31-second window, underlining how the averages are fundamental in reducing the uncertainty of the error on the estimation of the normal. It's worth noting that using larger averaging intervals, on the opposite, can lead to a loss of information, especially when the ratio of the length of such intervals to the total length of the magnetopause crossing becomes large.

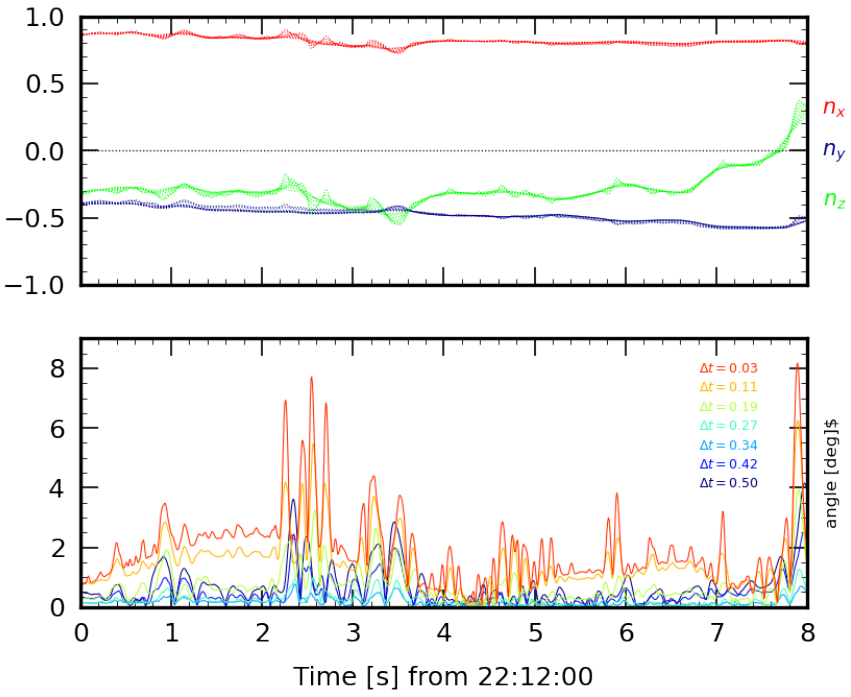

Figure 3.9: Top: variations of the normal components depending on the window temporal length. Bottom: Angles between the normal obtained using 0.31 seconds interval sliding window with normals averaged on different time intervals, as indicated in legend.

4 The Earth's magnetopause as a discontinuity

Contents

In this chapter we delve into the study of the magnetopause's structure, modeling it as a one-dimensional discontinuity. We aim to provide a deeper understanding of the magnetopause's complex properties by bridging theory and *in situ* observations. This approach proves to be a powerful one for investigating the regions that are far from reconnection sites or surface instabilities, which may render the magnetopause locally two-dimensional. These one-dimensional-like regions represent the vast majority of the magnetopause itself.

4.1 Theory of Discontinuities

Plasmas show a natural tendency to spontaneously self-organize into structured configurations, separated by thin layers. This is found both in space, in astrophysical environments, and in laboratory plasmas. Across such boundary layers, the downstream and upstream physical quantities are linked by the fundamental conservation laws: mass, momentum, energy and magnetic flux (Landau and Lifshitz, 1987). Whenever the number of conservation laws and the number of fields characterizing the plasma state are equal, the simplest scenario occurs. A typical example is the sonic shock wave in neutral gas, where the collisions guarantee an isotropic medium on both sides and the absence of heat flux (Belmont et al., 2012). In this simple scenario, the downstream state is uniquely determined as a function of the upstream state, independent of any non-ideal phenomena that may occur within the layer. Specifically, it becomes feasible to describe pressure variations without the need for any closure equation. In this case, the jumps of all quantities are determined by a single scalar parameter (namely the "shock parameter" in neutral gas).

We will refer hereafter in this manuscript to "Classic Theory of Discontinuities" (CTD) as the theory corresponding to this scenario, even if it has rarely been formalized as such in the literature. The main basis can be found in old textbooks, see *e.g.* Landau and Lifshitz (1975) and Landau and Lifshitz (1976), and it corresponds to the framework within which most of our intuition about discontinuities has been forged. This theory is applicable to both neutral media and magnetized plasmas. Here only the plasma case is analyzed[1]. To model the layer,

[1]This manuscript aims to provide an overview of the model. A more exhaustive analysis, which includes the algebraic derivations, can be found in Belmont et al. (2019).

the following simplifying assumptions are considered: a stationary layer, 1D variations, isotropic pressure, and the absence of heat flux on both sides. For plasmas, the assumption of an ideal Ohm's law on both sides is added (Belmont et al., 2019).

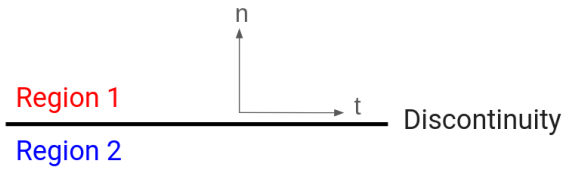

Figure 4.1: Schematic of the boundary in CTD and definition of normal and tangential directions.

Based on these assumptions, the integration of the magneto-fluid equations across the layer provides a set of conservation equations between the upstream and downstream physical quantities, the bulk velocity $\mathbf{u}$, the magnetic field $\mathbf{B}$, the density ρ, and the isotropic pressure p. The electric field $\mathbf{E}$ is given by the ideal Ohm's law on each side. This set of equations, namely the generalized Rankine-Hugoniot equations, is the equivalent of the Rankine-Hugoniot equations in neutral gases. The conserved quantities are the number density of particles, the momentum, the energy, and the normal and tangential magnetic flux. They will be denoted as ϕ_n, $\mathbf{\Phi}_m$, ϕ_e, ϕ_B, $\mathbf{\Phi}_E$ and are defined as follows:

$$\begin{cases} \phi_n = \rho u_n \\ \mathbf{\Phi}_m = \rho u_n \mathbf{u} + \left(p + \dfrac{B^2}{2\mu_0}\right)\mathbf{n} - \dfrac{B_n \mathbf{B}}{\mu_0} \\ \phi_e = \dfrac{1}{2}\rho u^2 u_n + \dfrac{5}{2} p u_n - \dfrac{1}{\mu_0}\mathbf{B}_t \cdot (B_n \mathbf{u}_t - u_n \mathbf{B}_t) \\ \phi_B = B_n \\ \mathbf{\Phi}_E = \mathbf{E}_t \text{ with } \mathbf{E} = -\mathbf{u} \times \mathbf{B} \end{cases} \tag{4.1}$$

Here we define the indices n and t to indicate the normal and tangential directions with respect to the layer, as shown in Figure 4.1 (we reserve the notation 'parallel' and 'perpendicular' for references with respect to the magnetic field, as usual in plasma physics). Hereafter, we will name the upstream and downstream regions with the indices "1" and "2" respectively.

N.b. The electric field can be chosen to be zero by choosing the tangential frame known as the de Hoffmann-Teller frame (De Hoffmann and Teller, 1950; Paschmann and Daly, 1998). Taking into account the ideal Ohm's law, this condition $\mathbf{E} = 0$ cancels the last term of the energy equation.

4.1.1 Discontinuities with $B_n \neq 0$

Let us first analyze the discontinuities in the general case $B_n \neq 0$. In this case, a special solution occurs when $u_n = u_{nA}$, with $u_{nA} = B_n^2/(\mu_0 \rho u_n)$. Specifically:

- for $u_n = u_{nA}$ we find the so-called "rotational discontinuity". This solution corresponds to an Alfvén wave in which p, B^2, and ρ are conserved separately. This discontinuity, which is schematized in Figure 4.3, is characterized by a rotation of the tangential component of the magnetic field without a variation of its module. Thus, examining the conservation of the momentum in the normal direction, we find that $p + B_t^2/2\mu_0$ is conserved. Additionally, the conservation of energy implies the preservation of B_t^2, leading to the separate conservation of p.

- for $u_n \neq u_{nA}$, *i.e.* for all other values of the incident normal velocity, we find the so-called "compressional discontinuity" (also known as *shock*). This solution is characterized by a variation of the magnetic field module (as well as the velocity and density) with no rotation of the magnetic field in the tangential plane. Figure 4.2 shows a schematization of the magnetic field variation. Three types of shock solutions exist, listed with increasing

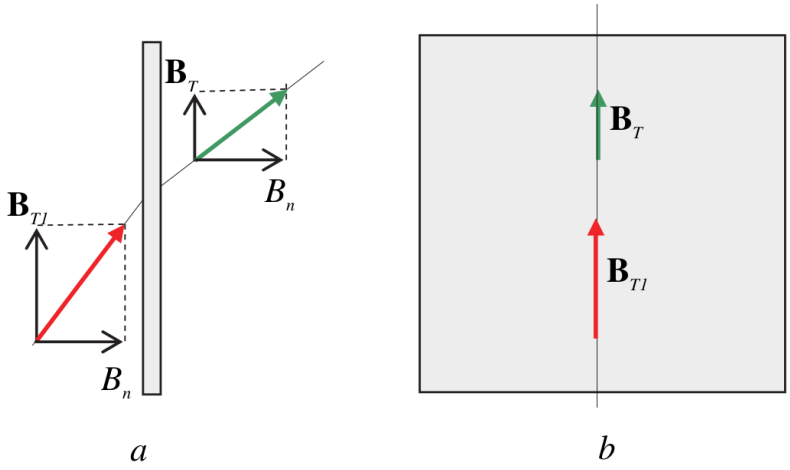

Figure 4.2: Evolution of the magnetic field across a shock: on the left, the projection in the plane perpendicular to the discontinuity, on the right, in the plane of the discontinuity. The upstream field is in red, downstream field is in green. Credit: (Belmont et al., 2019)

incident normal velocity:

1. Slow shock: Occurring for incident normal velocities between the slow mode velocity and the Alfvén speed. In this case, a decrease in normal velocity and tangential magnetic field is observed, while pressure and density increase;
2. Intermediate shock: Similar to slow shock, with a reversal of the magnetic field (and of the tangential velocity in the de-Hoffman Teller frame);
3. Fast shock: Occurring when the incident normal velocity is above the fast mode velocity. A decrease of the normal velocity, typical of all shocks, is observed while the tangential magnetic field, pressure and density increase.

- for $u_{n,2} = u_{n,1} = 0$ we find the so-called "contact discontinuity". This solution only presents a jump in density and temperature, while keeping the pressure value constant (equal to the product $p = nT$). This solution, however, is not expected to be observed in plasmas since diffusion-like mechanisms would quickly erode it.

4.1.2 Discontinuities with $B_n = 0$

Let us now focus the particular case $B_n = 0$.

- for $u_n \neq 0$ we find a fast shock with perpendicular propagation (a more detailed description can be found in Belmont et al. (2019)). This solution is regular since it is just the limit of the fast general solution when B_n tends to zero.

- for $u_n = 0$ we find the so-called "tangential discontinuity", corresponding to a degenerate solution of the system. In this condition, any relationship between the upstream and downstream values of both magnetic field and tangential velocity is lost, both being therefore decoupled. Only the conservation of the normal component of the momentum still provides a relationship between upstream and downstream states, corresponding to

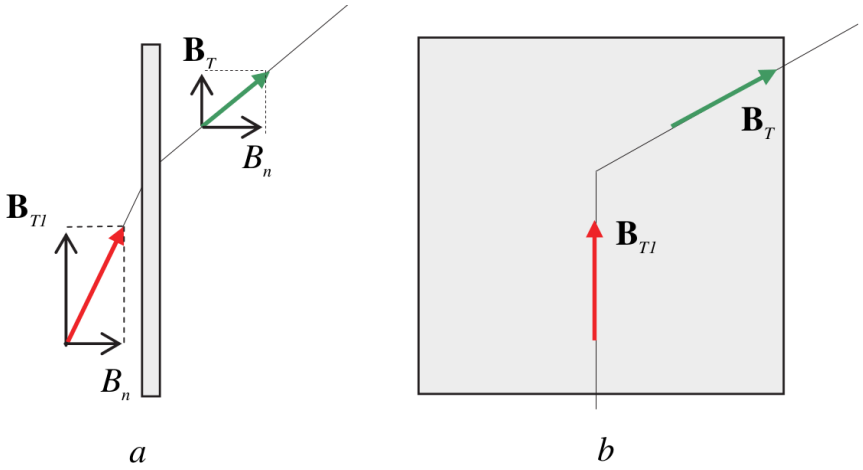

Figure 4.3: Evolution of the magnetic field across a rotational discontinuity: on the left, the projection in the plane perpendicular to the discontinuity, on the right, in the plane of the discontinuity. Upstream field in red, downstream field in green. Credit: (Belmont et al., 2019)

the conservation of the total pressure $p + B^2/2\mu_0$. This solution presents no plasma flow across the boundary and allows both rotation and compression. It is worth noticing that the tangential discontinuity is the only class in CTD to present both features. This solution is singular in the sense that it not the limit of one of the general solutions when B_n tends to zero. It is rather an arbitrary combination of the slow and rotational solutions.

4.1.3 Beyond CTD

The jump conditions in Eq. 4.1 can consistently be demonstrated by integrating the complete medium equations across the layer. In this sense, these equations can never be said to be "ideal MHD equations", as they are sometimes referred to, since ideal MHD is never valid inside the layer. As conservation equations, they are *a priori* much more general. It is important however to understand how all effects present inside the layer, fluid or kinetic, intervene in the integration and what is the role of the hypotheses done on the outside media (especially the isotropy of the pressure tensor).
At the MHD equations level, it is important to note that ideal terms always lead to the non-linear steepening of any gradient, thereby contributing to the formation of thin boundaries, being therefore responsible for the existence of thin boundaries and that non-ideal terms must necessarily be present inside the boundaries for explaining their stationary structure. The pertinent form of the jump equations therefore depends in general on the integration of these non-ideal terms, being null only in some particular cases. Here are some examples:

1. In Ohm's law, assuming the presence of non-ideal terms defined as $\mathbf{E}_{nid} = \mathbf{E} + \mathbf{u} \times \mathbf{B}$, the corresponding non-ideal term in Faraday's equation would be equal to $\mathbf{n} \times \mathbf{E}'_{nid}$ (with the $'$ symbol indicating the spatial variation), leading to a term $\mathbf{n} \times \Delta\mathbf{E}_{nid}$ in the jump equation for $\mathbf{\Phi}_E$ in the set of Equations 4.1. Here $\Delta\mathbf{E}_{nid}$ represents the variation of $\mathbf{E}_{nid}$ between the two sides of the discontinuity. This term is independent of the values of $\mathbf{E}_{nid}$ inside the layer and it is zero whenever $\mathbf{E}_{nid} = 0$ on both sides. This is valid in particular when the two asymptotic media are homogeneous, which is the most common hypothesis.

2. In the momentum equation, when we consider the presence of non-isotropic contribution one can write $p = p_{iso} + p_{ns}$ (with p_{ns} the non-isotropic contribution), which leads to that addition of a non-ideal term $\mathbf{n}.\Delta p_{ns}$ in the equation for $\mathbf{\Phi}_m$. As above, Δp_{ns} defines the variation between the two sides of the discontinuity of p_{ns}. This term is independent of the values of p_{ns} within the layer and can be zero at the condition that the non-isotropic

part of the pressure has the same value on each side of the layer, as discussed in detail in Section 4.4. For homogeneous asymptotic media, this term can be zero also in the case in which p_{ns} contains spatial derivatives, as the viscosity term in collisional plasmas. Otherwise, the validity of such a strong hypothesis is far from universal and has always to be checked, with the possibility of bringing noticeable change in the jump equation.

3. In the energy equation, one non-ideal term comes from the heat flux term, whose integration is $\mathbf{n}.\Delta\mathbf{Q}$. Again, this term is independent of the heat flux profile inside the layer, and it can be zero if the heat flux has the same value on both sides (such as the rather common hypothesis where it is assumed to be equal to zero).

4.2 Limitations of CTD at the magnetopause

CTD can be employed to investigate the magnetopause under several conditions, the first one being to consider the boundary as a "thin" layer separating two quasi-homogeneous media. Here, "thin" emphasizes that at the magnetopause variations in plasma quantities occur over a very small spatial interval relative to the dimensions of the magnetosphere. Thanks to *in situ* observations, we have gained a comprehensive -yet not complete- understanding of the main features of the magnetopause structure, now enabling us to check the validity of the whole set of conditions assumed in CTD. Over the entire surface of the Earth's magnetopause, both "rotational" variations (i.e. the variations associated with the rotation of the magnetic field and the tangential velocity, Sonnerup and Ledley (1974)) and "compressive" variations (those associated with the plasma quantities with plasma parameters such as density, temperature, pressure, and the magnitude of the magnetic field, Otto (2005)) are observed (Dorville et al., 2014). This occurs since the magnetosheath and the magnetosphere have distinct magnetic field directions and modules.

Since both kinds of variations occur within the same discontinuity, then the magnetopause is generally interpreted as a tangential discontinuity, implying the absence of particle flow across the boundary. Therefore, the prevailing paradigm suggests that the magnetopause is mainly a tangential discontinuity and only becomes "open" exceptionally at a few points where reconnection occurs (Paschmann et al., 2005b; Cowley, 1995) and where the 1D hypothesis therefore becomes invalid. Close to reconnection sites, observations have shown evidence of "rotational" layers, but the situation is then more intricate and generally implies several close discontinuities.

Do the experimental data support the tangential paradigm deriving from CTD? On the one hand, it's established that compressional and rotational variations are not always combined, as demonstrated by numerous observations of rotational discontinuities (Chou and Hau, 2 08). Another illustrative example is provided by Dorville et al. (2015b), where two distinct substructures (moving with respect to each other) have been found within the magnetopause: a rotational discontinuity and a slow shock. On the other hand, the tangential paradigm relies on the very radical hypothesis of a magnetopause completely impermeable to mass and magnetic flux, with B_n and u_n strictly null. However, experimental observations cannot distinguish between $B_n = 0$ and $B_n \simeq 0$, primarily due to uncertainties in determining the normal direction (Rezeau et al., 2018; Haaland et al., 2004; Dorville et al., 2015b). Hence, it becomes challenging to definitively identify a tangential discontinuity. What is known is that, at the magnetopause boundary, the components B_n and u_n are generally found to be non-null but very small. The limit of small values B_n and u_n is poorly described by CTD, as even infinitesimal values of these quantities would not permit the mixing of rotational and compressive features. Consequently, even slight variations in these quantities can significantly alter the corresponding topology of the structure, making singular the character of the tangential solution, as already mentioned. . This work will show that the main limitation of CTD in describing the magnetopause arises from the

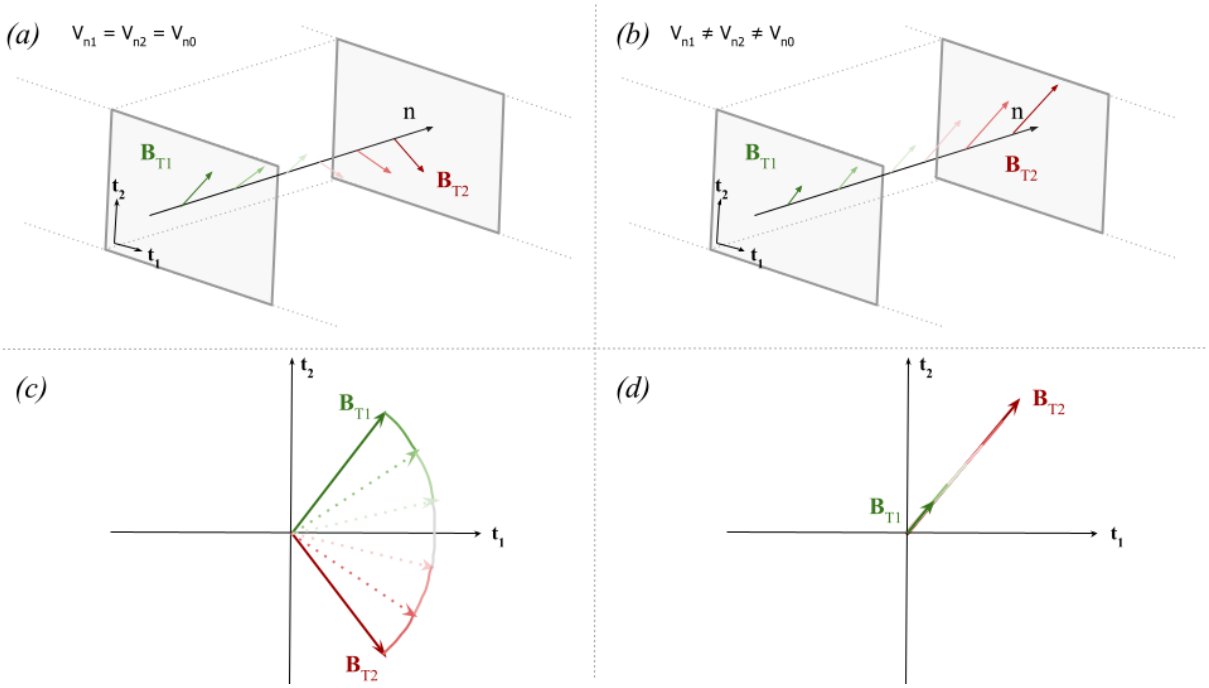

Figure 4.4: Cartoon showing the different variations of B between a rotational discontinuity (left) and a compressive one (right). The top panel shows in 3D the variation of B inside the magnetopause plane; the bottom panel shows the hodogram in this tangential plane: a circular arc for the rotational discontinuity and a radial line for shocks.

isotropy assumption. Indeed, as soon as this hypothesis is relaxed (Hudson, 1971), the number of conservation equations becomes insufficient to determine a unique downstream state for a given upstream state. As a consequence, the global result depends on the non-ideal processes occurring within the layer. This would provide the non-ideal effects that account for the jumps across the 1D stationary layer, opening the possibility to new types of discontinuities.
The paradigm of the magnetopause (outside of reconnection regions) as an impermeable tangential boundary is based on CTD. However, in this chapter, we aim at demonstrating, both theoretically and experimentally, why this theory fails at describing the magnetopause, leading to question this paradigm. We will illustrate that rotation and compression can coexist even in the 1D case, with finite B_n and u_n.

4.3 The magnetopause as a discontinuity: how to study *in situ* data

As discussed before, there is a clear difference between the rotational discontinuities and compressional ones. To investigate these differences, we can exploit the hodogram of the magnetic field in the plane tangential to the discontinuity (see Fig. 4.4), which can be easily obtained from *in situ* data. This analysis allows us to determine whether the magnetopause exhibits rotational, compressional, or both characteristics. Considering a magnetopause crossing from spacecraft data, if CTD was valid through all the crossings, the shape of the hodogram would depend on the discontinuity class. For a rotational discontinuity, the hodogram would correspond to a circular arc with constant radius, since the tangential component of the magnetic field is conserved. For a shock, the hodogram would correspond to a radial line because of the absence of rotation of the tangential component of the magnetic field. Such a distinction of hodograms is shown in the sketch in Fig. 4.4. Different attempts to classify magnetopause hodograms also exist in the literature, as seen in studies such as Sonnerup and Ledley (1974); Berchem and Russell (1982a). In these studies, hodograms were classified as C-shaped or S-shaped according to their shape, with some evidence suggesting that S-shaped hodograms could represent rotational

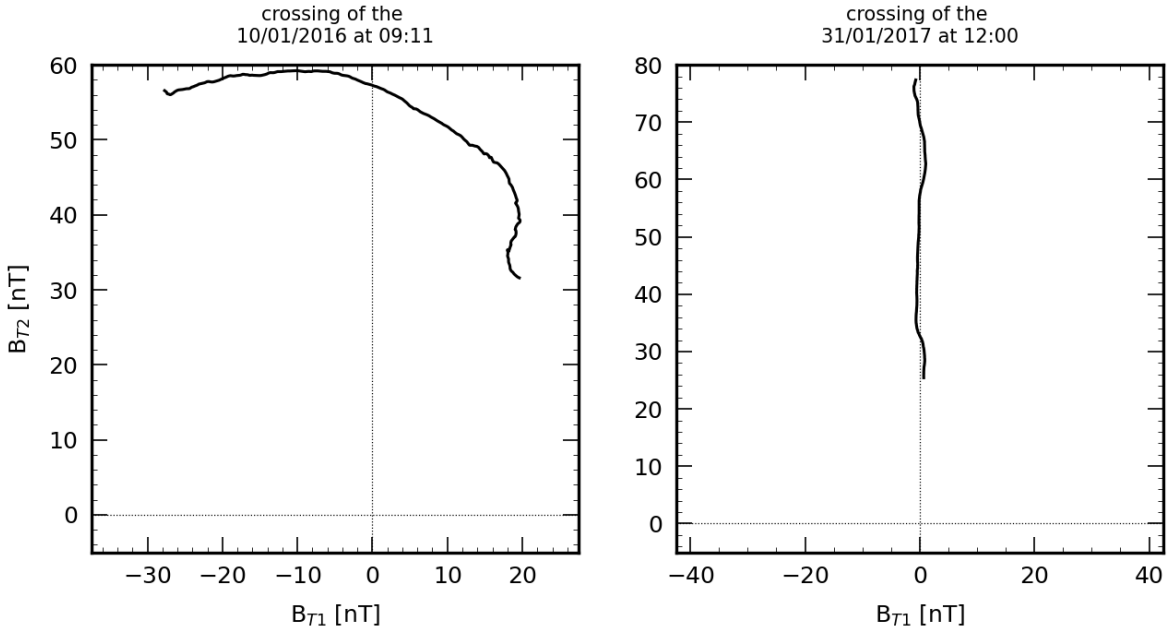

Figure 4.5: Hodograms of the magnetic field for magnetopause crossings showing typical features of a rotational (left) and compressive (right) discontinuities. B_{T1} and B_{T2} are the projections of $\mathbf{B}$ along the tangential directions computed as described in the text.

discontinuities formed during reconnection. However, this type of classification is not based on CTD but originates from the observations themselves. A more recent and comprehensive study on this can be found in (Panov et al., 2011), where a reconstruction of the magnetopause structure in the two different cases is reported. This previous classification however does not interpret hodograms in the context of CTD and therefore will not be used in this manuscript.

The first step to obtaining the hodogram from the data is to define a reference system in the tangent plane. However, such a frame of reference is a mere convention, as changing the reference system corresponds to a rotation in the plane of the hodogram that does not alter its shape and, therefore, the results. Here we choose the following directions in the tangent plane:

$$\mathbf{T}_1 = \mathbf{n}_{mean} \times \hat{\mathbf{b}} \tag{4.2}$$

$$\mathbf{T}_2 = \mathbf{n}_{mean} \times \mathbf{T}_1 \tag{4.3}$$

Here, the two tangential directions are defined as functions of the normal, obtained with the GF2 tool, and the direction of the magnetic field $\hat{\mathbf{b}} = \mathbf{B}/|\mathbf{B}|$, both averaged in the crossing interval and normalized to have unitary vectors. An example of two MMS crossing showing typical CTD features, for a rotational (left) and compressive (right) discontinuity is shown in Fig. 4.5.

The hodogram is, therefore, an effective instrument for the recognition of the cases where the CTD succeeds or fails in describing the magnetopause, especially when the observed hodogram corresponds or not to an arc of circumference or a radial line. Particularly interesting is the hodogram for the magnetopause crossing of MMS on 28.12.2015 discussed before in Chapter 3. This crossing presents one-dimensional and stationary characteristics required by the CTD model. To mitigate the possible impact of small non-monodimensional features observed in the last second of the crossing, we will not include this part of the interval in this study.

The hodogram for this crossing is presented in Fig. 4.6, showing that the result does not depend on the choice of averaging the normal over the interval. Indeed, by exploiting the local

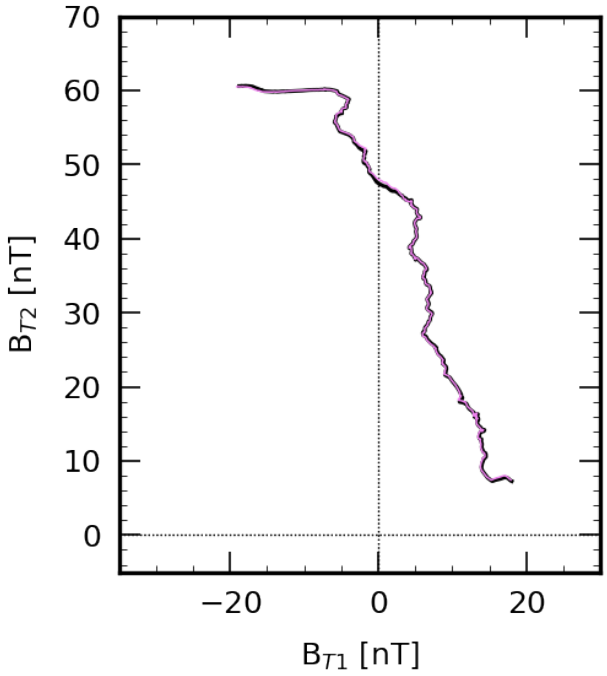

Figure 4.6: Hodogram in the tangential plane of the magnetic field for a magnetopause crossing by MMS in 28.12.2015 from 22:12:02 to 22:12:09. The black line (resp. violet) is the hodogram when the $\mathbf{n}_{mean}$ (resp. $\mathbf{n}$) value is used to define the reference frame.

(not averaged) normal (purple line), we see that the result is almost unchanged. This crossing is an example that exhibits a clear linear (though not radial) trend in the hodogram. This non-radial variation of the magnetic field, not predicted by the CTD, is a striking feature of the hodogram and rather common at the magnetopause[2]. It cannot be explained by a departure from the one-dimensional hypothesis, as we have determined that the crossing can be considered as one-dimensional with a good degree of accuracy. Therefore, it must be due to an intrinsic property of the layer itself.

4.4 A possible explanation: the role of the pressure tensor

To understand why the CTD fails to predict the linear hodogram of the magnetic field observed from the magnetopause data, we can initially trace back to the equation used to distinguish rotational and compressive structures in order to identify which assumption in CTD restricts the description of the magnetopause.
This equation is derived from the moment equation (Eq. 1.27) and the Faraday-Ohm law (Eq. 1.13-1.29) by assuming, as in CTD, the one-dimensionality of the structure, therefore presenting gradients only along the normal direction $\mathbf{n}$, and the exclusion of non-ideal terms in Ohm's law. Then, by integrating the two tangential equations across the layer and projecting them onto the tangential plane, we get:

$$\rho u_n \mathbf{u}_{t2} - B_n \mathbf{B}_{t2}/\mu_0 = \rho u_n \mathbf{u}_{t1} - B_n \mathbf{B}_{t1}/\mu_0 \tag{4.4}$$

$$B_n \mathbf{u}_{t2} - u_{n2} \mathbf{B}_{t2} = B_n \mathbf{u}_{t1} - u_{n1} \mathbf{B}_{t1} \tag{4.5}$$

Again, the indices n and t represent the projection along the normal and in the tangential plane, respectively, while indices 1 and 2 indicate the two sides of the discontinuity. Concerning

[2] A quantification of what we mean by common is made in Chapter 5

the second equation, it is notable that both sides could be set to zero if we adopt the "De Hoffmann-Teller" reference frame (defined as the reference frame where the electric field is zero, Belmont et al. (2019)). However, while this choice simplifies some calculations, it is not necessary here. Furthermore, B_n and ρu_n have no indices since they are identical on both sides (because of the divergence-free and continuity equations, respectively). We observe that all terms in these equations are proportional to B_n or u_n, implying that any non-ideal term, even if small, can become dominant where these two parameters tend to zero (unless they share the same behavior). From these two equations, we can now eliminate the variable $\mathbf{u}_t$ by performing a linear combination. We get:

$$(u_{n2} - u_{nA})\mathbf{B}_{t2} = (u_{n1} - u_{nA})\mathbf{B}_{t1} \tag{4.6}$$

where

$$u_{nA} = \frac{B_n^2}{\mu_0 \rho u_n} = \text{cst} \tag{4.7}$$

From this equation we obtain the shock solution when the tangential magnetic field direction remains unchanged between the two media, while a rotational discontinuity occurs when the terms inside the brackets are equal to zero. In the latter scenario, we find a discontinuity characterized by a propagation velocity equal to the normal Alfvén velocity, $u_{n1} = u_{n2} = u_{nA}$, and a lack of plasma compression, typical of the rotational cases.

However, we can easily observe that the pressure divergence terms are absent in Eq.4.4, and therefore in Eq.4.6, due to the assumption made in CTD that the pressure is isotropic on both sides of the layer. Indeed, due to this assumption, the integration of the pressure term in the momentum equation yields expressions of the form $(p_2 - p_1)\mathbf{n}$, devoid of any component in the tangential plane and, therefore, from Eq.4.4 and 4.6. This assumption can therefore be interpreted as the one limiting CTD from adequately describing the magnetopause conditions. For this reason, we can study how relaxing this assumption would alter the results from CTD. However, the inclusion of a full non-gyrotropy would require a full kinetic description or, at least, some expansions assuming that these effects are sufficiently small. Previous literature attempted to study this limit, such as in the case of the pioneering work of Braginskii (1965) or the work in Passot and Sulem (2006) and references therein.

To gain insight into these limitations, we can begin by studying a first limit that allows us to continue using fluid equations without adding further assumptions on the magnetopause structure. Let us study how a simple anisotropy preserving gyrotropy around $\mathbf{B}$ affects the results from CTD. This assumption can be straightfully taken into account for modeling the pressure tensor and using it in fluid equations.

4.4.1 CTD with anisotropic/gyrotropic conditions

We can now examine how changing the assumption on the pressure tensor, transitioning from the isotropic case to the "simple" anisotropic case, *i.e.* keeping the gyrotropy around $\mathbf{B}$, affects the separation between the rotational and compressive solution in CTD. In this scenario, the pressure tensor can be modeled as follows:

$$\mathbf{P} = p_{\parallel}\hat{\mathbf{b}}\hat{\mathbf{b}} + p_{\perp}(\hat{\mathbf{I}} - \hat{\mathbf{b}}\hat{\mathbf{b}}) \tag{4.8}$$

Here, $\hat{\mathbf{b}}$ is the versor indicating the direction of the magnetic field while $p_{\parallel}$ and $p_{\perp}$ are the thermal pressure parallel and perpendicular with respect to the magnetic field. In this limit, it has been shown by Hudson (1971) that the $\nabla \cdot \mathbf{P}$ term comes into play by linking upstream and downstream quantities. Specifically, this term introduces a new coefficient α in Eq.4.6, defined as follows:

$$\alpha = 1 - \frac{p_{\parallel} - p_{\perp}}{B^2/\mu_0} \tag{4.9}$$

Therefore, in the anisotropic case, the equation separating rotational and compressive solutions reads:

$$(u_{n2} - \alpha_2 u_{nA})\mathbf{B}_{t2} = (u_{n1} - \alpha_1 u_{nA})\mathbf{B}_{t1} \tag{4.10}$$

This coefficient can be interpreted as a change in the Alfvén velocity $V'^2_{An} = \alpha V^2_{An}$. From Eq. 4.10, we note that due to the relaxation of the isotropic hypothesis, the number of conservation equations is no longer enough to determine uniquely the downstream state as a function of the upstream conditions. Consequently, the global result depends on the non-ideal processes occurring within the layer. Notably, we observe that the values of α on both sides of the layer influence the properties of discontinuities. On one hand, coplanar solutions, which are the generalization of shocks in the isotropic limit, exists also in this limit (whenever $\mathbf{B}_{t2}$ and $\mathbf{B}_{t1}$ are collinear). The persistence of collinear solutions comes from the gyrotropic assumption: in the non-gyrotropic case, the magnetic field direction is no more the unique direction that breaks the isotropy and this property disappears. However, whenever the value of α is not equal on the two sides, the equivalent of the rotational discontinuity now implies compression:

$$u_{n2} \neq u_{n1} \qquad \text{if} \qquad \alpha_2 \neq \alpha_1 \tag{4.11}$$

Since $u_{n2} = \alpha_2 u_{n0}$ and $u_{n1} = \alpha_1 u_{n0}$. Therefore, in this limit, we observe a variation of the normal velocity with respect to the structure. This explains why the modified rotational discontinuity can be "evolutionary" (Jeffrey and Taniuti, 1964), where the non-linear steepening is counter-balanced at equilibrium by non-ideal effects for a thickness comparable with the characteristic scale of these effects.

Equation 4.11 demonstrates how the presence of a simple anisotropy can allow to describe the coexistence of compression and rotation without the condition $B_n = 0$ to be fulfilled. Specifically, this finding highlights the importance of considering the non-ideal effects within the magnetopause, which characterize its pressure tensor and determine the variation of α. Given that the ion Larmor radius ρ_i and the ion inertial length d_i are typically non-negligible with respect to the characteristic scale L of the magnetopause, Finite Larmor radius (FLR) effects have to be taken into account when describing the magnetopause. In other words, whenever the gyroradius of the particles cannot be neglected, the pressure tensor can become non-gyrotropic. Therefore, the divergence of the pressure tensor is no longer reduced to simply adding a coefficient α as in the anisotropic case since its tangential component is no longer collinear with $\mathbf{B}_t$. In the literature, the influence of these effects has already been reported and analyzed in the context of magnetic reconnection (Aunai et al., 2013b, 2011) and in kinetic modeling of purely tangential layers (Belmont et al., 2012; Dorville et al., 2015a). Further investigation has been done also in the case of linear modes where FLR effects are responsible for the transition from shear Alfvén into Kinetic Alfvén Wave (Hasegawa and Uberoi, 1982; Belmont and Rezeau, 1987; Cramer, 2001). However, it has never been introduced in the context of quasi-tangential discontinuities. To study the influence of FLR effects at the magnetopause, we will examine in detail the crossing of 28.12.2015, already discussed before. This crossing, showing features not included in CTD, will be used as a test case for FLR effects within the magnetopause.

4.4.2 Estimation of non-gyrotropy from data

Before delving into the detailed study of the MMS crossing with the linear-shaped magnetic hodogram, we start focusing on how we can quantitatively study non-gyrotropy (around $\mathbf{B}$). Although the definition of non-gyrotropy is clear, a single metric is difficult to define and therefore a quantification can vary depending on the application. We now briefly introduce the most common scalar indicators used to quantify the local non-gyrotropy of the pressure tensor. We then develop a new non-gyrotropy index.

The first indicator is the so-called *agyrotropy*, used, for instance, in Karimabadi et al. (2007); Scudder and Daughton (2008a); Pritchett and Mozer (2009) and Scudder et al. (2012). It uses

the eccentricity of the ellipse corresponding to the covariance matrix of the velocity distribution projected onto a plane perpendicular to the magnetic field. Consequently, its magnitude indicates the asymmetry of the distribution relative to the magnetic field. Finally, agyrotropy is defined as the difference between the two pressure eigenvalues associated with eigenvectors perpendicular (namely $p_{\perp,1}$ and $p_{\perp,2}$) to the mean magnetic field direction, normalized by the average of the two:

$$\mathcal{AG} = 2\frac{|p_{\perp,1} - p_{\perp,2}|}{p_{\perp,1} + p_{\perp,2}} \tag{4.12}$$

Another indicator of a scalar metric was presented in Aunai et al. (2013a). In this study, they defined a measure of nongyrotropy by estimating the gyrotropic and non-gyrotropic contributions to the pressure tensor. Specifically, to obtain this metric, the pressure tensor is split into two contributions as follows:

$$\mathbf{P} = \mathbf{G} + \mathbf{N} \tag{4.13}$$

Here $\mathbf{G}$ is defined as the gyrotropic part and $\mathbf{N}$ as the non-gyrotropic part of the full pressure tensor $\mathbf{P}$. Regarding the gyrotropic part $\mathbf{G}$, it can be expressed as the pressure tensor modeled in the anisotropic case (Eq. 4.8), where $p_{\parallel}$ and $p_{\perp}$ are derived from $\mathbf{P}$ as follows:

$$\begin{cases} p_{\parallel} = \hat{\mathbf{b}} \cdot \mathbf{P} \cdot \hat{\mathbf{b}} \\ p_{\perp} = (\mathrm{Tr}(\mathbf{P}) - p_{\parallel})/2 \end{cases} \tag{4.14}$$

From this decomposition, Aunai et al. (2013a) the non-gyrotropic index has been defined as follows:

$$D_{ng,A} = \frac{\sqrt[2]{\sum_{i,j} \mathbf{N}_{i,j}^2}}{\mathrm{Tr}(\mathbf{P})} \tag{4.15}$$

The strong point of this index lies in its ability to quantify the nongyrotropy of a velocity distribution by measuring the deviation of the pressure tensor from the strictly gyrotropic one, independently of the basis in which the tensors are represented, thus representing the energetically equivalent gyrotropic distribution.

In our study we define a new indicator similar to agyrotropy, focusing on the eccentricity of the pressure tensor in the perpendicular plane. However, it can be generalized to cases where none of the eigenvectors of the pressure tensor are parallel to the mean magnetic field.

To define this index, we introduce the matrix $\mathbf{P}_{\perp}$ as the projection of the pressure tensor in the perpendicular plane with respect to the magnetic field (therefore, $\mathbf{P}_{\perp} = \mathbf{P}_i - \mathbf{P}_{\parallel}$ with $\mathbf{P}_{\parallel} = p_{\parallel}\hat{\mathbf{b}}\hat{\mathbf{b}}$ and $p_{\parallel} = \hat{\mathbf{b}} \cdot \mathbf{P}_i \cdot \hat{\mathbf{b}}$). From this matrix, we can now define p_1 and p_2 the maximum and intermediate eigenvalues from which we estimate the non-gyrotropy as follows:

$$D_{ng,\perp} = \frac{p_1 - p_2}{p_1 + p_2} \tag{4.16}$$

This index has been utilized in Ballerini et al. (2024b) using the sliding window technique as in GF2.

4.5 Testing CTD from *in situ* data

In this section, we will analyze the crossing of December 28, 2015, and focus on the linear shape of its hodogram. The study consists of three consecutive steps: i) analysis the observed magnetic hodograms, focusing on which of the physically relevant directions in the problem influences the hodogram the most; ii) study of the relevant terms in Ohm's law and the momentum equation, aiming at testing which of the assumptions made in the CTD fails for this particular crossing; iii) quantification the non-gyrotropy using the non-gyrotropy indices as defined in the previous Section.

4.5.1 Hodogram principal directions

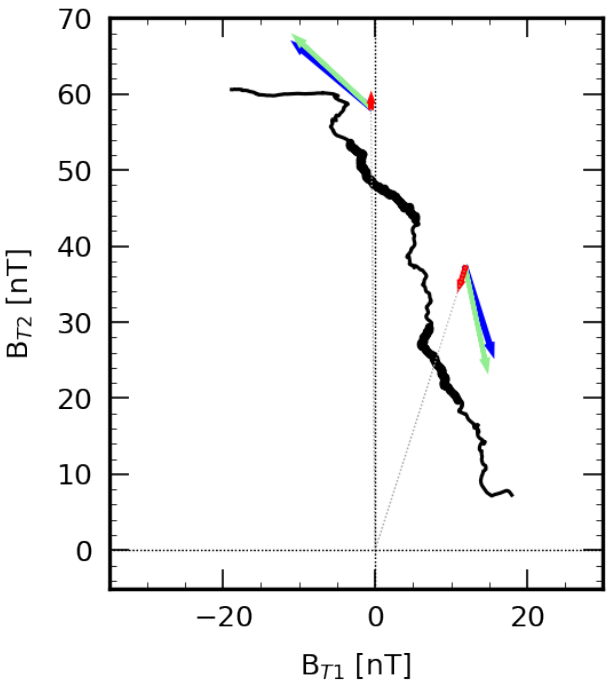

Figure 4.7: Hodogram in the tangential plane of the magnetic field for a magnetopause crossing by MMS on 28.12.2015 from 22:12:02 to 22:12:09. The bold regions indicate the two sub-intervals chosen for the analysis. See text for the significance of the arrows.

As a preliminary step, we revisit the analysis of the hodogram in the tangent plane. Specifically, we examine three physically significant directions within the tangent plane: *i*) The direction of the variation of the magnetic field in this plane, aligned with the hodogram, *ii*) the direction of plasma compression, which is radial, and *iii*) the direction of the divergence of the ion pressure tensor ($\nabla \cdot \mathbf{P}_{it}$).

For this analysis, we have selected two sub-intervals of the crossing[3] and computed the average magnitude of these three quantities. These intervals are highlighted in Fig. 4.7 as the bolded regions. We superimpose the three directions discussed above. The relative lengths of the arrows are chosen proportionally to the magnitudes of the corresponding terms. The hodogram direction is represented in green, the radial direction in red, and the divergence of the pressure in blue. The important result is that the total variation of the hodogram is mainly determined by the non-classic term of the divergence of the ion pressure and not by the radial classic one. This result provides initial evidence of the significant role played by the pressure tensor in this equilibrium, validating our previous assumptions that the non-gyrotropy may play a fundamental role at the magnetopause.

4.5.2 The Ohm's law and the momentum equation

A second confirmation of the role of the pressure in magnetopause equilibrium can be derived from the study of Ohm's law and the momentum equation. As we discussed earlier, starting from the integration of the tangential components of these two equations we obtain Eq. 4.6, distinguishing between rotational and compressive discontinuities. The comparison of the data with the model will indicate which terms are not included in CTD.

[3]Namely the intervals are 1 second long and start from 22:12:05 and 22:12:07.

To achieve this it is necessary to obtain an accurate determination of the normal direction to reduce experimental uncertainty in the measurements of the normal fluxes. Typically, the projections of all fluxes along the normal direction, which appear in the conservation equations, are significantly smaller than the tangential ones. This is why reducing the uncertainty on the normal direction is absolutely necessary to get a reliable estimation of these needed normal fluxes.

In this study, we consider the mean normal direction $\mathbf{n}_{mean}$ and the mean tangent direction $\mathbf{t}_{1,mean}$, obtained using the GF2 method (described in Section 3.4.1), averaged over the crossing time interval. The invariant direction defined in GF2, which completes the basis of the reference system, is not analyzed due to dominance by noise in the measurements. By using the mean values, we reduce statistical errors and minimize fluctuations in the two directions, enhancing interpretability. However, as discussed in Ballerini et al. (2024b), similar results in the analysis of the tangential components can also be obtained by exploiting local values of these two directions. The projections of the two equations along these directions are shown in Fig. 4.8. Specifically, the current is estimated from the gradient matrix of the magnetic field neglecting the displacement current in Faraday's law, while the divergence of the particle pressure, for both ions and electrons, is obtained from the gradient matrix of the pressure tensor. Both the magnetic field and pressure gradient matrix are obtained using the reciprocal vector method described in section 3.3.1.

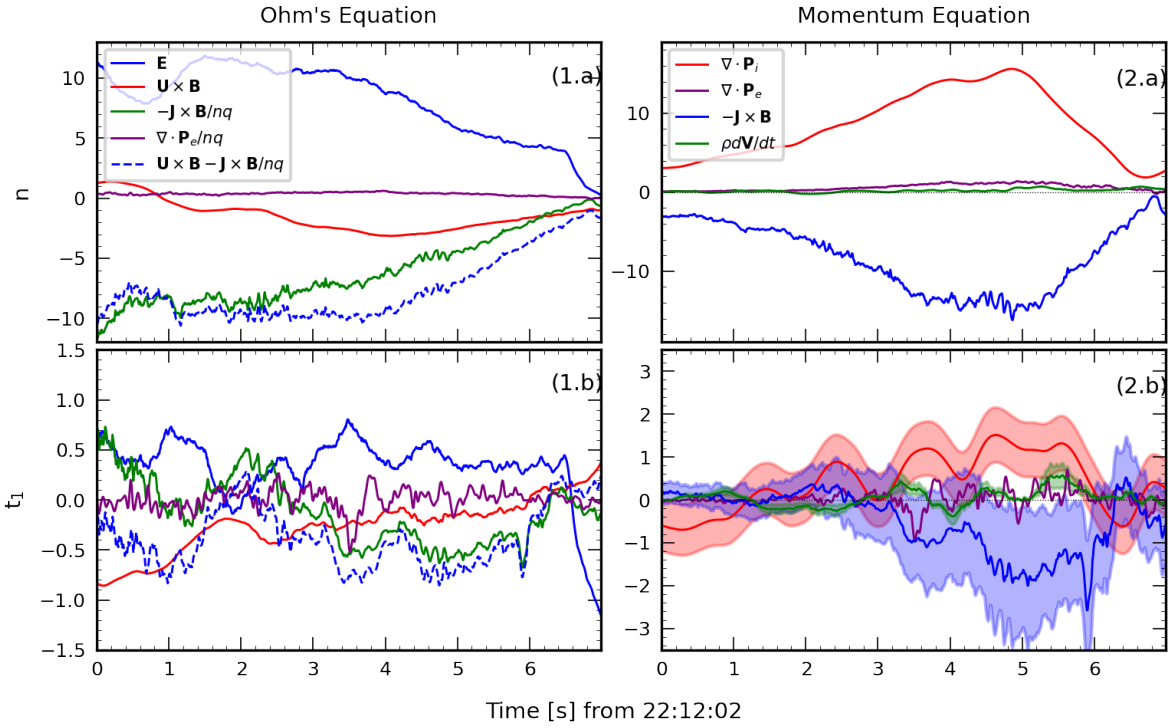

Figure 4.8: Terms of the Ohm's law (panel 1, units of mV/m) and the momentum equation (panel 2, units of $10^{-15} kg\, m/s^2$), projected in the normal direction n (a) and in the tangential direction (t_1 (b). To reduce the noise, a running average with a time window of 0.35s is applied to the electric field measurements. Shaded regions in panel 2.b represent the estimated uncertainties of the divergence of the pressure (red), the $\mathbf{J} \times \mathbf{B}$ (blue) and the classic inertial term (green). *N.b.* The terms of the tangential Faraday/ Ohm's law used in the text are just the derivatives of the ones in (a) (apart from a $\pi/2$ rotation).

The Ohm's law

We can now begin with the generalized Ohm's law terms, shown in the left panel of Fig. 4.8. It is observed that along the normal and tangential directions, the electric field is effectively counterbalanced by the $\mathbf{u} \times \mathbf{B}$ and $\mathbf{J} \times \mathbf{B}/nq$ terms (ideal and Hall terms). Additionally, at both extremities of the crossing, the ideal Ohm's law is satisfied. This demonstrates the consistency between the conditions for the Ohm's law, assumed ideal on both sides of the layer, in CTD and data. However, the $\nabla \cdot \mathbf{P}_e/nq$ is not always entirely negligible along the tangential direction (specifically at approximately 3.5 seconds). From the literature, it is known that the relevance of the electron pressure contribution can serve as a signature of magnetic reconnection, as it can be dominant close to and within an Electron Diffusion Region (EDR). This feature has been both predicted theoretically (Hesse et al., 2011, 2014) and observed experimentally (Torbert et al., 2016; Genestreti et al., 2018). However, in this crossing, this value is not dominant, this term is smaller than both the electric field and the $\mathbf{J} \times \mathbf{B}/nq$ components. Furthermore, $\nabla \cdot \mathbf{P}_e/nq$ is only non-negligible within a small sub-interval (with respect to the magnetopause temporal width). It is therefore not likely to be indicative of proximity to a reconnection point, but rather a small spatially localized phenomena at electron scales.

The momentum equation

Evidence of the importance of the divergence of the ion pressure in magnetopause equilibrium can be obtained through examination of the momentum equation, whose components are illustrated in the right panel of Figure 4.8 projected along the normal (top) and tangential (bottom) directions. An estimation of uncertainties is also provided for the terms in the tangential direction. The method used to calculate these uncertainties is elaborated below.

From this figure, it can be observed that the normal projection of this equation agrees with CTD, with the $\mathbf{J} \times \mathbf{B}$ term being counterbalanced by the divergence of the ion pressure tensor. Meanwhile, the tangential projection of this equation supports our hypothesis regarding the role of the divergence of the ion pressure in the equilibrium. Along this direction, indeed, it is observed that the $\mathbf{J} \times \mathbf{B}$ term is comparable in magnitude to the divergence of the ion pressure tensor, both being an order of magnitude larger than the other terms. Additionally, the $\mathbf{J} \times \mathbf{B}$ and $\nabla \cdot \mathbf{P}_i$ terms are opposite and balance each other. While in the initial three seconds of the interval, this conclusion is uncertain due to measurement uncertainty, in the time interval between 3.5 seconds and 6 seconds, it becomes evident that these two quantities counterbalance each other, while the classical inertia term $\rho d\mathbf{u}/dt$ is much smaller. However, as pointed out in Section 4.4, under isotropic conditions, we would expect the divergence of the ion pressure tensor to be zero in the tangential direction, or at least negligible compared to the classical inertial term $\rho d\mathbf{u}/dt$, while the latter term should be the one counterbalancing $\mathbf{J} \times \mathbf{B}$. Thus, these results serve as evidence that the tangential $\nabla \cdot \mathbf{P}_i$ term plays a crucial role in magnetopause equilibrium, further validating the significance of non-gyrotropy and FLRs within the magnetopause. Lastly, it is noteworthy that the $\nabla \cdot \mathbf{P}_e$ term is not entirely negligible in the tangential direction at approximately 3.5 seconds, as observed in Ohm's law. Nevertheless, the interpretation given above remains valid also in this case.

Error estimation for the momentum equation terms

The uncertainties depicted in Figure 4.8 represent an upper bound estimation of the errors associated with the quantities of interest. We opted for presenting the upper bound to enhance the validation of the results. This approach ensures that all sources of errors, even those not accurately modeled, are adequately included within the errorbars, leading to more robust conclusions. Therefore, to estimate the error related to the $\mathbf{J} \times \mathbf{B}$ term, we used an overestimation of the nominal error of the Fluxgate Magnetometer for magnetic field measurements. For the divergence of the ion pressure and the classical inertial terms, we relied on the estimation of

uncertainties from the Fast Plasma Instrument dataset. Specifically, the maximum error value in the entire crossing was taken for each measurement and spacecraft. From these uncertainties, the final estimation of errors on the terms of the momentum equation is derived by propagating the errors statistically (i.e., quadratically), assuming that the errors on the reciprocal vectors can be neglected compared to those of other physical quantities (due to the large precision on the spacecraft positions).

4.5.3 Evidence of non-gyrotropy at the Earth's magnetopause

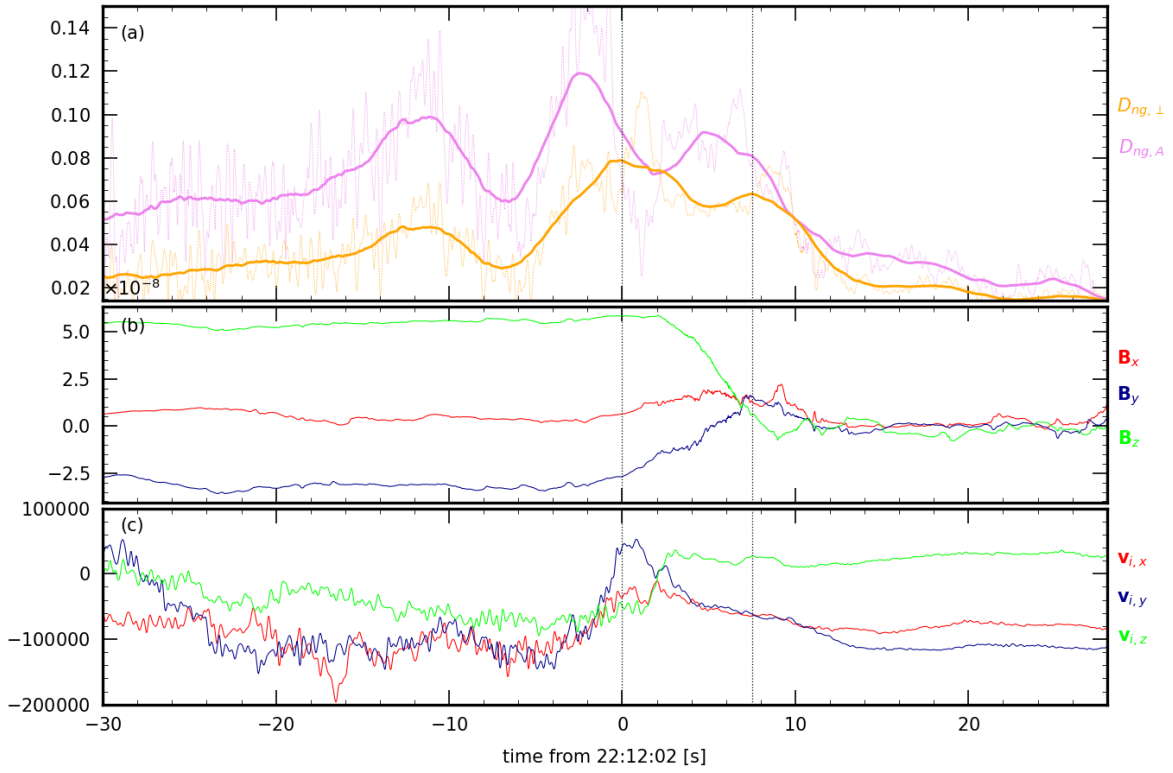

Figure 4.9: (*a*) Evolution of the non-gyrotropy indices, $D_{ng,\perp}$ in violet and $D_{ng,A}$ (Aunai et al., 2013b) in orange. Thin lines correspond to the real-time values while thick lines to an averaged window of 1 *s*; Panels *b* and *c* show the magnetic field and ion velocity for MMS1; analogous structures are observed for all four spacecraft. Dashed vertical lines indicate the crossing intervals studied in the previous sections.

We now want to quantify the non-gyrotropy by exploiting the indicators discussed in Section 4.4.2. Both the indices defined in Eq. 4.15 and 4.16 are shown in Fig. 4.9 for the case crossing of the 28.12.2015. We note here that both indices significantly deviate from zero, approximately of the order of 0.1 within the boundary. This suggests the presence of non-gyrotropic effects within the magnetopause, albeit not being predominant. However, despite a continuous decrease, these indices remain relatively high in the time interval just before the crossing, in a region where the magnetic field, density, and pressure tensor are nearly constant, as depicted in Figure 4.9 in panel *b* for the magnetic field. This observation can be attributed to the presence of an ion velocity gradient in this interval, implying that the non-diagonal terms of the pressure tensor may be influenced by a gyroviscous effect due to FLRs (Braginskii, 1965). However, in this interval, the ion pressure tensor exhibits low values. Therefore, relative errors are larger, which could partially influence this result.

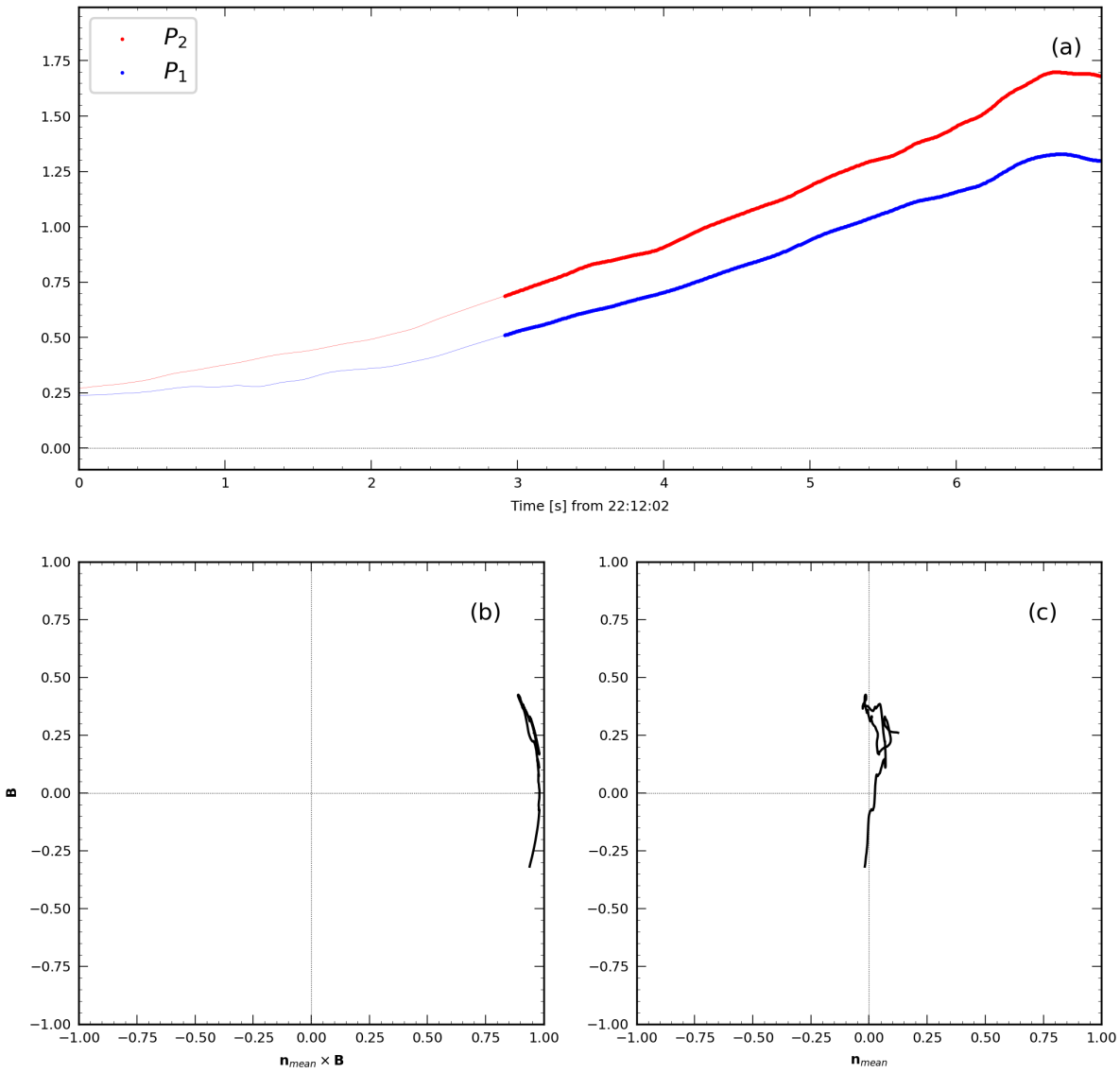

Figure 4.10: (a): Evolution of parameters P_1 and P_2. (b) and (c): projections of the gyrotropy direction in two planes. The ordinate is the direction of $\mathbf{B}$, the abscissa is the direction of $\mathbf{n}_{mean} \times \mathbf{B}$ for panel (b) and $\mathbf{n}_{mean}$ for panel (c).

While these results demonstrate the presence of non-gyrotropy, both indicators take into account a notion of non-gytropy defined around the magnetic field. However, for a more general conclusion, we may want to drop the hypothesis that the direction of the non-gyrotropy is around the magnetic field by analyzing the non-gyrotropy with respect to a generic direction, i.e., without imposing what this direction is. Specifically, we can now examine a direction denoted as $\mathbf{g}$ (corresponding to the gyrotropy direction), around which the rotated matrix could be reformulated as follows:

$$\begin{pmatrix} P_2 & & \\ & P_1 & \\ & & P_1 \end{pmatrix} \tag{4.17}$$

To achieve this, we use a minimization algorithm to derive the rotation matrix $\mathbf{M}$, allowing us to transform the pressure tensor data into a form as close as possible to the desired one. Figure 4.10 (shown here for MMS2) illustrates the direction of the non-gyrotropy obtained through this analysis. On the top panels, we observe the evolution of the two diagonal values of the rotated

matrix, P_1, and P_2, showing that the value parallel to the non-gyrotropy direction consistently exceeds the one in the gyrotropic plane. Additionally, we have imposed here an upper limit on the temporal variation of the gyrotropic direction $\mathbf{g}$, excluding points with significant temporal variations (indicated by the thin line). Consequently, the remaining points reflect instances where the direction of $\mathbf{g}$ can be considered as stable and reliable. The evolution of the non-gyrotropy direction is therefore compared to the main physical directions: the magnetic field and the magnetopause normal directions. For this purpose, this vector $\mathbf{g}$ is shown in panels *b* and *c*. Here it is evident that the direction of gyrotropy is not purely parallel to the magnetic field direction, as assumed in the definition of both the non-gyrotropy indices. Indeed, $\mathbf{g}$ is closer to $\mathbf{n}_{\text{mean}} \times \mathbf{B}$, while the component along the magnetic field is smaller and varies across the crossing. This result reminds us that at boundaries such as the magnetopause, strong gradients can break the isotropy as much, or even more, than the magnetic field so that that gyrotropy can occur around a vector other than the magnetic field. A similar observation had already been made in Belmont et al. (2012) concerning the modeling of a tangential discontinuity.

5 A statistical study of Earth's magnetopause crossings

Contents

In the previous chapters, the internal structure of the magnetopause has been studied using a case study of a crossing observed by MMS. This case was analyzed thanks to GF2, a novel tool for determining the normal direction of the magnetopause. The findings demonstrated the shortcomings of the Classical Theory of Discontinuities, in particular by demonstrating the role of Finite Larmor Radius effects in the magnetopause equilibrium.
To generalize these results and quantify the relevance of these effects at the magnetopause, we have extended the analysis to a database of magnetopause crossings performed by the MMS mission. For consistency, the selected magnetopause crossings must comply with the main features of the case crossing analyzed previously, specifically the one-dimensional geometry, burst measurements mode, and a crossing temporal interval long enough to have enough particle measurements within the magnetopause interval. In this chapter, we introduce the process of selecting this database, outlining the difficulties encountered, the selection criteria, and the objectives. Additionally, we discuss the results derived from this statistical study which can be found in detail in Ballerini et al. (2024b).

5.1 Magnetopause crossings: a global view

Selecting the magnetopause crossing database is very challenging because of the presence of strong fluctuations crossing the magnetopause structure and of the impact of the dynamical pressure driven by magnetosheath turbulence both contributing to the flapping of the magnetopause boundary. Consequently, when a spacecraft approaches the magnetopause, the measurements typically show a sequence of crossings, with the satellite passing through the magnetopause from the magnetosphere to the magnetosheath and vice-versa, due to the magnetopause's movement relative to the satellite. Typically, the spacecraft velocity is one order of magnitude lower than the magnetopause one. Figure 5.1 illustrates this phenomenon using data from the MMS1 spacecraft. Here we show the measurements of the magnetic field (top panel), density (center), and perpendicular and parallel ion temperature over one hour and ten minutes when the spacecraft approaches the magnetopause. At the beginning of this interval, the satellite is in the magnetosphere, showing a positive z component of the magnetic field and low densities. Throughout this interval, the satellite undergoes several magnetopause crossings, characterized by magnetic field reversals and changes in density and temperature values, finally entering stably into the magnetosheath near the end of the interval. We again underline that relatively large-amplitude magnetopause fluctuations complicate strongly the crossings selection procedure. Many of these

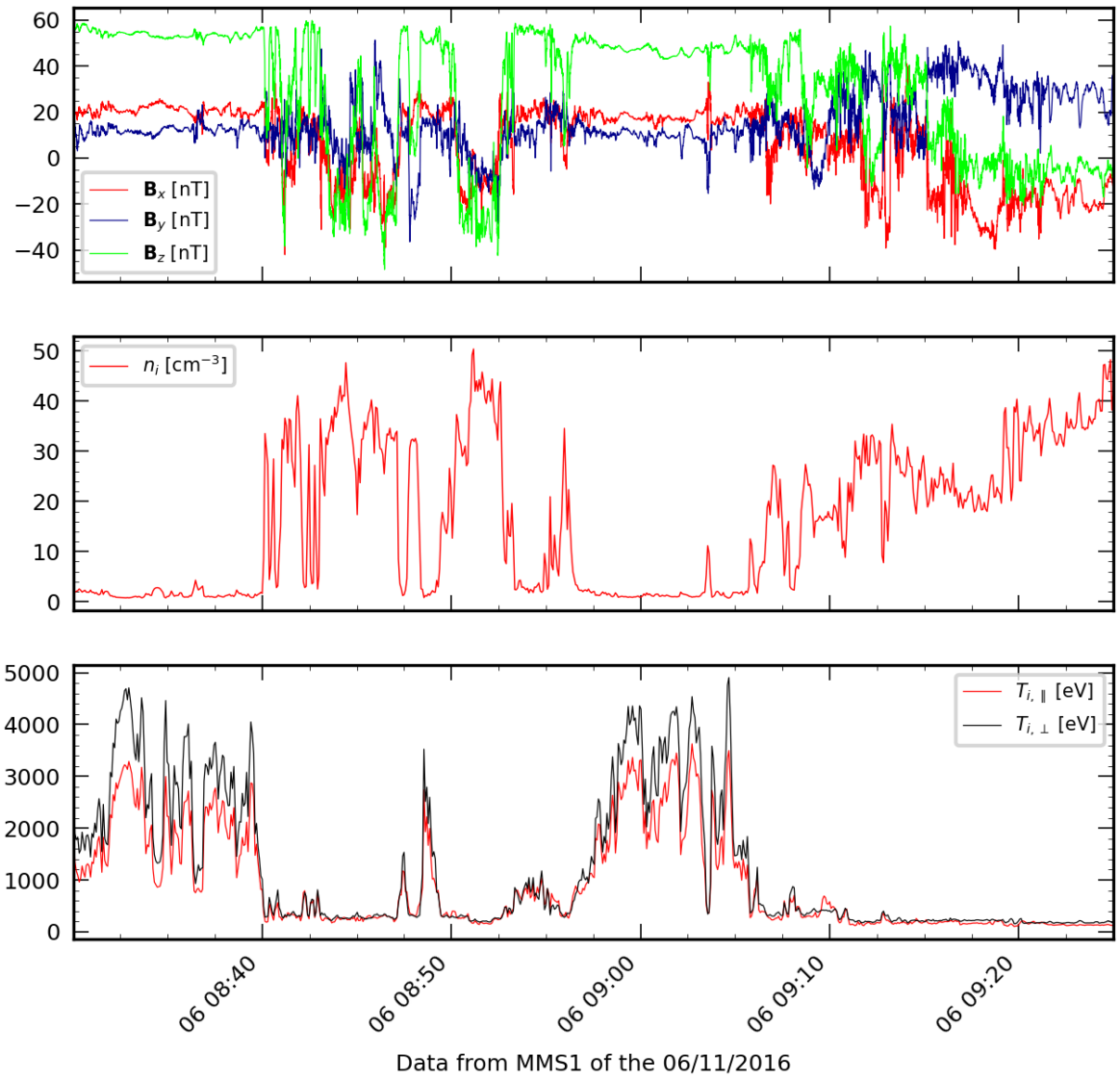

Figure 5.1: Measurements of the MMS1 spacecraft over a one-hour and ten-minute interval on the 6th November 2016. The panels display the magnetic field components (top), the ion density (center), and parallel, in red, and perpendicular, black, ion temperatures (bottom). All measurements here are in survey mode.

crossings are either partial or dominated by a two-dimensional-like geometry. Therefore only a fraction of the total magnetopause crossings can be used in our study.

In Figure 5.2, two examples of crossings that must be excluded from the database are shown. The left panel shows an incomplete crossing where the satellite briefly enters the magnetopause from the magnetosphere and comes out without completing the crossing. The right panel shows a complete crossing where the fluctuations of the measurements, superimposed on the magnetopause profile, are of the same order of magnitude as the magnetopause variation itself. Indeed, the typical magnetopause profile should exhibit a smooth, monotonic transition of parameters from the magnetosphere to the magnetosheath. In contrast, here we observe the density exhibiting multiple increases and decreases of its value before entering definitely in the magnetosheath. Similarly, all three components of the magnetic field display oscillatory behavior instead of a straightforward transition. These oscillations may result from strong waves propagating locally or from the relative motion between the spacecraft and the magnetopause, causing the back-and-

forth motion of the spacecraft within the magnetopause. Anyway, such crossings are excluded from our database because such fluctuations would significantly bias the study.

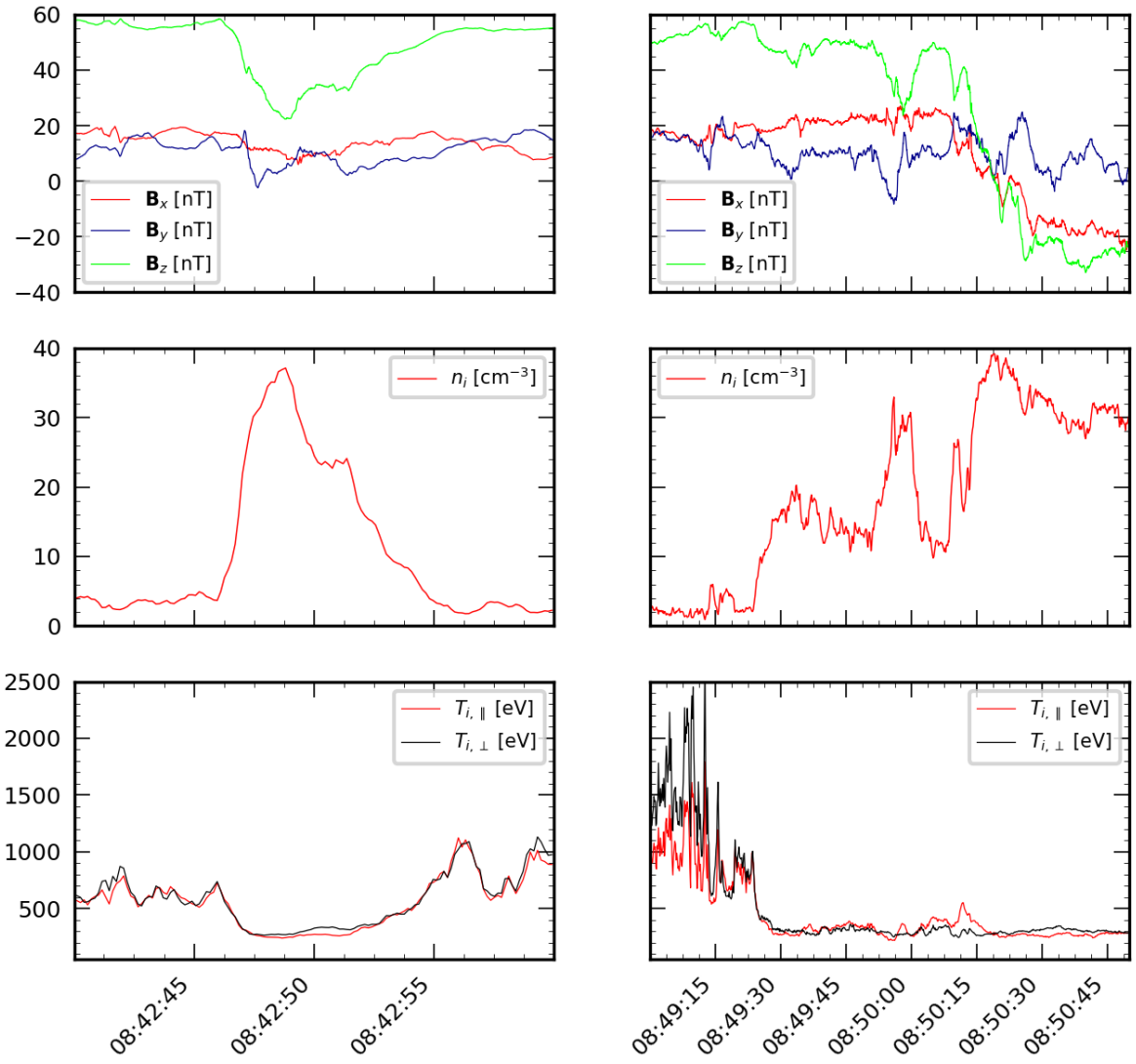

Figure 5.2: Example of magnetopause crossings showing incomplete (left) features or strong fluctuations superimposed over the magnetopause profile (right). Measurements from the MMS1 spacecraft on the 6th November 2016, here in burst mode. The panels display the magnetic field components (top), the ion density (center), and parallel, in red, and perpendicular, black, ion temperatures (bottom).

5.2 Dataset selection

We have created our database starting from the work that had already been done by previous researchers. Indeed, since the beginning of near-Earth exploration, databases of magnetopause crossings have been created to perform statistical analyses on this boundary (see for instance Berchem and Russell (1982b); Phan and Paschmann (1996); Panov et al. (2008); Hasegawa (2012); Haaland et al. (2014); Lukin et al. (2019); Nmeek et al. (2020)). Focusing on MMS data, two noteworthy examples are Paschmann et al. (2018) and Nguyen et al. (2022a). The latter was developed within the Laboratoire de Physique des Plasmas. An updated version of this database, described in Michotte de Welle (2024), was used as a starting point to select the

crossing of interest for the database of this study.

5.2.1 The Nguyen et al. (2022a) database

The Nguyen et al. (2022a) database is obtained by employing a gradient boosting classifier (GBC) algorithm, a machine learning technique based on boosting in a functional space (Friedman, 0 01), to classify data from several space missions (Double Star, MMS, Cluster, THEMIS, and ARTEMIS). Concerning MMS data, of interest for this study, data are resampled to a one-minute resolution. Subsequently, each measurement is associated with a corresponding class indicating the region where the measure was taken (i.e. magnetosphere, magnetosheath, or solar wind). This algorithm identifies magnetopause crossings using a 10-minute rolling window of data. Specifically, a magnetopause crossing is defined as the center point of a window containing five minutes of magnetosphere data and five minutes of magnetosheath data. Further details can be found in Michotte de Welle (2024).

5.2.2 The dataset of magnetopause crossings from Ballerini et al. (2024b)

By associating a 10-minute moving window to a magnetopause crossing, each event in Nguyen et al. (2022a) corresponds in practice to several, either partial or complete, magnetopause crossings, as discussed in Section 5.1 and shown in Figure 5.1. Nonetheless, such a database can be used as a starting point for the selection of a new dataset by rearranging the event list as a list of time intervals for a magnetopause crossings.

To set up the new dataset, each window identified by Nguyen et al. (2022a) was examined individually[1]. To match the time resolution exploited in the study in Chapters 3 and 4, only crossings with bursts data available for the four spacecraft are used. Furthermore, crossings lacking ion or electron measurements are excluded. Then, for each time window, the measurements are divided into individual magnetopause crossings, either complete or partial. Starting from this list of burst-data single-crossing measurements, the dataset is then selected by imposing the following conditions:

- The temporal length is between 3 and 15 seconds. Crossings shorter than 3 seconds lack sufficient data resolution (ion measurements are every 0.15 seconds) to analyze the structure properly. Those longer than 15 seconds, instead, may indicate non-stationary structures and generally present complex structures due to the relative velocity of the magnetopause and the spacecraft (see for example the right panel of Figure 5.2).

- Partial crossings were excluded using a threshold range on the ion density. Crossing in our dataset must have a density lower than 4 cm^{-3} in the magnetosphere and greater than 15 cm^{-3} in the magnetosheath. These threshold values are not strict when considering the average values of the magnetosphere and magnetosheath densities (see Section 3.2.2). However, they were allowed to properly select complete crossings.

- Finally, only crossings exhibiting simultaneous features in particle and magnetic field measurements were considered to ensure a consistent comparison of computed normals.

Additionally, we have excluded crossings showing two-dimensional like geometry. The dimensionality was quantitatively determined by using the dimensionality parameters presented in Chapter 3: the one introduced in Rezeau et al. (2018) (Eq. 3.8) and the one in Ballerini et al. (2024b) (Eq. 3.17). Specifically, we considered only crossings with an averaged value larger than 0.9 for D_1 and 0.8 for $\mathcal{D}_{GF2}$. While both these parameters are calculated at each time step

[1]The original windows have actually been reduced from ten to six minutes, so excluding the outer portions of the intervals. It does not result in a significant loss of information since the selected crossings are always in the central part of the intervals

within the magnetopause, we chose to use the averaged value (instead of a minimum, for instance) to include in the dataset the crossings in which two-dimensional structures are only local and, if present, are located within a small subpart of the magnetopause crossing. In conclusion, the crossings that respected the previous conditions were checked visually to ensure that none of the crossings presented peculiar features (such as, again, the right panel of Fig. 5.2).

The algorithm allowed us to select 146 crossings from September 2015 to December 2017. The following period was excluded since, starting from June 2018, a technical failure of four of the eight FPI electron spectrometers on MMS4 stopped the possibility of having a same-time electron measurement on four spacecraft. The detailed list of selected crossings and their key features are provided in Appendix A. The spatial distribution of these crossings is illustrated in Figure 5.3, showing an even distribution in the x, y plane, with a predominance of cases in the negative z direction.

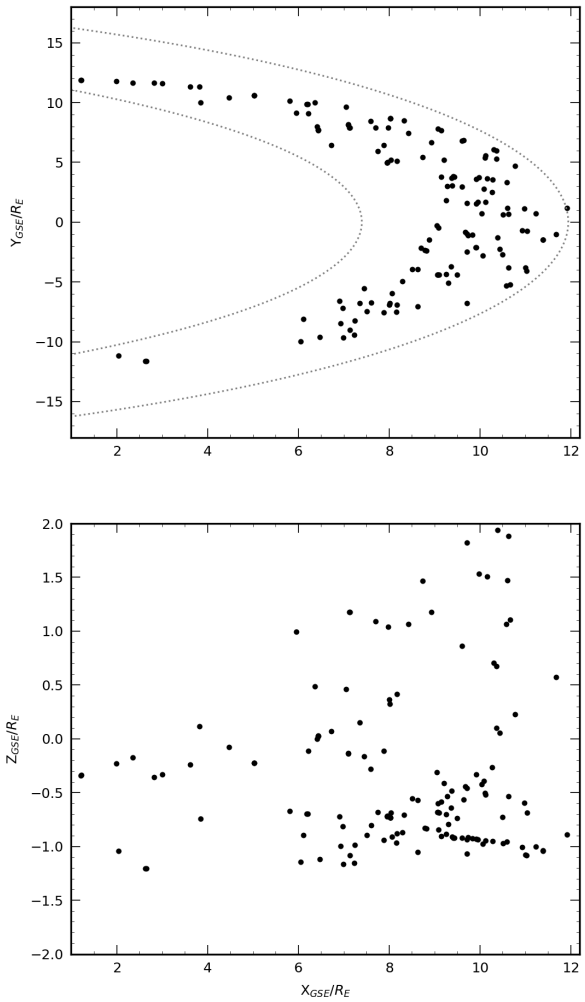

Figure 5.3: Spatial distribution of the selected database of crossings on the x, y (top) and x, z planes (bottom). The dashed grey lines represent the magnetopause location obtained using the Shue et al. (1997) model.

5.3 A statistical study on the magnetic field hodograms

From a statistical study perspective, the direct examination of the momentum equation terms (and specifically the tangential component of the gradient of the ion pressure tensor), as conducted in Section 4 for the case crossing of 28 Dec. 2015, is constrained by uncertainties in

pressure measurements. Due to this uncertainty, the ability to derive a clear statistical result necessitates an alternative approach. To evaluate the influence of Finite Larmor Radius effects (FLRs) at the Earth's magnetopause, we study the shape of the hodogram of the magnetic field in the tangential plane for the crossings. Specifically, we aim to estimate the number of crossings that deviate from the Classic Theory of Discontinuities (CTD) to quantify whether the results obtained in the previous chapters are unique to the case crossing or representative of typical magnetopause behavior. To this end, the hodogram of the magnetic field in the tangential plane is obtained for each of the crossings in the dataset by using the same procedure explained in Section 3. Then, each hodogram is classified depending on its shape into one of the following four categories:

- **Linear** hodograms: This category includes the hodograms that appear as lines not passing through the origin, similar to the 28/12/2015 case study (Fig. 4.6);
- **Radial** hodograms: These hodograms are linearly shaped and their best-fit lines pass through the origin (considering uncertainty). These crossings are indicative of CTD compressional discontinuities (Fig. 4.5, right panel).
- **Circular** hodograms: These hodograms have a constant distance from the origin and correspond to CTD rotational discontinuities (Fig. 4.5, left panel).
- **Other** hodograms: This class includes all the rest of the crossings, whose features are not included in the previous classes. Examples of features of hodograms in this class are circular hodograms not centered at the origin, crossings characterized by two different hodograms in two sub-intervals, and crossings that do not have an obvious distinction between the previous classes, due to noise.

5.3.1 Methodology used to classify hodogram shapes

To accurately classify each hodogram, we choose to study only the central time interval of each crossing, corresponding to the interval where the gradients are maximum. By extending this analysis to larger intervals we would include variations that are generally unrelated to the main boundary transitions, introducing complexity to the analysis. The temporal interval used for each crossing is obtained by using the algorithm used in Paschmann et al. (2018) and Haaland et al. (2004, 2014) to estimate the spatial scale of the magnetopause. Specifically, we define the magnetopause crossing-time interval ΔT as the part of the crossing in which we observe 75% of the variation of the $\mathbf{B}_L$[2] component. This procedure is sketched in Figure 5.4, where the red part of the curve corresponds to the chosen interval. After selecting the time interval for the crossing, the classification of hodograms involves a two-step process:

1. **Visual Inspection**: The first step consists of examining visually each hodogram to exclude those that are clearly neither linear nor circular, which are then categorized as 'Others.' For the remaining crossings, this step also involves a preliminary differentiation between those exhibiting circular and linear characteristics.
2. **Detailed Analysis**:
   (a) **Hodograms with Potential Circular Features**: To identify whether these crossings show circular features, we analyze the variation in the modulus of the magnetic field in the tangential plane. Specifically, to classify a hodogram as circular we impose a maximum variation of 20%, by taking into account the potential influence of turbulence and wave propagation along the magnetopause. Crossings that exceed this 20% variation are classified as 'Other'.

[2]Here $\mathbf{B}_L$ is the component of the magnetic field along the $\mathbf{L}$ direction in the LMN coordinate system, defined in Section 3.3.3, corresponding to the direction of maximum variance.

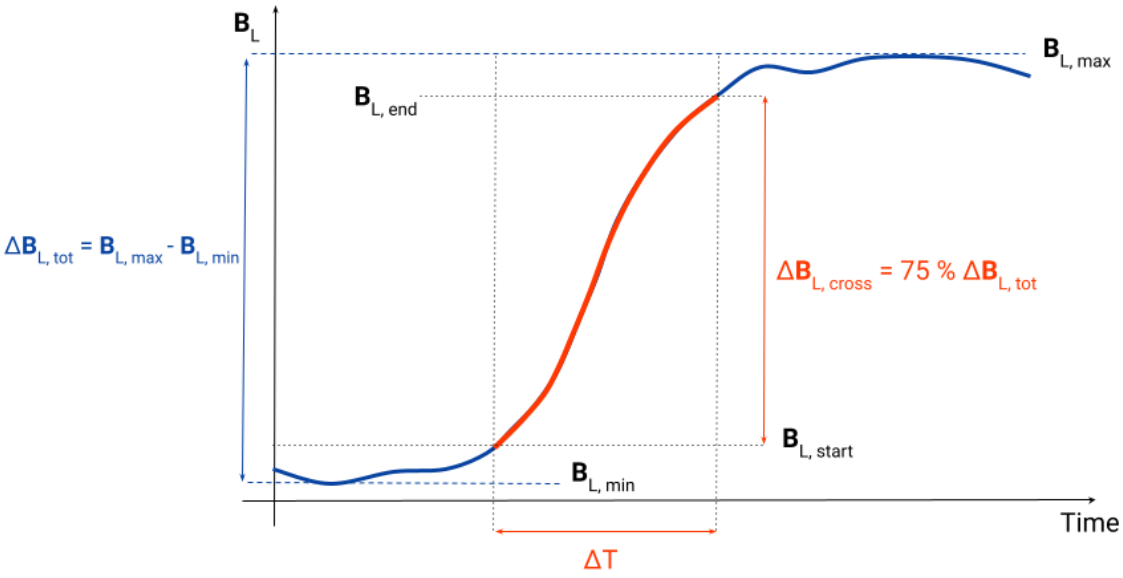

Figure 5.4: Sketch of the method used for selecting the magnetopause time interval ΔT, by exploiting the variation of the $\mathbf{B}_L$ component. The central time interval of the crossing (red part) is here chosen as the interval corresponding to 75% of the total variation of the value of $\mathbf{B}_L$ ($\Delta\mathbf{B}_L$=$\mathbf{B}_{L,max}$-$\mathbf{B}_{L,min}$).

(b) **Hodograms with Potential Linear or Radial Features**: For these crossings, firstly we evaluate their linearity by examining the width-to-length ratio. Any crossing with a ratio exceeding 20% is classified as 'Other'. Then, the hodograms showing linear features are classified as either radial or linear depending on whether their projection passes through the origin or not.

5.3.2 Results of the analysis

The results of this study are shown in Table 5.1. We observe that more than a third of the crossings in this database show linear features, while only less than 20 % of the crossings can be classified as expected in CTD (either circular or radial). This result emphasizes that FLR effects have a rather significant role in the magnetopause structure. It is noteworthy to underline that even if we only consider the central time interval for each boundary, this does not invalidate the result. Indeed, in gyrotropic conditions, rotational and compressional variations should remain mutually exclusive whatever the interval, as discussed in Section 4.4. Since we observe that this is not the case in 30% of the cases in this database, we can interpret these features as due to non-gyrotropy coming from kinetic effects. This confirms the limitation of CTD to describe the magnetopause. These effects can change the relations between upstream and downstream states since, as shown in Section 4.4.1, these jump relations do depend on the physical processes within the structure as soon as the medium is not assumed isotropic.

Class	Number of crossings	Percentage
Linear	53	36.3%
Circular	4	2.7%
Radial	23	15.8%
Other	66	45.2%

Table 5.1: Number of crossings and their corresponding percentages of incidence in the database for each class.

To conclude this analysis, the dataset can be used to examine the variations in non-gyrotropy among the four distinct classes exploiting the non-gyrotropy indices defined in Equations 4.16 and 4.15. The average value of the non-gyrotropy index $D_{ng,\perp}$ for the whole dataset is computed to be 0.07. This value is however only slightly higher (0.08) for linear hodograms. Similarly, the $D_{ng,A}$ index shows comparable averages for the four classes. Therefore, although non-gyrotropy has been demonstrated to play an important role in the previous analysis, the non-gyrotropy index alone is not enough to predict the shape of the hodograms unequivocally. The same result is found when studying the ratio between the width of the magnetopause and the ion Larmor radius, which is on average approximately 6.5 and only slightly smaller (6.1) for linear hodograms.

5.4 A comparison between the magnetic and the particles normals

We can also exploit this database to compare the magnetic field and ion flux structures at the magnetopause. For this purpose, we can look at the normals derived using the GF2 tool from both quantities and analyze their differences. A single average normal was used for each crossing, using the data from only the central part of the crossing found as described in the previous section. The same analysis has also been done with the original MDD method.

5.4.1 Determining the Shue et al. (1997) normal

To examine the differences between the two sets of normals, we analyze their deviations from the normal obtained via the Shue et al. (1997) model described in Section 3, indicating a magnetopause at equilibrium. This model estimates the position (and therefore the normal) of the magnetopause as a function of the IMF-z component and solar wind dynamic pressure. Therefore, to determine this normal it necessitates precise parameter measurements that can be estimated by using the OMNI database[3] (King and Papitashvili, 2005).
Over time, various algorithms have been developed to accurately pair OMNI measurements of solar wind parameters with a magnetopause crossing. The simplest method consists of using OMNI data at the same time as the magnetopause crossing, neglecting the propagation time from the bow shock nose to the measurement location. For this study, we employed the algorithm from Michotte De Welle et al. (2022), adapted from Safrankova et al. (2002), to estimate the time delay between the crossing and measurement times of solar wind parameters, involving the following steps:

1. Estimate the projection along the Earth-Sun axis distance from the bow shock nose, where OMNI data are defined, to the crossing location.
2. Estimate the solar wind's propagation time (t_{est}) between these points, assuming an average solar wind velocity of 400 km/s.
3. Determine the solar wind velocity (V_{sw}), averaging over a 2-minute OMNI-data interval centered on the crossing time adjusted by the time delay (t_{est}).
4. Calculate the final time delay based on V_{sw}.

This time delay is then used to obtain final values for the solar wind and IMF parameters. Crossings without OMNI data (10 out of 146) were excluded from the analysis.

[3]The OMNI database consists of multi-spacecraft measurements of plasma and IMF properties in the solar wind. These measurements, available at resolutions from one hour to one minute, include key parameters such as IMF components, dynamic pressure, and energetic proton fluxes. Data collection is carried out by a coordinated network of spacecraft including the Wind, the Advanced Composition Explorer (ACE), and the Deep Space Climate Observatory (DSCOVR) spacecraft, positioned near the L1 Lagrange point (approximately 230 Earth radii upstream from Earth along the Earth-Sun axis). The collected data are then propagated to the bow shock nose position using the analytical model by Farris and Russell (1994), ensuring an accurate representation of the solar wind conditions at the magnetosphere's boundary

5.4.2 Results

The angle between the Shue model normal and the magnetic and particle normals, respectively, are shown in Figure 5.5. We observe that most crossings align approximately along the diagonal, the two oblique lines indicating a maximum difference of 20 degrees between the two angles. These results underline how, for the majority of crossings (here 56.2 % of the crossings between the two lines, similar normals are found on average for ions and magnetic fields. A cluster of events is observed at low angles (less than 30 degrees), corresponding to magnetopause crossings close to the nominal Shue et al. (1997) model. However, a non-negligible part of the database exhibits angles above 40 degrees, even if close to one another. The latter cases can be interpreted as magnetopause crossings significantly deviating from the paraboloid shape assumed by the model. These deviations are likely to be related to surface waves on the boundary. From Figure 5.5 we also observe that deviations for the ion flux normal are on average higher than the ones from the magnetic normal, with more cases observed in the top left quadrant than in the bottom right. Nevertheless, crossings that do not align along the diagonal indicate instances where the ion flux normal and the magnetic normal differ significantly, with observed discrepancies reaching up to 90 degrees. This discrepancy is likely to be due to non-stationarity and two-dimensionality in the ion flux measurements. Indeed the criteria used for the dataset selection (except for the threshold imposed on the density values) were built from magnetic data, they are not as relevant when considering ion normals. A more detailed study can be found in Ballerini et al. (2024b) (see Chapter 9).

Figure 5.5b shows the distribution (histogram) of angles between the two magnetic field and ion flux normals. Most cases (82 out of 146) exhibit angles below 20 degrees, with the peak of the distribution at 10 degrees. This reinforces the previous result where the two normals were compared to the reference Shue model.

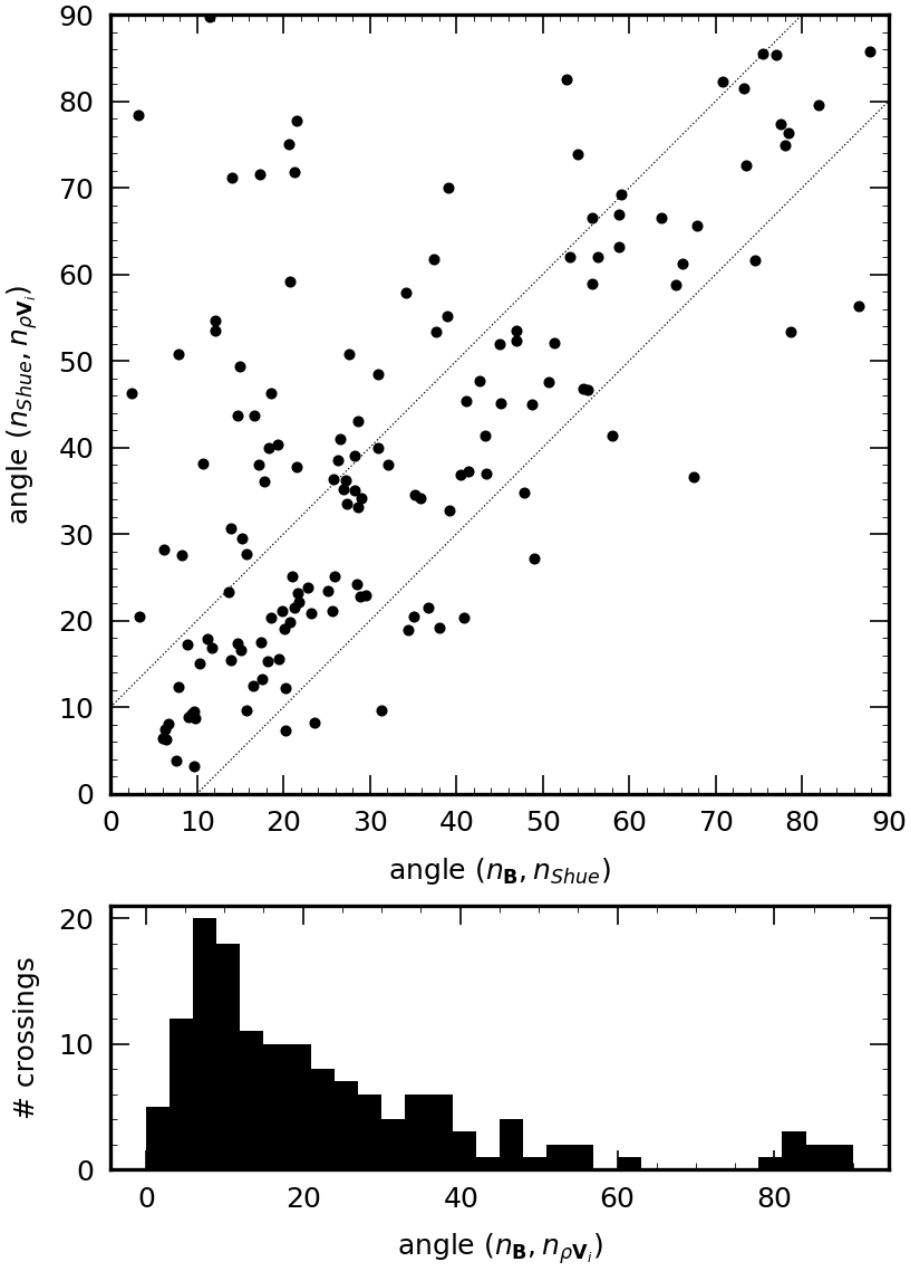

Figure 5.5: (a) Comparison between the angle between the Shue et al. (1997) normal and the magnetic and ion ones, (b) Histogram of the distribution of the angle between the magnetic and ion normals.

6 Simulating planetary magnetospheres

Contents

In the previous chapters, we outlined the tools utilized in the examination of Earth's magnetopause from an *in situ* data perspective, discussing what we learned from applying these methods. However, *in situ* data suffer from the inherent limitation of only capturing spatially and temporally localized phenomena. Even with the deployment of multi-spacecraft missions like the MMS mission, spacecraft data solely offer measurements of the plasma in their proximity, hiding the influence of the global magnetospheric dynamics. A statistical analysis has been conducted to exploit data for a more comprehensive reconstruction of the magnetospheric structure under varying solar wind conditions. However, this approach does not permit us to get a global understanding of the interaction between the solar wind and the magnetosphere and to properly establish the relationships between the local characteristics and the complex global dynamics. To get a complete picture from *in-situ* data, a huge number of satellites, tracking physical quantities across all scales and locations, would be necessary. Obviously, this is an unfeasible task. Hence, in addition to data analysis, numerical plasma models are employed to overcome these limitations. On one hand, simulations can be used to interpret and predict data observations; conversely, data can be used to validate and indicate the limitations of the adopted numerical model. Numerical simulations also enable the analysis of how each single parameter influences the structure and isolate elementary phenomena that are always mixed in spacecraft data. Therefore, coupling numerical models with *in situ* observations allows us to have a powerful tool for comprehending the intricate dynamics of space plasma environments. In this chapter, we introduce this approach, with a particular focus on presenting the most common numerical models studying a planetary magnetosphere, with a focus on the complexity of simulating the magnetopause. Alongside the numerical models, the selection of both the simulation parameters and the boundary conditions is crucial to achieve an accurate simulation that allows to realistically reproduce the physics of interest. Therefore, we also provide a brief overview of the typical setups used to simulate the magnetopause.

6.1 Numerical models for simulating a plasma

Due to the wide variety of plasma types, simulating their dynamics heavily depends on their specific characteristics. In this section, we will discuss the numerical models most suited for the study of the interaction between the solar wind and planetary magnetospheres. As outlined in Chapter 1, these plasmas are typically collisionless and magnetized. Furthermore, they are non-relativistic, with negligible gravitational effects. Selecting an appropriate model for simulating these plasmas is crucial for accurately understanding their dynamics and requires balancing computational resources with the specific objectives of the research. A trade-off between accuracy and complexity guides the choice of model.

For large-scale systems and global structures, the Magneto-Hydrodynamics (MHD) model, discussed in Chapter 1 is particularly suitable. This model is computationally not very demanding since it excludes *a priori* the ion and electron kinetic dynamics. This makes the MHD generally well-suited for analyzing scenarios where the primary interest lies in macroscopic, large-scale phenomena. However, the limitations of MHD become apparent when the dynamics at play reach, first, the ion kinetic scales and frequencies and when the dynamics of the velocity space are important, due for instance to resonant particles. Discontinuities as the magnetopause are therefore out of the scope of MHD because of their short spatial scale, and because a basic assumption of this model, the isotropy, is not fulfilled. In these cases, more detailed models, beyond the MHD framework, *i.e.* including 'non-ideal' effects, are necessary.
A balanced approach between the computational complexity and the phenomena here of interest can be obtained from those models positioned between the simplicity of MHD and the detailed nature of full-Vlasov descriptions. The most utilized models of this group are the so-called hybrid models. They include ion kinetic effects and keep the computational effort reasonable by modeling electrons as a fluid to eliminate their fast and small-scale dynamics. Typically, electrons are modeled as an isotropic fluid and are often treated as massless. While the hybrid scheme includes the full ion pressure tensor, it necessitates a fluid closure for electron pressure, commonly using isothermal or adiabatic closures. Models such as the Chew-Goldberger-Low (CGL, Chew et al. (1956)) allow one to incorporate an electron pressure anisotropy, via a double adiabatic closure, possibly enhancing the model's accuracy. In summary, the simplest massless isothermal electron closure, due to its computational simplicity, is likely to be the best choice for studying the Earth's magnetopause: as seen in the previous chapters, mainly the ion kinetic effects seem to have a relevant role in the boundary equilibrium. It must be kept in mind, however, that in some circumstances (such as the magnetic reconnection), a more accurate electron response model is needed as it influences the modeling of the full process.
To study electron dynamics and to properly describe phenomena where electron behavior plays a crucial role, full-kinetic models are mandatory. These models resolve electron kinetic scales, which are significantly smaller than the global system scales, thus requiring substantially higher computational resources. The complexity of the integrated equations in these models further contributes to the computational demand.

At present, two primary approaches fulfill the need for a comprehensive kinetic description of plasma: the semi-Lagrangian Particle-In-Cell (PIC) method and the Eulerian Vlasov approach. The PIC method, detailed further in the subsequent section, is widely used due to its balance between a kinetic representation and computational feasibility and cost. On the other hand, the Vlasov approach, despite offering an exhaustive kinetic description because of the almost zero noise even at the smallest scales (Valentini et al., 2007), is much less employed for magnetosphere simulations due to its high computational demands. PIC and Vlasov codes solve the multi-advection-partial differential Vlasov equation for one or all species, handling a six-dimensional distribution function that depends on both real and velocity spaces. The Vlasov equation(s) is(are) self-consistently coupled to the Maxwell equations.

Here we limit our discussion to (static-grid) PIC codes, most suited for global modeling of the interaction between the solar wind and the magnetosphere because of computational cost.

Codes including the adaptive mesh refinement (AMR)

A further distinction to be taken into account when selecting a numerical solver is in the numerical grids employed in their algorithm. While most of the existent numerical solvers exploit a fixed static grid, we would like to point out the existence of solvers incorporating adaptive mesh refinement (AMR). AMR allows the dynamic adjustment of the mesh resolution by increasing the grid cells in regions with complex features requiring higher accuracy. This capability is

particularly crucial when investigating the magnetopause, given its relatively small dimensions compared to the magnetosphere, allowing it to increase the resolution of the structure while keeping the computational time reasonable.
While AMR is commonly adopted in numerous fluid codes (Fryxell et al., 2000; Mignone et al., 2012), its implementation within the hybrid PIC framework can only be found in a few examples (Van Der Holst and Keppens, 2007; Mller et al., 2011). A notable example is the PHARE code Aunai et al. (2024), which is currently being developed at the Laboratoire de Physique des Plasmas. However, the three-dimensional version of PHARE is still under development and, therefore, it was not possible to exploit this solver during this thesis. Nonetheless, future application of such solvers promises new insights and advances in the study of the magnetopause.

6.1.1 The Particle-In-Cell (PIC) algorithm

When performing numerical simulations of plasma describing kinetic scales, the most commonly adopted approach is the Particle-In-Cell (PIC) algorithm (Hockney and Eastwood, 2021; Birdsall and Langdon, 1991). In the PIC scheme, the distribution function $f_\alpha(\mathbf{r}, \mathbf{v})$ of the species α, evolving following the Vlasov equation (Eq. 1.10), is split into a number N of distribution function slides called "macro-particles". These macro-particles serve as a way to sample the distribution function and are characterized by a statistical weight w and a shape in the phase space $S_p^{ph}(\mathbf{r}, \mathbf{v})$, so that the distribution function can be written as:

$$f_\alpha(\mathbf{r}, \mathbf{v}) = \sum_{p=1}^{N} w_p S_p^{ph}(\mathbf{r}, \mathbf{v}) \tag{6.1}$$

Typically, a Dirac delta is chosen as the shape in velocity space, while the choice for real space distribution depends on the specific application. We will assume here that $S_p^{ph}(\mathbf{r}, \mathbf{v}) = S(\mathbf{r} - \mathbf{r}_p)\delta(\mathbf{v} - \mathbf{v}_p)$, where $\mathbf{r}_p$ and $\mathbf{v}_p$ are the corresponding position and velocity for each macro-particle and are functions of time. This choice is specific to this work.
Furthermore, magnetic and electric fields are discretized on a spatial grid (typically a three-dimensional Cartesian grid) and are governed by the Faraday and Ampere equations. Therefore, the PIC method combines both the Lagrangian and Eulerian approaches, namely a semi-Lagrangian approach[1]. To merge these two approaches, interpolation is necessary. This is performed both for the electromagnetic fields, from the grid space to the macro-particle positions, and to compute the charge and current densities from the macro-particle positions to the grid. The iterative scheme of the PIC method is shown in Figure 6.1. After the initialization of the particles and fields, a four-step process is performed at each time step:

- **Field interpolation:** The values of the electric and magnetic fields are interpolated onto the position of the macro-particles as follows:

$$\mathbf{E}_p = \int \mathbf{E}(\mathbf{r}) S(\mathbf{r} - \mathbf{r}_p)\, d\mathbf{r} \tag{6.2}$$

$$\mathbf{B}_p = \int \mathbf{B}(\mathbf{r}) S(\mathbf{r} - \mathbf{r}_p)\, d\mathbf{r} \tag{6.3}$$

- **Particle push:** The interpolated electromagnetic fields are used to advance the macro-particle positions and velocities, allowing the distribution function to evolve in the phase

[1]The Lagrangian approach is defined as the description of tracking individual particles, following their trajectories and dynamics. In contrast, the Eulerian approach consists in focusing on specific spatial grid points, examining the changes of the plasma properties, such as density and velocity, at these fixed locations as the particles pass through, offering a field-based perspective of the plasma.

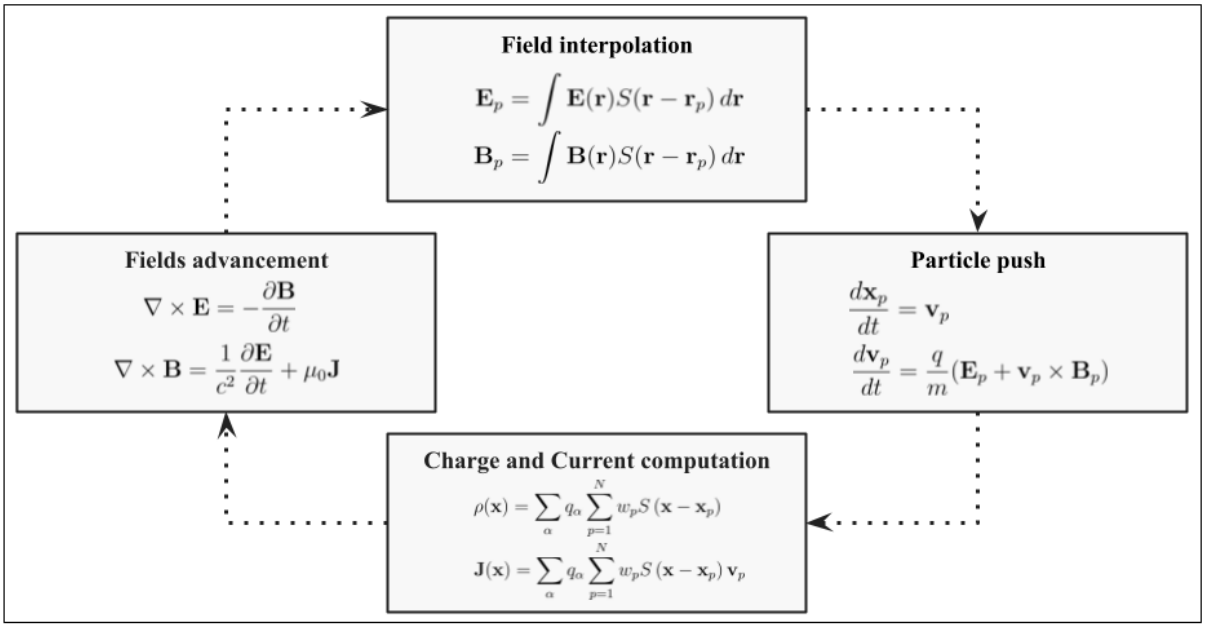

Figure 6.1: The PIC loop scheme.

space. Integrating the Vlasov equation (Eq. 1.10) and Eq. 6.1, one can demonstrate that the macro-particles follow Newton law:

$$\frac{d\mathbf{x}_p}{dt} = \mathbf{v}_p \tag{6.4}$$

$$\frac{d\mathbf{v}_p}{dt} = \frac{q}{m}(\mathbf{E}_p + \mathbf{v}_p \times \mathbf{B}_p) \tag{6.5}$$

- **Charge and Current computation:** Macro-particles's velocities and positions, interpolated on the electro-magnetic fields grid points are used to compute the charge and current densities:

$$\rho(\mathbf{x}) = \sum_\alpha \rho_\alpha = \sum_\alpha q_\alpha \int f_\alpha d\mathbf{v} = \sum_\alpha q_\alpha \sum_{p=1}^{N} w_p S(\mathbf{x} - \mathbf{x}_p) \tag{6.6}$$

$$\mathbf{J}(\mathbf{x}) = \sum_\alpha \mathbf{J}_\alpha = \sum_\alpha q_\alpha \int f_\alpha \mathbf{v} d\mathbf{v} = \sum_\alpha q_\alpha \sum_{p=1}^{N} w_p S(\mathbf{x} - \mathbf{x}_p)\, \mathbf{v}_p \tag{6.7}$$

- **Fields advancement:** The charge and current densities are then used to solve Faraday (Eq. 1.13) and Ampère (Eq. 1.14) laws on the grid, updating the electromagnetic fields.

These steps are iteratively repeated to simulate the plasma dynamics over time. Concerning time advancement, in general (*i.e.* not only PIC codes) the algorithms can be divided into two main categories: *explicit* or *implicit*. This distinction refers to how the solution at a new time step $t + \Delta t$ is computed. In explicit algorithms, the solution at time $t + \Delta t$ is obtained using only the fields at the time t. Implicit algorithms instead, calculate the new solution using the fields both at time t and $t + \Delta t$ (the new time). Each approach has its advantages and disadvantages, making the two approaches suitable for different applications. Explicit algorithms are relatively straightforward to implement, but they present more stringent computational constraints, requiring solving the fastest time scale of the system. Specifically, these algorithms must handle the electron plasma time (i.e. the inverse of the electron plasma frequency) and the Debye length. Implicit algorithms, while more complex to implement, offer more relaxed numerical constraints. This allows one to use larger time steps and spatial grid resolution, reducing the computational cost, but cutting out, and so loosing, the fast dynamics.

6.1.2 Limitations and Advantages of PIC models

PIC algorithms are a fundamental instrument for investigating plasma kinetic dynamics with better computational efficiency with respect to the Eulerian Vlasov approach. Nevertheless, despite the impressive progress of supercomputers using high-performance computing (HPC) architectures, even the PIC approach remains computationally very huge when modeling a realistic plasma system as the solar wind-magnetosphere environment where the dynamics is characterized by a very large separation between the largest and smallest involved spatial scale and frequency. For instance, in simulations of the Earth's magnetosphere, the ion inertial length d_i is approximately 40 times the electron inertial length d_e, and ion cyclotron frequency ω_{ci} is 1836 times the electron cyclotron frequency ω_{ce} while the magnetospheric length scale L is approximately 640 d_i. Therefore, the multi-scale characteristic of this system requires high computational costs even for PIC simulations.
To reasonably reduce the computational cost the hybrid approach using fluid electrons is very often adopted as well as parameter re-scaling. In particular, one can assume a reduced ion-to-electron mass ratio (mi/me) and a reduced cyclotron frequency ratio with respect to the fastest dynamics at play (ω_{ci}/ω). In simulations of space plasmas, the mass ratio is typically reduced to the range 25-400 while the frequency ratio is reduced to 10-500 (Deca et al., 2017; Pucci et al., 2018; Groelj et al., 2018; Lapenta et al., 2020; Arró et al., 2022; Lavorenti et al., 2022; Sun et al., 2023). Complementary, also the size of the system can be rescaled. This feature will be further analyzed in the next sections. The impact of such rescaled parameters has been widely investigated to understand the effects on plasma dynamics, demonstrating that rescaled parameters primarily influence the microphysics of the system while leaving large-scale quantities sufficiently unaffected (Shay and Drake, 1998; Bret and Dieckmann, 2010; Le et al., 2013; Verscharen et al., 2020; Lavorenti et al., 2022).

Another important limitation of PIC algorithms arises from the finite sampling of the distribution function, due to the limited number of macro-particles per cell. This feature introduces statistical noise into the computed fluid moments, which are obtained as per-cell averages. Therefore, this noise propagates to the electromagnetic fields (and consequently the Lorentz force). It can be demonstrated that this noise scales as $1/\sqrt{N_\alpha}$ (Birdsall and Langdon, 1991), where N_α denotes the number of macro-particles per cell. Therefore, this effect can be relatively mitigated by employing a sufficiently large N_α, where the appropriate number depends on both the specific code and application. However, this random noise can never be eliminated.

6.2 Simulating the magnetopause: global and local simulations

We focus now on the different approaches used to numerically model the magnetopause. There are two main categories: *local* and *global* simulations. Global models include the entire 3D magnetosphere in the computational domain, whereas local models focus on smaller specific subregions (1D, 2D, or 3D depending on the expected degree of realism), such as parts of the comet tail or the magnetopause. A detailed description of these models and their application in the magnetopause study follows.
We would like to point out here that, for the purpose of the analysis conducted in this thesis, we need to employ a three-dimensional simulation of the magnetopause. As anticipated in Rezeau et al. (2018), indeed, a two-dimensional model is not sufficient for obtaining enough information about the structure.

6.2.1 Local simulations of the magnetopause

Local magnetopause simulations consist of modeling a current sheet. These simulations are used in general to investigate the kinetic features of reconnection or plasma instabilities occurring at the magnetopause (such as Kelvin-Helmholtz). In particular, the magnetopause current sheet is

often modeled as a tangential sheet in these simulations, which can allow starting with approximate steady-state kinetic equilibria. These initial states are then generally perturbed to initiate instabilities (such as magnetic reconnection). However, these simulations require that the kinetic initialization is a steady-state equilibrium (or close to it, Belmont et al. (2012); Dorville et al. (2015a)). Indeed, for an initialization far from kinetic equilibrium, we don't know if the simulation relaxes to an equilibrium configuration before developing the instability of interest.

Over the years, numerous local models have been employed to study magnetopause, the Harris sheet (Harris, 1962) being one of the simplest. In this model, the solution is an analytical equilibrium of the Vlasov equation describing a plasma layer confined between two regions of oppositely directed magnetic field magnetic field. Specifically, the magnetic field is assumed to be coplanar:

$$\mathbf{B}(x) = B_0 \tanh\left(\frac{x}{L}\right)\hat{z} \tag{6.8}$$

where we have assumed the normal direction along x and we defined L as the characteristic scale of the sheet. This analytical equilibrium is built by expressing the distribution function as a function of the invariant of motion. Both ions and electrons are described by Maxwellian distributions with constant drift velocities, with a plasma density transitioning along the magnetic field across the discontinuity. The plasma density is analytically:

$$n(x) = \frac{n_0}{\cosh^2\left(\frac{x}{L}\right)} \tag{6.9}$$

Therefore, in this model, the magnetic field reverses without rotation and the density tends toward zero on both sides. To achieve more realistic simulations, this equilibrium is often modified to simulate the magnetopause, for instance by including a perpendicular magnetic field component or by adapting it to the double-Harris configuration. However, none of these configurations are at kinetic equilibrium.
However, all these simple traditional models assume symmetries between upstream and downstream media and are limited in their ability to capture the significant differences in densities and temperatures between the magnetosphere and the magnetosheath and therefore to well represent the magnetopause realistically. To address this, several (more complex) models have been developed. Notably, the BAS model (Belmont et al., 2012) assumes a coplanar asymmetric magnetic field and Maxwellian distributions with varying densities and temperatures. In particular, the distribution function is filled in phase space at each grid point in the direction of the discontinuity. This semi-analytical initialization is detailed in (Belmont et al., 2012) and can be also extended to non-coplanar conditions as demonstrated in (Dorville et al., 2015a). This extension also allows one for the inclusion of an electric field.
The advantage of a local approach in simulating the magnetopause comes from its ability to simulate the magnetopause while allowing a finely resolved spatial domain. However, local simulations fail to capture the inherent complexity of the magnetopause, not allowing one to consider the non-stationary nature of the magnetosheath plasma, which continuously influences the magnetopause. Therefore, to study the magnetopause structure without relying on semi-analytical assumptions, this project focuses on global simulations presented in the following.

6.2.2 Global simulations for studying the magnetopasue

Global simulations include the entire planetary magnetosphere within the computational domain, simulating the planet as a sphere embedded in a magnetic dipole. These simulations can also be generalized to celestial objects such as comets interacting with the solar wind. As discussed further later in 6.3.2, two approaches can be used to integrate the equations in global simulations: simulating the magnetosphere in the planetary reference frame or in the solar wind reference frame. Both methods with their respective advantages and drawbacks are analyzed in

detail in subsequent chapters.
The main limit of global simulations, especially for Earth's magnetosphere, lies in their high computational cost. This is particularly true for simulations when exploiting fully-kinetic models. Present computational resources are inadequate to resolve the detailed internal structure of the magnetopause while simultaneously modeling the entire Earth's magnetosphere. In this context, simulating magnetospheres of Earth-like planets using rescaled parameters or mini-magnetospheres such as Mercury, becomes more and more of crucial importance. As demonstrated by (Omidi et al., 2004; Karimabadi et al., 2014), a reliable metric for characterizing a magnetosphere is the ratio D_p between the magnetopause nose distance from the center of the planet and the ion inertial length in the solar wind. As pointed out in (Omidi et al., 2004), simulations with this ratio D_p greater than ~ 20 exhibit Earth-like characteristics in both the dayside and nightside magnetosphere. However, the smaller size of these magnetospheres reduces the transit time of the plasma when compared with Earth. This may affect the development of low growth rate wave modes before reaching the magnetopause, as they may not have time to develop. Nonetheless, this scaling allows us to resolve the kinetic scales and therefore the study of these mini-magnetospheres will also permit to gain insights into that of the Earth. This is in particular the case of the following study.

6.3 Numerical algorithms used in this work

During this thesis, two distinct PIC models were used to investigate planetary magnetospheres: the iPIC3D, a semi-implicit full-PIC model, and Menura, a hybrid PIC solver [2]. My work with both these solvers primarily involved the selection of parameters and the boundary conditions to be used to properly simulate the Earth's magnetopause and Mercury magnetosphere (see Chapter for further information). However, I also actively worked on code implementation, attending with the Menura team during a Hackathon organized by Cineca to increase the code performances. However, this particular work is still ongoing and escapes the scope of this thesis, and thus will not be discussed here. In this section, we provide a detailed discussion of both these models. These solvers' applications to the planetary magnetosphere study performed during this thesis are discussed in the following chapters.

6.3.1 The iPIC3D solver

The iPIC3D solver is a fully explicit Particle-in-Cell (PIC) solver, introduced by Markidis et al. (2010). This solver is optimized for execution on multiple Central Processing Units (CPUs) and is developed in C++ using the Message Passing Interface (MPI) standard.
Specifically, iPIC3D employs the traditional PIC loop, described in Section 6.1.1. Specifically, in iPIC3D, a zero-order B-spline function is used as the real-phase part of the shape function, $S(\mathbf{r} - \mathbf{r}_p)$, describing each macroparticle. Identical weights are assigned to all macroparticles. Furthermore, the particle pushing and field advancement algorithms are implemented using implicit schemes. While computationally more intensive than explicit methods, these schemes provide greater stability and allow for larger time steps, reducing the total number of iterations required for each simulation. The numerical implementation is further described in Markidis et al. (2010).

[2] All simulations discussed in this work were conducted by the author, except where explicitly stated otherwise. The study performed with both these solvers was performed on large HPC machines (as the machine TGCC-Irene for iPIC3D and IDRIS-Jean Zay, CINECA-Leonardo and CINECA-M100 for Menura). Concerning the Menura simulations, access to these machines was obtained by national grants. I am formally P.I. of two small computational allocations (ISCRA-C at Cineca, of 8k and 10k GPUh respectively) and a big one (ISCRA-B at Cineca, of 250k GPUh). I am also formally identified as "responsable technique" for a project at IDRIS (P.I. Pierre Henri).

6.3.2 The Menura solver

The Menura solver is a hybrid PIC solver first introduced by Behar et al. (2022). This solver is designed for execution on multiple Graphics Processing Units (GPUs) and is implemented in C++ with the CUDA programming model and the Message Passing Interface (MPI) standard. The Menura solution therefore corresponds to an improvement with respect to the first implementation of a hybrid-PIC model on GPUs, done by Fatemi et al. (2017), which was limited in memory and therefore presented a clear constraint for large-scale problems, such as those addressed in this thesis.
The Menura solver uses a Charge Assignment Method (CAM) algorithm, as described by Matthews (1994), allowing for a reduction of the computational steps required for particle treatment and thus minimizing computational cost. This algorithm has been used in Franci et al. (2015). The real-phase part of the shape function $S(\mathbf{r} - \mathbf{r}_p)$ is triangular-shaped, with each macroparticle contributing to the 9 adjacent grid nodes in 2D (and respectively 27 in 3D), using 9 different weights depending on the distance. As in iPIC3D, identical weights are used for each macroparticle. In Menura, the kinetic description of ions is coupled with a fluid description of electrons with a polytropic closure for the pressure $p_e n_e^{-\gamma} = const$, with the γ index left arbitrary. Furthermore, the Menura solver adopts a generalized Ohm's law assuming the quasi-neutral limit, neglecting electron inertia and displacement current as typical in relatively low frequency models. The latter hypothesis consists of ignoring the time derivative of the electric field in the Ampere equation so that the total current can be calculated via the curl of the magnetic field. In these conditions, the Ohm's law reads:

$$\mathbf{E} = -\boldsymbol{u}_\mathrm{i} \times \mathbf{B} + \frac{1}{en}\mathbf{J} \times \mathbf{B} - \frac{1}{en}\nabla \cdot p_e - \eta_\mathrm{h}\nabla^2\mathbf{J} \tag{6.10}$$

Here, a hyper-resistivity term ($\eta_\mathrm{h}\nabla^2\mathbf{J}$) is included to filter out other-frequency oscillations, as described in Maron et al. (2008), in order to ensure numerical stability. A more accurate description can be found in Behar, E. and Henri, P. (2023).
Consequently, only three variables (the magnetic field and particle positions and velocities) need to be advanced in time, with other variables obtained from these. A comprehensive explanation of the solver is given in Behar et al. (2022).

Simulating in the solar wind reference frame

A distinctive feature of the Menura algorithm is the fact that it performs the simulation within the solar wind reference frame, different to the traditional approach of planetary plasma simulations which use the planet's reference frame, with the obstacle being static and the wind flowing through the simulation domain. This choice is implemented for three main reasons.

- The reduction of small-scale artifacts propagating upstream. Such artifacts are indeed common in hybrid PIC simulations in the planetary reference frame and typically require filtering through resistivity or hyper-resistivity. In the solar wind reference frame, instead, such artifacts are inherently reduced without implementing hyper-resistivity, as demonstrated by comparative simulations in Behar et al. (2022).

- Simulating in the solar wind reference frame allows for magnetic field variations in all directions, including those relative to the plasma-object direction. Indeed, as discussed in Behar, E. and Henri, P. (2023), within the planetary frame of reference, a forced temporal variation of the component of the magnetic field along the solar wind flow cannot self-consistently influence the time evolution of the magnetic field, due to the ideal frozen-in condition,. Therefore, only variations of the magnetic field components perpendicular to the solar wind flow direction can be advected downstream. Working in the solar wind reference frame removes constraints on flow-aligned magnetic field variations and enables

us to perform numerical simulations including a wider range of solar wind events, such as coronal mass ejections, CMEs, or co-rotational interaction regions, CIRs.

- Studying the impact of turbulent solar winds on planetary magnetospheres, a peculiarity of Menura. By integrating the equations within this reference frame, it is possible to simulate the interaction between a pristine turbulent solar wind and a planetary magnetosphere, modeling it within the reference frame in which the turbulent dynamics are created.

In summary, in Menura, the obstacle moves within the simulation domain. To maintain the obstacle close to the center of the simulation domain, an algorithm is implemented that periodically shifts all particles and fields. Specifically, a shift of $n\Delta x$ along the planet's movement (the x direction) is performed every m iteration, with both n and m integers. This approach imposes a constraint on the value of the relative speed between the solar wind and the obstacle, being:

$$v_0 = \frac{n}{m}\frac{\Delta x}{\Delta t} \tag{6.11}$$

7 The magnetosphere of an Earth-like planet using the Menura solver

Contents

In previous chapters, by examining *in situ* magnetopause data, we have demonstrated that ion kinetic effects, in particular the finite Larmor radius (FLR) effects, can be essential to properly describe the magnetopause equilibrium. In contrast, spacecraft data have shown that the role of electrons can be less significant for the equilibrium.
A complementary study of this problem has been carried out numerically to have a more complete understanding of the magnetopause. In particular, for a more realistic representation, we have studied the magnetopause by exploiting three-dimensional global simulations of the magnetosphere of Earth-like planets. While local simulations could offer higher spatial resolution, allowing for a more accurate description of the plasma dynamics at different scales, they may not accurately replicate overall magnetopause conditions, making the results heavily dependent on the imposed boundary conditions. Global simulations provide a more comprehensive view by capturing the large-scale dynamics necessary for the understanding of the magnetopause.
To balance the computational efficiency and he vastness of the phenomena observed in data, we have employed the Menura solver, a hybrid particle-in-cell (PIC) solver introduced in Section 6.3.2. This approach allows us to realistically model the magnetopause and the relevant phenomena observed from *in situ* data at a reasonably computational cost but still enabling a sufficiently high resolution.
In this Chapter, we present two simulations of Earth-like planets conducted with this code. The first one, conducted in collaboration with the Menura team, represents the first simulation of a planetary magnetosphere interacting with the turbulent solar wind and was used by the Menura team to analyze the effects of solar wind turbulence on the bow shock and ion's foreshock. However, this simulation has no sufficient spatial resolution to serve as an accurate model for the magnetopause. Therefore, a second high-resolution simulation but exploiting a laminar solar wind has been performed.

7.1 Simulating a planetary magnetosphere interaction with a turbulent solar wind

The Menura team has performed the first-ever numerical simulation of an Earth-like planet's interaction with a turbulent solar wind. This simulation employs a dipole magnetic field rescaled with respect to the realistic conditions, covering a magnetopause nose distance from the planet's center of $D_{mp} = 200d_i$, instead of the actual 640 d_i[1]. This adjustment ensures a feasible computational load while maintaining the essential structural characteristics of the magnetosphere.

[1] In Menura, the Dipole strength is defined through the D_{mp} parameter.

In this section, we will provide an overview of the simulation setup and highlight the main results concerning the influence of turbulence on the bowshock and ion's foreshock.

7.1.1 Simulation setup

To accurately model the turbulence in the solar wind, Menura's simulations are executed through a two-step process. The first step consists of a three-dimensional simulation of solar wind decaying turbulence. In this step, periodic boundary conditions are used. The simulation runs until the solar wind reaches a quasi-stationary state, corresponding to a fully developed turbulence. The second step consists of using the final iteration from this turbulence simulation as the initial condition for a simulation of the interaction between the turbulent solar wind and the Earth-like planet. The magnetized planet is modeled, for the sake of simplicity, as a perfectly absorbing body, where incoming ions are removed from the simulation upon contact. Additionally, the planet is represented by a permanent magnetic dipole, described as an external magnetic field.

In this second phase, the boundary conditions are modified. The upstream boundary plays the role of an injection boundary, introducing a slice of turbulent fields and particles taken from the first simulation discussed before. At the other end, the downstream boundary is treated as an open boundary. The domain boundaries parallel to the flow are managed by imposing a zero spatial derivative perpendicular to these boundaries, achieved through ghost nodes at the simulation domain edges. Detailed boundary condition treatment for this phase is described in Behar et al. (2022) and Behar, E. and Henri, P. (2023). In both simulations, the equations are solved within the solar wind reference frame. Table 7.1 provides a summary of the main grid parameters employed in these simulations. This approach is essential for understanding the influence of solar wind turbulence on planetary magnetospheres, with implications for space weather forecasting and planetary environment studies.

Variable	Value
$\Delta X = \Delta Y = \Delta Z$	5 d_i
Δt	0.5 Ω_{ci}^{-1}
Box size[a] L_{box}	2000 d_i
Particles per cell N_{ppc}	600

Table 7.1: Grid parameters the simulations. [a] The box size is the same in all spatial directions .

The results obtained from the analysis of these simulations are not discussed here but can be found in Behar et al. (2024), currently under review at Astronomy and Astrophysics (the latest version of the draft of the article can be found in Chapter 9). These results are not discussed in this manuscript for two primary reasons. Firstly, they were obtained in collaboration with the Menura team, and my role was that of a collaborator. Secondly, these findings lie outside the primary scope of this thesis.

7.2 The magnetopause using Menura

The study of the magnetopause structure within a global numerical simulation presents significant computational challenges, primarily due to the need of accurately resolve its internal structure. This necessitates small-scale resolution within a simulation box that encompasses the entire magnetosphere, spanning several orders of magnitudes. For instance, while the previously discussed simulation is adequate for analyzing both the ion's foreshock and the bow shock and their response to solar wind turbulence, it falls short of resolving the small structures' internal equilibrium, including the bowshock. Consequently, this simulation is inadequate for a detailed

analysis of the magnetopause.

Specifically, the spatial grid resolution used in the simulations discussed in the previous section is 5 d_i while the magnetopause's width is of the order of a few ion inertial lengths, comparable to the simulation's grid. However, ion kinetic effects, crucial for understanding the magnetopause equilibrium, require a spatial resolution that can accurately resolve the ion inertial length. Achieving such high resolution within a large simulation box is impossible due to numerical constraints and therefore we are forced to make some assumptions to limit this numerical heaviness. These assumptions aim at reducing the simulation box size thus allowing one for the necessary grid resolution. In this context, we must always ensure that the simulation box remains sufficiently large to avoid the magnetosphere structure exiting the domain, which would destabilize the simulation. In other words, the regions of plasma close to the external box boundaries should always represent the solar wind. To address these challenges, the following assumptions were made:

1. **Scale the Planet's Dipole:** The planetary dipole was scaled to have a magnetopause stand-off distance of 90 d_i, closer to the conditions observed at Mercury[2]. The implications of this rescaling have been discussed in Chapter 6.

2. **Focus on the Dayside Magnetosphere:** The simulation concentrated on the dayside region, excluding most of the magnetotail region. This focus aligns with the data analysis presented in Chapter 5, where MMS crossings are primarily on the dayside magnetopause. By omitting the nightside region, we neglect potential backward-propagating waves or instabilities, which are assumed to have minimal impact on the magnetopause equilibrium being studied.

3. **Reduce the number of macroparticles per cell :** Although a higher number of macroparticles per cell improves the particle distribution function's sampling and reduces simulation noise, it also increases memory and computational demands. Particle treatment is indeed the bottleneck in PIC simulations, both in computational time and memory. This statistical noise is particularly problematic in low-density regions (the magnetosphere in this study). To mitigate this, we implemented a smoothing algorithm on the electric field, for each iteration, after calculating it from the generalized Ohm's law[3]. This allows us to reduce the influence of this noise. However, since we aim at studying the magnetopause, we had to take care that this change does not influence the equilibrium of this region and, therefore, invalidate the results.

Additionally, solar wind turbulence is excluded from this simulation to simplify the numerical setup and reduce computational stress. The influence of the turbulence on this region is left to a future study. It is worth noticing however that, even with a laminar solar wind, the magnetopause vicinity is not at all laminar, due to the development of local instabilities such as tearing or Kelvin-Helmholtz.

7.2.1 Simulation parameters and overview

This section introduces this simulation, to which we will refer to as the high-resolution simulation hereafter. This simulation employs a grid with a $\Delta x = 0.25 d_i$ and 64 particles per cell. Simulation physical parameters are normalized to solar wind values and are listed in Table 7.2. The solar wind parameters are compatible with the solar wind values at Earth. The solar wind is modeled with a southward orientation, optimizing the interaction between the magnetosphere and the solar wind, and allowing for magnetic reconnection at the magnetopause's nose to occur.

[2]The magnetosphere of Mercury will be discussed in detail in Chapter 8.

[3]Specifically, a Gaussian Filter is applied in cells with a density lower than 80% of the solar wind density, corresponding to equal or less than 50 macroparticles within the cell.

Solar wind parameters		Planet parameters		Grid parameters	
$n_{\rm sw}$	3 cm^{-3}	R_{planet}	50 d_i	Δx	0.25 d_i
$\mathbf{B}_{\rm sw}$	[0,0, -3] nT	$D_{\rm mp}$	90 d_i	Δt	0.01 $\omega_{c,i}^{-1}$
$\mathbf{v}_{\rm sw}$	472.1 $km\,s^{-1}$	$\tau_{\rm dip}$	[0,0,1]	L_x	285 d_i
T_i/T_e	1.			$L_y = L_z$	600 d_i
$\beta_{\rm sw} = \beta_i + \beta_e$	1.			$N_{\rm ppc}$	64
γ_e	1.			$\eta_{\rm hyp}$	0.01
				N_x	1140
				$N_y = N_z$	2400

Table 7.2: Solar wind, planetary, and grid parameters for the high-resolution run. The latter two are here normalized on the solar wind ion inertial length ($d_i = 131.5$ km) and ion cyclotron time ($\omega_{c,i}^{-1} = 0.03s$). Here $\tau_{\rm dip}$ is the versor indicating the planetary dipole orientation and γ_e is the polytropic index for electrons (isotropic closure). Here $\eta_{\rm hyp}$ is the hyper-resistivity coefficient (Menura includes a term of hyper-resistivity in Ohms law equal to $\eta_{\rm hyp}\nabla^2\mathbf{J}$, as discussed in Behar et al. (2022).

Concerning the planetary body, its center is positioned at [71.25, 300, 300] d_i in a box-size simulation of [285, 600, 600] d_i. The planet's radius is set to 50 d_i, compatible with that of the Earth, while the planetary dipole is oriented toward the positive $\hat{z}$. As mentioned above, the magnetopause distance to the nose is rescaled to 90 d_i. The simulation parameters are detailed in Table 7.2, and Figure 7.1 depicts the overall magnetosphere structure, showing the ion density in both equatorial ($x_{GSE} - y_{GSE}$) and meridian ($x_{GSE} - z_{GSE}$) planes. The figure also shows the topology of the magnetic field lines in the meridian plane. From this figure, we can easily distinguish the main regions of the magnetosphere depending on the density value. Starting from the right (Sun-ward), the light region corresponds to the solar wind, the red region, denser, is the magnetosheath while the dark blue region, with low-density plasma, corresponds to the magnetosphere. The bow shock and magnetopause are the corresponding separating regions. For this study, we focus in particular on the magnetopause.

7.3 Testing the GF2 tool on the numeric simulation

The high-resolution simulation introduced above can be used to test the GF2 tool, introduced in Chapter 3, and compare it with the state-of-the-art MDD tool. To perform this comparison we need to focus on the region within the magnetopause, specifically including areas exhibiting one-dimensional conditions and, therefore, far from reconnection regions. To this purpose, we chose to focus on the magnetopause segments far from the nose, where magnetic reconnection is observed due to the southward solar wind conditions. Specifically, we examine here the analysis of the magnetopause structure in the $x_{GSE} - y_{GSE}$ plane, at $\hat{z}_{GSE} = -20$ d_i. Analogous results are observed for different cuts.

Figure 7.2 illustrates the analyzed cut of the magnetopause, depicting the structure of the current modulus, magnetic field, and plasma density. Here we observe the key features of the magnetopause, including (*i*) a pronounced current density compared to adjacent areas (the magnetosphere on the left and the magnetosheath on the right), (*ii*) a significant magnetic field variation, with a bigger magnitude in the magnetosphere, a low one in the magnetopause and finally increasing again in the magnetosheath, and (*iii*) plasma density variation from magnetosphere low values (blue) to magnetosheath higher values (red). From this figure we observe an irregular structure of the magnetopause, with a thickness of approximately 5 d_i, which aligns with *in situ* observations. Furthermore, the spatial resolution of the simulation grid is sufficient to well resolve the structure (having around 20 points along its width) and calculate

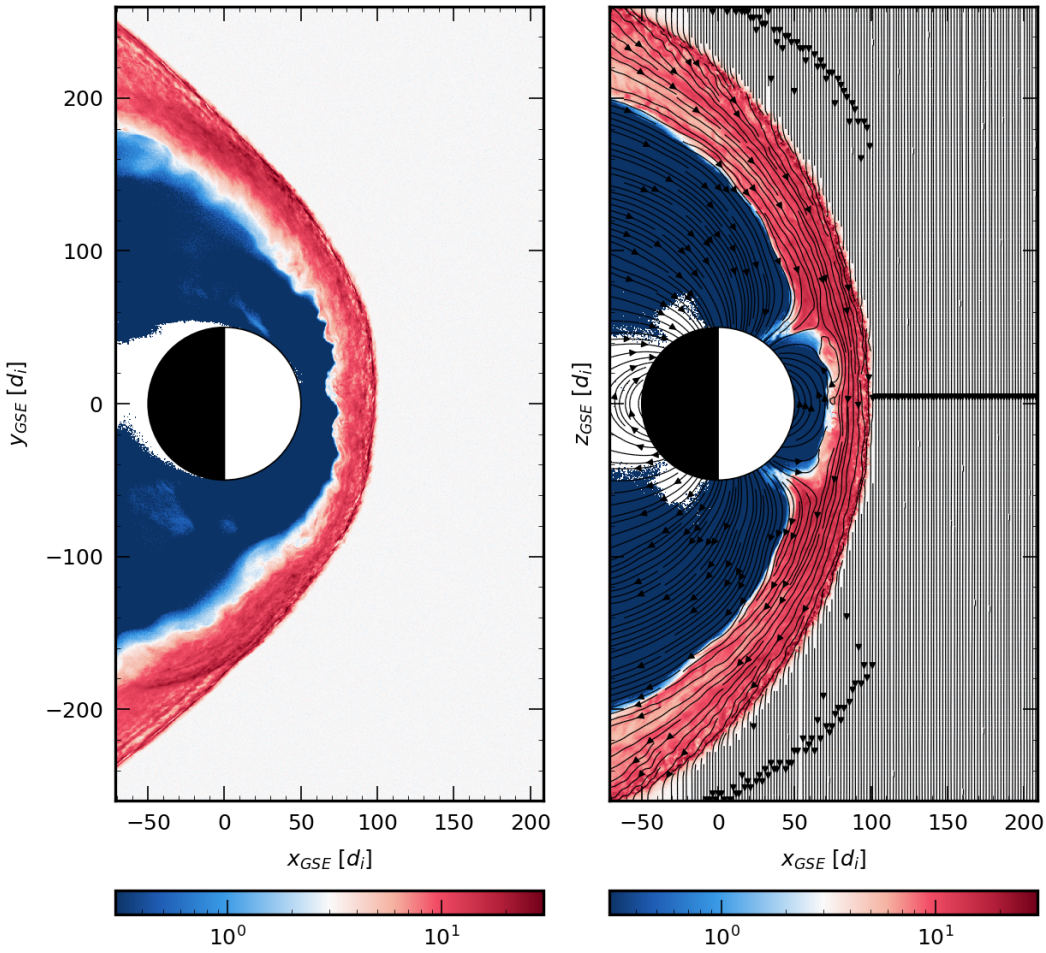

Figure 7.1: Overview of the structure of the ion density at the magnetosphere in the high-resolution simulation, on the meridian plane (top) and equatorial plane (bottom). This structure corresponds to the last time of the simulation.

gradients with adequate accuracy within the structure, enabling a comparison between GF2 and MDD results. Unfortunately, while the simulation enables us to interpret the differences between the two techniques, several reasons prevent us from usefully comparing the two results with a "real" normal direction. First, the 2D character is always present at short scales, making sometimes hardly relevant the notion of a local "normal". Then, calculating the matrix gradient $\mathbf{G}$ from finite differences between the grid points of a numerical simulation is a work quite comparable to getting it in *in-situ* data from four-point measurements: it brings uncertainties and leads to the use of techniques close to the MDD or GF2 to derive reliable normal directions from $\mathbf{G}$.

Before delving into the comparison, a consideration of the different conceptual approaches in the study of the magnetopause in this numerical simulation with respect to data analysis must be discussed. On one hand, satellite data typically observes the magnetopause moving with a much bigger velocity with respect to the spacecraft, which can therefore be approximated as stationary. In data, therefore, is the magnetopause to cross the satellite. On the other, when we study the magnetopause using a global simulation, the magnetopause position is generally relatively stable with the exception of the surface waves that can be observed to propagate on top of the boundary. Therefore, simulating the complete movement of the magnetopause with respect to a fixed grid point (corresponding in this case to a virtual spacecraft) is computationally intensive and requires a lot of data to be stored. One solution would be to save field values at

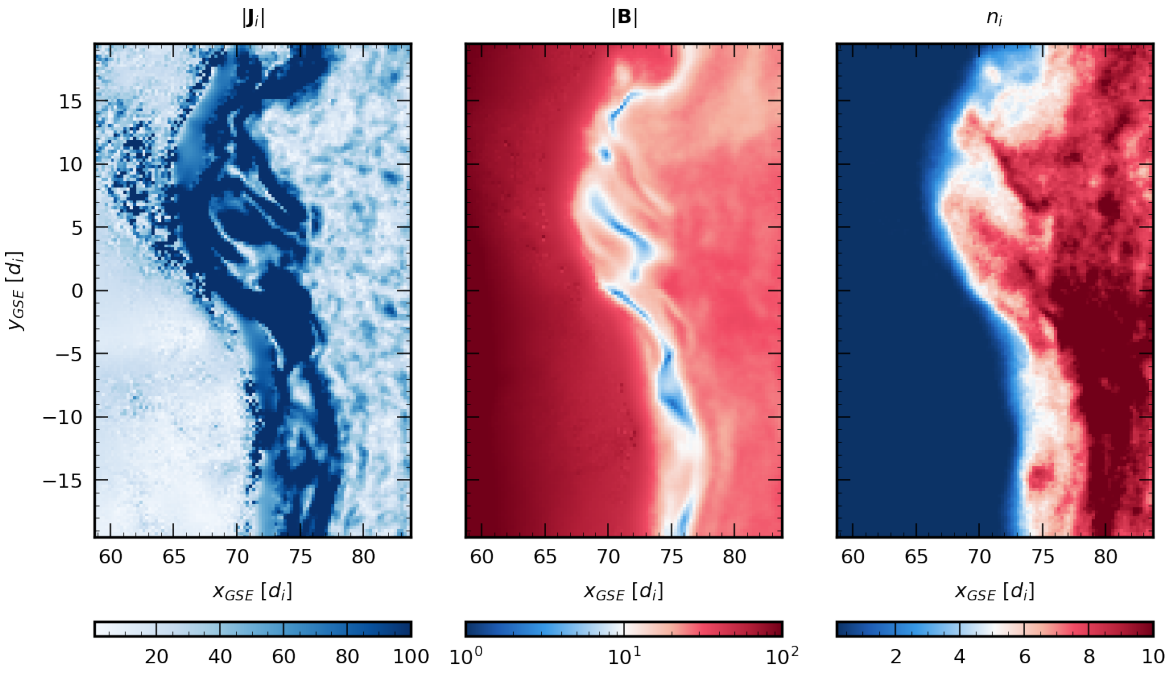

Figure 7.2: Cut of the plane analyzed to test the GF2 tool. From left to right, we show the module of the current density (in nA m^{-2}), the magnetic field (in nT), and the ion density (in cm^{-3}) in the $x_{GSE} - y_{GSE}$ plane at $\hat{z}_{GSE} = -20\ d_i$.

all time steps in the cell considered as the virtual spacecraft, allowing for a sequence of data analogous to in situ measurements. However, with this approach, we sacrifice the knowledge of the global feature of the structure since we lose all the information around to the virtual probe. Indeed, storing this information at each time step would be impractical due to the significant data storage requirements. On the contrary, for this study we chose to adopt a fixed-time stationary structure analysis, calculating temporal derivatives directly from the simulation. This method allows for a comprehensive study of the normal vectors across the magnetopause, allowing us to observe the variation of the normal all along the magnetopause.

7.3.1 Comparison of the GF2 and MDD magnetic field normals

To estimate the magnetopause normal with the two methods, it is necessary to obtain the magnetic field gradient matrix. In this section, we use the real value of that matrix, called $\mathbf{G}$, obtained through the finite differences method from the magnetic field at every point in the simulation box. In the next section we will compute the normals using the "experimental" method to obtain the gradient matrix ($\mathbf{G}_{exp}$), computed along the trajectory of virtual spacecraft, using the reciprocal vectors algorithm.

The GF2 and MMD normals' components, obtained from $\mathbf{G}$, are shown in Figure 7.3. Here we only show the values within the magnetopause. The magnetopause regions were identified by filtering the cells where the ion density varies in the range of 0.8 to 8 cm^{-3}. From *in situ* observations, we observe that this range of values always corresponds to the magnetopause. This rather stringent condition allows us to avoid taking into consideration the regions of low-density magnetosheath and those of high-density magnetosphere, both of them being out of the interface layer under study. The angle between the normals obtained by using these two techniques is shown in Figure 7.4, together with the dimensionality indices D_1 and $\mathcal{D}_{1,GF2}$ (both defined in Chapter 3). From this Figure, we observe that the two methods provide the same normal

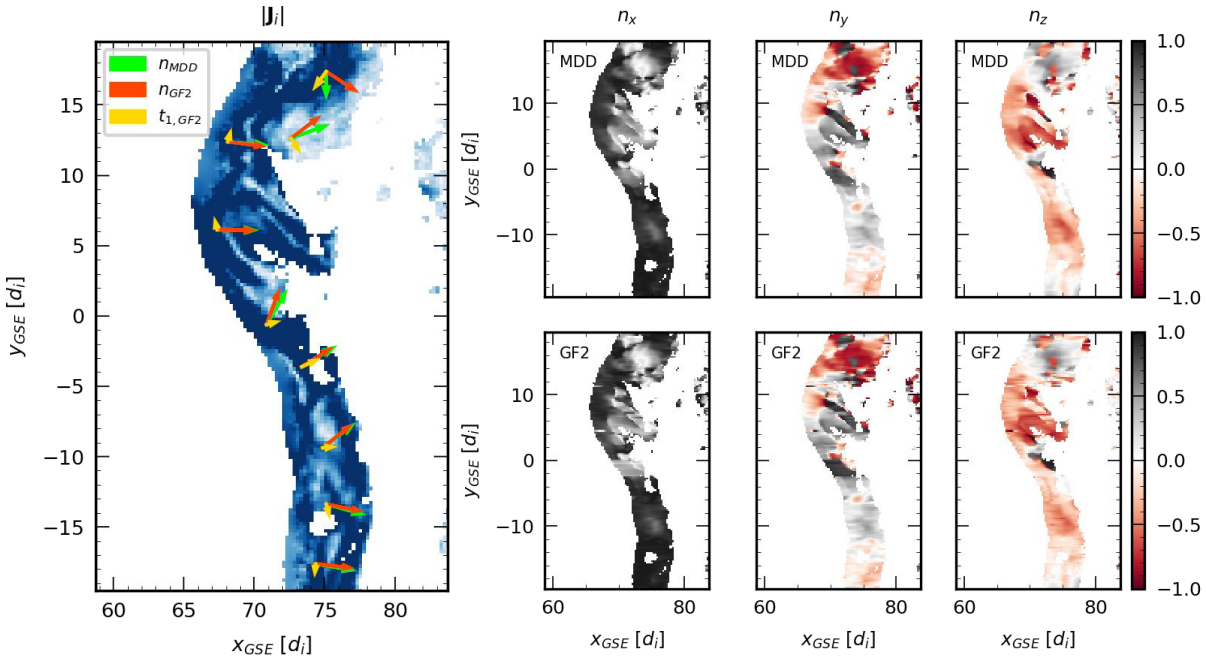

Figure 7.3: *Left*) Current density within the magnetopause. We overplot the projections of the three main directions: $\mathbf{n}_{MDD}$ (green), $\mathbf{n}_{GF2}$ (red), and $\mathbf{t}_1$ (yellow). *Right*) Components of the normal vectors (x, y, and z components from left to right) of the normals obtained using the two techniques, above for MDD and below from GF2.

(*i.e.* normals with less than 10 degrees differences compatible with the grid uncertainty) almost everywhere. Regions with larger discrepancies correspond to areas where the structure exhibits local two-dimensional characteristics, as indicated by the two dimensionality indices (the $\mathcal{D}_{1,GF2}$ index generally exhibits lower values than D_1, as already mentioned from *in-situ* data, but both vary in the same way).

To further elucidate these differences, we can examine the projections of the two normals ($\mathbf{n}_{MDD}$ and $\mathbf{n}_{GF2}$) and the tangent direction $\mathbf{t}_1$ obtained with GF2, corresponding to the direction tangent to the discontinuity and orthogonal to the invariance direction. These projections are shown in Figure 7.3 for a set of random points within the structure. The lengths of the arrows representing $\mathbf{n}_{GF2}$ and $\mathbf{t}_1$ are proportional to the magnetic field variations in these directions. In one-dimensional regions, where the tangent direction arrow is shorter, GF2 and MDD normals closely match or are equivalent. On the contrary, in regions with two-dimensional features, the MDD normal lies between the two GF2-derived directions, indicating the MDD sensitivity to non-uni-dimensionality and gradient directionality. These results show how GF2 effectively filters tangential and minor gradient components, providing normals compatible with state-of-the-art methods in purely one-dimensional structures while distinguishing gradient components from the normal direction in two-dimensional cases.

7.3.2 Calculation of gradient matrix using the reciprocal vectors method

In the previous section we demonstrated that by exploiting the gradient matrix $\mathbf{G}$ derived from the simulation data, the GF2 method can accurately determine the normal direction, even in two-dimensional regions where the MDD is limited due to small gradients in tangential directions. However, to perform a more complete study, we can test in the numerical simulation the method that we applied to the experimental data. Therefore we replicate the previous analysis (made on *in situ* data) by estimating the gradient matrix using the reciprocal vectors method

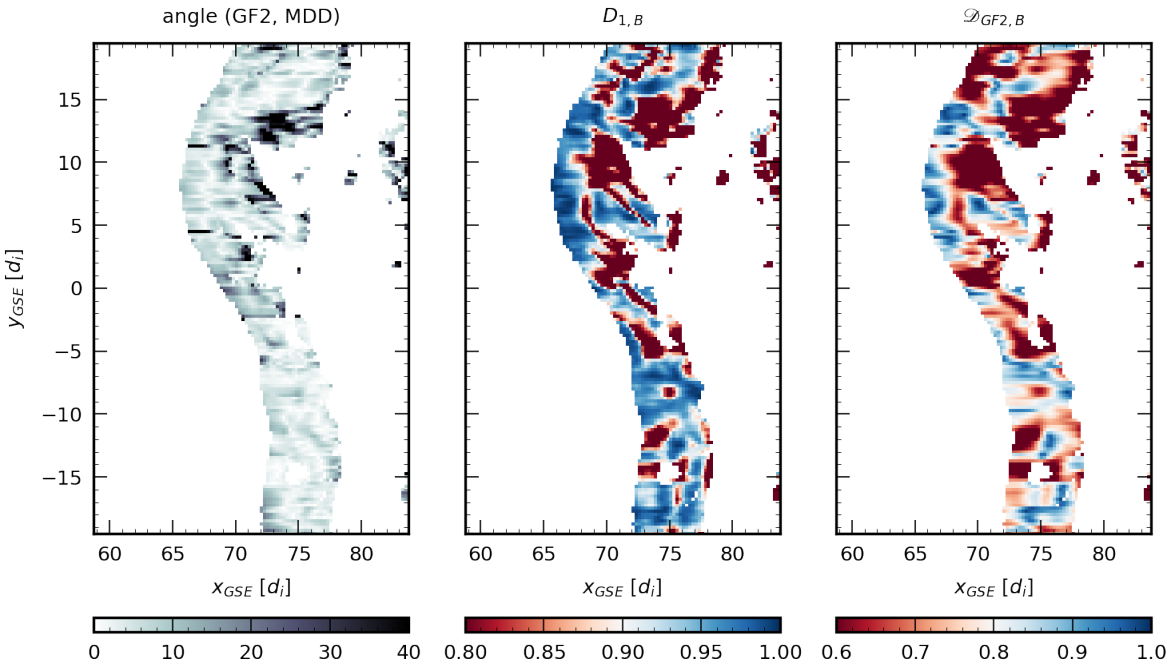

Figure 7.4: *Left*) Angle between the MDD and GF2 normal; *Center*) the D_1 and *Right*) the $\mathcal{D}_{1,GF2}$ dimensionality parameters.

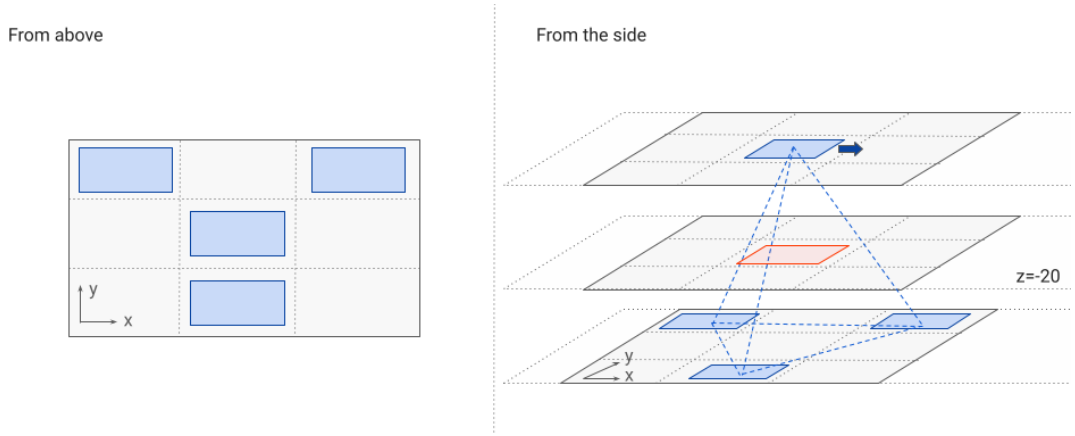

Figure 7.5: Scheme of the tetrahedron configuration of the virtual satellites in the simulation grid, from above (left) and on the side (right). The blue cells correspond to the values exploited to compute the gradient on the red cell.

along virtual spacecraft trajectories.

To estimate the gradient matrix in a cell within the examined plane, we used the field values on four adjacent cells, chosen to replicate the spacecraft conditions (and MMS particularly). These cells are selected to form a regular tetrahedron as depicted in Figure 7.5. Here we show in blue the cells simulating the virtual satellite measurements used to compute the gradient for the cell in red. Indeed, the reciprocal vector method gives an estimation of the gradient matrix at the center of the tetrahedron. It is important to note that we avoided any interpolation by utilizing the exact cells from the simulation data.
For each cell, spatial distances between the "virtual spacecraft" cells are used to obtain the reciprocal vectors via Equation 1, from which the gradient matrix $\mathbf{G}_{exp}$ is derived from Equation

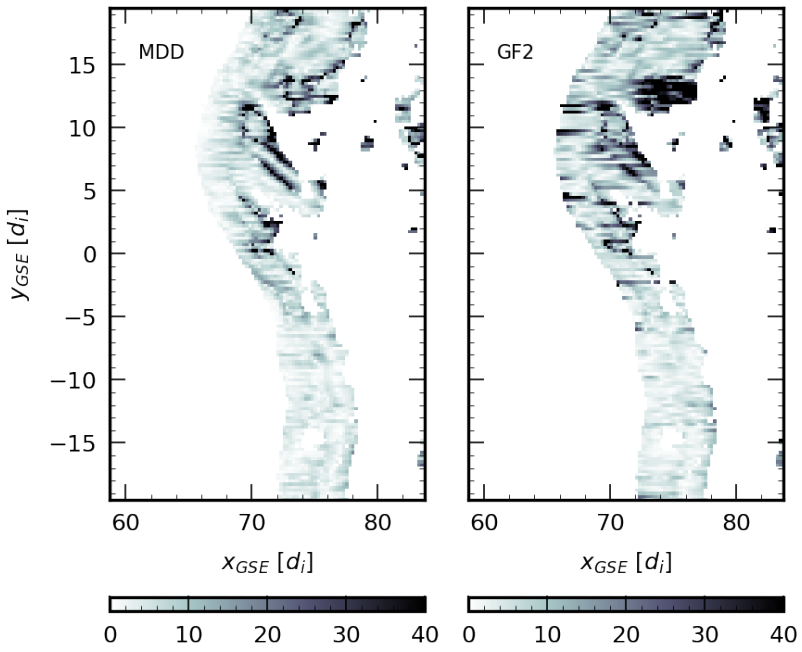

Figure 7.6: Angles between the magnetic normal obtained exploiting $\mathbf{G}_{exp}$ and $\mathbf{G}$, using the MDD (left) and GF2 (right) tools.

2. Subsequently, we analyze the normal vectors obtained using both the MDD and GF2 methods on this matrix. Figure 7.6 shows the angles between the normal vectors derived from $\mathbf{G}_{exp}$ and those previously obtained from $\mathbf{G}$, for both tools. The results indicate that the normal vectors derived from the two gradient matrices are consistent, except for a few cells where the normals differ more than 10 degrees. This could be due to local gradients smaller than the tetrahedron dimensions that cannot be obtained using the tetrahedron shape. The results shown here are therefore in agreement with what was discussed previously and validate the results also when using the estimation of the gradient matrix. Furthermore, we can also study the structure dimensionality derived from $\mathbf{G}_{exp}$ to verify its compatibility with earlier results. The dimensionalities obtained are presented in Figure 7.7 (top panel). Compared with Figure 7.4, it is evident that the dimensionality estimates from $\mathbf{G}_{exp}$ are consistent with those obtained from $\mathbf{G}$.

7.3.3 Ion mas flux magnetopause normal

A final step to evaluate GF2 involves examining the normal vectors derived from ion mass flux structure of the magnetopause. Here we show the normal vectors estimated from the gradient matrix derived from the simulation. Exploiting the reciprocal vector method shows consistency with these findings. Figure 7.8 illustrates the angles between the normal vectors of ions and the magnetic field, as determined by both the MDD and GF2 methods. Notably, the structure exhibits two distinct regions. On the left side, adjacent to the magnetosphere, the angles between the magnetic field normal and the ion normal are relatively small, approximately 10 degrees for both tools. In this part, most of the cells indicate compatibility between the GF2 and MDD normals. In contrast, on the right side, adjacent to the magnetosheath, the normal vectors show a significant departure from the magnetic field normals. This discrepancy is understood by examining the dimensionality of the ion structure, as shown in Figure 7.7 (bottom panel). Here, the region on the right appears two-dimensional according to both dimensionality indices. This result highlights that the ion structure can exhibit two-dimensional features even where

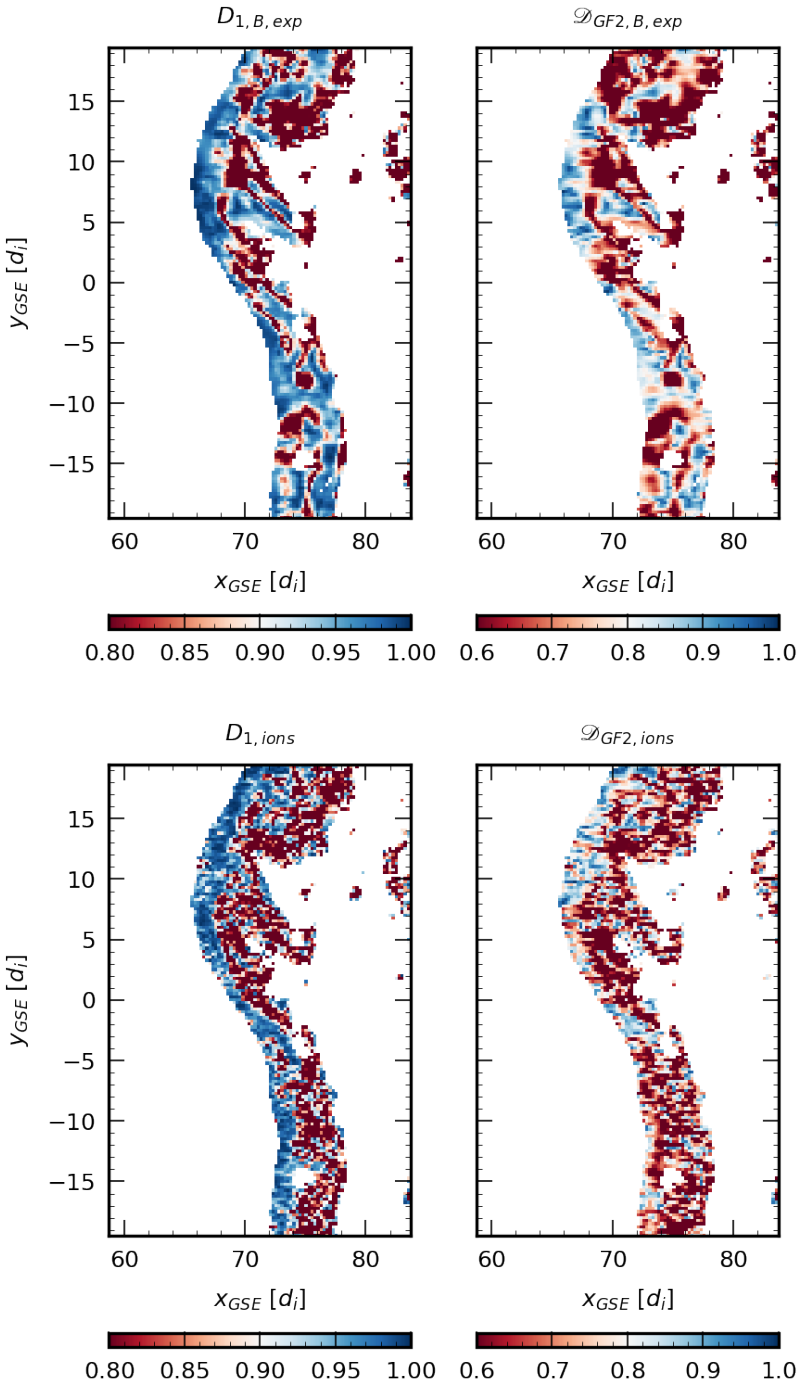

Figure 7.7: The D_1 (left) and $\mathcal{D}_{1,GF2}$ (right) dimensionality parameters. The top panels show the results for the magnetic field from $\mathbf{G}_{exp}$, and the bottom panel for the ions mass flux using $\mathbf{G}$.

the magnetic field is one-dimensional. However, as shown in Figure 7.4, also the magnetic field structure appears fragmented, with a predominance of one-dimensional regions on the magnetospheric side and two-dimensional regions on the magnetosheath side. This observation can be interpreted by considering that the magnetosheath region is more susceptible to local instabilities compared to the magnetosphere. Additionally, this finding is consistent with the data, where ion crossing structures can be narrower than those of the magnetic field, as observed in the MMS crossing on 12/28/2015 analyzed in Chapters 3 and 4. Furthermore, the results

obtained show that also in one-dimensional regions for both ion mass flux and magnetic field, different normal vectors can be found, in agreement with what was observed in the statistical study discussed in Chapter 5 and in Ballerini et al. (2024b). The understanding of this feature is left as future work, as discussed below.

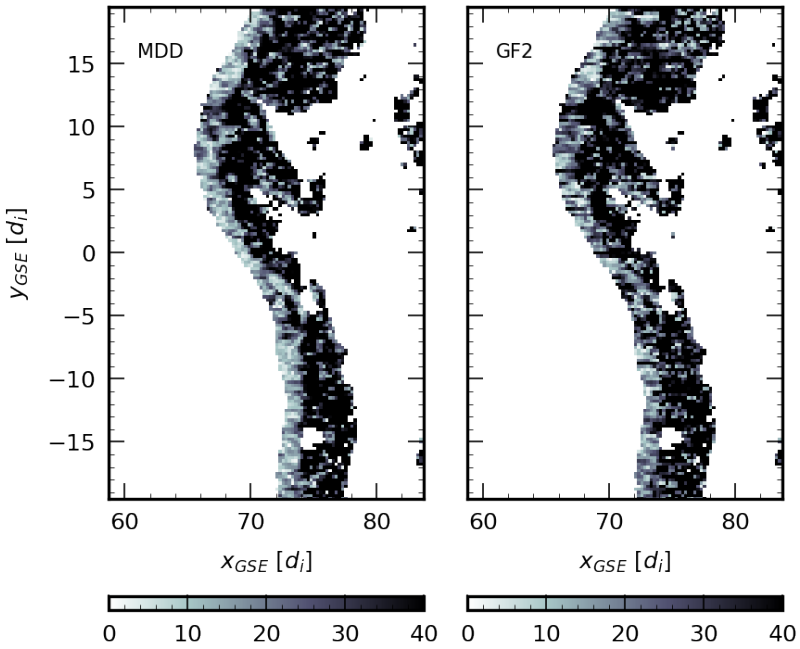

Figure 7.8: Angles between the normal obtained from the ion mass flux and the magnetic field, using the MDD (left) and GF2 (right) tools.

8 Simulating Mercury magnetosphere using the iPIC3D model

Contents

As introduced in Chapter 6, a fully kinetic description is required to have a complete model of the plasma dynamics, including electrons. In this chapter, we present new results obtained with the full-kinetic Particle-in-Cell (PIC) iPIC3D solver to simulate Mercury's magnetosphere[1]. This specific magnetosphere was analyzed for two main reasons. The first is to gain knowledge of the Hermean magnetospheric environment before the arrival of the JAXA/ESA BepiColombo mission, introduced in Section 8.2, in December 2025. The second is to exploit the full-kinetic description of mini-magnetospheres, such as the Hermean, to provide insights into the Earth one, which is computationally challenging to simulate with a full-kinetic model due to current computational constraints. This study dedicated to magnetospheric waves must be considered complementary to the main focus of this thesis. We remember that a fully-kinetic description is computationally very demanding and necessitates approximations and re-scaling of some plasma parameters, see Section 6.1.2. More specifically, this simulation will allow us to give a first overview of the dynamics at Mercury, in particular, to study magnetic reconnection in the magnetotail, with a specific emphasis on the generation of whistler waves near the reconnection region.

8.1 The magnetosphere of Mercury

Mercury is the innermost planet in the Solar System exhibiting a perihelion of approximately 0.307 AU and an aphelion of about 0.467 AU [2]. Therefore Mercury presents the most eccentric orbit among the planets in the Solar System. For comparison, the perihelion distance at the Earth is about 3.5 % less than its aphelion's distance. Mercury's diameter is about 38% of Earth's diameter, significantly smaller. A more detailed discussion on Mercury can be found in Sun et al. (2022).
As discussed in Section 2.2, Mercury is the only telluric planet, in addition to the Earth, to possess an intrinsic dipolar magnetic field (Ness et al., 1974, 1976). Mercury's surface magnetic field is of approximately 195 nT, with a dipole center offset of about 479 km northward from the planet's center, about 10% of the planet radius, and a tilt of less than 0.8^o relative to its spin axis (Anderson et al., 2012). Despite its weak magnetic field, Mercury has a magnetosphere separating the shocked solar wind from the planet's surface. Mercury's dayside magnetopause

[1] This research started from a collaboration with Federico Lavorenti, then a PhD student under the supervision of Francesco Califano that I met during my master's internship at the Observatoire de la Cte d'Azur, to acquire expertise in analyzing numerical simulations in preparation for subsequent work with Menura. The findings from this analysis are documented in Ballerini et al. (2024a).
[2] AU denotes the astronomical unit ($\sim 1.49610^{11}$ m), defined as the mean distance from Earth to the Sun.

is much closer to the planet, with a magnetopause sub-solar standoff distance typically between 1.35 and 1.55 times the planetary radius from the planet's center (Winslow et al., 2013), while the Earth presents a nominal distance of 10 - 14 Earth's radii (Spreiter et al., 1966b). The thickness of Mercury's magnetopause is estimated to be approximately 100 km, significantly thinner than Earth's, around 500 km (Dibraccio et al., 2013).
Due to the relatively weak intrinsic magnetic field and the strongly variable solar wind because of its proximity to the Sun (Raines et al., 2015), Mercury's magnetosphere is highly dynamic. *In situ* measurements have confirmed that magnetic reconnection occurs both at the dayside magnetopause and the nightside magnetotail (Slavin et al., 2009; Slavin et al., 2012; Dibraccio et al., 2013; Slavin et al., 2014; DiBraccio et al., 2015; Slavin et al., 2019). Magnetic reconnection on Mercury, like on Earth, leads to flux transfer events, plasmoids (Slavin et al., 2009; Slavin et al., 2012; Dibraccio et al., 2013), and dipolarization fronts (Sundberg et al., 2012; Imber et al., 2014; Sun et al., 2016). Furthermore, Mercury's magnetosphere directly interfaces with the planet's surface, unlike Earth where the inner magnetosphere is dominated by the co-rotating plasmasphere. Therefore, magnetic reconnection at Mercury influences the magnetosphere and interconnects various subsystems, including the exosphere and the planetary surface. *In situ* measurements have demonstrated the presence of the Dungey cycle in Mercury's magnetosphere (Slavin et al., 2009; Siscoe et al., 1975), already discussed for the Earth in Section 2.4.1. However, the Dungey cycle at Mercury has a short period, approximately 1-2 minutes, compared to Earth's, of about 1-hour (Baumjohann et al., 2006). Consequently, Mercury's magnetosphere can respond rapidly to variations in upstream plasma parameters. Since the IMF magnitude and direction are typically observed to change over periods of tens of minutes, the magnetosphere undergoes a series of quasi-steady-state configurations with steady IMF, separated by transient reconfiguration periods. Here we focus on the quasi-steady-state global modeling of the magnetosphere, neglecting the transient reconfiguration periods.

8.1.1 Solar wind conditions at Mercury

Due to its proximity to the Sun, Mercury experiences the most intense solar wind driving of any planet in the Solar System (Slavin and Holzer, 1981). However, the absence of upstream solar wind spacecraft at Mercury prevents a direct correlation between magnetosphere measurements and solar wind conditions. Therefore, estimating average solar wind conditions is essential for studying Mercury's magnetosphere. At Mercury's orbit, the average solar wind speed is slightly lower than at the Earth's. Nevertheless, the solar wind's density and magnetic field strength are greater at Mercury, as indicated in Table 2.1. Consequently, Mercury's magnetosphere exhibits higher Alfvén speed and increased solar wind ram pressure $P_{ram} = n_{sw} v_{sw}^2$ compared to Earth. Due to the eccentricity of Mercury's orbit, solar wind conditions differ significantly between perihelion and aphelion; for instance, the solar wind density at the aphelion is approximately half of the one at the perihelion. These variations induce seasonal changes in the magnetosphere's size and shape (Zhong et al., 2015, 2020), a peculiarity of Mercury among the planets in the Solar System, and affect the induced component of Mercury's dipolar magnetic field (Johnson et al., 2016). Detailed information on the solar wind conditions at Mercury can be found in Sarantos et al. (2007), James et al. (2017), Sun et al. (2022), and Dakeyo et al. (2022).
In situ measurements have also revealed that the IMF at Mercury exhibits a bimodal clock angle distribution centered around the dawnward and duskward directions (James et al., 2017).

The clock angle is defined as $\theta = \arctan(-B_y/B_z)$, with magnetic field components in MSO[3] coordinates. A bimodal distribution is also observed for the cone angle distribution $\phi = \arccos(-B_x/|B|)$, which is centered around 35° and 150° (James et al., 2017). These distributions indicate a typical Parker spiral angle of approximately ±35° at Mercury, which is smaller than the ∼ 45° angle observed at Earth (Milillo et al., 2020).

8.1.2 Chorus-mode Whistler Waves in the Magnetosphere of Mercury

To present the results of this study, it is useful to provide first an introduction to chorus-mode whistler waves and their role in planetary magnetospheres.
Whistler-mode chorus are electromagnetic waves characterized by a right-handed polarization, a quasi-parallel propagation, and frequencies typically below the electron gyrofrequency. The dispersion relation governing these waves is the same as the one for whistler waves, and in the cold plasma limit it reads (Stix, 1992; Omura et al., 2008):

$$c^2k^2 = \omega^2 + \frac{\omega\omega_{pe}^2}{\omega_{ce} - \omega} \tag{8.1}$$

From observations, we know that whistler-chorus waves generally exhibit narrowband and quasi-coherent characteristics. These waves are characterized by discrete chirping elements packets with rapidly varying central frequencies over time, resembling the chirping of birds at dawn (Burtis and Helliwell, 1976; Tsurutani and Smith, 1974). This feature is responsible for their name. Typically, these waves are observed in two frequency bands: a lower band (below $0.5\omega_{ce}$, with ω_{ce} the equatorial electron gyro-frequency) and an upper band (in the range between 0.5 and 0.8 ω_{ce}).

Electron temperature anisotropy from thermal electrons is considered to be the source of whistler waves, requiring the electron perpendicular temperature $T_{\perp,e}$ to be higher than the parallel one, $T_{\parallel,e}$ (Kennel and Petschek, 1966; Le Contel et al., 2009; Liu et al., 2011; Yu et al., 2018). The condition for the onset of whistler anisotropy instability, is given by (Kennel and Petschek, 1966):

$$\frac{T_{e,\perp}}{T_{e,\parallel}} - 1 > \left(\frac{|\omega_{ce}|}{\omega} - 1\right)^{-1} \tag{8.2}$$

Whistler waves have a fundamental role both in the solar wind (Vocks and Mann, 2003; Pagel et al., 2007; Kajdi et al., 2016; Tang et al., 2020) and in planetary magnetospheric dynamics (Summers et al., 1998; Thorne et al., 2013; Horne et al., 2008; Woodfield et al., 2019). They are responsible for accelerating high-energy electrons to relativistic energies via cyclotron resonance, thereby enhancing the population of radiation belt electrons (Omura et al., 2015; Allison et al., 2021; Glauert and Horne, 2005; Hua et al., 2022, 2023; Summers et al., 2007; Xiao et al., 2014). Chorus emissions have been widely observed at Earth since early *in situ* measurements (Oliven and Gurnett, 1968; Burtis and Helliwell, 1969; Lauben et al., 1998; Horne et al., 2005). Observations of whistler-chorus waves have been also obtained at Jupiter (Kurth and Gurnett, 1991; Gurnett et al., 1979; Scarf et al., 1979), Saturn (Kurth and Gurnett, 1991), Uranus (Gurnett et al., 1986), and Mars (Teng et al., 2023). Recently, chorus waves have been detected at Mercury by the BepiColombo mission, introduced in the following section. BepiColombo/Mio have observed evidence of chorus waves during the first two Mercury flybys (Ozaki et al., 2023),

[3]The **Mercury Solar Orbital (MSO)** coordinate system is an orthogonal system used for the study of Mercury's magnetosphere and it is defined as follows:

- The **x** axis lies in the Mercury-Sun direction and points toward the Sun;
- The **z** axis is anti-parallel to Mercury's magnetic dipole;
- The **y** is defined subsequently, pointing from dawn to dusk.

highlighting the ubiquity of chorus emission waves in the magnetospheres of all magnetized planets within our Solar System. However, our knowledge of the interaction of chorus waves and electrons at Mercury still requires a better understanding. In particular, we still lack an *in situ* data geographical distribution of these waves at Mercury.

8.2 *In situ* measurements at Mercury: The BepiColombo mission

The first mission to sample Mercury's environment *in situ* was NASA's Mariner 10 mission, performing three flybys at the planet between 1974 and 1975 (Russell et al., 1988). This mission provided the first observations of Mercury's planetary magnetic field (Ness et al., 1974) and the plasma environment (Ogilvie et al., 1977). Mariner 10 measured the core of the electron distribution function within the energy range from 13.4 to 687 eV throughout most of its orbit inside Mercury's magnetosphere (Christon, 1987). Due to a technical failure, Mariner 10 could not observe the ions (Ogilvie et al., 1974).

The next and only other spacecraft to visit Mercury was the MErcury Surface, Space ENvironment, GEochemistry, and Ranging (MESSENGER) mission. Launched in 2004 and arrived at Mercury in 2011, MESSENGER conducted four years of orbital observations (Solomon et al., 2018). Unlike Mariner 10, MESSENGER was equipped to observe ions while being limited to detect high-energy electrons (above 10 keV), thereby excluding the bulk of the electron distribution function (Andrews et al., 2007). More details on the MESSENGER mission and its scientific achievements can be found in MESSENGER book (Solomon et al., 2018).

Due to the instrumental constraints of both missions, the data at our disposal provide an incomplete picture of the Hermean magnetosphere. Therefore, to enhance our understanding, the BepiColombo mission has been launched (Benkhoff et al., 2021). Jointly developed by the European Space Agency (ESA) and the Japan Aerospace Exploration Agency (JAXA), BepiColombo was launched in October 2018. The mission trajectory includes nine planetary gravity assists: one at Earth (April 10, 2020), two at Venus (October 2020 and August 2021), and six at Mercury, culminating to the orbit insertion expected in December 2025. At the time of writing of this manuscript, three flybys of Mercury have been performed by BepiColombo. Detailed information on the payload can be found in (Benkhoff et al., 2021; Lavorenti et al., 2023).
BepiColombo is composed of two spacecraft: the Mercury Planetary Orbiter (MPO) supported by ESA, and the Mercury Magnetospheric Orbiter (Mio) supported by JAXA. BepiColombo is the first mission to provide simultaneous multi-point measurements of Mercury's environment. The MPO spacecraft aims to characterize Mercury globally, examining its interior, surface, exosphere, and magnetosphere. Furthermore, MPO is also expected to test Einstein's theory of general relativity. The Mio spacecraft will instead focus on Mercury's surrounding environment, including its exosphere and magnetosphere, and their interactions with the solar wind. Mio will explore previously unexplored regions of Mercury's magnetosphere using a set of plasma instruments capable of performing more accurate measurements including ions, electrons and neutrals across various energy ranges, and plasma waves in different frequency bands. LPP, where this thesis was done, contributed to two experiments among the six that fly on the Mio spacecraft: the Plasma Wave Instrument (PWI), providing the broadband fluxmeter DBSC (Dual Band Search Coil) as a part of the Search Coil Magnetometer, and the Mercury Plasma Particle Experiment (MPPE), providing the ion spectrometer MSA (Mass Spectrum Analyzer)[4].
The search coil magnetometers of PWI, detailed in Kasaba et al. (2020), are the ones that allowed to measure for the first time whistler waves at the Mercury magnetosphere.
During the cruise phase, both spacecraft are mounted together on the Mercury Transfer Module (MTM), primarily propelled by Solar Electric Propulsion (SEP). Additionally, the Mio spacecraft

[4]LPP has also built the PICAM analyzer, flying on MPO under the responsibility of LATMOS

is shielded by a Sunshield (MOSIF) during this phase. Upon arrival, the MTM will be discarded, and chemical propulsion will be used to place both spacecraft into their designated polar orbits.

8.3 Simulation set-up

Solar wind parameters		Planet parameters		Grid parameters	
$n_{\rm sw}$	30 cm^{-3}	R_{planet}	5.5 d_i	Δx	0.08 d_i
$\mathbf{B}_{\rm sw}$	[0,0, -20] nT	—$\tau_{\rm dip}$—	200 nT/R_M^3 d_i	Δt	2.8 $\cdot 10^{-3}$ $\omega_{c,i}^{-1}$
$\mathbf{v}_{\rm sw}$	400. $km\,s^{-1}$	$\tau_{\rm dip}$ versor	[0,0,1]	L_x	82.5 d_i
$T_i = T_e$	21.5 eV	d_{off}	0	$L_y = L_z$	66 d_i
$\beta_{\rm sw} = \beta_i + \beta_e$	1.3			$N_{\rm ppc}$	64
				N_x	960
				$N_y = N_z$	768

Table 8.1: Solar wind, planetary, and grid parameters used in the simulation. Here $d_i = 42.5$ km is the solar wind ion inertial length and $\omega_{c,i}^{-1} = 0.54s$ is the ion cyclotron time. Here $\tau_{\rm dip}$ is the planetary dipole orientation, chosen in agreenment with observations Anderson et al. (2012), and d_{off} the dipole offset from the center of the planet.

To investigate the magnetopause of Mercury, we employ a three-dimensional simulation using the iPIC3D solver. Unlike the Menura simulation presented in Chapter 7, this simulation is performed within the planetary reference frame. In this simulation, a uniform solar wind plasma, with a southward-directed magnetic field, is injected from the sunward direction[5]. Table 8.1 details the parameters used in our simulation, which are consistent with those previously used in Lavorenti et al. (2022). We choose different boundary conditions at the planet: all macroparticles entering are removed from the simulation domain. Furthermore, we increased the output frequency to achieve a higher resolution to study the dynamics around the nightside reconnection site. In Table 8.1 we include the value of the magnetic field on the planetary surface, used to compute the dipole in iPIC3D.
To ensure computational feasibility, several assumptions were made (that were already done in previous works such as Lavorenti et al. (2022)):

1. Mercury's size is scaled down by a factor of 10, setting the radius of $R_M = 5.5 d_i$, with d_i the ion inertial length in the solar wind. Consequently, the dipole strength is scaled so that we maintain the surface magnetic field as in real measurements, allowing us to preserve the relative shape of the magnetosphere with respect to the planet. This reduces the computational domain size by a factor of 10 in each direction, decreasing the computational time by a factor of 1000. This approach has been widely adopted in previous studies (Lapenta et al., 2022; Trávníček et al., 2007, 2009, 2010) to facilitate multi-scale numerical simulations. The implications of this scaling on the results are discussed below.

2. The ion-to-electron mass ratio and the electron plasma-to-cyclotron frequency ratio are reduced to $\rm m_i/m_e = 100$ and $\omega_{pe}/\omega_{ce} = 17.8$), respectively. This reduces the separation between ion and electron scales while preserving large-scale properties, as discussed in Section 6.1.2. As demonstrated below, a rescaling maintaining $m_i/m_e \geq 100$ and $\omega_{p,i}/\omega_{c,i} \geq 10$ weakly impacts the simulation results while significantly reducing computational time, thus

[5]Assuming a purely southward IMF is not entirely representative of Mercury's average IMF conditions, as discussed in Section 8.1.1. Since the IMF direction plays a critical role in determining the magnetosphere's topology (Ip and Kopp, 2002; Kallio and Janhunen, 2003, 2004; Slavin, 2004; Slavin et al., 2012; Exner, 2021), this configuration is selected to maximize magnetic coupling between the solar wind and Mercury, enhancing energy transfer from the solar wind to the magnetosphere through magnetic reconnection at the magnetopause nose Lavorenti et al. (2022).

enabling feasible simulations. As demonstrated in Lavorenti (2023), this scaling preserves the correct global structure and dynamics of the magnetosphere.

3. We use 64 macroparticles per cell, a number sufficient to capture the key physical processes. However, the numerical noise associated with the low number of macroparticles does not adequately model the non-diagonal terms of the pressure tensor (Scudder and Daughton, 2008b). Consequently, we will not analyze the role of off-diagonal pressure tensor terms in magnetic reconnection.

In this simulation, the dipole is centered on the planet, differing from MESSENGER observations where an offset is observed (see Section 8.1.1) Complementary numerical simulations including the dipole shift have yielded compatible results with those presented in the subsequent section. Here, and in the Ballerini et al. (2024a) paper, we discuss the simulation not including the dipole offset to emphasize how the existence of these waves near the reconnection point is found to be a universal characteristic of mini-magnetospheres, rather than being a peculiarity of Mercury.

An overview of the magnetosphere structure in the last screenshot of the simulation is shown in Figure 8.1.

8.4 Analysis of the simulation results

This simulation is used to investigate the reconnection region in the magnetotail, focusing on the influence of the magnetic field topology on the distribution of energetic particles. In addition, we observe the generation of waves close to the reconnection region, propagating parallel to the magnetic field, that have been identified as whistler waves. In this section, a summary of the results of this study is discussed. A more in-depth study can be found in Ballerini et al. (2024a), where these results are published, included in Chapter 9. Hereafter, we use the Mercury-centered Solar Orbital (MSO) reference frame.

8.4.1 Magnetic reconnection in Mercury magnetotail

The signatures of magnetic reconnection are observed at the magnetotail starting approximately from the time $t \sim 2.5 R_M/v_{sw,x}$. The location of the reconnection region, highlighted by the gray box in Figure 8.1, is compatible with the typical position observed via MESSENGER observations (Poh et al., 2017) (x_{MSM} ranging between -1.4 to -2.6 R_M). Here we analyze the region surrounding the magnetotail reconnection site before the initiation of the whistler wave to avoid the interference of wave signatures on the reconnection features. With that purpose, Fig. 8.2 shows the typical magnetic reconnection features observed in the simulation just after the onset of the reconnection (i.e. at $t = 3R_M/v_{sw,x}$). We observe here the characteristic quadrupolar out-of-plane magnetic field (panel (e)), outward escaping ion and electron jets (both in the reconnection plane, panels f and g, and the equatorial one, panels b and c), and an enhancement of the $\mathbf{E} \cdot \mathbf{J}$ quantity within the reconnection region (panels d and h).

The presence of magnetic reconnection within the simulation domain was exploited to investigate how electron spatial distribution is affected by magnetic reconnection and field topology. In particular, we observed that low-energy electrons (energies lower than 1 KeV) exhibit a nearly uniform distribution in the spatial domain, whereas energetic electrons (energies above 1 KeV) are predominantly confined within regions characterized by closed magnetic field lines on the planet. Therefore, a clear association between the magnetic topology and electron energy distribution is found in the simulation domain, explained by the fact that energetic particles remain trapped within magnetic field lines-closed regions. Instead, energetic particles in open field regions escape the simulation domain and consequently the planetary environment

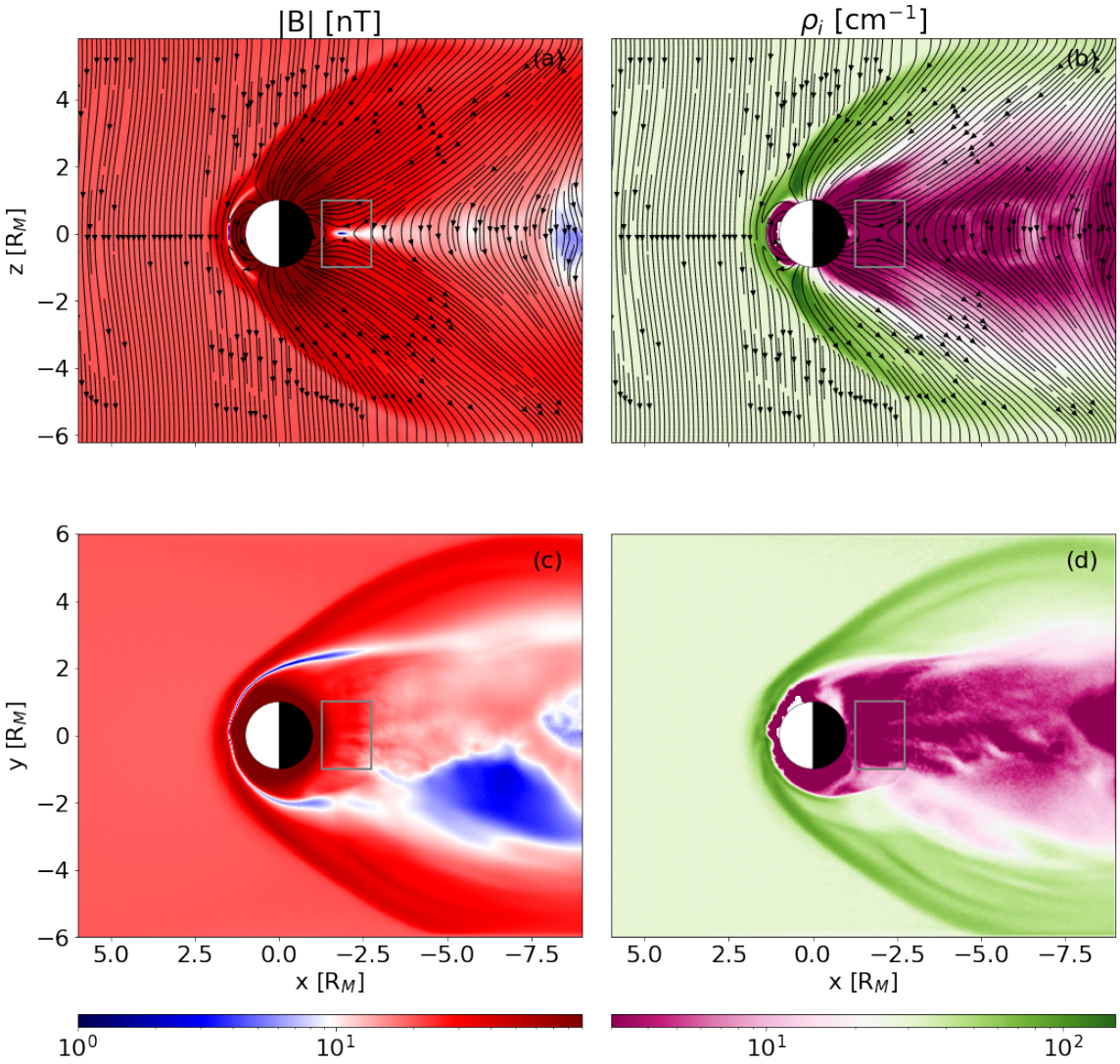

Figure 8.1: Overview of the structure of Mercury magnetosphere in the simulation. Here we show the the module of the magnetic field (left) and the ion density (right), both on the meridian plane (top, where the magnetic field lines are shown) and the equatorial plane (bottom). Both quantities are computed at time $t = 11R_M/v_{sw,x}$, the final step of the simulation.

8.5 Whistler-mode waves in Mercury's magnetotail

The most interesting result obtained from the analysis of this simulation is the development of narrow-band whistler waves in the vicinity of the magnetotail X-point region. These waves begin to develop after $t \sim 4R_M/v_{sw,x}$ and are characterized by a relatively large amplitude, a clear right-hand polarisation, and a propagation nearly parallel to the magnetic field, primarily along the separatrices. Both the magnetic and electric fields, as well as the electron current, exhibit the narrow-band nature of these waves, as shown in Figure 8.3. Nonetheless, these waves are also characterized by a strong electrostatic component $\mathbf{E}_{\parallel}$ and a parallel electron current, as illustrated in the same figure. The waves also show a minor component in the ions current, though it is considerably smaller in magnitude. These features are shown in Figure 8.3 which zooms in on the diffusion region in the x, z plane where the waves are most intense. Magnetic field lines are overplot to highlight the parallel propagation of the waves.

This wave was identified as a whistler mode through a study of the dispersion relation. To this purpose, outputs were collected with a time step of $0.5\omega_{pi,sw}^{-1} \sim 0.1\omega_{pi,loc}^{-1}$ to resolve the

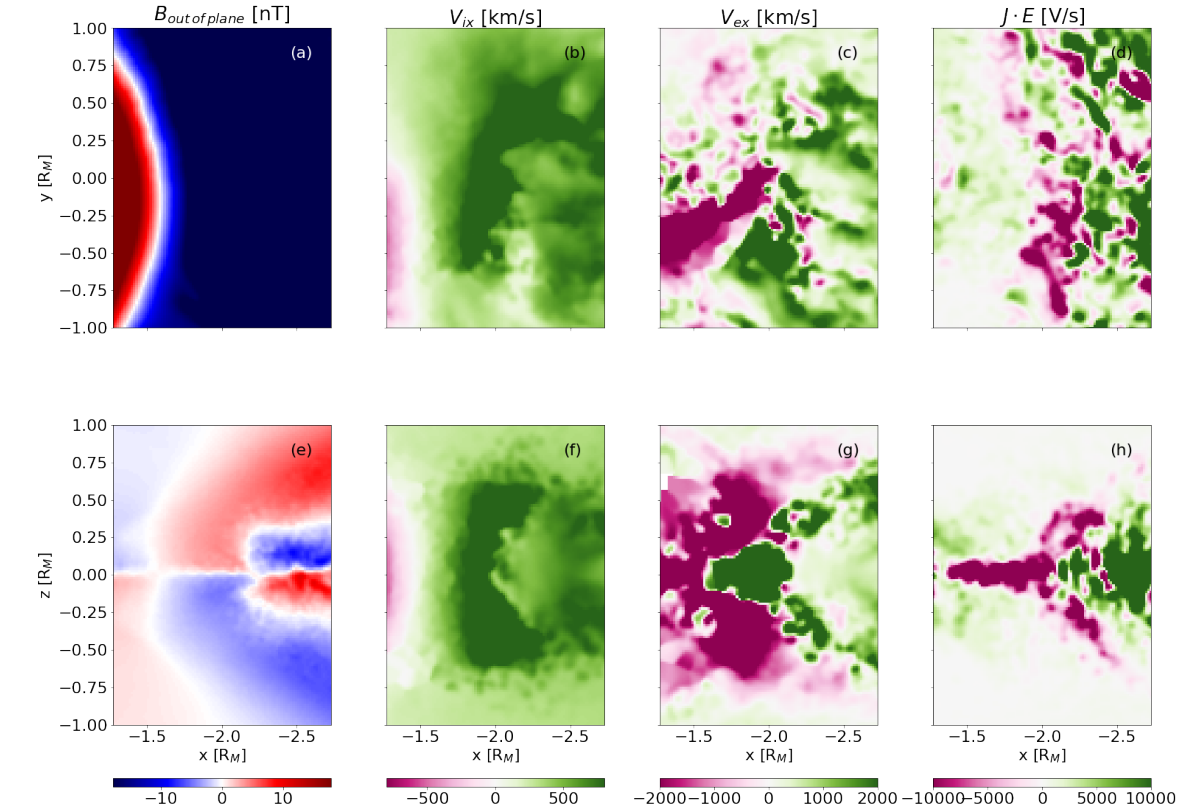

Figure 8.2: Focus on the reconnection region in the magnetotail. From left to right, the out-of-plane magnetic field component, the ion velocity, electron velocity, and $\mathbf{J} \cdot \mathbf{E}$, on the equatorial plane (top) and meridian (bottom). Data is shown at $t = 3R_M/v_{sw,x}$.

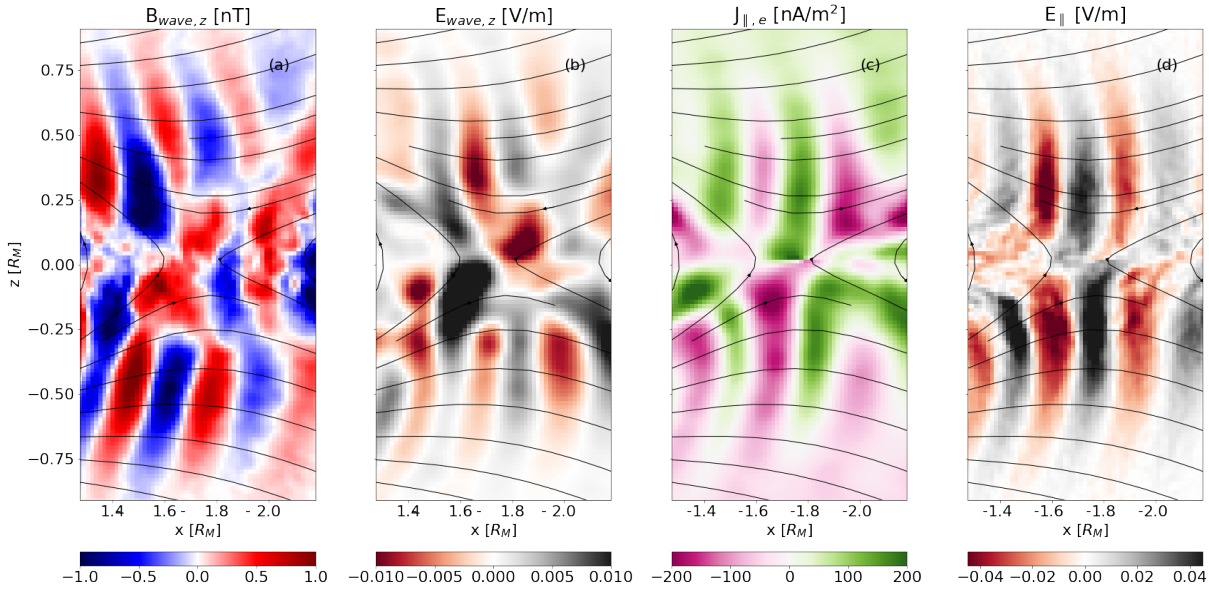

Figure 8.3: Waves components, obtained by subtracting the mean field, in the magnetic field (a), perpendicular (with respect to the magnetic field) electric field (b), parallel electron current (c) and parallel electric field (b) at $t \sim 11R_M/v_{sw,x}$. Data are shown in the plane at $y = -0.5R_M$, where the wave features are more clear.

wave oscillations adequately. Here, the indices *sw* and *loc* denote whether the frequencies are computed in the solar wind or local frame, respectively, differing due to variations in density.

The observed wave has a wave-vector $kd_{i,loc} \sim 14$ and an angular velocity $\omega \sim 0.5\omega_{ce,loc}$, where d_i is the ion inertial length and ω_{ce} is the electron cyclotron frequency. Since density and magnetic field are not constant within the region where the waves are observed, local averaging was required to compute the ratio between these quantities locally and in the solar wind. The mode's frequency range aligns with whistler waves, as shown in Figure 8.4. Here we compare the computed dispersion relation, obtained via Fourier transform in space and time, to that of whistler waves in the cold plasma limit (Equation 8.1). In this case, the "cold" hypothesis can be consider valid since the ion thermal velocity is two orders of magnitude lower than the phase velocity.

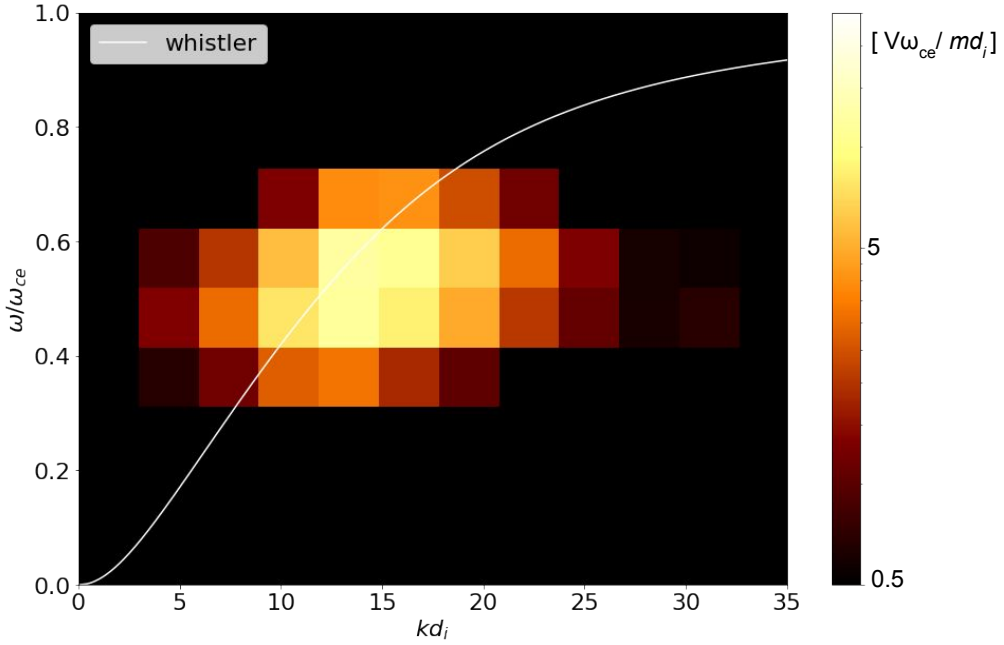

Figure 8.4: Amplitude of the Fourier transform in both space and time of the observed waves compared with the theoretical dispersion relation for whistler waves (Eq. 8.1). Quantities computed at $t \sim 11R_M/v_{sw,x}$.

Nonetheless, these waves lack the typical "chirping" feature of whistler-chorus waves (see Section 8.1.2). This could be due either to the phenomenon itself being absent or to a limit of the simulation, whose simulated temporal interval (limited by the numerical constraints) is not long enough to allow for the chirping effect to develop. Consequently, we here refer to these waves as narrow-band whistler waves.

These waves are likely to be generated by the electron temperature anisotropy. Figure 8.5 illustrates the electron anisotropy $T_{e,\parallel}/T_{e,\perp}$ (to which the wave contour is superimposed), showing that the perpendicular electron temperature exceeds the parallel temperature around the reconnection region and closer to the planet. Specifically, the red regions in the figure indicate the regions where the condition in Eq. 8.2 is met, rendering the whistler mode unstable. On the contrary, $T_{e,\parallel} > T_{e,\perp}$ is observed along the separatrices and farther from the reconnection plane. A comparison of the electron parallel thermal velocity and the whistler wave phase velocity indicates a difference of approximately two orders of magnitude, excluding the role of wave-particle interactions with the observed whistler waves in the increase of the parallel temperature. Therefore, this increase is likely due to other processes within the diffusion region, such as electron parallel acceleration.

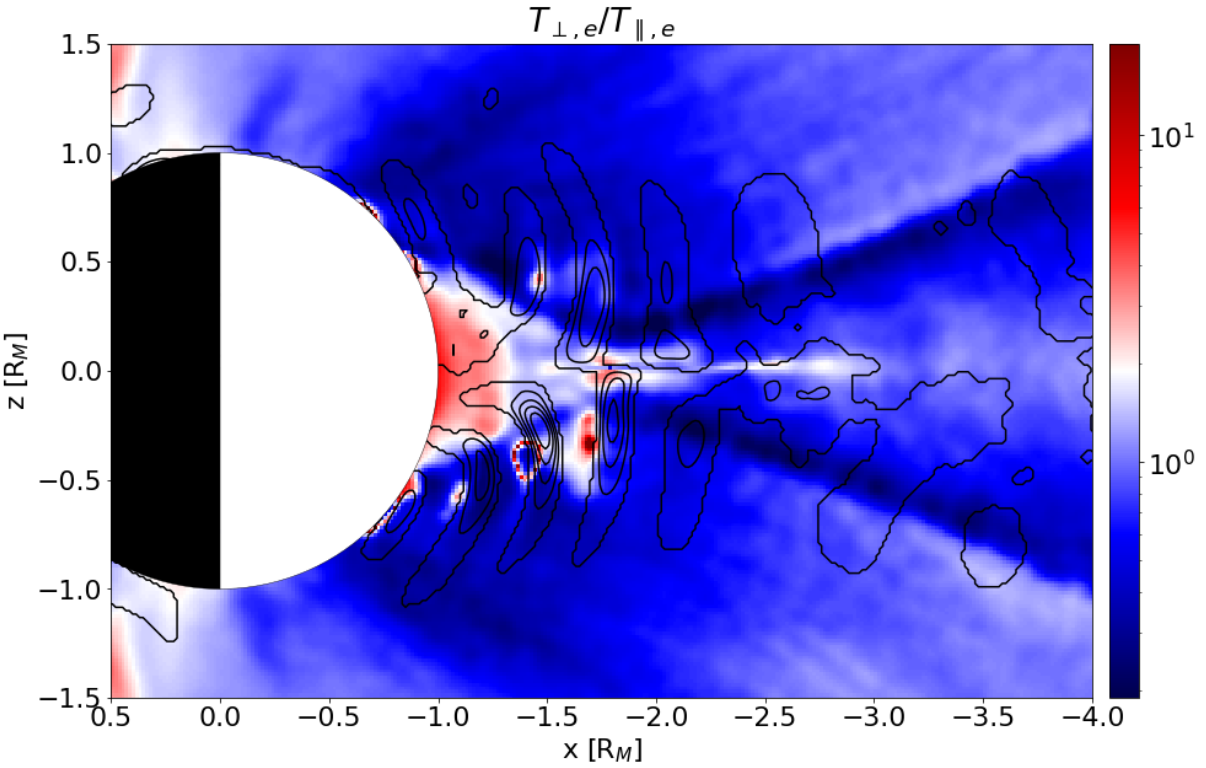

Figure 8.5: Ratio of electron perpendicular to parallel temperature in the meridian plane, for $t \sim 11 R_M/v_{sw,x}$. Black lines are the contour plots of the waves, shown to facilitate the comparison with the waves' location.

A noteworthy result of this study comes from the possibility of providing an early study of the distribution of chorus waves in the Hermean magnetosphere. Developing a comprehensive distribution map holds significant importance for understanding the energetic electron loss mechanism, as discussed by Ozaki et al. (2023). Figure 8.6 shows the location of these waves in our simulation, showing a low latitude propagation with respect to the equatorial plane, with altitudes ranging from -1 to 1 RM. These waves are distributed almost symmetrically with respect to the equatorial plane, with a slight bias toward the dawnside [6]. However, this map is likely influenced by the purely southward IMF configuration that is used in the simulation. A more comprehensive map would require investigation of the influence of upstream solar wind properties, and specifically the IMF direction, on the location and amplitude of these waves. This analysis is left as future work.

Consequences of Radius Rescaling

In this section, we discuss the implications of rescaling the planet radius, as introduced in Section 1, on the results discussed above.
Concerning the magnetic reconnection, the impact of this rescaling has been previously addressed in Lavorenti et al. (2022) and Lavorenti et al. (2023). By decreasing the planet's radius, the ion and electron diffusion region in the tail moves closer to the planetary surface. Therefore, we find that in this simulation the ion diffusion region is marginally displaced from the planet, while the electron diffusion region is more largely separated. Therefore, we expect that, while

[6] Current observations (Ozaki et al., 2023) have detected whistler waves on Mercury's dawn side, while observations in the magnetotail region are still pending. These observations were possible thanks to the PWI measurements, enabling for the first time to observe the electric fields, plasma waves, and radio waves in the Hermean magnetosphere.

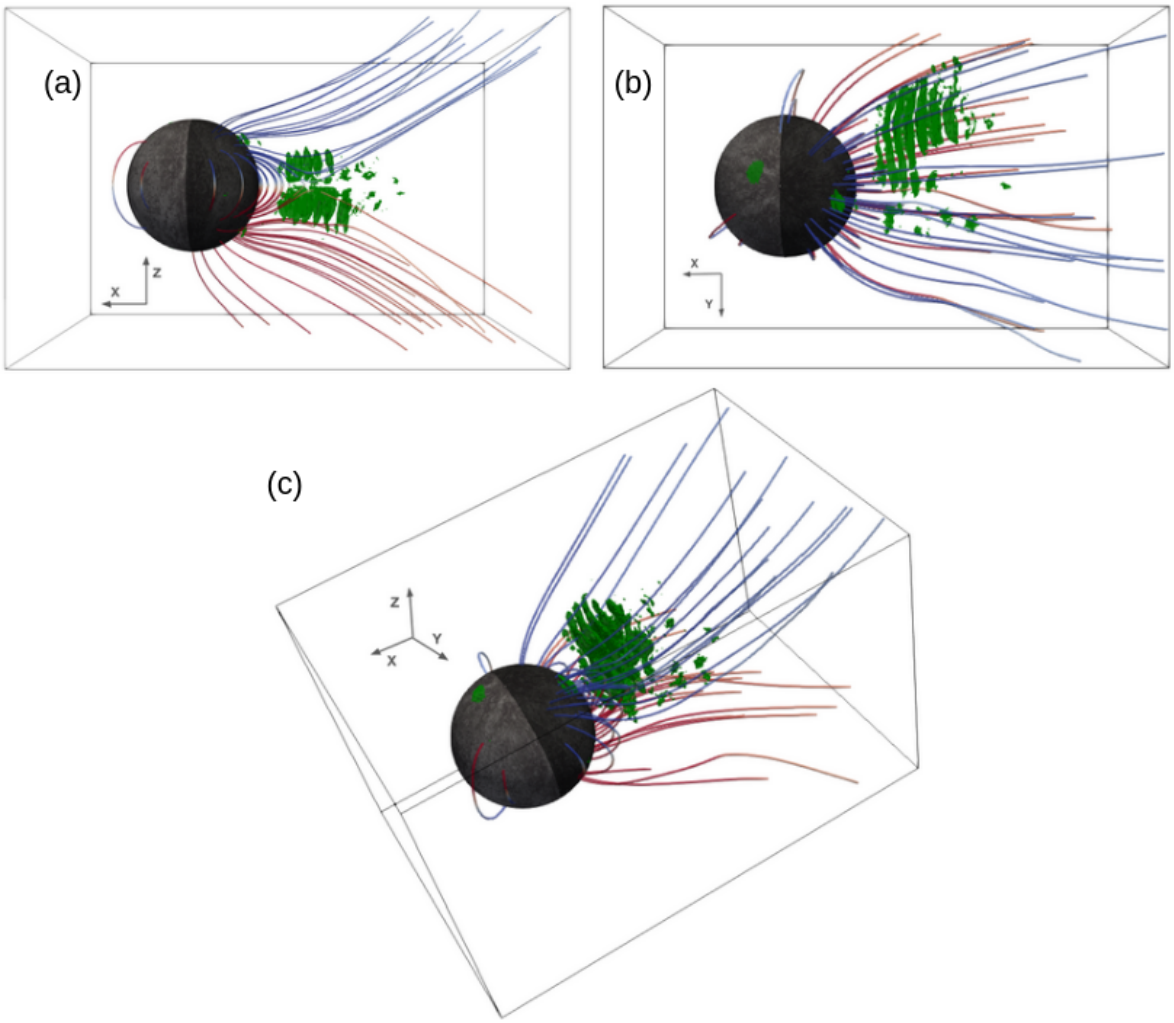

Figure 8.6: Locations of whistler waves, in green, within the simulation domain at $t \sim 11 R_M/v_{sw,x}$. The location is obtained by showing the cells for which the parallel component of the electric field is above a threshold of 26 mV/m. (a), (b) and (c) shows the distribution from different perspectives.

electron dynamics remain unaffected by the rescaling, the ion should be, at least partly, affected. Notably, the high-energy electron signatures, discussed above, remain valid.

The influence of planet scaling on the whistler-waves features was analysed by conducting an additional simulation (referred hereafter to as *Run2*) using the iPIC3D solver. In *Run2*, the planet radius was furtherly reduced to $R_{M,2} = 2.75 d_i$, half of the radius used in the simulation discussed before. The magnetic dipole field of *Run2* is scaled to maintain the same surface magnetic field strength, thereby ensuring the relative magnetosphere shape, with respect to the planetary radius, to remain equal with the initial simulation. This analysis was crucial for distinguishing which properties are not affected by this scaling. Specifically, in *Run2* we observe the same waves to develop as in the initial simulation. By comparing the wave modes between the two simulations, we found that both the dispersion relation and the wave features do not differ, allowing us to conclude that the rescaling does not influence the wave properties. However, the scaled distance between the reconnection region, where the waves originates, and the planet could affect the spatial distribution of these waves. This phenomenon is not observed in *Run2* and it is left for future work since it requires big computational effort to increase the planetary radius, even of a factor 2.

Conclusions and Future Works

The primary objective of this thesis is the study of the Earth's magnetopause. Specifically, we focused on those regions where the magnetopause presents one-dimensional and stationary features (representing the majority of the structure), where the magnetopause can be modeled as a discontinuity. These regions are generally modeled by using the State-of-the-Art Classic Theory of Discontinuities (CTD). However, *in situ* data show a disagreement with this theory, whose physical assumption should therefore be questioned when describing the magnetopause. This theory was used as a starting point to enhance our understanding of the magnetopause, allowing us to study the role of the pressure tensor on the magnetopause equilibrium. The primary question that was addressed is: why CTD fails in describing *in situ* observations? To investigate this, we have analyzed complementary data from the Magnetospheric Multiscale (MMS) mission and numerical simulations. In particular, we have exploited the high-resolution data from four satellites, allowing us to calculate separately the spatial and temporal gradients.

The first part of this thesis is focused on the development of a new tool allowing us to obtain an accurate determination of the normal direction of the magnetopause from *in situ* measurements. A precise estimation of the normal vector is crucial for this study since it allows us to separate normal and tangential components of any physical quantities at the boundary. Theoretically, we have shown that the the normal transport across the magnetopause is of fundamental importance for understanding the boundary properties, particularly the magnetic variations in the tangential plane (hodograms). As these normal transport, carried by B_n and u_n, is much smaller than the corresponding tangential values, a too large uncertainty on the normal direction would distort their estimation. On the contrary, a good estimation of this quantity will enable one to establish which terms, in the general expression of the transported fluxes, are relevant and not included in the state-of-the-art models. The tool presented here, namely the Gradient matrix Fitting (GF2) tool, is derived from the Minimum Directional Derivative (MDD) tool, one of the most common and accurate techniques hitherto. Both tools are gradient-based since they estimate the normal vector from the gradient matrix of a given vector (typically the magnetic field). They provide an estimation of the normal direction at each time step, requiring multi-satellite measurements while allowing for the study of local variations of the normal of the magnetopause. The GF2 tool incorporates a fitting procedure allowing to impose physical constraints directly within the algorithm, such as $\nabla \cdot \mathbf{B} = 0$ in the case of magnetic field measurements. This feature is different with respect to what done in MDD, where physical constraints are checked at posteriori. The GF2 tool was tested on an MMS magnetopause crossing on the 28th of December 2015, showing comparable results with other state-of-the-art methods. However, a more accurate test of this tool can be only done with numerical simulation data.

To this end, complementary to *in situ* data analysis, we have carried out a numerical study of the magnetopause using global simulations (*i.e.* simulations that included the entire structure of the magnetosphere). Although these simulations offer a lower resolution of the magnetopause compared to local simulations (*i.e.* in simulations where the magnetopause is treated as a current sheet), they provide a higher degree of realism necessary for our study. Specifically, we have used the Menura solver, a hybrid-PIC code, to simulate an Earth-like magnetosphere and to test the GF2 tool by comparing it with MDD, as for *in situ* data. While a quantitative study would require a comparison to an exact calculation of the normal vector to determine the accuracy, several factors prevent the calculation of a "real" normal direction. The main ones are the unavoidable two-dimensional nature at short scales and the uncertainties in calculating the matrix gradient from finite differences that affect the reliability in calculating the normal direction.

This test shows that, while the two methods provide the same result in regions with a one-dimensional magnetopause, the GF2 tool, unlike MDD, effectively enables to separate the major and minor directions of gradients, the too-small scales being filtered out in both directions, in regions where the magnetopause exhibits two-dimensional features. However, higher-resolution simulations are needed for an exact quantification of the performance of the GF2 tool. This requires substantial computational resources, making such study currently infeasible with a global simulation approach. A possible analysis could be done with (less realistic) local simulations. Such a study is left as a future work.

GF2 was then applied to study the magnetopause structure by using the MMS crossing of the 28th of December 2015, used previously to test the GF2 tool. Specifically, this crossing revealed properties not described by CTD, such as simultaneous compression and rotation, and a linear magnetic field hodogram in the tangential plane of the discontinuity. The analysis have shown that the divergence of the ion pressure tensor plays a key role in magnetopause equilibrium, violating the isotropy hypothesis of CTD. We show that this is due to finite Larmor radius (FLR) effects responsible for making the pressure tensor non-gyrotropic. To test this feature, two non-gyrotropy indices were exploited confirming a significant, albeit small, non-gyrotropy in the ion pressure tensor. In addition, we have shown that the direction of non-gyrotropy differs from that of the magnetic field for this crossing, aligning approximately with the direction $\mathbf{n}_{mean} \times \mathbf{B}$.
To generalize these results, a statistical study was conducted alongside the case-crossing analysis. We selected a dataset of 146 magnetopause crossings showing one-dimensional characteristics to establish a robust statistical foundation. For each of these crossings, we studied the hodogram of the magnetic field in the tangential plane by classifying its shape. This analysis revealed that over one-third of the selected crossings are in disagreement with CTD, indicating that FLRs at the magnetopause are significant, even if not predominant. Even though the statistical study confirms the result obtained from the case crossing analysis, a more complete analysis would benefit from the study of the pressure tensor calculated in numerical simulations. In particular, we could exploit the same simulation used to test the GF2 tool. However, due to time constraints, we were unable to conduct this analysis within this thesis. This study is left for future research. Moreover, an increase in the number of particles per cell should be required to enhance the accuracy of pressure tensor determination. This increase necessitates additional computational resources, potentially requiring a trade-off with spatial resolution to obtain computational feasibility. A detailed study will be conducted in the future to identify the optimal balance between computational cost and resolution accuracy. Overall, this study underscores the relevance of FLR effects at the magnetopause, providing a framework for future investigations. These efforts will enhance our understanding of the complex dynamics at the magnetopause, contributing to the broader field of space plasma physics.

In addition, GF2 was used to compare the geometrical properties of magnetic and ion structures at the magnetopause. Specifically, we exploited the dataset of crossing used for the statistical analysis and compared the normals obtained from magnetic field and ion flux measurements. This analysis showed that most of the crossings present similar structures, with 56.2 % of the crossings having normals differing less than 20 degrees, while a part of the dataset exhibited significant differences, likely due to strong non-stationarities. The role of the non-stationarities in the ion flux is not discussed within this manuscript, but it is further discussed in the paper. Again, numerical simulations are crucial for contextualizing these results. To this end, the Menura numerical simulation was exploited showing comparable results: in regions showing one-dimensional ion flux structures, the normals obtained from the magnetic field and ion flux are close (with differences of the order of 10 degrees). The predominant part of the structure shows

two-dimensional features for the ion mass flux, showing ion flux normals up to ninety degrees from the magnetic ones. A more accurate study, extending to a larger amount of magnetopause regions should allow to quantify this result and further understand the results obtained from the statistical study.

In addition to the Earth's magnetopause study, a numerical investigation of Mercury's magnetosphere using the iPIC3D solver was conducted. The study focused on Mercury's magnetosphere for two primary reasons: i) to prepare for the arrival of the JAXA/ESA BepiColombo mission to Mercury and *ii*) to exploit the full-kinetic description of the mini-magnetosphere of Mercury to gain insights of the global characteristics of the Earth's one. Due to current computational constraints, simulating the Earth's magnetosphere while capturing kinetic scales remains not feasible computationally without rescaling.
The iPIc3D simulation was exploited to analyze the development of magnetic reconnection in the magnetotail and related dynamics in the magnetotail, with a particular focus on narrow-band whistler waves that are observed to originate around the nightside reconnection region. This result is noteworthy since whistler-mode chorus waves have been detected during the two flybys of Mercury performed by BepiColombo. While these waves are observed in the localized dawn sector, measurements in the magnetotail are still lacking. These observations did not indeed provide the distribution of these waves at Mercury's magnetosphere. Our analysis brings an answer to this question. However, a completely southward solar wind magnetic field was used in the simulation performed. To understand how this assumption affects the wave distribution, further numerical simulations with varying solar wind magnetic field orientations are necessary and planned for future work. Additionally, further numerical simulations are required to test the influence of the radius rescaling applied in this simulation on the wave features and dispersion relation.

In summary, this research allowed for a first analysis of whistler-mode waves within a global simulation, setting the stage for future studies and the upcoming observations from the BepiColombo mission. A further investigation with different simulation parameters will be crucial for advancing our knowledge of the Mercury magnetosphere.
The results discussed in this thesis are presented in two papers: "Role of FLR effects in magnetopause equilibrium," accepted by the Journal of Plasma Physics, and "Whistler-mode waves in the tail of Mercury's magnetosphere: a numerical study," accepted by Astronomy & Astrophysics. Additionally, I actively participated with the Menura team in the execution and analysis of the first simulation to study the consequences of solar wind turbulence on an Earth-like planet. This analysis is summarized in a paper "Impact of solar wind turbulence on the Earth's bow shock" which I co-authored and that should be submitted in the coming months to Astronomy & Astrophysics.

9 Papers

Contents

9.1 Ballerini et al (2024b)

[1]

[1]Section 7 contains a minor imprecision. The term $\nabla \cdot \mathbf{P}_e/nq$ is mistakenly referred to as $\nabla \cdot \mathbf{P}_e$ in both the text and Figure 6. However, the term depicted in the figure and discussed in the text is correct.

Role of FLR effects in magnetopause equilibrium

G. Ballerini† [1,2] and L. Rezeau[1] and G. Belmont[1] and F. Califano[2]

[1]LPP, CNRS/Sorbonne Université/Université Paris-Saclay/Observatoire de Paris/Ecole Polytechnique, Institut Polytechnique de Paris, Paris, France

[1]Dipartimento di Fisica E. Fermi, University of Pisa, Italy

(Received xx; revised xx; accepted xx)

The Earth magnetopause, when sufficiently plane and stationary at a local scale, can be considered as a "quasi-tangential" discontinuity, since the normal component of the magnetic field B_n is typically very small but not zero. Contrary to observations, the "Classic Theory of Discontinuities" (CTD) predicts that rotational and compressional jumps should be mutually exclusive in the general case $B_n \neq 0$, but allows only one exception: the tangential discontinuity provided that B_n is strictly zero. Here we show that Finite Larmor Radius (FLR) effects play an important role in the quasi-tangential case, whenever the ion Larmor radius is not fully negligible with respect to the magnetopause thickness. By including FLR effects, the results suggest that a rotational discontinuity undergoes a change comparable to the change of a Shear Alfvén into a Kinetic Alfvén wave when considering linear modes. For this new kind of discontinuity, the co-existence of rotational and compressional variations at the magnetopause does no more imply that this boundary is a strict tangential discontinuity, even in 1D-like regions far from X-lines if any. This result may lead to important consequences concerning the oldest and most basic questions of magnetospheric physics: how can the magnetopause be open, where and when? The role of FLR being established theoretically, the paper then shows that it can be proved experimentally. For that, we make use of MMS data and process them with the most recent available 4 spacecraft tools. First, we present the different processing techniques that we use to estimate spatial derivatives, such as $grad(B)$ and $div(P)$, and the magnetopause normal direction. We point out why this normal direction must be determined with extremely high accuracy to make the conclusions unambiguous. Then, the results obtained by these techniques are presented in a detailed case study and on a statistical basis.

Introduction

In space physics, there is a natural tendency of the medium to self-organize into distinct cells, separated by thin layers. This behavior can be observed at very different scales. Notable examples are planetary magnetospheres, which are bubbles in the solar wind stream and which are separated from it by bow shocks and magnetopauses (Parks 2019; Kivelson & Russell 1995; Belmont *et al.* 2014). The interaction of the solar wind with unmagnetized bodies such as comets also produces similar bubbles (Coates 1997; Bertucci 2005). The Solar System itself is a bubble in the flow of the local interstellar cloud, and it is separated from it by the heliopause and at least one shock ("termination shock") (Lallement 2001; Richardson *et al.* 2022). Similar cells and thin layers can also form spontaneously, far from any boundary condition as in the context of a turbulent medium (Frisch 1995; Chasapis *et al.* 2015).

Among all these thin layers, the terrestrial magnetopause plays a particular role. This region has been explored by a large number of spacecraft since the beginning of the space era, up to the most recent multi-spacecraft missions as Cluster (Escoubet *et al.* 1997, 2001) and MMS (Burch & Phan 2016), allowing for a detailed description of its properties. In addition, due to a very small

† Email address for correspondence: giulio.ballerini@lpp.polytechnique.fr

normal component of the magnetic field with respect to the magnetopause (defined $B_n = \mathbf{B} \cdot \mathbf{n}$ where $\mathbf{B}$ is the magnetic field and $\mathbf{n}$ the magnetopause's normal) it can be identified as a "quasi-tangential" layer. This feature is a direct consequence of the frozen-in property that prevails at large scales, on both sides of the boundary, almost preventing any penetration of magnetic flux and matter between the solar wind and the magnetospheric media (both of them being magnetised plasmas). By large scales here we refer to the fluid scales where an ideal Ohm's law holds, as in the ideal magnetohydrodynamic (MHD) regime. However, small departures from a strict separation between the two plasmas do exist, at least locally and for a given time interval, and they are known to have important consequences for all the magnetospheric dynamics: substorms, auroras, etc (McPherron 1979; Tsurutani *et al.* 2001).

Knowing when and where plasma injection occurs through the magnetopause has been one of the hottest subjects of research since decades (Haaland *et al.* (2021) and references therein, Lundin & Dubinin (1984); Gunell *et al.* (2012); Paschmann *et al.* (2018*a*)). The largest consensus presently considers the equilibrium state of the boundary, valid on the major part of its surface, as a tangential discontinuity, with a strictly null B_n, while plasma injection is allowed only around a few reconnection regions, where the gradients characterizing the layer present 2D features. For that purpose, many studies have been carried out to understand where magnetic reconnection occurs the most (Fuselier *et al.* 2011; Trattner *et al.* 2021). Moreover, the conditions under which the magnetopause opens due to magnetic reconnection has been studied theoretically (Swisdak *et al.* 2003) and experimentally (Gosling *et al.* 1982; Paschmann 1984; Phan *et al.* 2000; Fuselier *et al.* 2011; Vines *et al.* 2015). The results of the present study may allow reconsidering this paradigm by questioning the necessity of a strictly tangential discontinuity for the basic equilibrium state.

In the whole paper hereafter, we will call one-dimensional all geometries in which the gradients of all parameters are in the same direction $\mathbf{N}$. In this sense, a plane magnetopause with not tangential gradient is said here to be 1D, while it would be considered 2D if considering real space instead of k space.

1. Classic Theory of Discontinuities

At every layer, the downstream and upstream physical quantities are linked by the fundamental conservation laws: mass, momentum, energy and magnetic flux (Landau & Lifshitz 1987). The simplest case occurs whenever the number of conservation laws is equal to the number of parameters characterizing the plasma state. When this condition is met, the possible downstream states are uniquely determined as a function of the upstream state, regardless of the (non-ideal) physics at play within the layer. In particular, it is possible to describe pressure variations without any closure equation. In this case, the jumps of all quantities are determined by a single scalar parameter (namely the "shock parameter" in neutral gas).

We refer hereafter to the "Classic Theory of Discontinuities" (CTD) as for the theory corresponding to this condition, which is used both for neutral media and (magnetized) plasmas. CTD is characterized by the following simplifying assumptions: a stationary layer, 1D variations, and isotropic pressure on both sides. For plasmas, the additional assumption of an ideal Ohm's law on both sides is considered (Belmont *et al.* 2019).

In CTD the conservation laws provide a system of jump equations between the upstream and downstream physical quantities, namely the Rankine-Hugoniot conditions in neutral media and generalized Rankine-Hugoniot conditions in plasmas.

The sets of equations used to compute the linear modes in hydrodynamics (HD) and MHD are similar to these jump equations system. simply because the HD and MHD models rely on the same conservation laws as Rankine-Hugoniot and generalized Rankine-Hugoniot respectively

A direct consequence is that many properties are shared by the solutions of the two types of systems: linear modes and discontinuities. For a neutral medium, the linear sound wave solution corresponds to the well-known sonic shock solution, while for a magnetized plasma, the two magnetosonic waves correspond to the two main types of MHD shocks: fast and slow. However, an additional discontinuity solution, the intermediate shock, has no linear counterpart. The intermediate shock presents a reversal of the tangential magnetic field through the discontinuity, which is not observed neither in the fast nor in the slow mode. Furthermore, a non-compressional solution exists in both types of systems, represented by the shear Alfvén mode for linear MHD, and by the "rotational discontinuity" solution for the generalized Rankine-Hugoniot system.

Focusing on magnetized plasma physics, CTD leads to distinguish compressive and rotational discontinuities. An important feature of these solutions is that the compressional and rotational solutions are mutually exclusive: the shock solutions are purely compressional, without any rotation of the tangential magnetic field (this is called the "coplanarity property"), while the rotational discontinuity does imply such a rotation but without any variation of the magnetic field amplitude and without any compression of the particle density (Fig.1). This distinction persists whatever the fluxes along the discontinuity normal, even when the normal components u_n and B_n of the velocity and the magnetic field are arbitrarily small. The only exception is the "tangential discontinuity" when both normal fluxes are strictly zero. This solution would correspond, for the magnetopause, to the case without any connection between solar wind and magnetosphere. It appears as a singular case since the tangential discontinuity, with $B_n = 0$, is not the limit of any of the general solutions with $B_n \neq 0$. While the limit always implies two solutions, one purely rotational and the other purely compressional, the singular solution $B_n = 0$ only provides one solution where the two characters can coexist.

In the solar wind, discontinuities are routinely observed and several authors have performed statistics for a long time to determine the proportion of the different kinds of discontinuities, mainly focusing on the tangential and rotational ones. They conclude that in most cases tangential discontinuities (*i.e.* with B_n small enough to be barely measurable) are the most ubiquitous (see Colburn & Sonett (1966), for a pioneering work in this domain and Neugebauer (2006); Paschmann *et al.* (2013); Liu *et al.* (2022), and references therein, for more recent contributions). In these studies, rotational discontinuities are identified only when B_n is large enough. However, many discontinuities present features that are typical of both rotational and tangential discontinuities and are classified as "either" of the two. Extending these studies in the range of small B_n, where all discontinuities are not necessarily "tangential discontinuities" in the CTD sense, requires the study of the quasi-tangential case.

2. The Earth's magnetopause

Thanks to *in-situ* observations, the Earth's magnetopause has a pivotal role in testing the discontinuity theories. Indeed, the Earth's magnetopause boundary exhibits, over its entire surface, both a rotation of the magnetic field (Sonnerup & Ledley 1974) and a density variation (Otto 2005) since it is the junction of two media, the magnetosheath and the magnetosphere where the magnetic field and the density are different (Dorville *et al.* 2014).

As stated above, the usual paradigm is that the magnetopause is always a tangential discontinuity and that it becomes "opens" only exceptionally at a few points where the boundary departs from one-dimensionality due to magnetic reconnection. Does it mean that it justifies the very radical hypothesis of a magnetopause nearly completely impermeable to mass and magnetic flux, with strictly null B_n and u_n and quasi-independent plasmas on both sides (apart from the normal pressure equilibrium)? From a theoretical point of view, it is clear that the singular limit from $B_n \simeq 0$ to $B_n = 0$ remains to be solved. From an experimental point of view, if the components B_n and u_n are known to be always very small, the observations can hardly

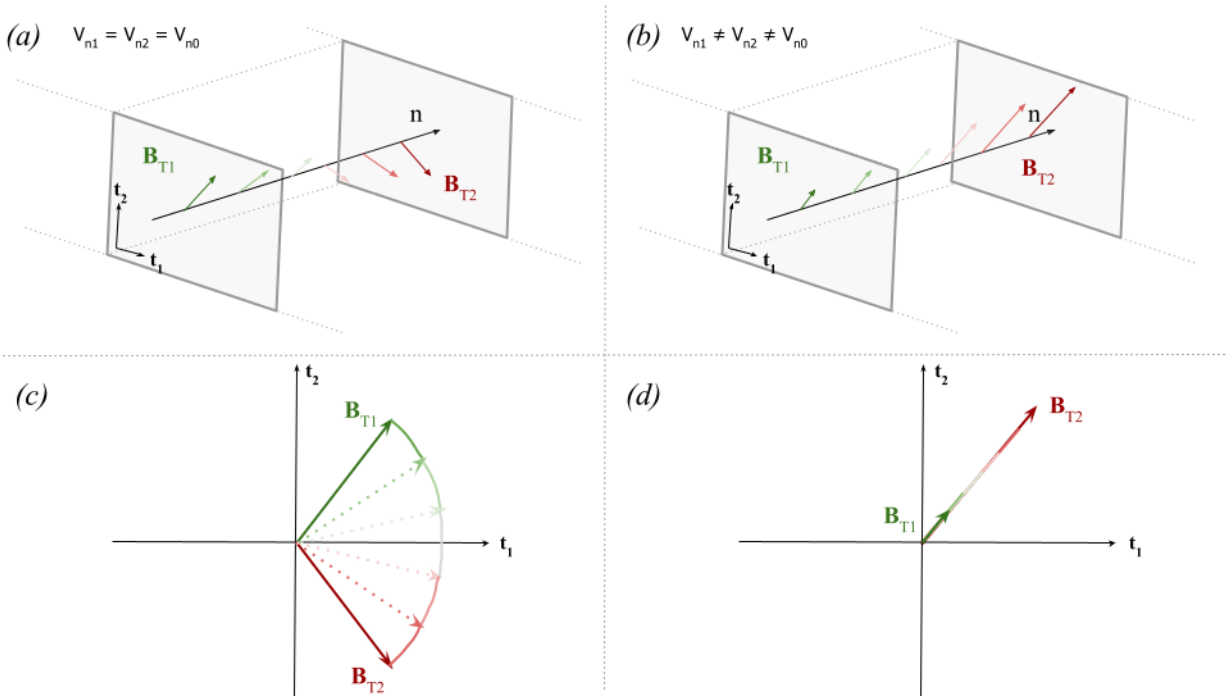

FIGURE 1. Cartoon showing the different variations of B between a rotational discontinuity (left) and a compressive one (right). The top panel shows in 3D the variation of B inside the magnetopause plane; the bottom panel shows the hodogram in this tangential plane: a circular arc for the rotational discontinuity and a radial line for shocks.

distinguish between $B_n \simeq 0$ and $B_n = 0$ because of the uncertainties, due to the fluctuations and the limited accuracy in determining the normal direction (Rezeau *et al.* 2018; Haaland *et al.* 2004; Dorville *et al.* 2015*b*).

The results of the present paper will question the above paradigm. We will show theoretically and experimentally that CTD fails at the magnetopause and that rotation and compression can actually coexist with finite B_n and u_n, even in the 1D case. Such a paradigm change may be reminiscent of a similar improvement in the theoretical modeling of the magnetotail in the 70's studies (Coppi *et al.* (1966); Galeev (1979); Coroniti (1980) and references therein). In that case the authors demonstrated that even a very weak component of the magnetic field across the current layer was sufficient to completely modify the stability properties of the plasmasheet, so that the finite value of B_n had to be taken into account, contrary to the pioneer versions of the tearing instability theories.

3. The role of pressure

In CTD the separation between the compressional and rotational properties of the discontinuities comes from only two equations projected on the tangential plane. These equations are the momentum equation and the Faraday - Ohm's law, that read:

$$\rho \frac{d\mathbf{u}}{dt} + \nabla \cdot \mathbf{P}_i + \nabla \cdot \mathbf{P}_e = \mathbf{J} \times \mathbf{B} \tag{3.1}$$

$$\nabla \times \mathbf{E} = -\frac{\partial \mathbf{B}}{\partial t}$$

$$\text{where} \quad \mathbf{E} = -\mathbf{u} \times \mathbf{B} + \frac{1}{ne}\mathbf{J} \times \mathbf{B} - \frac{1}{ne}\nabla \cdot \mathbf{P}_e \tag{3.2}$$

where $\mathbf{B}$ is the magnetic field and $\mathbf{u}$ is the flow velocity in a reference frame where the layer is steady.

Considering one-dimensional gradients along the normal direction **n**, neglecting the non-ideal terms in Ohm's law and integrating across the layer, these two equations, projected on the tangential plane, give:

$$\rho_2 u_{n2}\,\mathbf{u}_{t2} - B_{n2}\,\mathbf{B}_{t2}/\mu_0 = \rho_1 u_{n1}\,\mathbf{u}_{t1} - B_{n1}\,\mathbf{B}_{t1}/\mu_0 \tag{3.3}$$

$$B_{n2}\,\mathbf{u}_{t2} - u_{n2}\,\mathbf{B}_{t2} = B_{n1}\,\mathbf{u}_{t1} - u_{n1}\,\mathbf{B}_{t1} \tag{3.4}$$

Due to the divergence free equation, the values B_{n1} and B_{n2} are equal and will be written as B_n without index in the following. Similarly, $\rho_1 u_{n1}$ and $\rho_2 u_{n2}$ are equal because of the continuity equation and will be simply noted ρu_n in the following. Here, the indices n and t indicate the projection along the normal and in the tangential plane, respectively, while indices 1 and 2 indicate the two sides of the discontinuity. It is important to note that, in CTD, the pressure divergence terms do not appear in Eq.(3.3) because of the assumption done in this theory that the pressure is isotropic on both sides so that their integration gives terms of the form $(p_2 - p_1)\mathbf{n}$, with no component in the tangential plane.

We see that all terms in these two equations are proportional to B_n or u_n, so that any non-ideal term, even small, can become dominant when these two quantities tend to zero (if these non-ideal terms do not tend to zero at the same time). As the distinction between compressional and rotational character fully relies on this system of equations, this evidences the necessity of investigating the quasi-tangential case for resolving the usual singularity of the tangential discontinuity. We note that the LHS and RHS of equation 3.4 can be put equal to zero by choosing the "De Hoffmann-Teller" tangential reference frame where the electric field is zero (Belmont *et al.* 2019). However, this choice, even if it can simplify some calculations, is not necessary here. Finally, the variables $\mathbf{u}_t$ can be eliminated from the system by a simple linear combination of the two equations, leading to:

$$(u_{n2} - u_{n0})\mathbf{B}_{t2} = (u_{n1} - u_{n0})\mathbf{B}_{t1} \tag{3.5}$$

where

$$u_{n0} = \frac{B_n^2}{\mu_0 \rho u_n} = \text{cst} \tag{3.6}$$

Equation (3.5) leads to the distinction between shocks, where the tangential magnetic fields on both sides are collinear (but with different modules), and rotational discontinuities, where the terms inside the brackets must be equal to zero. Rotational discontinuities correspond to a propagation velocity equal to the normal Alfvén velocity, and imply $u_{n1} = u_{n2} = u_{n0}$, and therefore an absence of compression of the plasma.

As previously stated, the separation between the compressional and rotational characters mainly derives, in CTD, from the assumption of isotropic pressures on both sides, which prevents the pressure divergences to have tangential components. When the isotropic hypothesis is relaxed (Hudson 1971), the set of conservation equations is no longer sufficient to determine a unique downstream state for a given upstream one. As a consequence, the global result depends on the non-ideal processes occurring within the layer. In addition to anisotropy effects, Finite Larmor Radius (FLR) effects can be expected to break the gyrotropy of the pressure tensor around **B** in the case of thin boundaries between different plasmas. This means that the main effect that explains departures from CTD comes from the tangential component of the divergence of the pressure tensor, which must be taken into account in the momentum equation. On the other hand, the non-ideal effects related to the generalized Ohm's law are negligible, at least in the examples shown in this paper. The possible types of discontinuities in an anisotropic plasma have been discussed in several papers long time ago (Lynn 1967; Abraham-Shrauner 1967; Chao 1970; Neubauer 1970), and the present paper improves the analysis in the light of the new experimental possibilities given by the MMS measurements.

When the dynamics drives the conditions for the pressure tensor to become anisotropic (and *a fortiori* in the non-gyrotropic case) the $\nabla \cdot \mathbf{P}$ term comes into play linking upstream and downstream quantities. Considering the "simple" anisotropic case, *i.e.* keeping the gyrotropy around $\mathbf{B}$, it has been shown (Hudson 1971) that the $\nabla \cdot \mathbf{P}$ term then just introduces a new coefficient:

$$\alpha = 1 - \frac{p_{\parallel} - p_{\perp}}{B^2/\mu_0} \tag{3.7}$$

This coefficient has been interpreted as a change in the Alfvén velocity $V'^2_{An} = \alpha V^2_{An}$, but it appears more basically as a change in Eq.(3.5):

$$(u_{n2} - \alpha_2 u_{n0})\mathbf{B}_{t2} = (u_{n1} - \alpha_1 u_{n0})\mathbf{B}_{t1} \tag{3.8}$$

This equation shows that, in this simple anisotropic case, coplanar solutions still exist ($\mathbf{B}_{t2}$ and $\mathbf{B}_{t1}$ are collinear), but that whenever α_2 is not equal to α_1, the equivalent of the rotational discontinuity now implies compression:

$$u_{n2} \neq u_{n1} \qquad \text{if} \qquad \alpha_2 \neq \alpha_1 \tag{3.9}$$

Since $u_{n2} = \alpha_2 u_{n0}$ and $u_{n1} = \alpha_1 u_{n0}$. The variation of u_n explains why the modified rotational discontinuity can be "evolutionary" (Jeffrey & Taniuti 1964), the non linear steepening being counter-balanced at equilibrium by non-ideal effects for a thickness comparable with the characteristic scale of these effects.

There is actually no additional conservation equation available that would allow the jump of the anisotropy coefficient α to be determined. Consequently, there is no universal result that gives the downstream state as a function of the upstream one, regardless of the microscopic processes going on within the layer. This remains valid for the full anisotropic case, with non-gyrotropy. As soon as the ion Larmor radius ρ_i and the ion inertial length d_i are not fully negligible with respect to the characteristic scale L of the layer, kinetic effects, and in particular FLR effects, which make the pressure tensor non-gyrotropic, must be taken into account to describe self-consistently the internal processes. Then, the effect of the divergence of the pressure tensor is no longer reduced to adding a coefficient α since its tangential component is no longer collinear with $\mathbf{B}_t$. Such effect has been already reported and analyzed in the context of magnetic reconnection (Aunai *et al.* 2013, 2011) and in kinetic modeling of purely tangential layers (Belmont *et al.* 2012; Dorville *et al.* 2015*a*). It has been also investigated in the case of linear modes where they are responsible for the transition from shear Alfvén into Kinetic Alfvén Wave (Hasegawa & Uberoi 1982; Belmont & Rezeau 1987; Cramer 2001). On the other hand, it has never been introduced in the context of quasi-tangential discontinuities.

If a simple anisotropy preserving gyrotropy around $\mathbf{B}$ can be straight fully taken into account for modeling the pressure tensor and using it in fluid equations, introducing non-gyrotropy does not lead to a general and simple modeling for the pressure tensor. It would demand *a priori* a full kinetic description or, at least, some expansions assuming that these effects are small enough (see Braginskii (1965) for the pioneer work in this field and Passot & Sulem (2006) and references therein). Several papers have investigated the changes in rotational discontinuities when such non-ideal effects are introduced (Lyu & Kan 1989; Hau & Sonnerup 1991; Hau & Wang 2016). These theoretical papers used different analytical models based on different simplifying assumptions. Contrary to these papers, we will not use such kind of assumptions. Instead, we will just analyze the observed magnetic hodograms, and show that their shape is incompatible with a gyrotropic pressure.

4. The magnetopause normal

When studying the magnetopause with *in situ* measurements, the most basic geometric characteristic to be determined is the normal to its surface (which may vary during the crossing). An accurate determination of the magnetopause normal is actually a fundamental condition for determining reliable estimates of the normal components of both the magnetic and the mass fluxes. Moreover, having a good estimation of the normal direction is also necessary to determine the speed of the structure and its thickness. Quantitatively speaking, to determine the normal component of the magnetic field sufficiently well (assuming that $B_n/|\mathbf{B}| \sim 2\%$), an accuracy of the normal should be of the order of $\delta\theta < 1^o$. In the literature, a good accuracy of determination of the normal is considered to be of the order of 5% (Denton *et al.* 2018).

Beyond determining the normal direction, some "reconstruction methods" can be used to provide a more global view of the large scale structure around the spacecraft. Although these methods have proven to provide remarkable results (De Keyser 2008; Hasegawa *et al.* 2005; Denton *et al.* 2020) they will not be used here (the first two studies assume the Grad-Shafranov equations to be valid, implying stationary MHD, and are therefore not appropriate to investigate the non-MHD effects such as the FLR effects).

Over the years, several methods have been developed with the purpose to precisely determine the normal direction (see e.g. (Haaland *et al.* 2004; Shi *et al.* 2019)). The most common is the minimum variance (MVA) introduced with the first measurements of the magnetic field in space (Sonnerup & Cahill 1967; Sonnerup & Scheible 1998). This method, which requires single spacecraft measurements, provides a *global* normal, *i.e.* a single normal vector for each entire time series across the boundary. The tool is based on the assumption that the boundary is a perfectly one-dimensional and stationary layer crossing the spacecraft. Other notable examples are the Generic Residue Analysis (GRA) technique (Sonnerup *et al.* 2006), which consist in a generalisation of the MVA to other parameters than **B**, and the BV method (Dorville *et al.* 2014), which combines magnetic field and velocity data. Even though these methods can give an accurate normal determination (Dorville *et al.* 2015*b*), they provide, like MVA, a *global* normal and thus they cannot provide the necessary basis for investigating the variations of the magnetopause normal within the structure and test the possible departures from mono-dimensionality. Let us finally recall that waves and turbulence, which are always superimposed to the laminar magnetopause profiles, bring strong limitations in the normal direction accuracy for all methods, in particular these global ones.

In this context, multi-spacecraft missions have represented a fundamental step in increasing the accuracy of the normal determination, allowing to determinate the gradients of the measured fields. A notable example is the Minimum Directional Derivative (MDD, Shi *et al.* (2005)) method. This tool generally uses the magnetic field data, but it must be kept in mind that it is not based on specific properties of this field. The MDD technique is a so-called "gradient based method" since the calculation of the normal is based on the experimental estimation of the dyadic tensor $\mathbf{G} = \nabla\mathbf{B}$. This tensor gradient can be obtained from multispacecraft measurements using the reciprocal vector method (Chanteur 1998). The MDD method consists in diagonalizing the matrix $\mathbf{L} = \mathbf{G} \cdot \mathbf{G}^T$, finding the normal direction as the eigenvector corresponding to the maximum eigenvalue. Moreover, the gradient matrix can also be used for estimating the dimensionality of the boundary from the ratio between the eigenvalues. A way of finding a quantitative determination of this dimensionality was proposed in Rezeau *et al.* (2018).

For the vector **B**, the MDD method makes use only of the spatial derivatives $\partial_i\mathbf{B}$, which are accessible at each time step thanks to the 4-point measurements today available with multi-spacecraft space missions. In this sense, it is the opposite of the MVA method, which makes use only of the temporal variances of the **B** components. It therefore allows for an instantaneous determination of the normal at any point inside the layer, while MVA can only provide a single

normal for a full crossing. In addition, contrary to MVA, MDD does not make any assumption about the geometry of the layer (1D variations or not), and about the physical properties of the vector used. Indeed, it can be applied to the magnetic field data but also to any other vector since the property $\nabla \cdot \mathbf{B} = 0$ is not used.

However, due to waves and turbulence, the magnetopause can present locally two-dimensional properties that are insignificant for the profiles we are looking for. For this reason, we will focus here on intervals where the magnetopause is mainly one-dimensional, discarding the crossings in which local 2D features are observed. The intervals considered as one-dimensional are those for which $\lambda_{max} \gg \lambda_{int}$. Here λ_{max} and λ_{int} are defined as the highest and the intermediate eigenvalues of the matrix $\mathbf{G}$. In this limit, the ordering between λ_{int} and λ_{min} (*i.e.* the smaller eigenvalue) is not relevant in defining the intervals. Specifically, we use the parameter, $D_1 = (\lambda_{max} - \lambda_{int})/\lambda_{max}$, which enables us to quantify this mono-dimensionality of the magnetopause as a function of time.

A more recent tool proposed to study the magnetopause is the hybrid method presented in Denton *et al.* (2016, 2018), in which the orientation of the magnetopause is obtained through a combination of the MDD and MVA methods, resulting in an improved accuracy of the normal direction.

The only limitation to the MDD accuracy comes from the uncertainty of the spatial derivatives that it uses. In particular, the local gradient matrix is calculated through the reciprocal vector technique (Chanteur 1998), which assumes linear variations between the spacecraft. Because small-scale waves and turbulence are always superimposed on the magnetopause profiles being searched for, this assumption cannot be well respected without some filtering. This filtering actually leads to introduce part of the temporal information on the variations, but it still allows keeping local information inside the layer whenever one filters only the scales sufficiently smaller than those associated to the full crossing duration. The quality of the filtering is therefore the biggest challenge to complete for getting accurate results. For instance, simple gaussian filters done independently on the four spacecraft would provide insufficient accuracy: this can be observed by the fact that, when doing it, the relation $\nabla \cdot \mathbf{B} = 0$ is violated in the result. In the following section, it is shown how the MDD method can be included in a fitting procedure of the four spacecraft simultaneously and where this relation can be imposed as a constraint. We also show that, when no constraint is added, this procedure justifies the use of MDD with data that are filtered independently.

5. A new tool

The tool we present here, namely GF2 (Gradient matrix Fitting), has been derived from the MDD method. The digit 2 indicates that in the version of the tool that we use here the data are fitted with a 2D model (it can be shown that fitting with a 1D model is mathematically equivalent to the standard MDD technique used with smoothed data). Differently from the original method, we assume that the structure under investigation can be fitted locally (*i.e.* in each of the small sliding window used along the global crossing), by a two-dimensional model. This does not imply that the magnetopause is assumed globally two-dimensional. As for MDD, the instantaneous gradient matrix $\mathbf{G}$ is obtained from the data using the reciprocal vector's technique (Chanteur 1998). When performing the 2D fit in each sliding window, we then impose some physical constraints, which could be checked only *a posteriori* with the classic MDD method.

The model $\mathbf{G}_{fit}$ is obtained as follows:

$$\mathbf{G}_{fit} = \mathbf{e}_0 \, \mathbf{B}'_{e0} + \mathbf{e}_1 \, \mathbf{B}'_{e1} \tag{5.1}$$

where we define $\mathbf{e}_0$ and $\mathbf{e}_1$ as two unit vectors in the plane perpendicular to the direction of invariance and $\mathbf{B}'_{e0}$ and $\mathbf{B}'_{e1}$ as the variation of the magnetic field along these two directions.

By performing the fit, we impose $\nabla \cdot \mathbf{B} = 0$ (as used in MVA but ignored in standard MDD). In the model, this can be written as:

$$\mathbf{e}_0 \cdot \mathbf{B}'_{e0} + \mathbf{e}_1 \cdot \mathbf{B}'_{e1} = 0 \tag{5.2}$$

In order to fit the experimental $\mathbf{G}$ by the model $\mathbf{G}_{fit}$, the following quantity has to be minimised

$$\begin{aligned} D_2 &= \mathrm{Tr}[(\mathbf{G}_{fit} - \mathbf{G}).(\mathbf{G}_{fit} - \mathbf{G})^T] \\ &= \mathbf{B}'^2_{e0} - 2\mathbf{e}_0.\mathbf{G}.\mathbf{B}'_{e0} + \mathbf{B}'^2_{e1} - 2\mathbf{e}_1.\mathbf{G}.\mathbf{B}'_{e1} + Tr(\mathbf{G}\mathbf{G}^T) \end{aligned} \tag{5.3}$$

We can disregard the last term, since it is independent of the fit parameters. To impose the physical constraints, we use Lagrange multipliers, minimizing:

$$\begin{aligned} D_2 =& \mathbf{B}'^2_{e0} - 2\mathbf{e}_0.\mathbf{G}.\mathbf{B}'_{e0} + \mathbf{B}'^2_{e1} - 2\mathbf{e}_1.\mathbf{G}.\mathbf{B}'_{e1} + 2\lambda(\mathbf{e}_0 \cdot \mathbf{B}'_{e0} + \mathbf{e}_1 \cdot \mathbf{B}'_{e1}) \\ =& \mathbf{B}'^2_{e0} - 2\mathbf{e}_0.(\mathbf{G} - \lambda\mathbf{I}).\mathbf{B}'_{e0} + \mathbf{B}'^2_{e1} - 2\mathbf{e}_1.(\mathbf{G} - \lambda\mathbf{I}).\mathbf{B}'_{e1} \end{aligned} \tag{5.4}$$

By assuming in the first approximation that the direction of invariance $\mathbf{e}_2$ is known, we can choose the two vectors $\mathbf{e}_0$ and $\mathbf{e}_1$ as an arbitrary orthonormal basis for the plane of variance. For performing the minimisation, we have just to impose equal to zero the derivatives with respect to $\mathbf{B}'_{e0}$, $\mathbf{B}'_{e1}$ and λ, obtaining Equation 5.2 and:

$$\mathbf{B}'_{e0} = \mathbf{e}_0.(\mathbf{G} - \lambda\mathbf{I}) \tag{5.5}$$

$$\mathbf{B}'_{e1} = \mathbf{e}_1.(\mathbf{G} - \lambda\mathbf{I}) \tag{5.6}$$

By introducing these two equations in Equation 5.2 we obtain:

$$\lambda = \frac{G_{00} + G_{11}}{2}, \tag{5.7}$$

from which we get the values of $\mathbf{B}'_{e0}$ and $\mathbf{B}'_{e1}$. At this point, the matrix $\mathbf{G}_{fit}$ is fully determined. We can then look for its eigenvalues and eigenvectors, as in the standard MDD method, and get the normal $\mathbf{n}$ and the tangential directions $\mathbf{t}_1$ (*i.e.* the one orthogonal to the direction of invariance) from this smooth fit.

The choice of the direction of invariance has actually no major influence on the determination of the normal direction, neither on the estimation of the 2D effects. For large 2D effects, one could choose the direction of minimum variance obtained by applying directly the standard MDD method to the data. Nevertheless, for almost 1D cases (the most common situation), the spatial derivatives in the tangential directions are generally much smaller than the noise, so this result is not reliable. We simply choose here the constant M direction given by MVA, which is often considered as the direction of the X line if interpreted in the context of 2D models of magnetic reconnection (*cf.* for instance Phan *et al.* (2013) for a typical use of this choice and Aunai *et al.* (2016); Liu *et al.* (2018); Denton *et al.* (2018) for discussions about it).

Finally, another useful by-product of the method can be obtained: comparing the spatial derivatives and the temporal ones and using a new fitting procedure, we can compute the two components of the velocity of the structure V_{n0} and V_{t1} with respect to the spacecraft. Only the motion along the invariant direction then remains unknown.

5.1. *Normal from ions mass flux*

This tool can be easily adapted to any other vector dataset by just changing the physical constraint. In particular, we chose to study the structure using the ion mass flux data. In this case we impose mass conservation $\nabla \cdot \boldsymbol{\Gamma}_i = -\partial_t n_i$ (with $\boldsymbol{\Gamma}_i = n_i \mathbf{u}_i$). Eq.5.2 now writes

$$\mathbf{e}_0 \cdot \boldsymbol{\Gamma}'_{e0} + \mathbf{e}_1 \cdot \boldsymbol{\Gamma}'_{e1} + \partial_t n_i = 0 \tag{5.8}$$

Therefore, when using the Lagrange multipliers, Eq.5.4 changes to:

$$\begin{aligned} D_2 =& \boldsymbol{\Gamma}'^2_{e0} - 2\mathbf{e}_0.\mathbf{G}.\boldsymbol{\Gamma}'_{e0} + \boldsymbol{\Gamma}'^2_{e1} - 2\mathbf{e}_1.\mathbf{G}.\boldsymbol{\Gamma}'_{e1} + 2\lambda(\mathbf{e}_0 \cdot \boldsymbol{\Gamma}'_{e0} + \mathbf{e}_1 \cdot \boldsymbol{\Gamma}'_{e1} + \partial_t n_i) \\ =& \boldsymbol{\Gamma}'^2_{e0} - 2\mathbf{e}_0.(\mathbf{G} - \lambda\mathbf{I}).\boldsymbol{\Gamma}'_{e0} + \boldsymbol{\Gamma}'^2_{e1} - 2\mathbf{e}_1.(\mathbf{G} - \lambda\mathbf{I}).\boldsymbol{\Gamma}'_{e1} + 2\lambda\partial_t n_i \end{aligned} \tag{5.9}$$

By using the same algorithm as above, the constraint can now be written as:

$$\lambda = \frac{G_{00} + G_{11} + \partial_t n_i}{2} \tag{5.10}$$

5.2. *Dimensionality index*

From this procedure, we can also derive another significant result: we can obtain an indicator of the importance of the 2D effects in the profiles, free of the parasitic noise effects. Specifically, we can estimate the variation of the magnetic field along the normal by projecting the $\mathbf{G}_{fit}$ matrix along it $\mathrm{var}_n = |\mathbf{G}_{fit}.\mathbf{n}|$. Consequently, if we designate the variation along $\mathbf{t}_1$ as var_t, we can introduce a new dimensionality index:

$$\mathcal{D}_{GF2} = \frac{\mathrm{var}_n - \mathrm{var}_t}{\mathrm{var}_n} \tag{5.11}$$

This index can usefully be compared with the instantaneous index $D_1 = (\lambda_{max} - \lambda_{int})/\lambda_{max}$ of Rezeau *et al.* (2018).

6. Expected accuracy and tests of the tool

In this section we test the accuracy of the GF2 tool. To accomplish this, we exploit a case crossing, which will be investigated in detail in the following section. The crossing considered comes from MMS data (Burch & Phan 2016), taking place at around 22:11 on 28th December 2015. For this study we use data from the FluxGate Magnetometers (FGM, Russell *et al.* (2016)), providing the magnetic field data, the Electric Double Probe (EDP, Lindqvist *et al.* (2016); Ergun *et al.* (2016)), for the electric field, and Dual Ions and Electrons Spectrometer instrument (DIS, DES, Pollock *et al.* (2016)), for plasma measurements. An overview of the event is shown in Fig. 2, where both the magnetic field and ion bulk velocity are given in Geocentric Solar Ecliptic (GSE) coordinates. For this event, the spacecraft are located in [7.6, -6.7, -0.8] R_E in GSE coordinates (where R_E is the Earth's radius).

The temporal interval in which we observe the shear in the magnetic field and the crossing in the particle structure is about 8 seconds, enough to allow for high resolution for both sets of measurements. The crossing is chosen by also analyzing the dimensionality of the magnetic field measurements averaged along the crossing. In particular, the dimensionality parameter defined in Eq. 5.11, denoted as $\mathcal{D}_{GF2}$, and the one introduced in Rezeau *et al.* (2018), denoted as D_1, were considered. In this interval, indeed, we have $D_{1,mean} = 0.97 \pm 0.03$ while $\mathcal{D}_{GF2} = 0.89 \pm 0.06$, both highlighting that the crossing exhibits one-dimensional features throughout the time interval. We remind here that in burst mode, the frequency of magnetic field measurements is 132Hz while it is 6,67 Hz for ions. To conduct the following study, it is necessary to interpolate all measurements at the same times. We did it by testing two sampling frequencies: the magnetic field and the ion ones. The results obtained are consistent with the two methods. All figures shown in the paper are obtained with the sampling times of the MMS1 magnetic field. Furthermore, the crossing is observed quasi-simultaneously for the two quantities, with a large interval where the two kinds of results can be compared.

As a first test, we compare in Fig.3 the normals obtained by GF2 and those by the standard MDD technique (using data smoothed in a 0.31s time-window), for both the magnetic field and the ion data. For reference, we also compare the result of $GF2_B$ with the MVA one.

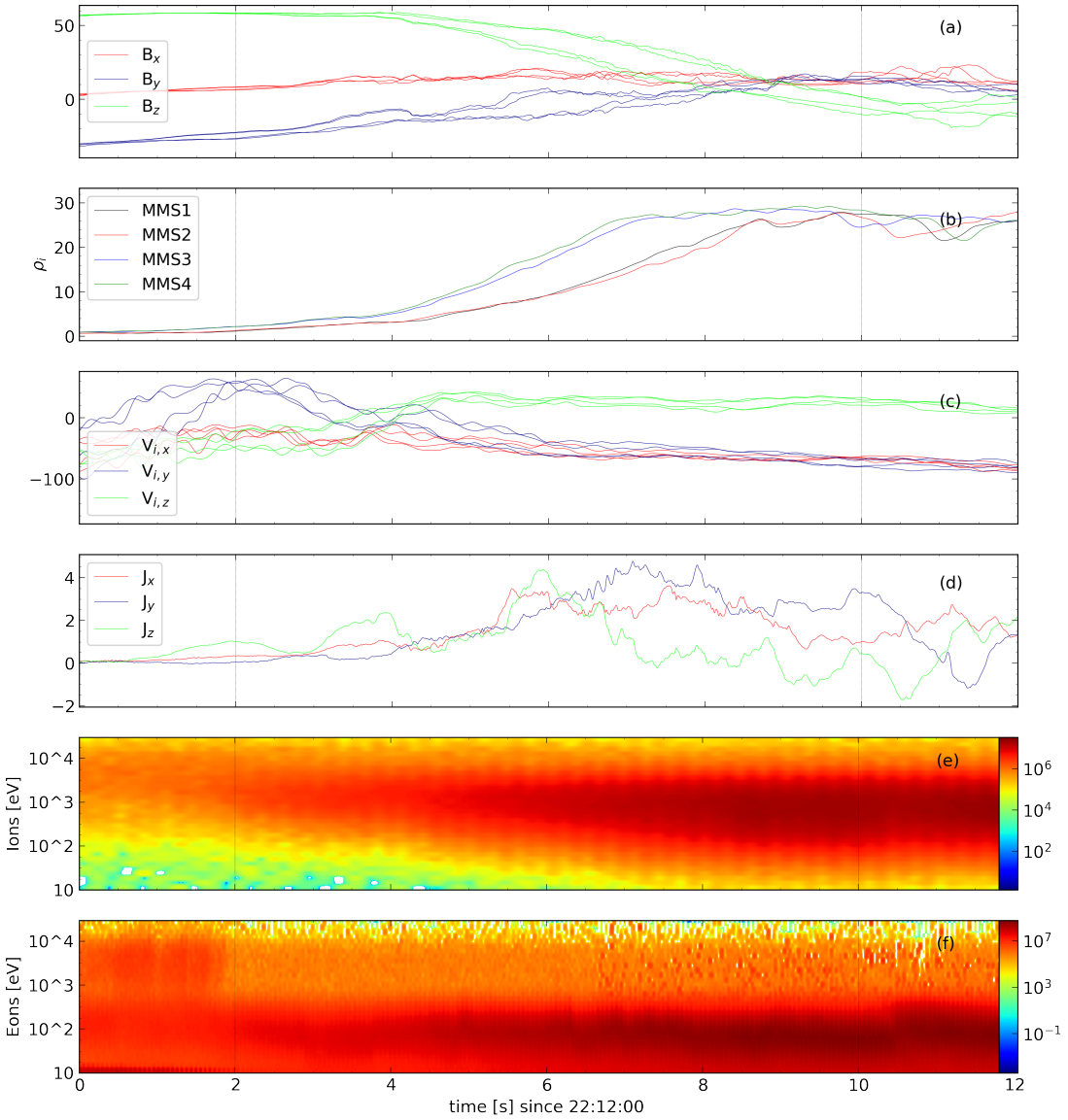

FIGURE 2. Main features of the crossing of the 28th December 2015. From top to bottom: (a) the magnetic field (in nT), (b) the ion particle density (in m^{-3}), (c) ion velocity (in km/s), (d) total current (computed from the curlometer (Dunlop *et al.* 1988), in nA/m^2), (e) the ion and (f) electron spectrograms (energies are shown in eV). Vertical lines indicate the time interval chosen for the case study.

Vertical dashed lines indicate the time interval during which all the satellites are inside the boundary. We observe that the time required for the ions flux to complete the crossing (of about $5s$) is shorter than for the magnetic field (about $8s$). To perform a quantitative analysis of the differences, we studied the angles between the different normals obtained through GF2, MDD and MVA, as shown in Fig. 4.a.

The first striking result is that all these results are quite consistent. Almost all the directions are less than ten degrees apart from each other, with an average difference of about five degrees. The major exception concerns the comparison between MVA and $GF2_B$ during the last second of the interval where the two directions appear to be up to 35 degrees apart. This can be explained by the fact that the local normals are observed (by $GF2_B$ as well as by MDD_B) to differ noticeably in this part from their averaged value and that MVA is not able to detect such a change. Looking in more detail, we can see a slight difference between the first part of the crossing (between $2s$ and $\sim 6.5s$), where the two normals $GF2_B$ and MDD_B differ by less than 5 degrees, and the second part, where the angle between the normals can be up to ten degrees (probably due to a

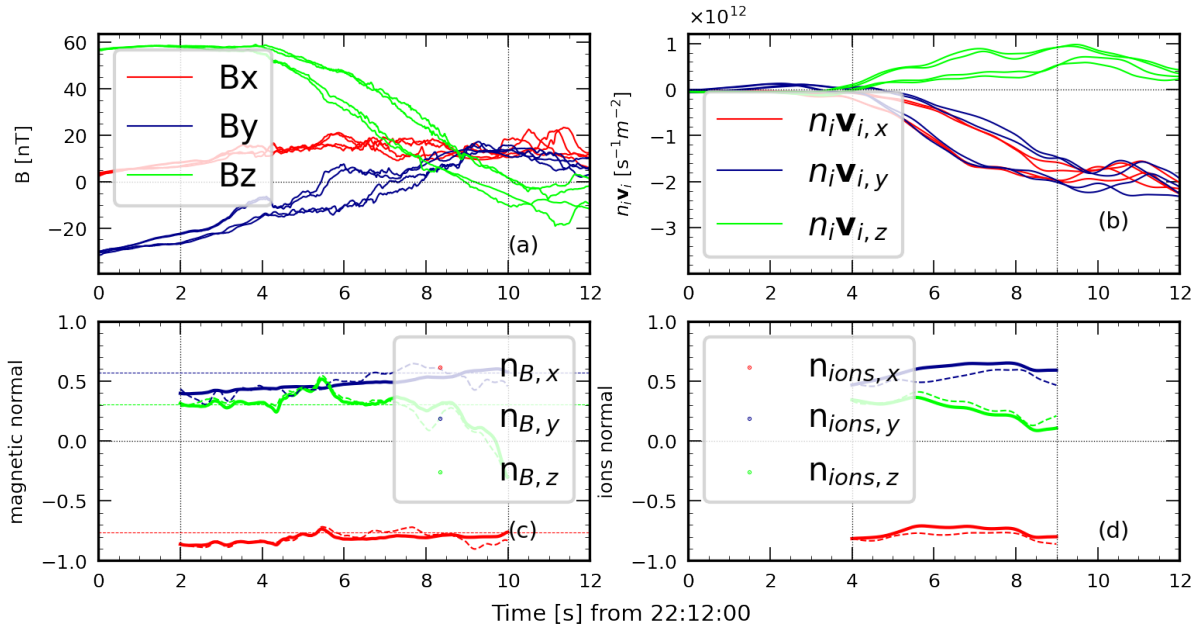

FIGURE 3. Comparison for the normals obtained with GF2 with respect to the MDD tools. (*a*) shows the magnetic field and (*b*) the ion mass flux, measured by the four MMS spacecraft. (*c*) and (*d*) shows the magnetic and the ion normal, respectively. The continuous (resp. dashed) line correspond to the components of GF2 (resp. MDD) normal. Horizontal dotted lines indicate the MVA normal obtained along the whole interval. Vertical dashed lines correspond to the time interval boundaries for the crossing, which are different for the magnetic field and the ion mass flux.

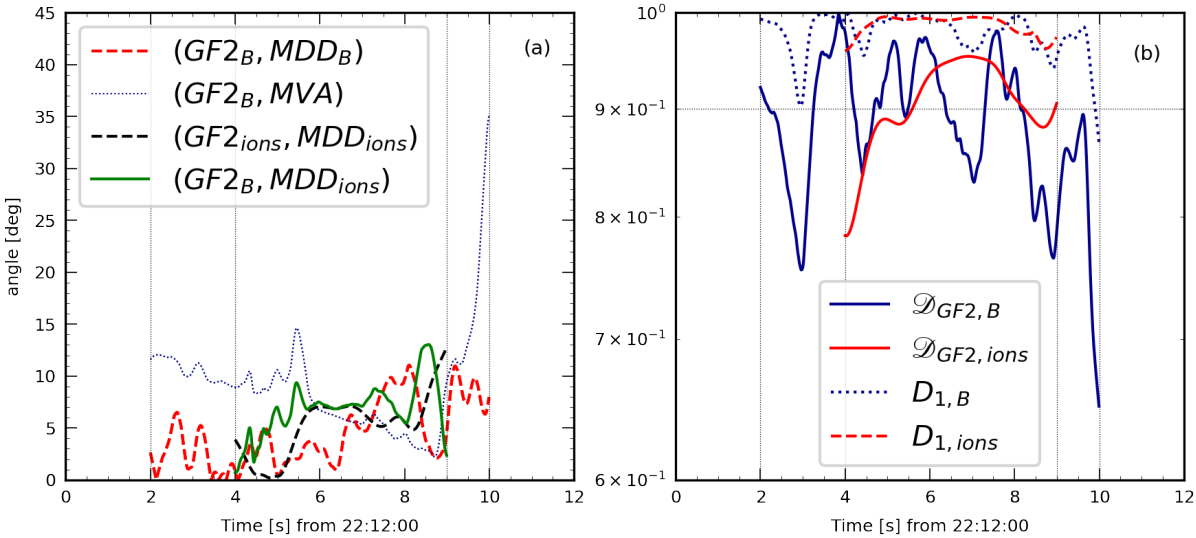

FIGURE 4. (*a*) Angle between the normals obtained using the state-of-the-art tools (MDD, MVA) and GF2. The subscript *B* and *ions* indicates whenever the magnetic field or the ion flux measurements are used. (*b*) Dimensionality of the structure as a function of time; here both the $\mathcal{D}_{GF2}$ (continuous line) and the D_1 (dashed line) indices are shown, for both the magnetic field (blue) and ions (red) data.

smaller ratio signal/noise for the gradient matrix $\mathbf{G}$). The normals derived from ion measurements are not much different from those derived from the magnetic field, showing that the particle and magnetic structures are approximately identical. In Fig. (4.b), the dimensionality of the structures is analyzed as a function of time, by using both the $\mathcal{D}_{GF2}$ and the D_1 (Rezeau *et al.* (2018)) parameters, as explained above. Even if the numerical values of the two indices are slightly different, they both indicate structures close to one-dimensionality in the first part, with a -small

Model	**Normal** [GSE]	angle with $\mathbf{n}_{GF2,B}$ [deg]
$\mathbf{n}_{GF2,B}$	[0.82, -0.49, -0.29]	x
$\mathbf{n}_{GF2,ions}$	[0.76, -0.59, -0.26]	7.2
MVA	[0.76, -0.57, -0.30]	6.1
MDD	[0.83, -0.49, -0.28]	0.7
Denton	[0.82, -0.49,-0.29]	0.4

TABLE 1. Magnetopause normal vectors obtained with the main tools presented above averaged in the time interval and their angle with respect to the normal obtained with GF2 using the magnetic field data (in degrees).

but significant- decrease in the second part. This increased departure from mono-dimensionality can explain the slight difference between the two parts when comparing the normals from standard MDD and GF2 techniques.

The present test does not allow us to state that GF2 is more accurate than standard MDD (this will be checked in future work by comparing the two tools in a global simulation involving realistic turbulence) but it shows at least a good agreement between the two approaches. We will see in the following that this accuracy is anyway sufficient to prove the role of FLRs.

In order to smooth the small fluctuations over the time interval and to reduce the statistical error associated with the determination of the normal, we can compare the directions averaged along the crossing time. Mean values obtained through the tools presented above are shown in Table 1. Here we observe that all the averaged normals differ by less than 10 degrees. Specifically, we observe that the normals obtained with GF2, MDD and (Denton *et al.* 2018) are similar, with a difference of less than one degree (with ours being closer to the one from Denton *et al.* (2018)). MVA normal, instead, differs around 6 degrees from all these other normals. Finally, we also observe that the one computed with ions flux data is the most distant. This is interpreted to be due to the higher uncertainty of particles measurements.

7. Case study

In this section, we undertake a detailed analysis of the previously mentioned crossing case by employing the normal obtained using the GF2 tool. Here, we focus on the time interval between 2 *s* and 9 *s* in Fig 2. To mitigate the potential influence of non-unidimensionality effects, we chose to exclude the last second of the time interval studied in the preceding section for the magnetic field (where both $\mathcal{D}_{GF2}$ and D_1 show that the structure is less one-dimensional and where we observe that the normal is more different from the averaged one). To carry out this analysis, we study the hodogram of the magnetic field in the tangential plane. Here the tangential results are presented in a basis $(\mathbf{T}_1, \mathbf{T}_2)$ chosen as:

$$\mathbf{T}_1 = \mathbf{n}_{mean} \times \hat{\mathbf{b}} \tag{7.1}$$

$$\mathbf{T}_2 = \mathbf{n}_{mean} \times \mathbf{T}_1 \tag{7.2}$$

where $\hat{\mathbf{b}} = \mathbf{B}/|\mathbf{B}|$ and $\mathbf{n}_{mean}$ is the directions of the averaged normal in the chosen time interval. Note that the choice of the reference frame $(\mathbf{T}_1, \mathbf{T}_2)$ is just a convention. The shape of the hodogram remains unaffected by this choice except for the corresponding rotation in this tangential plane. The direction $\mathbf{t}_1$, which characterizes the direction of the second dimension of the model in GF2 and which is also in the tangential plane is generally different from $\mathbf{T}_1$.

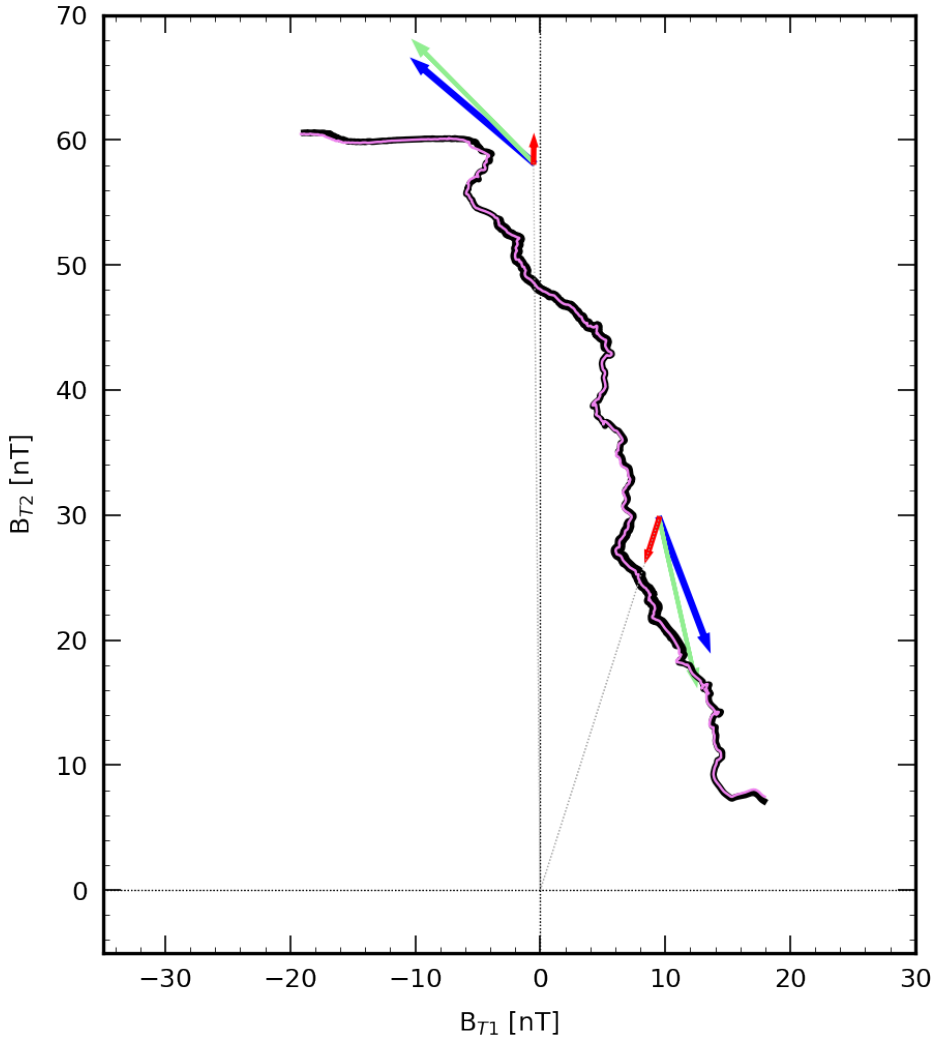

FIGURE 5. Hodogram in the tangential plane of the magnetic field for a magnetopause crossing by MMS in 28.12.2015 from 22:12:02 to 22:12:09. See text for the significance of the arrows. B_{T1} and B_{T2} are the projections of **B** along the tangential directions computed as described in the text. The black line (resp. violet) is the hodogram when the $\mathbf{n}_{mean}$ (resp. **n**) value is used to define the reference frame.

If CTD was valid everywhere, the hodogram of the magnetic field in the tangential plane for a rotational discontinuity would correspond to a circular arc with constant radius while a shock would correspond to a radial line (as shown in Fig. 1). For this reason, the hodogram is a good tool to recognize the cases for which the CTD fails at describing the magnetopause. The hodogram for this case is shown in Fig. 5. We observe a clear "linear" (although not radial) hodogram. This non-radial variation of the magnetic field although not predicted by CTD, is a striking feature of the hodogram. It cannot be explained by a departure from the 1D assumption since we have measured that the crossing can be considered as one-dimensional to a good degree of accuracy. It is therefore due to an intrinsic property of the layer itself. Also, in Fig. 5, we present the hodogram derived from the local normal (un-averaged, violet line). It is clear that averaging does not affect the shape of the hodogram.

To further analyze the causes of the disagreement between the hodogram of this case crossing and what is expected from CTD, we compare the different terms of the tangential momentum equation and Faraday/Ohm's law. As discussed above, indeed, these two equations are responsible for the distinction between the rotational and tangential discontinuities in CTD. This is the object of Figure 6, where we plot the different terms of the two equations projected

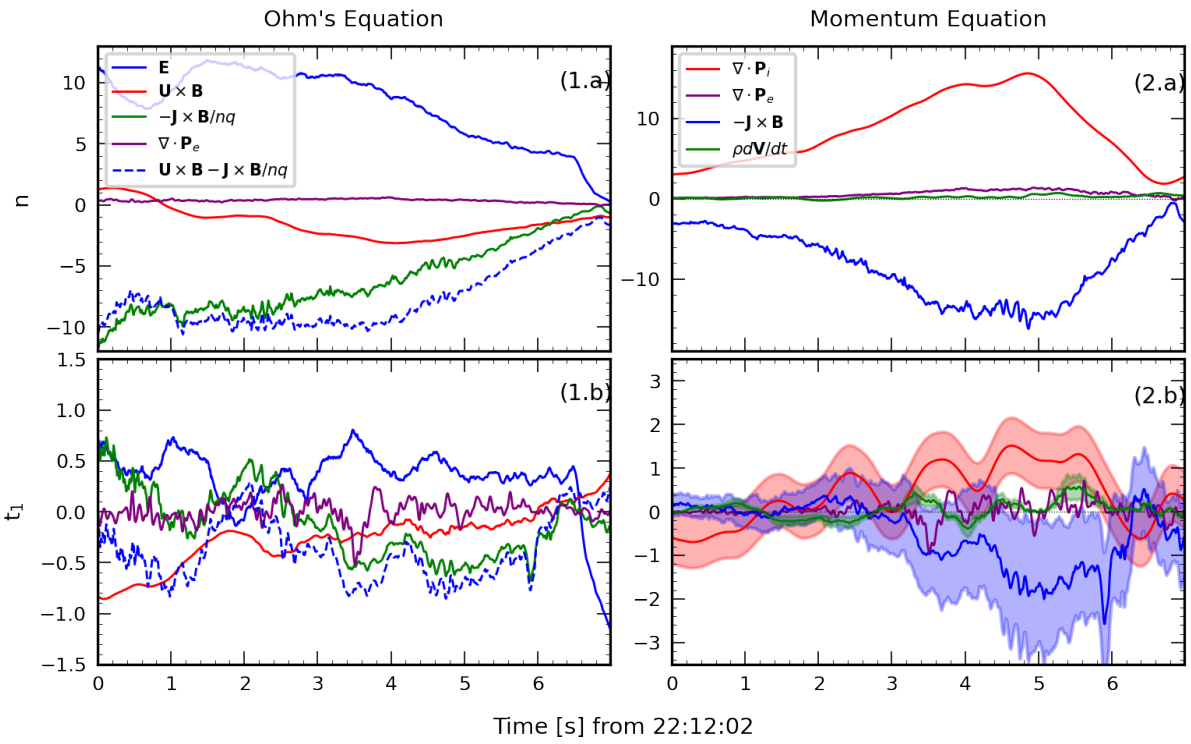

FIGURE 6. Terms of the Ohm's law (panel 1, units of mV/m) and the momentum equation (panel 2, units of $10^{-15} kg\, m/s^2$), projected in the normal direction n (a) and in the tangential direction t_1 (b). To reduce the noise, a running average with a time window of 0.35s is applied to the electric field measurements. Shaded regions in panel 2.b represent the estimated uncertainties of the divergence of the pressure (red), the $\mathbf{J}\times\mathbf{B}$ (blue) and the classic inertial term (green). Concerning the Ohm's law, we included the sum $\mathbf{U}\times\mathbf{B}-\mathbf{J}\times\mathbf{B}/nq$ to facilitate the readability (blue dashed line).
N.b. The terms of the tangential Faraday/ Ohm's law used in the text are just the derivatives of the ones in (a) (apart from a $\pi/2$ rotation).

along the $\mathbf{n}_{mean}$ and $\mathbf{t}_{1,mean}$ directions obtained using the GF2 tool (averaged over the whole time interval). The influence of the averaging of the $\mathbf{t}_{1,mean}$ direction on the results is discussed in Appendix A. We do not show the quantities along the direction of invariance, which are dominated by noise. The current and the gradient matrix for the pressure term are obtained via the reciprocal vector method described in Chanteur (1998).

Concerning the Ohm's law (Figure 6, panel 1), we see that the electric field is well counter-balanced by the $\mathbf{u}\times\mathbf{B}$ and $\mathbf{J}\times\mathbf{B}/nq$ terms (ideal and Hall terms). Outside the layer, on both sides, the ideal Ohm's law is satisfied, as assumed in CTD (this is not visible on the figure, which is a zoom on the inner part of the layer, and where the Hall term is important). It has been shown in the literature that $\nabla\cdot\mathbf{P}_e$ is not always negligible in the Ohm's law and that it can even be dominant close to an Electron Diffusion Regions (EDR). This has been predicted theoretically (Hesse *et al.* 2011, 2014) and observed experimentally (Torbert *et al.* 2016; Genestreti *et al.* 2018), but it is not the case for events like this one. We observe that at approximately 3.5 seconds, the $\nabla\cdot\mathbf{P}_e$ is not entirely negligible along the tangential direction (a similar peak can also be observed in panel 2.b for the term associated with the electron pressure in the momentum equation). However, during this time interval, this value is not dominant, this term being smaller than both the electric field and the $\mathbf{J}\times\mathbf{B}/nq$ components. Furthermore, this effect exhibits a local characteristic, as $\nabla\cdot\mathbf{P}_e$ is only non-negligible within a small sub-interval (with respect to the magnetopause temporal width). It is therefore not likely to be indicative of proximity to a reconnection point.

Concerning the momentum equation, shown in panel 2 of Figure 6, we observe that, in the normal direction, the $\mathbf{J}\times\mathbf{B}$ term is counter-balanced by the divergence of the ion pressure tensor,

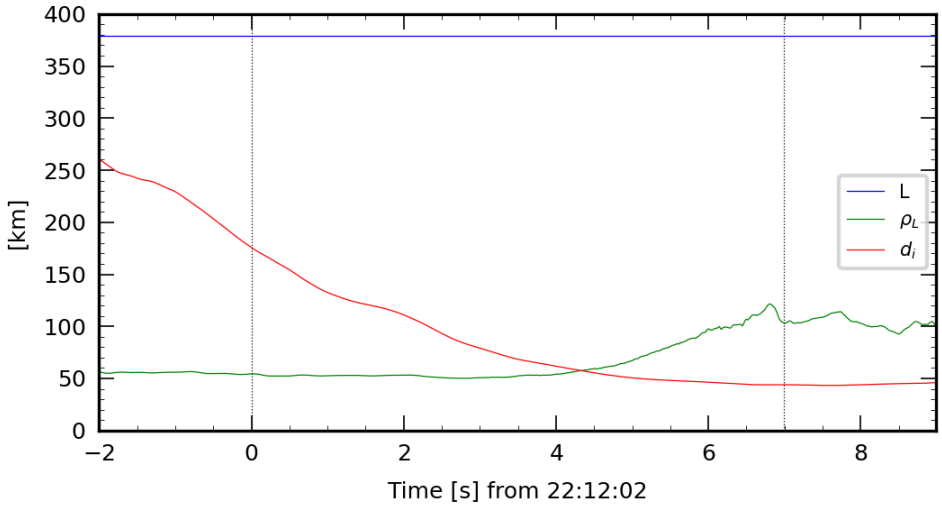

FIGURE 7. Comparison of the magnetopause width (L) with the ion inertial length (d_i) and the ions Larmor radius (ρ_L). Vertical lines highlight the considered temporal interval.

as expected. But, if the isotropic condition assumed in CTD was valid, we would expect the divergence of the ion pressure tensor to be zero in the tangential direction, or at least negligible with respect to the inertial term $\rho d\mathbf{u}/dt$. On the contrary, we observe that the $\mathbf{J}\times\mathbf{B}$ term along $\mathbf{t}_1$ is of the same order of magnitude as the divergence of the ion pressure tensor, and one order of magnitude larger than all the other terms. Panel 2.*b* also shows an estimation of the error on the relevant terms: $\mathbf{J}\times\mathbf{B}$, $\nabla\cdot\mathbf{P}_i$ and the classical inertial term. It is known that measurements errors are difficult to estimate, especially at small scales. In order to validate our results, however, we sought to obtain an upper bound of the error associated with the quantities of interest. For that purpose, an overestimation of the uncertainty of the measurements (acquired as the maximum during the crossing of the errors available in FPI datasets for the pressure tensor and from the FGM nominal error for the magnetic field) was exploited. These values are propagated as a statistical (*i.e.* quadratic) error (by assuming that the errors on the reciprocal vectors can be neglected with respect to that of other physical quantities).

From panel 2.*b* of Fig. 6, we see that the $\mathbf{J}\times\mathbf{B}$ and the $\nabla\cdot\mathbf{P}_i$ terms are pointing in opposite directions and balancing each other. If valid in the first part of the interval, this conclusion cannot be safely trusted due to measurement uncertainty, but we observe that in the middle part (particularly between $3.5s$ and $6s$) it is evident that the two quantities counterbalance each other while the classical inertia term $\rho d\mathbf{u}/dt$ is much lower with respect to the others. This proves that the tangent $\nabla\cdot\mathbf{P}_i$ term plays a fundamental role in the magnetopause equilibrium.

This point can be emphasized also by analyzing the hodogram. In Fig. 5, the arrows are directed along the directions of the tangential plane that are physically relevant for the problem: *i*) the tangent to the hodogram (green), which indicates the total variation of $\mathbf{B}_t$; *ii*) the radial direction (red), which corresponds to the plasma compression; *iii*) the $\nabla\cdot\mathbf{P}_{it}$ direction (blue), which is the direction of the divergence of the ion pressure tensor in the tangential plane, and therefore corresponds to a term which is absent in CTD. The relative lengths of the arrows are chosen proportional to the corresponding term magnitudes. These directions are averaged in two sub-intervals (bold hodogram). The striking result is that the total variation is mainly determined by the non-classic term $\nabla\cdot\mathbf{P}_{it}$ and not by the radial classic one. This explains the very recurrent (even if not reported in the literature hitherto) feature that the hodograms are almost linear but not radial.

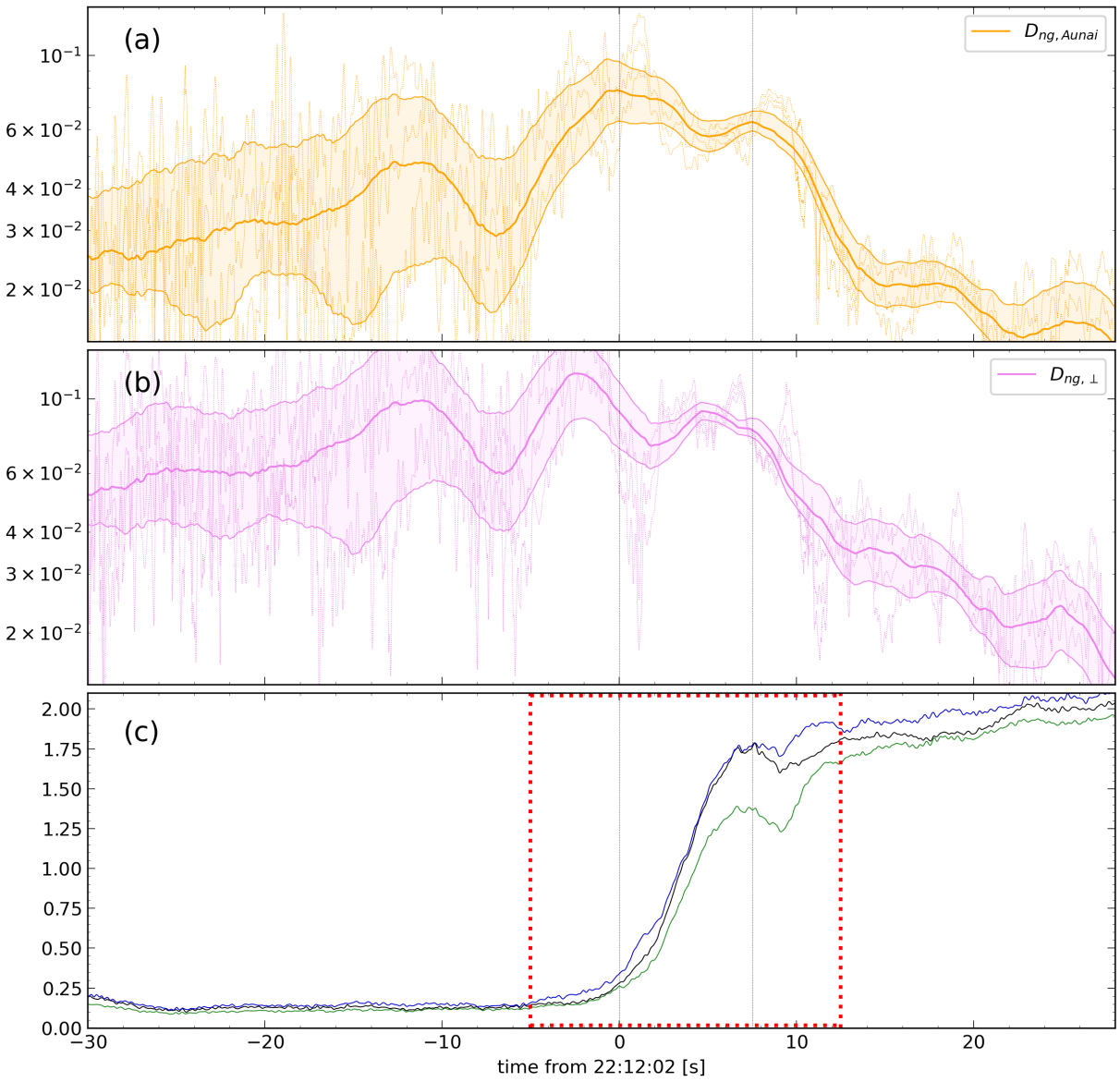

FIGURE 8. Panels *a* and *b* show the evolution of the $D_{ng,\perp}$ and $D_{ng,Aunai}$ (Aunai *et al.* 2013) indices, respectively, along with their estimated uncertainties. Thin lines correspond to the real-time values while thick lines to an averaged window of 1 s; (*c*) Evolution of the eigenvalues of the $\mathbf{P}_i$ matrix (averaged on the four spacecraft). The dotted line indicates the magnetopause crossing. The red dotted lines in panel *c* highlight the time interval studied in Fig. 9

7.1. *Comparison of the width of the magnetopause to relevant physical lengths*

Finally, we compare the width of the magnetopause (L) to the two main ion-related lengths: the ion Larmor radius (ρ_L) and the ion inertial length (d_i). The magnetopause width is estimated using the normal velocity obtained from the $GF2$ tool. By averaging the velocity of the magnetopause in the normal direction, we can estimate $L = \mathbf{V}_{n,mean}\Delta t$ (where Δt is the time length of the full crossing). These three scales are shown in Fig.7. We observe that this width is larger than the ion Larmor radius and the ion inertial length all across the crossing, but only two to five times larger, which appears sufficient to drive the observed kinetic effects.

8. Ion pressure tensor analysis

To further investigate the question of the ion non-gyrotropy with respect to the magnetic field and quantify this effect, let us now examine the properties of the ion pressure tensor and introduce

a new non-gyrotropy index. For that purpose, we define the matrices $\mathbf{P}_{\parallel} = p_{\parallel}\mathbf{bb}$, where $\mathbf{b} = \mathbf{B}/|\mathbf{B}|$ and $p_{\parallel} = \mathbf{b} \cdot \mathbf{P}_i \cdot \mathbf{b}$, and $\mathbf{P}_{\perp} = \mathbf{P}_i - \mathbf{P}_{\parallel}$. By defining p_1 and p_2 the maximum and intermediate eigenvalues of the $\mathbf{P}_{\perp}$ matrix, we define:

$$D_{ng,\perp} = \frac{p_1 - p_2}{p_1 + p_2} \tag{8.1}$$

In Fig. 8.a, this parameter is compared to the non-gyrotropy index presented in Aunai *et al.* (2013). The two indices define nongyrotropy differently, (Aunai *et al.* 2013)'s index defining nongyrotropy as the ratio of the nongyrotropic to the gyrotropic part of the tensor (instantaneous), while ours makes use of the 2D modeling of the data used in GF2 (averages on sliding windows). We note how both indices are significantly different from zero, approximately of the order of 0.1 within the boundary, corresponding to clearly present, although not predominant, non-gyrotropic effects. We note a decrease in both indices outside the magnetopause, as expected, but it is worth noting also that, despite a continuous decrease, these indices remain relatively high in the time interval just preceding the crossing, in a region where magnetic field, density and pressure tensor are almost constant. This can be understood by noting that an ion velocity gradient is observed in this interval, suggesting that the non-diagonal terms of the pressure tensor could be due there to a kind of gyroviscous effect, the non-diagonal terms of the pressure tensor (Braginskii 1965) being due to FLRs (Stasiewicz 1993). One must take care that, in this interval, the pressure tensor has low values characterized by larger relative errors, which could partially influence this result. To further analyze this question, we have estimated the uncertainties on both non-gyrotropy indices. This estimation is derived from the nominal uncertainties of the FPI dataset. The diagonal terms have higher values and lower relative errors. Concerning the time interval before the crossing that we discuss here, the diagonal terms have errors of approximately 5%, whereas off-diagonal terms have an average relative error about 50% . We observe on Fig. 6 that this way of estimating the uncertainty well encompasses the variance of the results. It confirms that, within the crossing interval, all relative errors are smaller than 10 %, as considered in the Ohm's law study (Fig. 6). In addition, a preliminary study appears to confirm the validity of the gyroviscous interpretation. Using the theoretical expressions given in Stasiewicz (1989), we can compare the variations of the non-diagonal terms of the pressure tensor with the spatial derivatives of the flow velocity, and evidence a fairly good correlation (see Appendix B).
Fig. 8 (panel *c*) also shows the evolution of the eigenvalues of the $\mathbf{P}_i$ tensor, averaged on the four spacecraft. This figure shows how outside of the magnetopause the three eigenvalues tend to converge towards each other meaning that these media are close to isotropy. However, inside the magnetopause, we note a transition in the behavior of the intermediate eigenvalue, shifting from a value close to the minor one to being closer to the major eigenvalue. The minor eigenvalue exhibits a significant deviation from the other two towards the last part of the crossing.

Focusing on the temporal interval marked by the red square in Fig. 8, this transition is further investigated in Fig. 9 where we show the ions' distribution functions in the tangential plane (with respect to the magnetopause) for four different intervals during the crossing, highlighting the non-gyrotropy of the ions' distribution function over time. VDFs (printed using a linear 2D interpolation on a cartesian grid in the chosen plane using the Pyspedas library) are here averaged in the corresponding time intervals framed with the same color as in the bottom plot where the eigenvalues of the ion pressure tensor are plotted again (the time length decreases as the density increases).

Finally, we analyzed the non-gyrotropy with respect to a generic direction, *i.e.* without imposing that this direction is the magnetic field direction. Specifically, we have looked at a

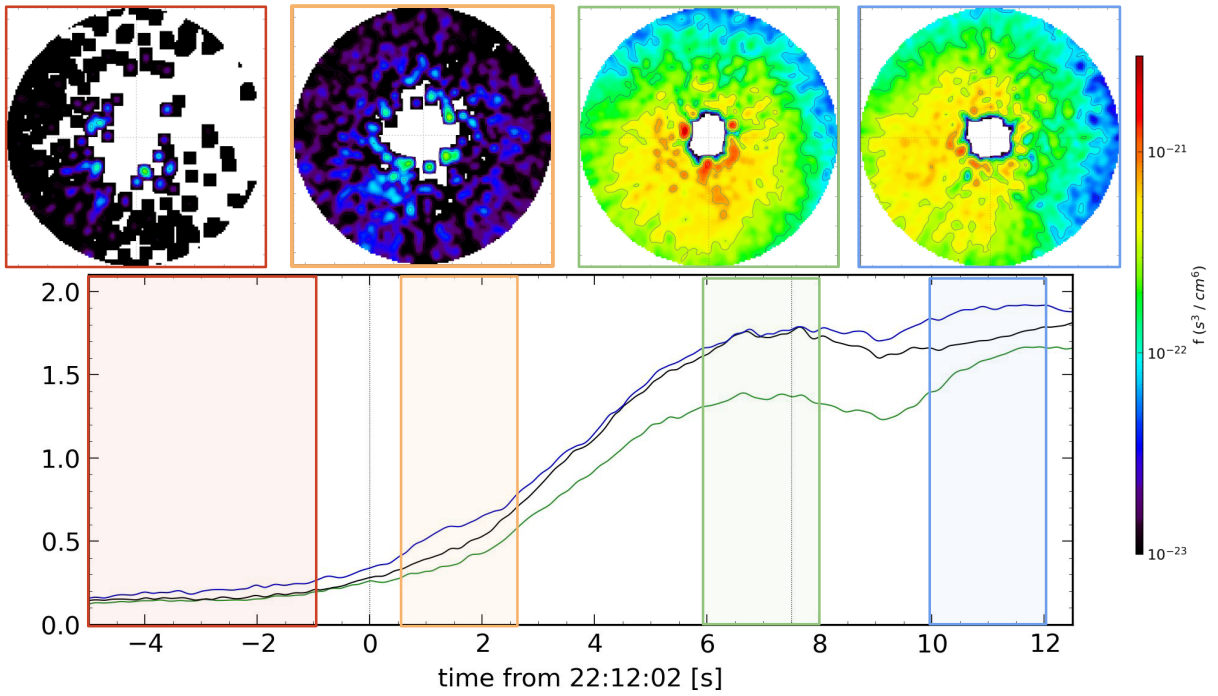

FIGURE 9. Top: Ions' velocity distribution functions in the tangential plane (the $\mathbf{T}_1$- $\mathbf{T}_2$ plane) averaged in four different time periods. Velocities axes are between -220 km/s and 220 km/s. Bottom: Eigenvalues of the pressure tensor (same interval as in the red dashed square of Fig. 8.c). The four colored boxes are used to distinguish the four time intervals.

direction, denoted as **g**, around which the rotated matrix could be rewritten as follows:

$$\begin{pmatrix} P_2 & 0 & 0 \\ 0 & P_1 & 0 \\ 0 & 0 & P_1 \end{pmatrix} \tag{8.2}$$

To achieve this, we employ a minimization algorithm to derive the rotation matrix **M** that allows us to put the pressure tensor data under a form as close as possible to this one. Results from this study are shown in Fig. 10 (here shown for MMS2). Panel *a* displays the variation of P_1 and P_2 along the crossing, where P_2 consistently exceeds P_1. In addition, we imposed an upper limit on the temporal variation of the gyrotropic direction **g**, excluding points with significant temporal variations (indicated by the thin line). Consequently, the remaining points reflect instances where the direction of **g** can be considered as stable and reliable. The vector **g** itself is represented in panels *b* and *c*, where it is clear that the direction of gyrotropy is not close to the magnetic field direction: it is close to $\mathbf{n}_{mean} \times \mathbf{B}$, the component along **B** being smaller and varying. This result reminds us that at boundaries such as the magnetopause, the strong gradients can break the isotropy as much, and even more here, than the magnetic field, so that gyrotropy can be around another vector than **B**. A similar remark had already been made in Belmont *et al.* (2012) concerning the modeling of a tangential discontinuity.

9. Dataset selection

In order to expand the results on a statistical basis, we selected a dataset of 146 crossings, chosen from the largest one reported in Nguyen *et al.* (2022) and Michotte De Welle *et al.* (2022). From this database, the following conditions were required in order to carry out an accurate study:

(i) MMS data are in burst mode.

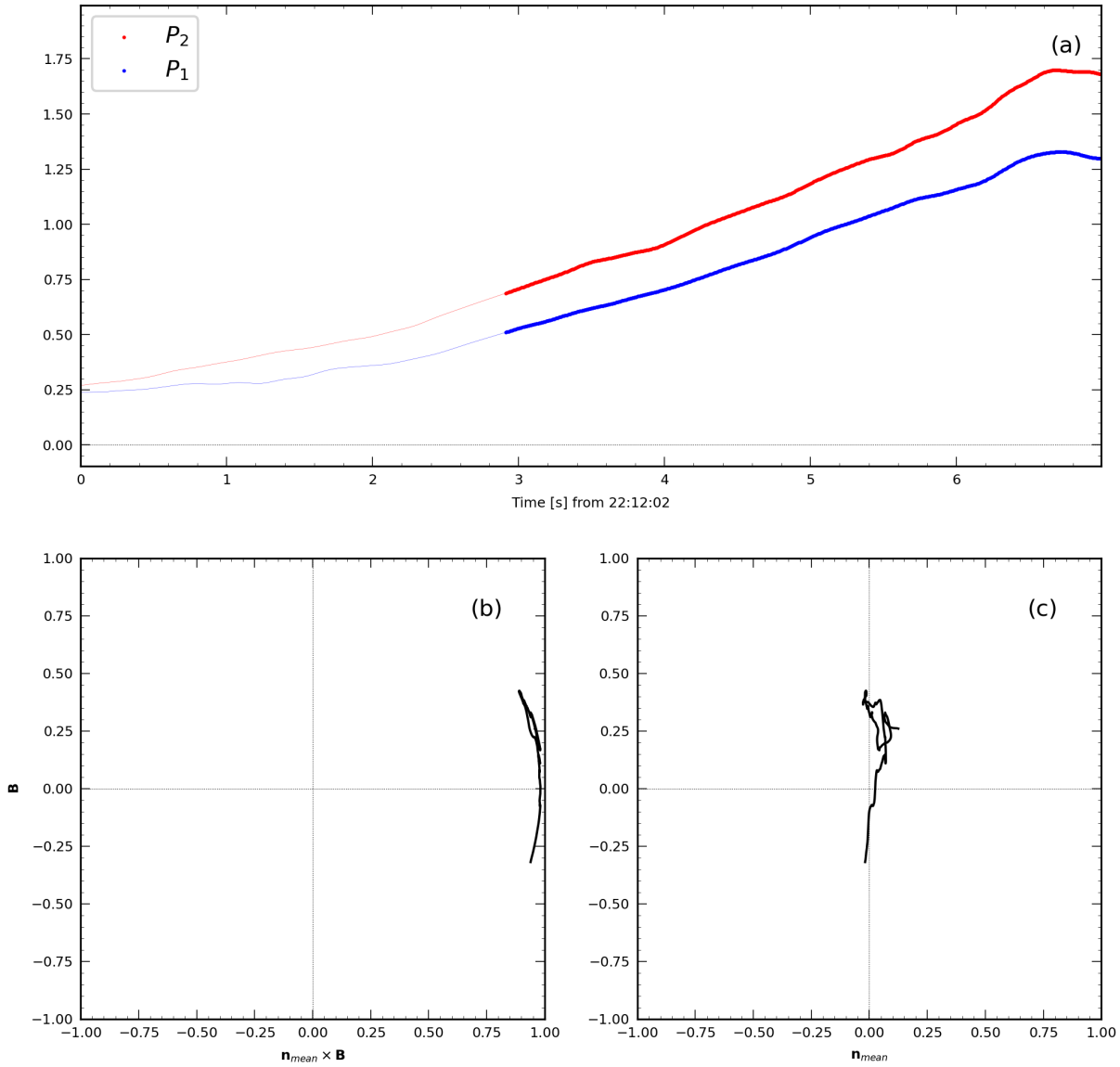

FIGURE 10. (*a*): Evolution of parameters P_1 and P_2. (*b*) and (*c*): projections of the gyrotropy direction in two planes. The ordinate is the direction of **B**, the abscissa is the direction of $\mathbf{n}_{mean} \times \mathbf{B}$ for panel (*b*) and $\mathbf{n}_{mean}$ for panel (*c*).

(ii) The crossing duration is between 3 and 15 seconds. Too short crossings do not have a sufficient number of points within the structure (ion measurements are every 0.15 s). Too long crossings may imply non-stationary structures.

(iii) Partial crossings are discarded. For that, we impose a density threshold less than 4 cm^{-3} in the magnetosphere and larger than 15 cm^{-3} in the magnetosheath.

(iv) Only cases presenting simultaneous crossing features in particles and magnetic field are considered, in order to compare normals computed at the same time.

In addition to these basic requirements, we also excluded some of the selected crossings for criteria that demand a more detailed analysis of the internal structure of the boundary. First, we excluded two-dimensional features. The quantitative determination of the dimensionality was done with the parameters presented in Rezeau *et al.* (2018) and the dimensionality index presented in Section 5.2, which are functions of the ratio between the eigenvalues of the gradient matrix. Namely, we considered only crossings with $D_1 > 0.9$ and $\mathcal{D}_{GF2} > 0.8$, these two parameters being averaged on the crossing interval. These parameters are calculated at each time

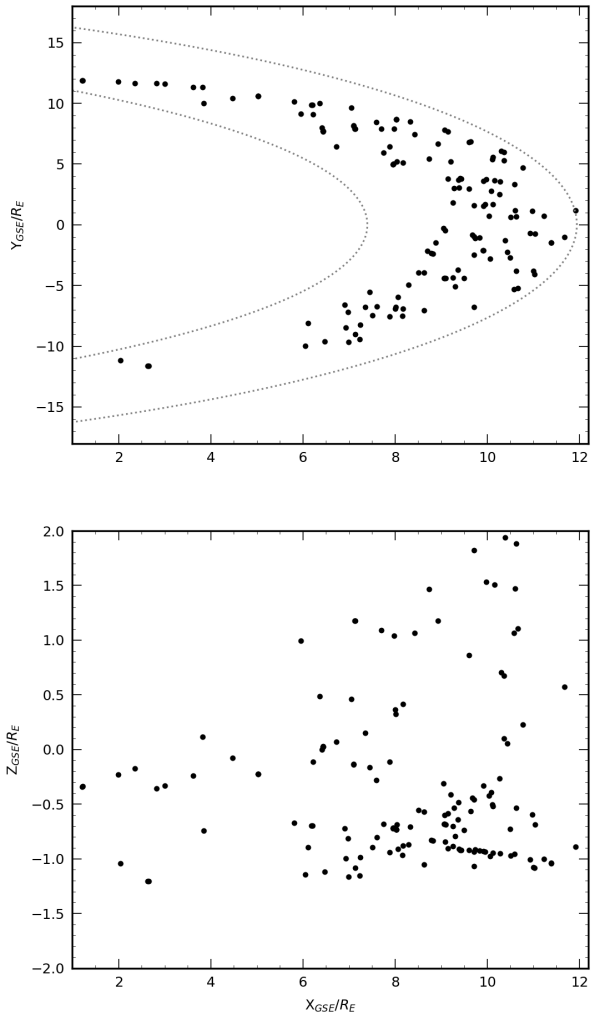

FIGURE 11. Spatial distribution of the selected database of crossings on the x, y (top) and x, z planes (bottom). The dashed grey lines represent the magnetopause location (Shue *et al.* 1997).

step but, due to waves and turbulence, attention must be paid that some of these two-dimensional features can be only local and insignificant for the profiles we are looking for. It is the reason why we use only the averaged values. The 146 selected crossings span from September 2015 to December 2017 (included). We can observe in Figure 11 that the crossings are evenly distributed in the x, y plane. Regarding the z component, there is a prevalence of cases at negative z.

The list of crossings can be found in Supplementary Materials. For each crossing, the classification and the physical quantities relevant for the study (normals, dimensionality index, non-gyrotropy index, and the main characteristic lengths discussed above for the case crossing) are included.

10. Statistical study of the magnetic hodograms

The previous results about the role of the FLR effects at the magnetopause are now carried out statistically. This study aims to generalize the results obtained from the case crossing studied in the previous section and to estimate the role played by FLRs at the magnetopause.

The database described above has first been used to perform a statistical study on the hodogram shapes, to determine how often linear hodograms are observed in magnetopause crossing. Having an estimation of the percentage of crossings that do not conform to CTD allows us to gauge how frequently the assumptions made by this theory do not accurately represent the magnetopause.

For this purpose, we separate the crossings in different classes, this classification being based on CTD distinctions and on the preceding findings:

(i) *Linear* crossings, *i.e*. straight lines not passing through the origin as in the above case study.
(ii) *Radial* crossings, including all linear crossings whose best fit line passes through the origin (considering uncertainty). These crossings correspond to CTD compressional discontinuities.
(iii) *Circular* crossings, when the distance from the origin is constant. These cases correspond to CTD rotational discontinuities.
(iv) *Other* crossings, whose features are not included in the previous classes. This class includes crossings with various features, *e.g*. circular hodograms not centered on the origin, crossing characterised by two different hodograms in two sub-intervals, etc., and crossings that do not have an obvious distinction between the previous classes, due to noise.

To classify each crossing, we only focus on its central time interval, where the gradients are maximum. By considering larger time intervals, the hodograms' shape becomes more complex because the variations out of this interval are generally unrelated to the main boundary jumps. Selecting only the middle part of the crossing provides simpler and more conformal hodograms. Even if the boundary jumps are not fully completed in this part, this will not prevent comparing the experimental results with CTD predictions since this theory, when valid, is based on conservation laws for any sub-interval of the discontinuity. When this theory fails to reproduce the observed properties, we can interpret those new features as coming from kinetic effects, therefore confirming the limitation of CTD to describe the magnetopause boundary. To that purpose, for each dataset we selected the crossing temporal interval following the algorithm used in Haaland *et al.* (2004, 2014) and Paschmann *et al.* (2018*b*) to estimate the spatial scale of the magnetopause (intervals are identified as 75% of the magnetic field $\mathbf{B}_L$ component variation).

The classification performed here differs from previous attempts to classify magnetopause hodograms, as seen in studies such as Sonnerup & Ledley (1974); Berchem & Russell (1982) and Panov *et al.* (2011). In these previous works, hodograms were categorized as C-shaped or S-shaped based on their form in the tangential plane. However, unlike those studies, we considered the central part of the crossing, rather than considering the entire temporal interval. Our classification of hodograms involves a two-step process:

(1) Visual Inspection: Initially, all hodograms are visually inspected to identify the cases that are clearly not linear or circular, which are classified separately as 'Others'. Additionally, a preliminary distinction is made between crossings with circular and linear features.
(2.a) Analysis of hodograms with possible circular features: For these crossings, we analyze the variation of the modulus of the magnetic field in the plane, allowing for a maximum possible variation of 20%. This accounts for factors such as turbulence and waves propagating alongside the magnetopause. Any crossings exceeding this 20% threshold are categorized as 'Others.'
(2.b) Analysis of hodograms with possible linear or radial features: These crossings undergo an initial assessment to confirm their linearity. This involves examining the width-to-length ratio of the crossing, with any ratio exceeding 20% classified as 'Other.' Finally, the remaining crossings are classified as either radial or linear based on whether their projection passes through the origin.

From this database, we found the following distribution:

- 36.3% (53/146) of the crossings present linear features.
- 2.7% (4/146) of the crossings present circular features (rotational discontinuity).
- 15.8% (23/146) of the crossings present radial features (compressional discontinuity).

- 45.2% (66/146) of the crossings could not be interpreted definitely as either of the three before (presenting more than one feature at the same time).

It follows that more than a third of the selected crossings show linear features, emphasizing that the fundamental role FLR effects have on magnetopause structure is found in a significant number of crossings.

It could be interesting to compare the above results with the several classifications that were previously published (see Liu *et al.* (2022) and references therein). These previous classifications were not based on the analysis of the rotational and compressional properties as done here, but on the normal component of the magnetic field and its magnitude (background and variation) (Smith 1973; Burlaga *et al.* 1977; Tsurutani & Smith 1979; Neugebauer *et al.* 2010). For such a comparison, however, one should take care that there are important differences in the definitions: in these previous classifications in particular, any discontinuity is named "tangential", whatever its other properties, as soon as the measured B_n is sufficiently smaller than B, the threshold for this ratio being for instance of the order of 0.3 (Liu *et al.* 2022; Smith 1973; Burlaga *et al.* 1977; Tsurutani & Smith 1979; Neugebauer *et al.* 2010). This is of course a very different approach from the one we use here since, even when B_n is small (and even if barely measurable), we consider that different kinds of discontinuities exist, with different properties.

As done for the case study above, it was possible to study on a statistical basis *i*) the ratio between the width of the magnetopause and the ion Larmor radius and *ii*) the non-gyrotropy index. For both parameters, the case study appears rather typical. On average, the magnetopause was found to be approximately 6.5 times the ion Larmor radius, only slightly smaller (6.1) for linear hodograms. Similarly, the non-gyrotropy index $D_{ng,\perp}$, has an average value of 0.07, only slightly higher (0.08) for linear hodograms. The $D_{ng,Aunai}$ index has even comparable averages for the four different classes. It therefore seems that, although non gyrotropy has been demonstrated above to play an important role, the non-gyrotropy index alone is not decisive for predicting unequivocally the shape of the hodograms. This question should be the subject of future works.

11. A comparison between the magnetic and the particles normals

For each crossing, both the magnetic and the particles normals were computed with the GF2 tool. Thanks to the high resolution of the MMS measurements, we can measure the local fluctuations of the normals inside the magnetopause around their mean values. However, in order to compare the magnetic and ion geometries, a single average normal was used for each case. The mean normal is obtained inside the same time interval as in the previous study.

To study the differences between the two normals, we compared them via their departure from the Shue model's normal (where the magnetopause is assumed to be a paraboloid, (Shue *et al.* 1997)). This normal was obtained using the solar wind and IMF properties from the OMNI data set (King & Papitashvili 2005). The time delay between the crossing time and the measurement time of the solar wind relevant parameters is estimated by using the propagation method used in Michotte De Welle *et al.* (2022) (which was adapted from Šafránková *et al.* (2002)). The procedure for acquiring these parameters is as follows: *i*) the distance from the bow shock's nose (where OMNI data are defined) to the crossing location, projected along the Earth-Sun axis, is estimated; *ii*) we estimate the solar wind's propagation time (t_{est}) between these two points, assuming an average solar wind velocity of 400 km/s; *iii*) the solar wind velocity V_{sw} is then determined from the OMNI dataset, averaging over a 2-minute interval centered on the crossing time adjusted by the time delay t_{est}; and (IV) ultimately, a final time delay is computed based on V_{sw}, which is subsequently utilized to obtain final values of solar wind and IMF parameters. The crossings for which OMNI data computed with this procedure are missing (10 out of 146) were left out of this analysis.

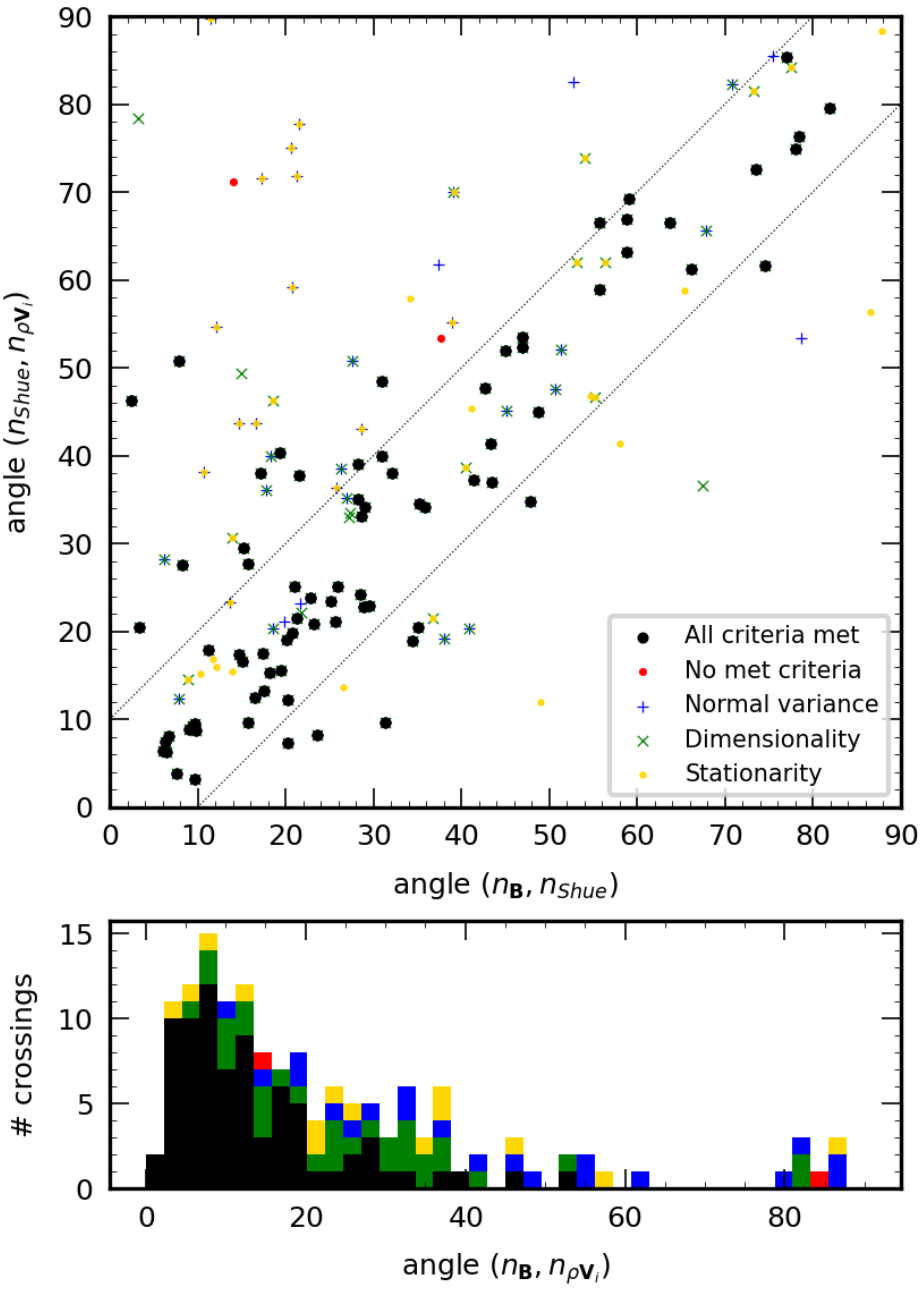

FIGURE 12. (*a*) Comparison between the angle between the theoretical normal (Shue *et al.* 1997) and the magnetic and ion normals, (*b*) Distribution of the angle between the magnetic and ion normals. Here the the markers for each point is chosen depending on whether each crossing respects the criteria on dimensionality, stationarity, and normal variance on the ions flux measurements (see Appendix C for further details). Colors in the histograms are used accordingly. Blue, green and yellow points indicate the crossing with small variance on the ions normal direction within the crossing, good one-dimensionality and good stationarity. Black points indicate the crossings respecting all criteria, red points not any criteria.

In Figure 12.*a*, we plot the angle between the nominal normal and the magnetic and particles normals respectively. In this figure we observe that most of the crossings are along the diagonal, corresponding to cases where the two normals, ionic and magnetic, are similar (82 points out of 146 are between the two thin lines, which indicate differences of $\pm 10^o$).

The cases are distributed throughout the plane, with many cases above 40^o, although we observe a cluster at lower angles, between zero and 30^o. The largest angles correspond to a magnetopause very far from the paraboloid shape assumed in Shue's model, which relies on the

assumption of a magnetopause at (or near) equilibrium. The departures are likely to be related to surface waves on the boundary itself.

Finally, the distribution of the angles between the two normals is shown in Fig. 12.*b*. Here we evidence again that most of the cases studied (82 out of 146) are below 20^o, with the maximum of the distribution at 10^o. However, we also observe again that several cases have much larger angles, up to 90^o. The strongest departures are problematic and deserve further investigation. This appears to be due to the more complex ion structure with respect to the magnetic one. As the criteria used for the dataset selection were built from magnetic data, they are not as relevant when considering ion normals. This is evidenced in Figure 12, where the colors indicate how several ion criteria are satisfied. These criteria concern respectively the dimensionality, the stationarity, and the variance of the normal direction. All details are given in Appendix C. Focusing on points respecting all the criteria for the ions flux (black markers and hodogram), we observe that only a few crossings are outside the diagonal. Only two of these crossings have angles above 40^o.

12. Conclusions

The study of the properties of the magnetopause is a very important issue for understanding the penetration of the solar wind plasma into the magnetosphere. In the theoretical part, we show that the notion of "quasi-tangential" discontinuity has to be introduced to complete the theory of discontinuities and understand the limit when the crossing fluxes tend to zero as in the magnetopause case. We emphasize that, in presence of anisotropy, the physical processes occurring inside the layer play a fundamental role because they are responsible for the conditions linking the downstream and upstream quantities. In particular, for thin current layers, the FLR corrections corresponding to the non-gyrotropic pressure tensor components must be taken into account.

The tool GF2 presented in the paper and used for determining the normal direction to the boundary derives from the MDD method. It includes in addition a fitting procedure, which allows introducing a part of the temporal information via a 4-point filtering of the data and adding constraints such as $\nabla \cdot \mathbf{B} = 0$. It is shown here to provide results quite compatible with the original method (when used with smoothed data), which is enough for drawing reliable physical conclusions on the magnetopause equilibrium. We expect that this approach could bring more precise information concerning the magnetopause gradients. Unfortunately, investigating this point in more detail cannot be done using MMS data but requires testing the tool in fully 3D kinetic simulations with realistic turbulence. This point is the subject of future work. Here, we have applied this tool on a particular crossing case and compared with other state-of-the-art normals. We have shown that the local normal (at each time step during the crossing) differs by less than ten degrees from the one calculated by all the other models. When averaging over the whole crossing, the normal obtained with the GF2 is even less than one degree apart from the normals from Shi *et al.* (2005); Denton *et al.* (2018).

Although we cannot claim to have achieved the ideal accuracy of about one degree, the reached accuracy is sufficient to evidence the correct physics at play, resumed as FLR effects. We have presented the results for a crossing observed by the four MMS spacecraft. For this crossing, the "linear" hodogram in the tangential plane shows that the boundary properties differ from those predicted by CTD. This discrepancy is explained by looking at the tangential components of the momentum equation, which highlights the role of the pressure tensor symmetries in the magnetopause equilibrium. This result agrees with the theoretical results of the first part and it is likely to hold more generally for all quasi-tangential discontinuities. The ion pressure tensor has been analyzed for this purpose. We have used two indices of non-gyrotropy, which both confirm the presence of a significant, even if small, non-gyrotropic part in this tensor. Furthermore, we have shown that the non-gyrotropy direction differs from the magnetic field one, aligning

779 approximately with the $\mathbf{n}_{mean} \times \mathbf{B}$ direction. Finally, the analysis of the VDFs directly confirms
780 the presence of non-gyrotropic distributions.

781 To show that our methodology applies to cases that CTD cannot handle, we have selected a
782 substantial number of magnetopause crossings with one-dimensional characteristics to have a
783 proper statistical basis for our findings. For all these crossings, we have plotted the hodogram
784 of the magnetic field in the tangential plane and classified them depending on their geometry.
785 Our results show that 36.3% of the crossings evidence clear linear features, incompatible with
786 the CTD description, while only 18.5% of the crossings show either circular or radial hodograms
787 as predicted by CTD. In other words, a significant number of cases escapes the classic theory,
788 proving that the relevance, even if not a predominance, of FLR effects at the magnetopause can
789 be generalized and that the case crossing presented in the first section is rather typical. It is well-
790 known that the linear version of the rotational discontinuity is the MHD shear Alfvén wave. Here
791 it appears that the magnetopause-like "quasi-tangential" discontinuities correspond in the same
792 way to the quasi-perpendicular "Kinetic Alfvén Waves" (Hasegawa & Uberoi 1982; Belmont &
793 Rezeau 1987; Cramer 2001).

794 Several papers have investigated the changes in rotational discontinuities when various non-
795 ideal effects are introduced. These theoretical papers have addressed the problem as a Riemann
796 problem using the methodology of a "piston" to study the formation of different discontinuities.
797 Some introduced FLRs and gyroviscosity in the layer while assuming isotropy on both sides
798 (Lyu & Kan 1989; Hau & Sonnerup 1991), and others introduced anisotropy everywhere while
799 assuming gyrotropy in the layer (Hau & Wang 2016). These different papers lead to different
800 conclusions; in particular concerning the role of electron inertia in the layer equilibrium.
801 It is worth noticing that the hodograms of **B** obtained with these theoretical studies were never
802 far from circular ones, contrary to the almost linear shapes shown in the present paper. Our
803 methodology has been different here: without assuming pre-defined forms for the non-ideal
804 terms, we look experimentally to the hodograms and the form of the **P** tensor and explain
805 theoretically how the second can explain the first ones.

806 Finally, we have used the same database of crossings to compare the geometric properties
807 of the magnetic and ion structures. We have compared the normal obtained from the magnetic
808 field and the ion flux measurements to the one expected from Shue *et al.* (1997) model. Many
809 crossings differ by more than 40 degrees from the nominal equilibrium condition, underlining a
810 very dynamical environment, but it is worth noticing that the two kinds of determination are most
811 often in agreement with each other, and therefore confirm the result. Furthermore, an accurate
812 study of the ion flux measurements have shown that crossings showing bigger discrepancies
813 between the magnetic field and ion flux normals are generally due to non-stationarities, non-one-
814 dimensionality, or variations in the ion flux normals. When excluding these cases from the study,
815 the ion and magnetic flux normals are compatible with only two crossings (over 77) showing
816 angles larger than forty degrees.

817 Data availability

818 Magnetospheric Multiscale satellite data were accessed through the MMS Science
819 Data Center, `https://lasp.colorado.edu/mms/sdc/public/`. Furthermore, all the
820 softwares employed, from interpolation of the data to the analysis itself, can be found at
821 `https://github.com/GiulioBallerini/Notebooks_FLR.git`.

822 The authors strongly thank Nicolas Aunai and Bayane Michotte de Welle for useful
823 discussions. The French involvement on MMS is supported by CNES and CNRS.

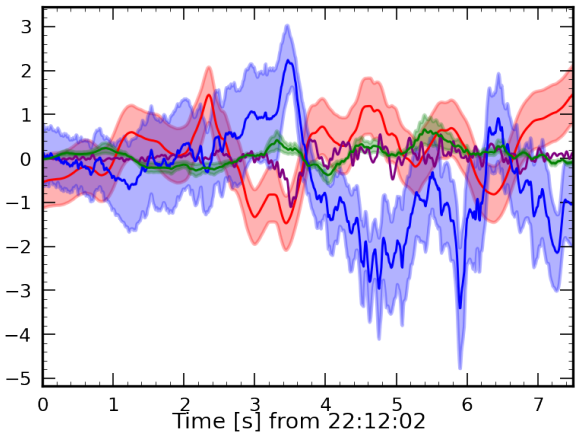

FIGURE 13. Terms of the momentum equation (units of $10^{-15} kg\, m/s^2$), projected on the local tangential direction ($\mathbf{t}_1$). Shaded regions are estimated uncertainties of the divergence of the pressure (red), the $\mathbf{J} \times \mathbf{B}$ (blue) and the classic inertial term (green).

Appendix A. Influence of averaging the $\mathbf{t}_1$ direction in the momentum equation balance

In this section, we investigate the impact of using an averaged tangential direction along the crossing on the outcomes concerning the role of the pressure tensor in the momentum equation. In Fig. 13 we show the projection of the terms of the momentum equation along the local $\mathbf{t}_1$ direction (*i.e.* without averaging). We observe here some reversals of the sign of the dominant terms, that were not observed in the averaged case. Nonetheless, it is still evident that the pressure tensor counterbalances the $\mathbf{J} \times \mathbf{B}$ term, hereby confirming our earlier findings.

Appendix B. Analysis of the gyroviscous effects

In this section, we use the magnetopause crossing analysed in detail above to study the validity of the gyroviscous interpretation. In particular, we employ the Braginskii gyroviscosity term (Braginskii 1965) as applied by Stasiewicz (1989) to the magnetopause, to analyze the pressure tensor. In this case, the pressure tensor is considered as the sum of an isotropic component, $\mathbf{P}_{iso}$ and a viscosity term, σ:

$$\mathbf{P}_i = \mathbf{P}_{iso} - \sigma \tag{B 1}$$

To investigate the viscosity term, we use the reference system where the normal direction is aligned with the z-axis (the x and y directions are chosen accordingly to form an orthogonal triad). By exploiting the definition of σ, we focus here on its projection along the normal yielding the following relation:

$$-\sigma.\mathbf{n} = \begin{pmatrix} P_{nx} \\ P_{ny} \\ P_{nn} \end{pmatrix} = \rho\nu \begin{pmatrix} 0 & b_n & b_y \\ -b_n & 0 & -b_x \\ b_y & -b_x & 0 \end{pmatrix} . \begin{pmatrix} u'_x \\ u'_y \\ u'_n \end{pmatrix} \tag{B 2}$$

Here ν is the gyroviscosity coefficient, $\hat{\mathbf{b}} = (b_x, b_y, b_z)$ the normalized magnetic field, and $\mathbf{u}' = (u'_x, u'_y, u'_z)$ is the vector of the spatial derivatives of the velocity components along the normal. We now consider the first two components of this equation, yielding the following expressions that allow us to compare the non-diagonal terms with the velocity changes:

$$\frac{P_{nx}}{\rho} = \nu(b_n u'_y + b_y u'_n) \tag{B 3}$$

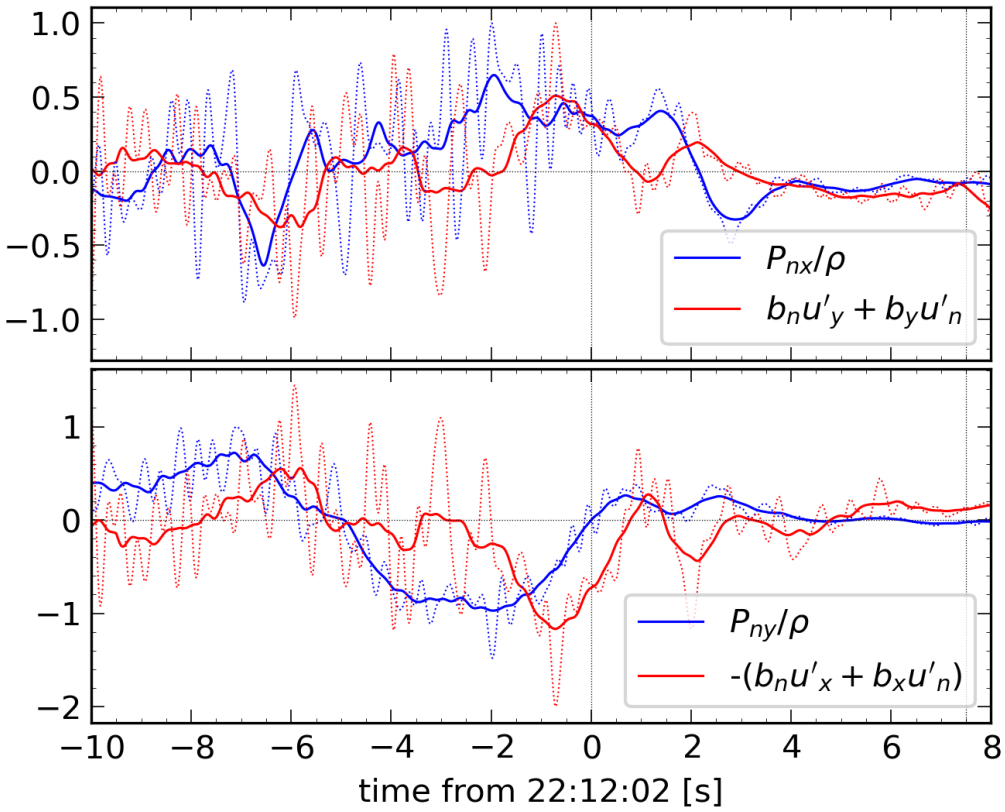

FIGURE 14. Left (blue) and right (red) hand sides for Equations B 3 (top) and B 4 (bottom). Thin-dotted lines correspond to the real-time values while thick lines to an averaged window of 1 *s*. All terms are normalized.

$$\frac{P_{ny}}{\rho} = -\nu(b_n u'_x + b_x u'_n) \tag{B 4}$$

The terms of these equations are shown (normalized) in Figure 14. Here we observe a fairly good correlation between the non-diagonal terms of the pressure tensor and the spatial derivatives of the flow velocity.

Appendix C. Quality indices for the ion normals

In the absence of additional caution, Figure 12 shows that the angle between the normal obtained with the magnetic field and the one with the ion flux reaches very high values, up to 90 degrees. This result requires a more accurate study, as the criteria used for the dataset selection are based on the magnetic field (except for the threshold imposed on the density values).
To interpret the results accurately, the following parameters were considered:

(i) Dimensionality of ion flux. For this purpose, we exploit the dimensionality index defined in Equation 5.11, computed from the ion flux measurements.
(ii) Stationarity of the ion flux measurements. To evaluate stationarity, we exploit the GF2 tool. Specifically, we consider the quality of the fit of the gradient matrix as an index of stationarity. By defining $\mathbf{D} = \mathbf{G}_{\text{fit}} - \mathbf{G}$ we can introduce the stationarity index:

$$S = \frac{\text{Tr}(\mathbf{D}.\mathbf{D}^T)}{\text{Tr}(\mathbf{G}.\mathbf{G}^T)} \tag{C 1}$$

Since for a truly stationary magnetopause, S should be equal to zero, deviations from zero suggest potential non-stationarity.

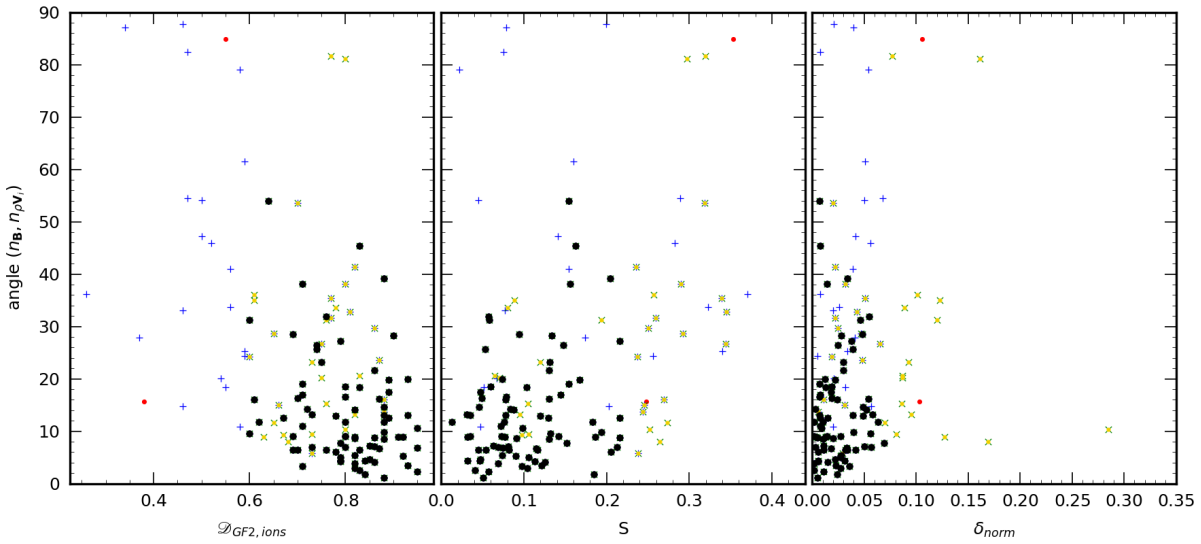

FIGURE 15. Dimensionality (left), stationarity (center), and normal variance (right) averaged for each crossing as a function of the angle between the magnetic field normal and the ion flux one. Green, blue, and yellow indicate crossings respecting the $\mathcal{D}_{GF2,ions} > 0.6$, $\delta_{norm} > 0.07$, $S > 0.22$ criteria individually. Black dots indicate the crossings for which all the criteria are met, and red dots (two cases) when no condition is met.

(iii) Variance of the normal. In some crossings of the database, the normal associated with ion flux exhibits local differences with respect to the mean value, such as fluctuations or rotations within a plane, with one component varying within the crossing. In these cases, the ion flux is therefore characterized by more complex structures and the mean normal is not meaningful. To exclude such cases, we examined the variation of the normal around the mean value, defined as follows:

$$\delta_{norm} =< |\mathbf{n}_i - \mathbf{n}_{mean,i}|^2 > \qquad \text{(C 2)}$$

Small values of δ_{norm} indicate almost constant normals.

The average values of these three parameters for each crossing are shown in Figure 15 as a function of the angles between the normal of the magnetic field and the ion flux. We observe here that crossings showing the largest angles occur when at least one of these conditions fails. To select the cases for which the ions are characterized by a stationary and one-dimensional structure, for which the normal has no variations around the mean value, we applied the following thresholds: $\mathcal{D}_{GF2,ions} > 0.6$, $\delta_{norm} > 0.07$, $S > 0.22$. Specifically, crossings individually meeting one of these criteria are shown in green, blue, and yellow, respectively. When all criteria are met, crossings are indicated by black dots. This Figure underlines a correlation between the difference between the two normals and the values of these three parameters, showing how cases with higher $\mathcal{D}_{GF2,ions}$ and smaller δ_{norm} and S are the ones with smaller differences between the two normals.

REFERENCES

ABRAHAM-SHRAUNER, BARBARA 1967 Propagation of hydromagnetic waves through an anisotropic plasma. *Journal of Plasma Physics* **1** (3), 361–378.

AUNAI, NICOLAS, HESSE, MICHAEL & KUZNETSOVA, MARIA 2013 Electron nongyrotropy in the context of collisionless magnetic reconnection. *Physics of Plasmas* **20** (9), 092903, arXiv: https://doi.org/10.1063/1.4820953.

AUNAI, N., HESSE, M., LAVRAUD, B., DARGENT, J. & SMETS, R. 2016 Orientation of the X-line in asymmetric magnetic reconnection. *Journal of Plasma Physics* **82** (4), 535820401.

AUNAI, N., RETINÒ, A., BELMONT, G., SMETS, R., LAVRAUD, B. & VAIVADS, A. 2011 The proton pressure tensor

as a new proxy of the proton decoupling region in collisionless magnetic reconnection. *Annales Geophysicae* **29** (9), 1571–1579.

Belmont, G., Aunai, N. & Smets, R. 2012 Kinetic equilibrium for an asymmetric tangential layer. *Physics of Plasmas* **19** (2), 022108.

Belmont, Gérard, Grappin, Roland, Mottez, Fabrice, Pantellini, Filippo & Pelletier, Guy 2014 *Collisionless plasmas in astrophysics*. Wiley.

Belmont, G. & Rezeau, Laurence 1987 Finite Larmor radius effects: the two-fluid approach. *Annales Geophysicae* pp. vol. 5, no2, pp. 59–69.

Belmont, Gérard, Rezeau, Laurence, Riconda, Caterina & Zaslavsky, Arnaud 2019 *Introduction to plasma physics*. ISTE Press.

Berchem, Jean & Russell, C. T. 1982 Magnetic field rotation through the magnetopause: ISEE 1 and 2 observations. *Journal of Geophysical Research: Space Physics* **87** (A10), 8139–8148.

Bertucci, C. 2005 Structure of the magnetic pileup boundary at mars and venus. *Journal of Geophysical Research* **110**, A01209.

Braginskii, S. I. 1965 Transport Processes in a Plasma. *Reviews of Plasma Physics* **1**, 205, aDS Bibcode: 1965RvPP....1..205B.

Burch, J. L. & Phan, T. D. 2016 Magnetic reconnection at the dayside magnetopause: Advances with mms. *Geophysical Research Letters* **43** (16), 8327–8338.

Burlaga, L. F., Lemaire, J. F. & Turner, J. M. 1977 Interplanetary current sheets at 1 AU. *Journal of Geophysical Research* **82** (22), 3191–3200.

Chanteur, Gérard 1998 Spatial interpolation for four spacecraft: Theory. *ISSI Scientific Reports Series* **1**, 349–370, ADS Bibcode: 1998ISSIR...1..349C.

Chao, J.K. 1970 *Interplanetary collisionless shock waves*. Vita. Bibliography: leaves 148-150. Sc D.

Chasapis, A., Retinò, A., Sahraoui, F., Vaivads, A., Khotyaintsev, Yu. V., Sundkvist, D., Greco, A., Sorriso-Valvo, L. & Canu, P. 2015 THIN CURRENT SHEETS AND ASSOCIATED ELECTRON HEATING IN TURBULENT SPACE PLASMA. *The Astrophysical Journal* **804** (1), L1.

Coates, A.J. 1997 Ionospheres and magnetospheres of comets. *Advances in Space Research* **20** (2), 255–266.

Colburn, David S. & Sonett, Charles P. 1966 Discontinuities in the solar wind. *Space Science Reviews* **5**, 439–506.

Coppi, B., Laval, G. & Pellat, R. 1966 Dynamics of the geomagnetic tail. *Physical Review Letters* **26**, 1207–1210.

Coroniti, F. V. 1980 On the tearing mode in quasi-neutral sheets. *Journal of Geophysical Research: Space Physics* **85** (A12), 6719–6728.

Cramer, Neil F. 2001 *The Physics of Alfvén Waves*. John Wiley and Sons, Ltd.

De Keyser, J. 2008 Empirical reconstruction. *SSI Scientific Reports Series* **8**, 91–98.

Denton, R. E., Sonnerup, B. U. Ö., Hasegawa, H., Phan, T. D., Russell, C. T., Strangeway, R. J., Giles, B. L., Gershman, D. & Torbert, R. B. 2016 Motion of the MMS spacecraft relative to the magnetic reconnection structure observed on 16 October 2015 at 1307 UT. *Geophysical Research Letters* **43** (11), 5589–5596.

Denton, R. E., Sonnerup, B. U. Ö., Russell, C. T., Hasegawa, H., Phan, T.-D., Strangeway, R. J., Giles, B. L., Ergun, R. E, Lindqvist, P.-A., Torbert, R. B., Burch, J. L & Vines, S. K. 2018 Determining $\boldsymbol{L}$ - $\boldsymbol{M}$ - $\boldsymbol{N}$ Current Sheet Coordinates at the Magnetopause From Magnetospheric Multiscale Data. *Journal of Geophysical Research: Space Physics* **123** (3), 2274–2295.

Denton, R. E., Torbert, R. B., Hasegawa, H., Dors, I., Genestreti, K. J., Argall, M. R., Gershman, D., Le Contel, O., Burch, J. L., Russell, C. T., Strangeway, R. J., Giles, B. L. & Fischer, D. 2020 Polynomial reconstruction of the reconnection magnetic field observed by multiple spacecraft **125** (2), e2019JA027481.

Dorville, Nicolas, Belmont, Gérard, Aunai, Nicolas, Dargent, Jérémy & Rezeau, Laurence 2015*a* Asymmetric kinetic equilibria: Generalization of the BAS model for rotating magnetic profile and non-zero electric field. *Physics of Plasmas* **22** (9), 092904.

Dorville, Nicolas, Belmont, Gérard, Rezeau, Laurence, Grappin, Roland & Retinò, Alessandro 2014 Rotational/compressional nature of the magnetopause: Application of the BV technique on a magnetopause case study. *Journal of Geophysical Research: Space Physics* **119** (3), 1898–1908.

Dorville, Nicolas, Haaland, Stein, Anekallu, Chandrasekhar, Belmont, Gérard & Rezeau, Laurence 2015*b* Magnetopause orientation: Comparison between generic residue analysis and BV method: GRA/BV COMPARISON. *Journal of Geophysical Research: Space Physics* **120** (5), 3366–3379.

Dunlop, M.W., Southwood, D.J., Glassmeier, K.-H. & Neubauer, F.M. 1988 Analysis of multipoint magnetometer data. *Advances in Space Research* **8** (9-10), 273–277.

Ergun, R. E., Tucker, S., Westfall, J., Goodrich, K. A., Malaspina, D. M., Summers, D., Wallace, J., Karlsson, M., Mack, J., Brennan, N., Pyke, B., Withnell, P., Torbert, R., Macri, J., Rau, D., Dors, I., Needell, J., Lindqvist, P.-A., Olsson, G. & Cully, C. M. 2016 The axial double probe and fields signal processing for the MMS mission. *Space Science Reviews* **199** (1), 167–188.

Escoubet, C.P., Fehringer, M. & Goldstein, M.L. 2001 Introduction The Cluster mission. *Annales Geophysicae* **19** (10-12).

Escoubet, C.P., Schmidt, R. & Goldstein, M.L. 1997 Cluster -Science and mission overview. *Space Science Reviews* **79** (11-32).

Frisch, Uriel 1995 *Turbulence: The Legacy of A.N. Kolmogorov*, 1st edn. Cambridge University Press.

Fuselier, S. A., Trattner, K. J. & Petrinec, S. M. 2011 Antiparallel and component reconnection at the dayside magnetopause: MULTIPLE MAGNETOPAUSE RECONNECTION. *Journal of Geophysical Research: Space Physics* **116** (A10), n/a–n/a.

Galeev, A.A. 1979 Reconnection in the magnetotail. *Space Science Reviews* **23** (3).

Genestreti, K. J., Nakamura, T. K. M., Nakamura, R., Denton, R. E., Torbert, R. B., Burch, J. L., Plaschke, F., Fuselier, S. A., Ergun, R. E., Giles, B. L. & Russell, C. T. 2018 How Accurately Can We Measure the Reconnection Rate $\boldsymbol{E}_{m}$ for the MMS Diffusion Region Event of 11 July 2017? *Journal of Geophysical Research: Space Physics* **123** (11), 9130–9149.

Gosling, J. T., Asbridge, J. R., Bame, S. J., Feldman, W. C., Paschmann, G., Sckopke, N. & Russell, C. T. 1982 Evidence for quasi-stationary reconnection at the dayside magnetopause. *Journal of Geophysical Research: Space Physics* **87** (A4), 2147–2158.

Gunell, H., Nilsson, H., Stenberg, G., Hamrin, M., Karlsson, T., Maggiolo, R., André, M., Lundin, R. & Dandouras, I. 2012 Plasma penetration of the dayside magnetopause. *Physics of Plasmas* **19** (7), 072906.

Haaland, S., Hasegawa, H., Paschmann, G., Sonnerup, B. & Dunlop, M. 2021 20 Years of Cluster Observations: The Magnetopause. *Journal of Geophysical Research: Space Physics* **126** (8), e2021JA029362.

Haaland, S., Reistad, J., Tenfjord, P., Gjerloev, J., Maes, L., DeKeyser, J., Maggiolo, R., Anekallu, C. & Dorville, N. 2014 Characteristics of the flank magnetopause: Cluster observations. *Journal of Geophysical Research: Space Physics* **119** (11), 9019–9037.

Haaland, S. E., Sonnerup, B. U. Ö., Dunlop, M. W., Balogh, A., Georgescu, E., Hasegawa, H., Klecker, B., Paschmann, G., Puhl-Quinn, P., Rème, H., Vaith, H. & Vaivads, A. 2004 Four-spacecraft determination of magnetopause orientation, motion and thickness: comparison with results from single-spacecraft methods. *Annales Geophysicae* **22** (4), 1347–1365.

Hasegawa, Akira & Uberoi, Chanchal 1982 *The Alfvén wave*. Oak Ridge, TN (USA): U.S. Department of Energy Technical Information Center.

Hasegawa, H., Sonnerup, B. U. Ö., Klecker, B., Paschmann, G., Dunlop, M. W. & Rème, H. 2005 Optimal reconstruction of magnetopause structures from Cluster data. *Annales Geophysicae* **23** (3), 973–982.

Hau, L.-N. & Sonnerup, B. U. Ö 1991 Self-consistent gyroviscous fluid model of rotational discontinuities **96**, 15767–15778.

Hau, L.-N. & Wang, B.-J. 2016 Slow shock and rotational discontinuity in MHD and hall MHD models with anisotropic pressure **121** (7), 6245–6261.

Hesse, Michael, Aunai, Nicolas, Sibeck, David & Birn, Joachim 2014 On the electron diffusion region in planar, asymmetric, systems. *Geophysical Research Letters* **41** (24), 8673–8680.

Hesse, Michael, Neukirch, Thomas, Schindler, Karl, Kuznetsova, Masha & Zenitani, Seiji 2011 The Diffusion Region in Collisionless Magnetic Reconnection. *Space Science Reviews* **160** (1-4), 3–23.

Hudson, P.D. 1971 Rotational discontinuities in an anisotropic plasma. *Planetary and Space Science* **19** (12), 1693–1699.

Jeffrey, A. & Taniuti, T. 1964 *Non-linear Wave Propagation: With Applications to Physics and Magnetohydrodynamics (Mathematics in science and engineering ; v. 9)*. Academic Press.

King, J. H. & Papitashvili, N. E. 2005 Solar wind spatial scales in and comparisons of hourly Wind and ACE plasma and magnetic field data. *Journal of Geophysical Research: Space Physics* **110** (A2), 2004JA010649.

Kivelson, M. G. & Russell, C. T., ed. 1995 *Introduction to space physics*. Cambridge University Press, OCLC: 1124679918.

Lallement, R. 2001 Heliopause and asteropauses. *Astrophysics and Space Science* **277**, 205–2017.

Landau, L. D. & Lifshitz, E. M. 1987 *Fluid mechanics*. Pergamon Press.

Lindqvist, P.-A., Olsson, G., Torbert, R. B., King, B., Granoff, M., Rau, D., Needell, G., Turco, S., Dors, I., Beckman, P., Macri, J., Frost, C., Salwen, J., Eriksson, A., Åhlén, L., Khotyaintsev, Y. V., Porter, J., Lappalainen, K., Ergun, R. E., Wermeer, W. & Tucker, S. 2016 The spin-plane double probe electric field instrument for MMS. *Space Science Reviews* **199** (1), 137–165.

Liu, Yi-Hsin, Hesse, M., Cassak, P. A., Shay, M. A., Wang, S. & Chen, L.-J. 2018 On the collisionless asymmetric magnetic reconnection rate. *Geophysical Research Letters* **45** (8), 3311–3318.

Liu, Y. Y., Fu, H. S., Cao, J. B., Wang, Z., He, R. J., Guo, Z., Xu, Y. & Yu, Y. 2022 Magnetic discontinuities in the solar wind and magnetosheath: Magnetospheric multiscale mission (mms) observations. *The Astrophysical Journal* **930**.

Lundin, R. & Dubinin, E. 1984 Solar wind energy transfer regions inside the dayside magnetopause—I. Evidence for magnetosheath plasma penetration. *Planetary and Space Science* **32** (6), 745–755.

Lynn, Y. M. 1967 Discontinuities in an anisotropic plasma. *Physics of Fluids* **10** (10), 2278.

Lyu, L. H. & Kan, J. R. 1989 Structures of alfvén shocks: S-shaped magnetic hodogram observed at the magnetopause **16** (5), 349–352.

McPherron, Robert L. 1979 Magnetospheric substorms. *Reviews of Geophysics* **17** (4), 657–681.

Michotte De Welle, B., Aunai, N., Nguyen, G., Lavraud, B., Génot, V., Jeandet, A. & Smets, R. 2022 Global Three-Dimensional Draping of Magnetic Field Lines in Earth's Magnetosheath From In-Situ Spacecraft Measurements. *Journal of Geophysical Research: Space Physics* **127** (12), e2022JA030996.

Neubauer, Fritz Manfred 1970 Jump relations for shocks in an anisotropic magnetized plasma. *Zeitschrift für Physik A Hadrons and nuclei* **237** (3), 205–223.

Neugebauer, M. 2006 Comment on the abundances of rotational and tangential discontinuities in the solar wind. *Journal of Geophysical Research: Space Physics* **111** (A4), 2005JA011497.

Neugebauer, Marcia, Giacalone, Joe, Maksimovic, M., Issautier, K., Meyer-Vernet, N., Moncuquet, M. & Pantellini, F. 2010 Progress in the Study of Interplanetary Discontinuities. In *AIP Conference Proceedings*, pp. 194–197. Saint-Malo, (France).

Nguyen, G., Aunai, N., Michotte De Welle, B., Jeandet, A., Lavraud, B. & Fontaine, D. 2022 Massive Multi-Mission Statistical Study and Analytical Modeling of the Earth's Magnetopause: 1. A Gradient Boosting Based Automatic Detection of Near-Earth Regions. *Journal of Geophysical Research: Space Physics* **127** (1), e2021JA029773.

Otto, Antonius 2005 *The Magnetosphere*, pp. 133–192. Berlin, Heidelberg: Springer Berlin Heidelberg.

Panov, E. V., Artemyev, A. V., Nakamura, R. & Baumjohann, W. 2011 Two types of tangential magnetopause current sheets: Cluster observations and theory: TANGENTIAL MAGNETOPAUSE STRUCTURE. *Journal of Geophysical Research: Space Physics* **116** (A12), n/a–n/a.

Parks, George K. 2019 *Physics of space plasmas: an introduction*. *"The Advanced book program."* . Routledge, Taylor & Francis Group.

Paschmann, Götz 1984 Plasma and particle observations at the magnetopause: Implications for reconnection. In *Geophysical Monograph Series* (ed. Edward W. Hones), , vol. 30, pp. 114–123. Washington, D. C.: American Geophysical Union.

Paschmann, G., Haaland, S., Sonnerup, B. & Knetter, T. 2013 Discontinuities and Alfvénic fluctuations in the solar wind. *Annales Geophysicae* **31** (5), 871–887.

Paschmann, G., Haaland, S. E., Phan, T. D., Sonnerup, B. U. Ö., Burch, J. L., Torbert, R. B., Gershman, D. J., Dorelli, J. C., Giles, B. L., Pollock, C., Saito, Y., Lavraud, B., Russell, C. T., Strangeway, R. J., Baumjohann, W. & Fuselier, S. A. 2018*a* Large-Scale Survey of the Structure of the Dayside Magnetopause by MMS. *Journal of Geophysical Research: Space Physics* **123** (3), 2018–2033.

Paschmann, G., Haaland, S. E., Phan, T. D., Sonnerup, B. U. Ö., Burch, J. L., Torbert, R. B., Gershman, D. J., Dorelli, J. C., Giles, B. L., Pollock, C., Saito, Y., Lavraud, B., Russell, C. T., Strangeway, R. J., Baumjohann, W. & Fuselier, S. A. 2018*b* Large-Scale Survey of the Structure of the Dayside Magnetopause by MMS. *Journal of Geophysical Research: Space Physics* **123** (3), 2018–2033.

Passot, T. & Sulem, P. L. 2006 A fluid model with finite Larmor radius effects for mirror mode dynamics. *Journal of Geophysical Research: Space Physics* **111** (A4), 2005JA011425.

Phan, T. D., Kistler, L. M., Klecker, B., Haerendel, G., Paschmann, G., Sonnerup, B. U. Ö., Baumjohann, W., Bavassano-Cattaneo, M. B., Carlson, C. W., DiLellis, A. M., Fornacon, K.-H., Frank, L. A., Fujimoto, M., Georgescu, E., Kokubun, S., Moebius, E., Mukai, T., Øieroset, M., Paterson, W. R. & Reme, H. 2000 Extended magnetic reconnection at the Earth's magnetopause from detection of bi-directional jets. *Nature* **404** (6780), 848–850.

Phan, T. D., Shay, M. A., Gosling, J. T., Fujimoto, M., Drake, J. F., Paschmann, G., Oieroset, M., Eastwood, J. P. & Angelopoulos, V. 2013 Electron bulk heating in magnetic reconnection at Earth's magnetopause: Dependence on the inflow Alfvén speed and magnetic shear. *Geophysical Research Letters* **40** (17), 4475–4480.

Pollock, C., Moore, T., Jacques, A., Burch, J., Gliese, U., Saito, Y., Omoto, T., Avanov, L., Barrie, A., Coffey, V., Dorelli, J., Gershman, D., Giles, B., Rosnack, T., Salo, C., Yokota, S., Adrian, M., Aoustin, C., Auletti, C., Aung, S., Bigio, V., Cao, N., Chandler, M., Chornay, D., Christian, K., Clark, G., Collinson, G., Corris, T., De Los Santos, A., Devlin, R., Diaz, T., Dickerson, T., Dickson, C., Diekmann, A., Diggs, F., Duncan, C., Figueroa-Vinas, A., Firman, C., Freeman, M., Galassi, N., Garcia, K., Goodhart, G., Guererro, D., Hageman, J., Hanley, J., Hemminger, E., Holland, M., Hutchins, M., James, T., Jones, W., Kreisler, S., Kujawski, J., Lavu, V., Lobell, J., LeCompte, E., Lukemire, A., MacDonald, E., Mariano, A., Mukai, T., Narayanan, K., Nguyan, Q., Onizuka, M., Paterson, W., Persyn, S., Piepgrass, B., Cheney, F., Rager, A., Raghuram, T., Ramil, A., Reichenthal, L., Rodriguez, H., Rouzaud, J., Rucker, A., Saito, Y., Samara, M., Sauvaud, J.-A., Schuster, D., Shappirio, M., Shelton, K., Sher, D., Smith, D., Smith, K., Smith, S., Steinfeld, D., Szymkiewicz, R., Tanimoto, K., Taylor, J., Tucker, C., Tull, K., Uhl, A., Vloet, J., Walpole, P., Weidner, S., White, D., Winkert, G., Yeh, P.-S. & Zeuch, M. 2016 Fast plasma investigation for magnetospheric multiscale. *Space Science Reviews* **199** (1), 331–406.

Rezeau, L., Belmont, Gerard, Manuzzo, Roberto, Aunai, Nicolas & Dargent, J. 2018 Analyzing the magnetopause internal structure: New possibilities offered by mms tested in a case study. *Journal of Geophysical Research: Space Physics* **123**.

Richardson, J. D., Burlaga, L. F., Elliott, H., Kurth, W. S., Liu, Y. D. & von Steiger, R. 2022 Observations of the outer heliosphere, heliosheath, and interstellar medium. *Space Science Reviews* **218** (4), 35.

Russell, C. T., Anderson, B. J., Baumjohann, W., Bromund, K. R., Dearborn, D., Fischer, D., Le, G., Leinweber, H. K., Leneman, D., Magnes, W., Means, J. D., Moldwin, M. B., Nakamura, R., Pierce, D., Plaschke, F., Rowe, K. M., Slavin, J. A., Strangeway, R. J., Torbert, R., Hagen, C., Jernej, I., Valavanoglou, A. & Richter, I. 2016 The magnetospheric multiscale magnetometers. *Space Science Reviews* **199** (1), 189–256.

Shi, Q. Q., Shen, C., Pu, Z. Y., Dunlop, M. W., Zong, Q.-G., Zhang, H., Xiao, C. J., Liu, Z. X. & Balogh, A. 2005 Dimensional analysis of observed structures using multipoint magnetic field measurements: Application to cluster: STRUCTURE DIMENSIONALITY DETERMINATION. *Geophysical Research Letters* **32** (12), n/a–n/a.

Shi, Q. Q., Tian, A. M., Bai, S. C., Hasegawa, H., Degeling, A. W., Pu, Z. Y., Dunlop, M., Guo, R. L., Yao, S. T., Zong, Q.-G., Wei, Y., Zhou, X.-Z., Fu, S. Y. & Liu, Z. Q. 2019 Dimensionality, Coordinate System and Reference Frame for Analysis of In-Situ Space Plasma and Field Data. *Space Science Reviews* **215** (4), 35.

Shue, J.-H., Chao, J. K., Fu, H. C., Russell, C. T., Song, P., Khurana, K. K. & Singer, H. J. 1997 A new functional form to study the solar wind control of the magnetopause size and shape. *Journal of Geophysical Research: Space Physics* **102** (A5), 9497–9511.

Smith, Edward J. 1973 Identification of interplanetary tangential and rotational discontinuities. *Journal of Geophysical Research* **78** (13), 2054–2063.

Sonnerup, B. & Scheible, M. 1998 Minimum and maximum variance analysis. In *Analysis Methods for Multi- Spacecraft Data*, pp. pp. 185–220. Int. Space Sci. Inst./Eur. Space Agency, Bern/Paris.

Sonnerup, B. U. O. & Ledley, B. G. 1974 Magnetopause rotational forms. *Journal of Geophysical Research* **79** (28), 4309–4314.

Sonnerup, B. U. Ö & Cahill, L. J. 1967 Magnetopause structure and attitude from Explorer 12 observations. *Journal of Geophysical Research* **72** (1), 171.

Sonnerup, B. U. Ö., Haaland, S., Paschmann, G., Dunlop, M. W., Rème, H. & Balogh, A. 2006 Orientation and motion of a plasma discontinuity from single-spacecraft measurements: Generic residue analysis of Cluster data. *Journal of Geophysical Research: Space Physics* **111** (A5), 2005JA011538.

Stasiewicz, Krzysztof 1989 A fluid finite ion larmor radius model of the magnetopause layer. *Journal of Geophysical Research* **94**, 8827–8834.

Stasiewicz, K. 1993 Finite larmor radius effects in the magnetosphere **65** (3), 221–252.

Swisdak, M., Rogers, B. N., Drake, J. F. & Shay, M. A. 2003 Diamagnetic suppression of component magnetic reconnection at the magnetopause. *Journal of Geophysical Research: Space Physics* **108** (A5), 2002JA009726.

Torbert, R. B., Burch, J. L., Giles, B. L., Gershman, D., Pollock, C. J., Dorelli, J., Avanov, L., Argall, M. R., Shuster, J., Strangeway, R. J., Russell, C. T., Ergun, R. E., Wilder, F. D., Goodrich, K.,

Faith, H. A., Farrugia, C. J., Lindqvist, P.-A., Phan, T., Khotyaintsev, Y., Moore, T. E., Marklund, G., Daughton, W., Magnes, W., Kletzing, C. A. & Bounds, S. 2016 Estimates of terms in Ohm's law during an encounter with an electron diffusion region. *Geophysical Research Letters* **43** (12), 5918–5925.

Trattner, K. J., Petrinec, S. M. & Fuselier, S. A. 2021 The Location of Magnetic Reconnection at Earth's Magnetopause. *Space Science Reviews* **217** (3), 41.

Tsurutani, B.T., Zhou, X.-Y., Vasyliunas, V.M., Haerendel, G., Arballo, J.K. & Lakhina, G.S. 2001 Interplanetary Shocks, Magnetopause Boundary Layers and Dayside Auroras: The Importance of a Very Small Magnetospheric Region. *Surveys in Geophysics* **22** (2), 101–130.

Tsurutani, Bruce T. & Smith, Edward J. 1979 Interplanetary discontinuities: Temporal variations and the radial gradient from 1 to 8.5 AU. *Journal of Geophysical Research: Space Physics* **84** (A6), 2773–2787.

Vines, S. K., Fuselier, S. A., Trattner, K. J., Petrinec, S. M. & Drake, J. F. 2015 Ion acceleration dependence on magnetic shear angle in dayside magnetopause reconnection. *Journal of Geophysical Research: Space Physics* **120** (9), 7255–7269.

Šafránková, J., Němeček, Z., Dušík, Š., Přech, L., Sibeck, D. G. & Borodkova, N. N. 2002 The magnetopause shape and location: a comparison of the Interball and Geotail observations with models. *Annales Geophysicae* **20** (3), 301–309.

9.2 Ballerini et al (2024)

Astronomy & Astrophysics manuscript no. output
June 13, 2024

Whistler-mode waves in the tail of Mercury's magnetosphere: a numerical study

Giulio Ballerini[1,2], Federico Lavorenti[2,3], Francesco Califano[2], and Pierre Henri[3,4]

[1] LPP, CNRS/Sorbonne Université/Université Paris-Saclay/Observatoire de Paris/Ecole Polytechnique Institut Polytechnique de Paris, Palaiseau, France
e-mail: giulio.ballerini@lpp.polytechnique.fr
[2] Dipartimento di Fisica "E. Fermi", Università di Pisa, Pisa, Italy

[3] Laboratoire Lagrange, Observatoire de la Côte d'Azur, Université Côte d'Azur, CNRS, Nice, France

[4] LPC2E, CNRS, Université d'Orléans, CNES, Orléans, France

June 13, 2024

ABSTRACT

Context: Mercury presents a highly dynamic, small magnetosphere where magnetic reconnection plays a fundamental role.
Aim: We aim to model the global characteristics of magnetic reconnection in the Hermean environment. In particular, we focus on waves that have been observed during the third BepiColombo flyby.
Method: In this work, we use two fully kinetic three-dimensional simulations done with the `iPIC3D` code that models the interaction of the solar wind with the Hermean magnetosphere. For the simulations, we use southward solar wind conditions that allow maximum magnetic coupling between the solar wind and the planet.
Results: Our simulations show that a significant wave activity, triggered by magnetic reconnection, develops near the diffusion region in the magnetotail and propagating at large scale in the night-side magnetosphere. We observe an increase in electron temperature close to the diffusion region. Specifically, narrowband whistler waves developing near the reconnection region are observed. These waves propagate nearly parallel to the magnetic field at frequency $f \sim 0.5 f_{ce}$. The waves, in addition to the electromagnetic component, also exhibit an electrostatic one. Furthermore, we observe a strong electron temperature anisotropy, suggesting its role as the source of these waves.

Key words. Mercury, whistler waves, kinetic, magnetosphere, magnetotail, magnetic reconnection, BepiColombo

Introduction

Mercury is the closest planet to the Sun. For this reason, Mercury is one of the least explored planets in the Solar System. The first *in situ* measurements of the Mercury environment were performed by the NASA Mariner10 mission in the 1970s, with its three flybys (Russell et al. 1988). Mariner10 showed that Mercury is - with the Earth - the only telluric planet exhibiting a significant intrinsic dipolar magnetic field and, consequently, a magnetosphere (Ness et al. 1974, 1976). Differently from the Earth, Mercury's dayside magnetopause is much closer to the planet, so that its magnetosphere is much smaller. The Hermean sub-solar standoff distance, also known as the Chapman-Ferraro distance, is typically located around $1.35-1.55 R_M$ from the center of the planet (Winslow et al. 2013), while the Earth's one is nominally at $10-14 R_E$ (Spreiter et al. 1966). The primary knowledge on the Hermean environment acquired by Mariner10 was then significantly further deepened by the NASA MESSENGER mission (Solomon & Anderson 2018). During the four years of orbital observations, the MESSENGER mission evidenced a highly dynamical plasma environment, caused by the relatively weak intrinsic magnetic field of Mercury and by the near-Sun, highly variable solar wind (Raines et al. 2015). The mission addressed various plasma processes occurring at the global planetary scale (of the order of 2400 km) and down to the kinetic scales of ions (of the order of 100 km).

Due to the mission's instrumental constraints, MESSENGER did not investigate the plasma processes occurring at the electron scale (of the order of 2 km). Moreover, MESSENGER only observed electrons with energies above $\sim$ 10 keV, thus excluding the bulk of the distribution function. The ESA/JAXA BepiColombo (Benkhoff et al. 2021) mission has been designed to shed light on the Mercury environment. BepiColombo is composed by two spacecraft (Mercury Planetary Orbiter, named MPO, and Magnetospheric Orbiter, Mio) equipped with advanced instruments enabling to measure down to the electron scale (Milillo et al. 2020). BepiColombo is the first mission able to provide a simultaneous multi-point measurement of the Mercury environment.

MESSENGER measurements have shown that magnetic reconnection takes place on both the dayside magnetopause and nightside magnetotail of Mercury (Slavin et al. 2009; Slavin et al. 2012; Dibraccio et al. 2013; Slavin et al. 2014; DiBraccio et al. 2015; Slavin et al. 2019). Magnetic reconnection is a fundamental plasma process over which magnetic field energy is released via reconfiguration of the field topology. Magnetic reconnection relies on the formation of a two-layered diffusion region where the magnetic field breaks and reconnects: the elec-

tron diffusion region (hereafter EDR) where the frozen-in condition is broken for electrons being there demagnetized, and a larger ion diffusion region (IDR), encompassing the EDR, where ions become demagnetized. Theory and modeling have shown that the thickness of the diffusion region is approximately the inertial length of the corresponding particle (Drake & Kleva 1991; Mandt et al. 1994; Biskamp et al. 1997; Fujimoto et al. 2011; Khotyaintsev et al. 2019), while its width being of the order of ten inertial lengths (Fuselier et al. 2017). MESSENGER measurements have also shown that the Dungey cycle (Dungey 1961) is at play at the Hermean magnetosphere, as for the Earth (Slavin et al. 2009; Siscoe et al. 1975). The Dungey cycle consists of a circulation of plasma, magnetic flux, and energy, starting at the dayside magnetopause X-line, extending through the cross-tail current layer to the nightside X-line, and eventually returning to the dayside magnetosphere.

Magnetic reconnection at Mercury leads to flux transfer events, plasmoids (Slavin et al. 2009; Slavin et al. 2012; DiBraccio et al. 2013) and dipolarization fronts (Sundberg et al. 2012; Imber et al. 2014; Sun et al. 2016). Furthermore, magnetic reconnection plays a significant role in the magnetotail by causing the transfer of energy and momentum into the planet's inner tail region. This transfer allows for the conversion of magnetic energy stored in the lobes into kinetic energy within the plasma sheet. While on the Earth the inner regions of the magnetosphere are dominated by the rotation of the planet, forming the plasmasphere, at Mercury one observes a direct boundary between the planet surface and the magnetosphere. This implies that at Mercury, magnetic reconnection plays a crucial role not only for the magnetosphere but also in connecting of all the different subparts of the system (e.g. exosphere and surface).

An important role in the dynamics of magnetospheric electrons is played by whistler-mode chorus waves (Summers et al. 1998; Thorne et al. 2013; Horne et al. 2008; Woodfield et al. 2019) around magnetized planets. Indeed, via cyclotron resonance, whistler chorus modes are responsible of the acceleration of high energy electrons to relativistic electrons enhancing the radiation belt electrons (Omura et al. 2015; Allison et al. 2021; Glauert & Horne 2005; Hua et al. 2022, 2023; Summers et al. 2007; Xiao et al. 2014). Whistler mode waves are electromagnetic wave emissions that have right-handed polarization and typical frequencies below the electron gyro frequency. Observations at the Earth show that chorus waves typically occur in two distinct frequency bands, a lower-band (0.1–0.5 ω_{ce}) and an upper-band (0.5–0.8 ω_{ce}), where ω_{ce} represents the equatorial electron gyro-frequency. Chorus waves propagate quasi-parallel along the background magnetic field. Whistler waves are thought to be generated by thermal electrons with temperature anisotropy (requiring $T_{\perp,e} > T_{\parallel,e}$) (Kennel & Petschek 1966; Le Contel et al. 2009; Liu et al. 2011; Yu et al. 2018). Chorus emission have been observed at the Earth since early *in situ* observations (Oliven & Gurnett 1968; Burtis & Helliwell 1969; Lauben et al. 1998; Horne et al. 2005), but also at Jupiter (Kurth & Gurnett 1991; Gurnett et al. 1979; Scarf et al. 1979), Saturn (Kurth & Gurnett 1991) and Uranus (Gurnett et al. 1986).

Before the BepiColombo mission, neither the Mariner 10 nor the MESSENGER spacecraft were equipped with wave instruments able to observe the range of frequencies of chorus waves. The Mio spacecraft of the BepiColombo mission, instead, carries a suite of experiments dedicated to waves measurements at Mercury, gathered within the PWI consortium (Kasaba et al. 2020). The electric (resp. magnetic) field measurement capabilities ranges from DC (resp. 0.3 Hz) to 10 MHz (resp. 640 kHz), therefore including all characteristic plasma frequencies in the near-Mercury solar wind and in the Hermean magnetosphere. Indeed, BepiColombo/Mio has already observed evidence of chorus waves during the first two Mercury flybys (Ozaki et al. 2023) on the 1st October 2021 and the 23rd June 2022, respectively. This result emphasized that chorus emission waves are ubiquitous in all magnetized planets in our Solar System.

Despite the great importance of spacecraft observations in the study of magnetospheric dynamics, their inherent limitation is to show spatially and temporally localized phenomena. Consequently, the comprehensive reconstruction of the temporal sequence and global perspective of magnetospheric dynamics exclusively through *in situ* spacecraft data presents a significant challenge. Therefore, to study temporally localized phenomena, numerical simulations are used. In particular, global simulations can be used to reconstruct the global perspective of the magnetosphere. Such simulations enable the interpretation of *in situ* measurements within a three-dimensional framework, facilitating the differentiation between temporal and spatial fluctuations and thereby enhancing the understanding of magnetospheric dynamics. Concerning the study of the whistler-mode chorus waves in numerical simulations, this has been achieved by local hybrid and full kinetic one-dimensional simulations based on actual magnetospheric conditions in the equatorial plane (Omura et al. 2008; Hikishima et al. 2009; Nogi et al. 2020; Ozaki et al. 2023). In this study, we perform fully kinetic 3D (also refereed to as 3D-3V) global numerical simulations of the Hermean environment. In other words, the ion and electron distribution function evolve in the phase space characterized by 3 dimensions in physical space and velocity space. In particular, we do not impose any ad-hoc hypothesis on the velocity distribution functions in this model.

To date, most of the global numerical simulations studying the Hermean environment have been limited to magnetohydrodynamic (MHD, Kabin (2000); Ip & Kopp (2002); Yagi et al. (2010); Pantellini et al. (2015); Jia et al. (2015, 2019)), multifluid and hybrid (i.e. kinetic ions and fluid massless electrons) models (Benna et al. 2010; Müller et al. 2012; Exner et al. 2018; Fatemi et al. 2018; Exner et al. 2020). However, such models do not allow a self-consistent evolution of the electrons but instead prescribe a given closure that can strongly depart from the actual electron dynamics in the magnetosphere, in general, and the magnetotail, in particular. For instance, hybrid models used to simulate the Mercury magnetosphere use a polytropic closure, not allowing any electron temperature anisotropy, although it is known from observation to be a strong source of free energy in the magnetospheric global system.

Two notables examples of numerical simulations studying the Mercury environment are Dong et al. (2019) and Chen et al. (2019). In the former, a ten-moment multifluid model was used to investigate the physics of magnetotail reconnection. In particular, they highlighted the asymmetry in hot electrons distributions and the role of the off-diagonal elements of the electron pressure tensor in the reconnection. The latter consists of a first attempt to include locally electron kinetic physics in a global MHD simulation. This model has been used to study the role of electrons in the magnetotail reconnection region. However, this model cannot reproduce dynamical processes such as, for example, the global electron circulation around the planet. More recently, global full-kinetic numerical simulations of the Mercury environment have been presented in Lavorenti et al. (2022) and further analyzed in Lavorenti et al. (2023); Lavorenti (2023). These simulations focused on the electron dynamics in Mercury's magnetosphere.

In this study, we perform two three-dimensional global simulations of the Mercury magnetosphere using the iPIC3D solver (Markidis et al. 2010; Lavorenti et al. 2022). Firstly, we study the magnetic reconnection happening at the magnetotail. In particular, we focus on the influence of the magnetic topology on the spatial distribution of energetic particles. Furthermore, we observe the creation of narrow-band whistler-mode waves in the magnetotail, propagating parallel to the magnetic field.

The paper is organized as follows. In Section 1, we present the simulations set-up and model. In Section 2, we study the main features of magnetic reconnection as observed in the magnetotail, focusing on the influence of the magnetic topology on the plasma features. In Section 3, finally, the observed whistler waves are studied, focusing on the dispersion relation and the electron anisotropy around the reconnection region.

1. Methods

The numerical simulations used in this work to address the dynamics of the magnetosphere of Mercury are performed by using the semi-implicit, fully kinetic particle-in-cell (PIC) code iPIC3D (Markidis et al. 2010). The code solves the Vlasov-Maxwell system of equations for both ions and electrons by discretizing the distribution functions using macro-particles. Hereafter, we use the Mercury-centered Solar Orbital (MSO) reference frame, defined as follows: the x-axis points from the planet center to the Sun, the z-axis is anti-parallel to Mercury's magnetic dipole, and the y-axis points from dawn to dusk. In the simulation, the density and the magnetic field are normalized to a reference value (here the solar wind) and velocities are normalized to the speed of light. Lengths and times are normalized to the solar wind ion inertial length ($d_i = c/\omega_{pi} = c\sqrt{m_i/4\pi n_i e^2}$) and ions plasma frequency ($\omega_{pi} = c\sqrt{m_i/4\pi n_i e^2}$), respectively. The solar wind parameters considered in the simulations are given in Table 1.

Quantity	Value
$\mathbf{B}_{0,z}$	20 nT
n_i (= n_e)	30 cm^{-3}
T_i (= T_e)	21.5 eV
β_i	1.3
$\mathbf{v}_{sw,x}$	400 km/s

Table 1. Solar wind parameters for *Run1* and *Run2*. These values are similar to those used in previous simulations (Lavorenti et al. 2021; Aizawa et al. 2021), which are considered as representative of solar wind conditions in the proximity of Mercury at aphelion (James et al. 2017; Sarantos et al. 2007).

The simulations setup includes a uniform, solar-wind plasma, with a southward magnetic field injected from the sunward direction. Mercury is modeled as a magnetized planet. MESSENGER observations have revealed a Parker spiral angle at Mercury of approximately $\pm 35^o$ (James et al. 2017). However, in our model, we choose to consider a purely southward Interplanetary Magnetic Field (IMF). Although we acknowledge that this is not entirely representative of the average IMF conditions at Mercury, our choice comes from the fact that such configuration enables the maximum magnetic coupling between the solar wind and the planet and has been shown to be particularly favorable to enhance the energy injection from the solar wind to the magnetosphere through dayside magnetic reconnection at the nose of the magnetopause Lavorenti et al. (2022). Since strong variations in magnitude and direction of the IMF are observed in the inner solar wind, it is likely that IMF configurations that are southward-like would occur at Mercury. Such IMF variations are typically observed at Mercury on timescales of tens of minutes Cuesta et al. (2022), i.e. on timescales larger than that of the fast global reconfiguration of the Hermean magnetosphere, one would therefore expect a quasi-steady-state response of the magnetosphere. As demonstrated by observations (Slavin 2004; Slavin et al. 2012) and numerical simulations (Ip & Kopp 2002; Kallio & Janhunen 2003, 2004; Exner 2021), the direction of the IMF is one of the main parameters in determining the topology of the magnetosphere.

For practical numerical reasons, Mercury's size is scaled-down by a factor 10. The planet rescaling approach has been intensively adopted in past works (Lapenta et al. 2022; Trávníček et al. 2007, 2009, 2010) to enable multi-scale numerical computations. Consequently, in the reported simulations, the radius of Mercury is rescaled to $R_M = 5.5d_i$. We have reduced the ion-to-electron mass ratio $m_i/m_e = 100$ and the electron plasma-to-cyclotron frequency ratio $\omega_{pe}/\omega_{ce} = 17.8$. These rescalings are the same as those chosen and discussed in (Lavorenti et al. 2022). As demonstrated in Lavorenti (2023), this scaling-down of the planet preserves the correct global magnetosphere structure and dynamics.

We use a spatial grid spacing $dx = dy = dz = 0.015R_M = 1.5\ \rho_e$ ($R_M = 100\rho_e$), where $\rho_e = cT_e m_e/eB_0$ is the electron gyro-radius in the solar wind. We use a time step $dt = 1.4$ ms, much smaller than the electron gyro-period in the solar wind ($\tau_{ce} = 2\pi/\omega_{ce} = 31.5$ ms). We initialize 64 macroparticles per cell (ppc) for both (electron and ion) species. We want to stress here that, while this number of ppc allows to well reproduce the physics at play, the associated numerical noise fails to satisfactorily model the non-diagonal terms of pressure tensor, i.e. agyrotropy (Scudder & Daughton 2008). For this reason, we will not analyze the role of the off-diagonal terms in the pressure tensor in magnetic reconnection. The total time length of the simulation is 11 $R_M/v_{sw,x}$. In order to avoid any transients due to the initialization of the simulation, we wait until a dynamic equilibrium is reached to study the reconnection, typically after $\sim 2R_M/v_{sw,x}$.

The first and main simulation, hereafter referred to as *Run1*, exploits the same plasma parameters as in Lavorenti et al. (2022). Differently from the original, we increased the output frequency in order to have a higher resolution to study the evolution of both the magnetic reconnection and the waves. Concerning the boundary conditions, we remove all the macro-particles falling into the planet.

The second simulation, hereafter referred to as *Run2*, was run to study how the observed wave features are influenced by the planet radius scaling adopted in *Run1*. In particular, a smaller planet with a radius of $R_{M,2} = 2.75d_i$ is used (while $R_M = 5.5d_i$ for *Run1*). For this simulation, the magnetic field dipole is therefore also rescaled according to the smaller planet radius so that the magnetic field at the planet's surface is kept equal to that of *Run1*. This choice ensures that the pressure balance between the magnetic pressure - associated with the planet's magnetic field - and the solar wind dynamical pressure leads to the same magnetopause distance (in terms of planet radius) in both simulations *Run1* and *Run2*. Note that the magnetopause distance is chosen to be about 1.5 planet radius, in accordance with MESSENGER observations at Mercury. In this paper, all figures show results from *Run1*. The analysis of *Run2* is nevertheless necessary to properly identify which properties remain unaffected by the scaling of the planet size, and therefore assess the influence of such a (numerical) rescaling on the (physical) results we report in this paper.

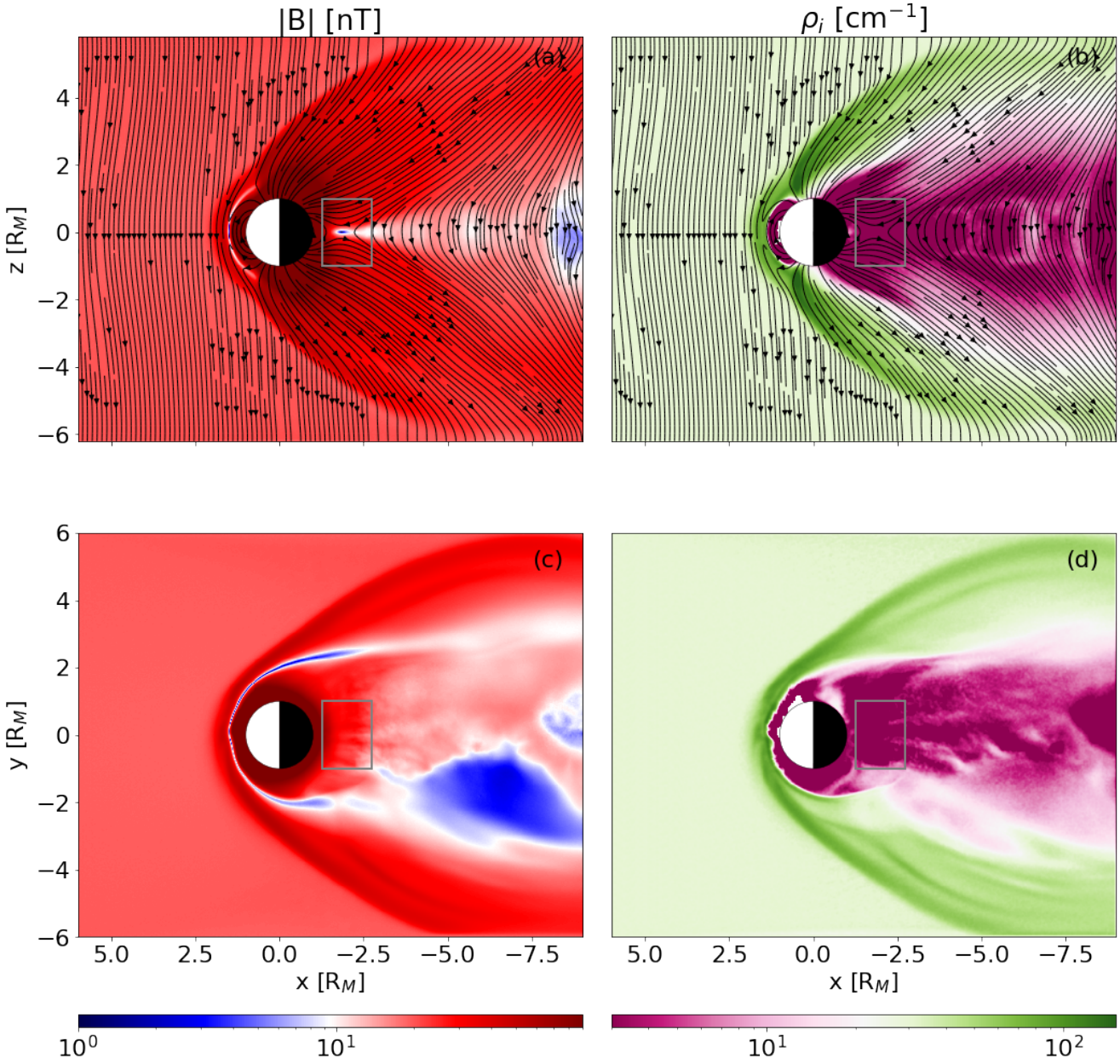

Fig. 1. Overview of the structure of the magnetosphere in *Run1*, on the meridian plane (top) and equatorial plane (bottom). On the left, the module of the magnetic field and, on the right, the ion density. Both quantities are computed at time $t = 11R_M/v_{sw,x}$.

2. Magnetic reconnection in the magnetotail

In *Run1* and *Run2* magnetic reconnection occurs at the magnetotail and at the nose of the magnetopause. Here we focus on magnetotail reconnection.

Fig. 1 shows at the end of the simulation, $t = 11R_M/v_{sw,x}$, an overview of the structure of the resulting magnetosphere for *Run1*. The figure shows the topology of the magnetic field lines in the equatorial plane. The location of the reconnection region is in agreement with the one from past observations (Poh et al. 2017). From MESSENGER observations, indeed, the typical position x_{MSM} of the reconnection point was found between -1.4 to -2.6 R_M. The first signatures of magnetic reconnection are observed after a time $t \sim 2.5R_M/v_{sw,x}$ mainly in the grey rectangular box in Fig. 1 and displayed in Fig. 2. We observe the typical quadrupolar out of plane magnetic field, frame (*e*). We also observe ions and electrons outward escaping jets, both in the reconnection plane, frame (*f* and *g*), and in the equatorial plane, frame (*b* and *c*). These quantities are shown at $t = 3R_M/v_{sw,x}$, before the onset of whistler wave generation (discussed in Section 3) in order to better highlight the main features of magnetic reconnection, without overlapping with the wave signatures. Focusing on the equatorial plane, we see that these jets, particularly for ions, are spread all along the reversal line (observed in frame (*a*)), emphasizing the presence of an X-line in the magnetotail. We observe, as expected, an enhancement of the $\mathbf{E} \cdot \mathbf{J}$ quantity in the region where magnetic reconnection occurs (frame *d* and *h*).

As a first step, we study how the topology of the magnetic field lines affects the spatial distribution of the electrons. We split the domain according to the magnetic topology: those corresponding to magnetic field lines closed at both ends on the planet; those closed at one end; and finally the magnetically open ones. For each of these regions, we look at the distribution of

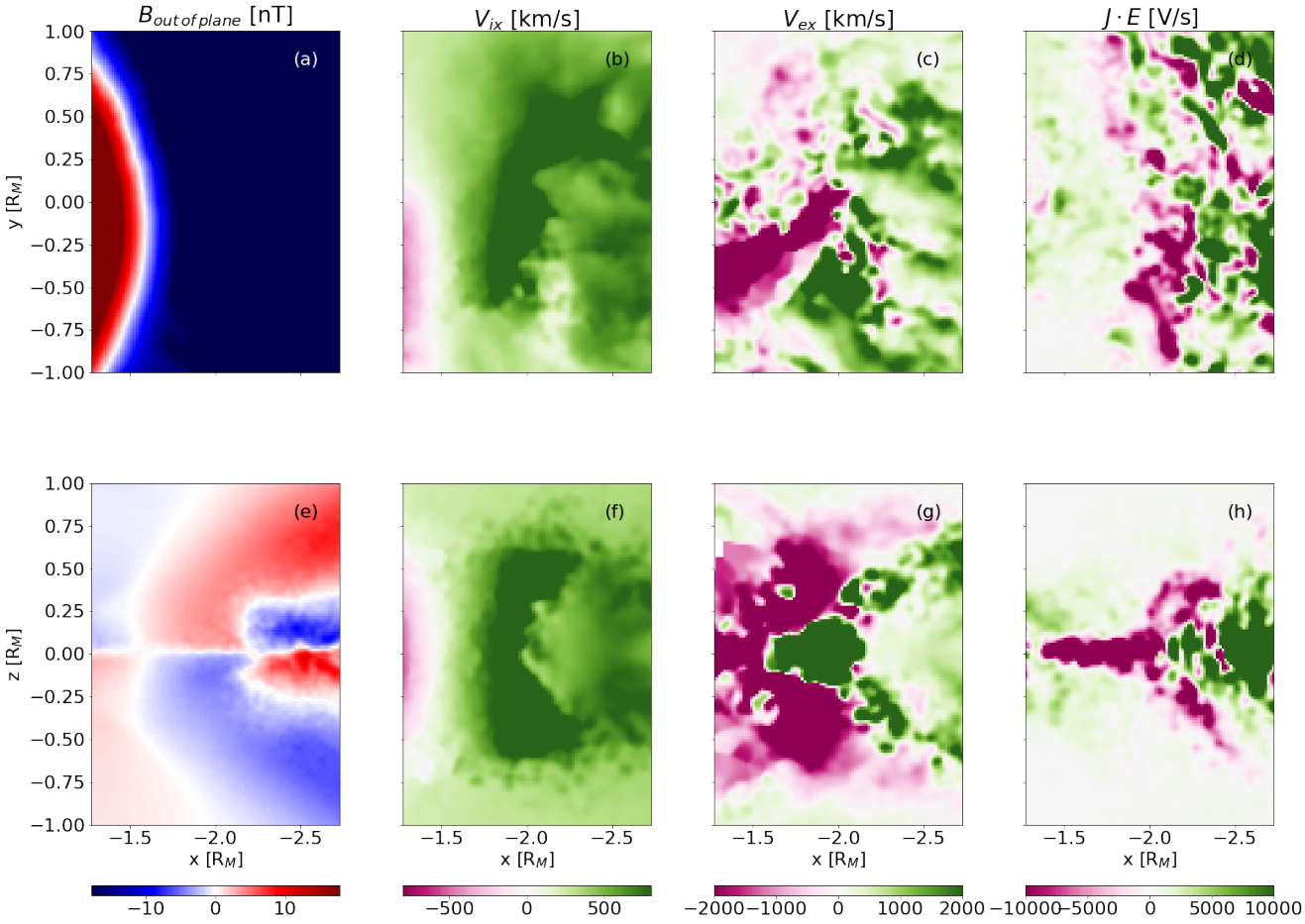

Fig. 2. Overview of the diffusion regions in *Run1*. From left to right, the out of plane magnetic field component, the ion velocity, electron velocity and $J \cdot E$, on the equatorial plane (top) and meridian (bottom). All quantities are computed at $t = 3R_M/v_{sw,x}$.

electrons as a function of temperature. After the onset of magnetic reconnection at $t \sim 2R_M/v_{sw,x}$, an increase of electron energy is observed. High energy electrons, initially equally spread in the three topological regions are eventually only visible, because trapped, in magnetic closed regions. In Fig. 3 we show the distribution of electrons for temperatures greater than 100 eV (top) and 1 keV (bottom), in the reconnection meridian plane, averaging along the out-of-plane direction, at $t = 11R_M/v_{sw,x}$. The figure has been realized by plotting the number of cells with electron temperature over the considered threshold.

We observe that, for energies below 1 KeV, electrons are almost equally distributed in the three different regions (subplots *a*, *b* and *c*). Considering energetic electrons (with temperatures over the Kev) they are only found in regions with magnetic field lines closed on the planet (*d*), while no energetic electrons are observed in regions with one-side (*e*) or completely open (*f*) magnetic field. These results indicate a clear link between magnetic topology and electron energy distribution. This can be explained by the fact that energetic particles stay trapped in the closed regions, while those in open field regions (also on just one side) escape the simulation domain, and therefore the planetary environment. Moreover, in Fig. 4 we show the distribution of electrons trapped in the closed magnetic field regions, for energies above 100 eV (*a*) and 1 KeV (*b*). In Fig.4, we observe an asymmetry between positive and negative y, in both energy ranges. Concerning the region behind the planet for $-2 < x < -4$, we observe that this asymmetry aligns with the density asymmetry that is also observed in Fig.1. Specifically, lower particle densities are observed for negative y (see the dawn side of the magnetosphere, local time around 6h). This results is consistent with what was previously observed and discussed in Lavorenti et al. (2022) on the role of the loss-cone mechanism creating inhomogeneous distribution of high energy electrons inside the magnetosphere of Mercury. The evolution of the distribution in this plane can be observed in Video 1 (attached in Supplementary material).

3. Whistler-mode waves in the magnetotail

On top of the magnetic reconnection dynamics, after $t \sim 4R_M/v_{sw,x}$ we observe waves developing nearby the X-point region in the magnetotail. These waves, observed until the end of the simulation, exhibit a narrow-band shape in the magnetic and electric fields, as well as in the electron current. In Fig. 5 we show in the x, z plane the magnetic field and perpendicular electric field (with respect to the magnetic field) fluctuations. The figure zooms at around the diffusion region where the waves are more intense and we over-plot the magnetic field lines to highlight the parallel propagation of the waves. These waves of relatively large amplitude originate from the diffusion region and propagate nearly parallel to the magnetic field, mainly along the separatrices, as shown in Fig. 5. The formation region and propagation direction of the waves can be even better observed in Video 2 (see Supplementary material). These waves, in addition to the electromagnetic component, are also characterised by the presence of a strong electrostatic component $\mathbf{E}_\parallel$ and paral-

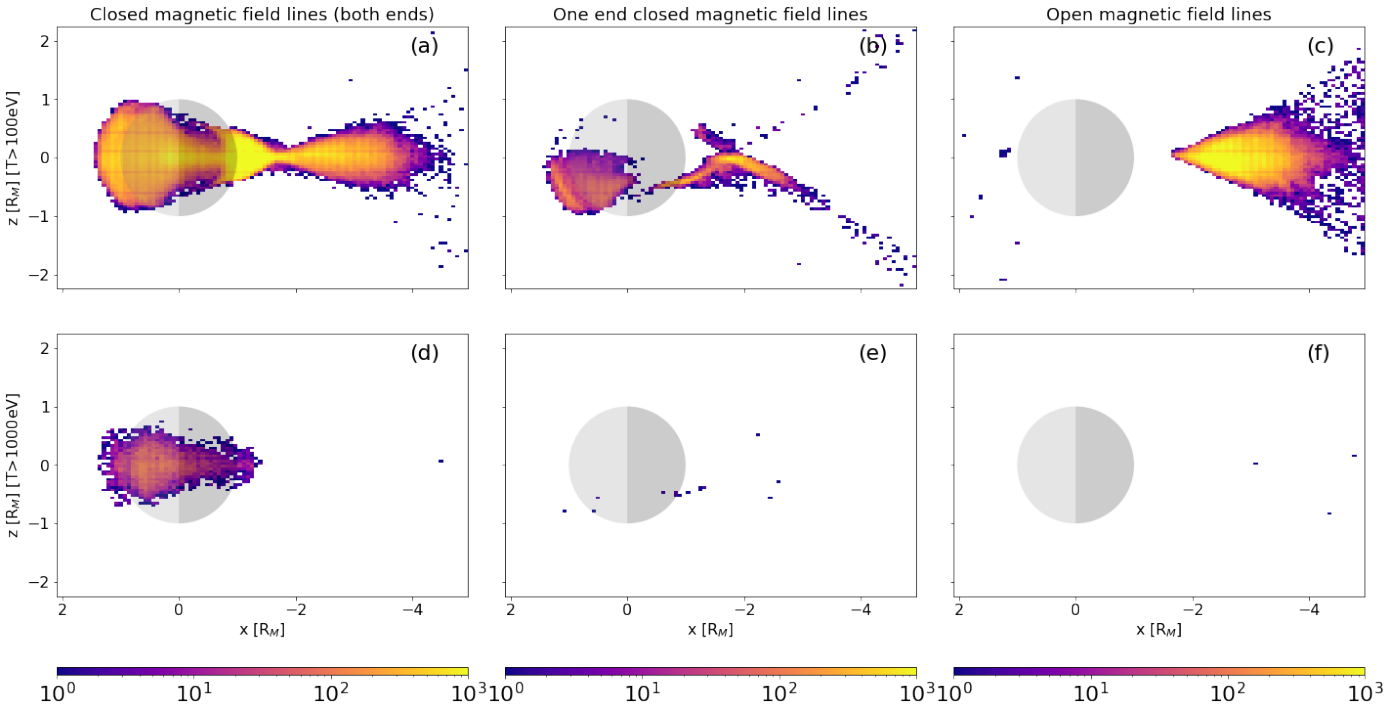

Fig. 3. Histograms of the number of cells in *Run1* for which the electron temperature is above 100 eV (top) and 1 KeV (bottom), in the meridian plane, averaging along the out-of-plane direction, in the magnetic field region closed with the planet (left), open with respect to the planet (right) and with one open and one closed extremity (center), in the meridian plane, averaging along the out-of-plane direction. Quantities computed at at $t = 11R_M/v_{sw,x}$.

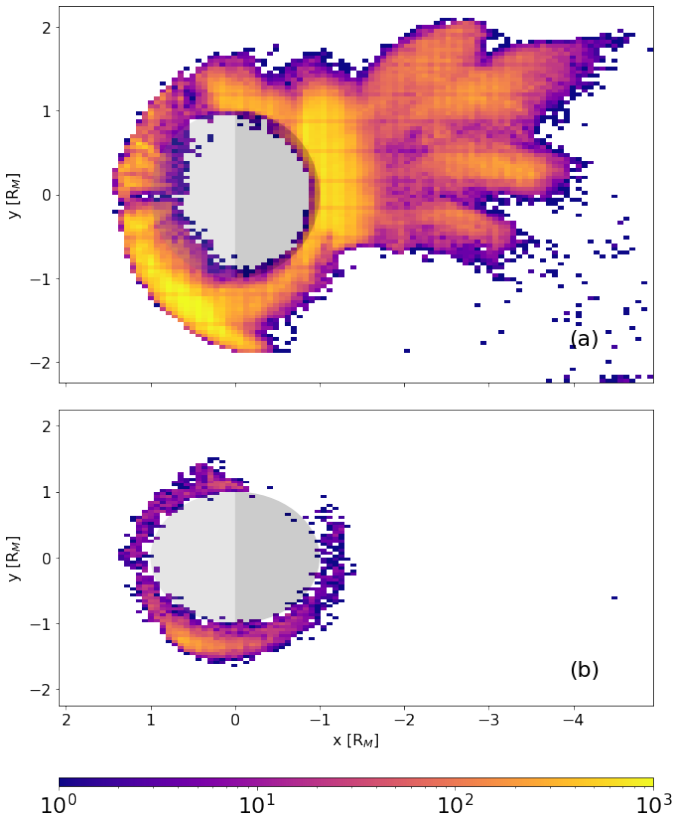

Fig. 4. Histograms of the number of cells in *Run1* for which the electron temperature is above 100 eV (top) and 1 KeV (bottom), in the reconnection equatorial plane, averaging along the z direction, in the magnetic field region closed with the planet. Quantities computed at at $t = 11R_M/v_{sw,x}$.

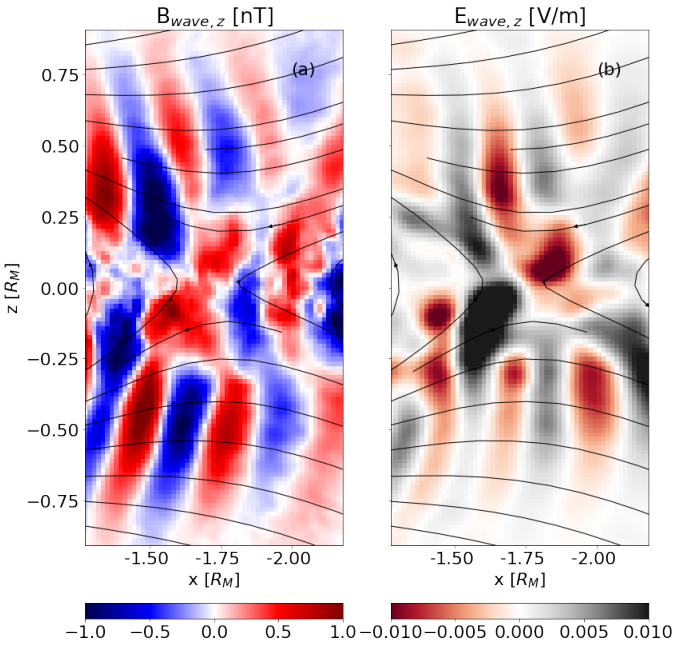

Fig. 5. Magnetic field (a) and electric field (b, perpendicular to the magnetic field) wave components, for $t \sim 11R_M/v_{sw,x}$. Waves are in the plane at $y = -0.5R_M$, where the waves features are more clear. Wave components are obtained by subtracting the mean field for both. Black lines are the magnetic field lines.

lel electron current, as shown in Fig. 6. We also observe a small wave component in the ions current, albeit significantly smaller in magnitude.

In order to identify the mode, we have studied its polarization and dispersion relation. Concerning the polarization, these

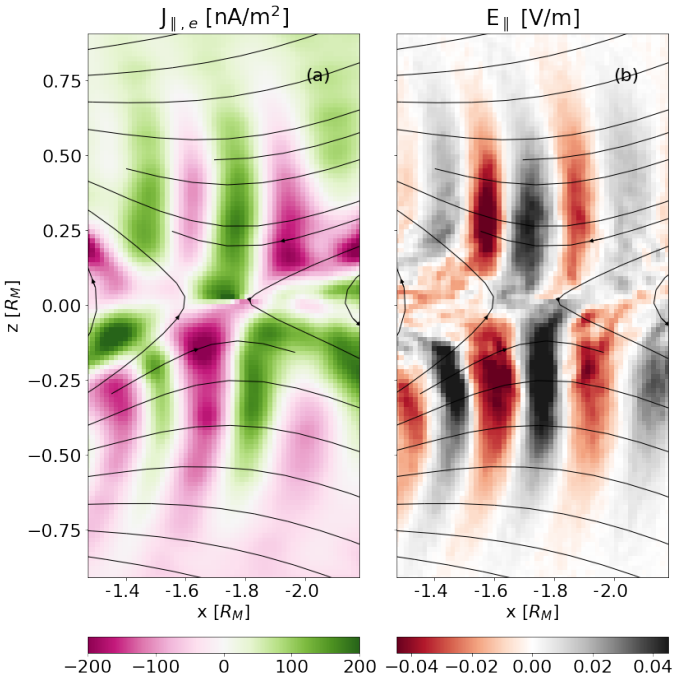

Fig. 6. Parallel electron current (*a*) and electric field (*b*) wave components, for $t \sim 11 R_M/v_{sw,x}$. Waves are in the plane at $y = -0.5 R_M$, where the waves features are clearer. Black lines are the magnetic field lines.

waves present a clear right-hand polarization. This is shown in Fig. 7, where we draw the hodogram in the perpendicular plane assuming the wave-vector as exactly parallel to the mean magnetic field. Concerning the dispersion relation, we collected the

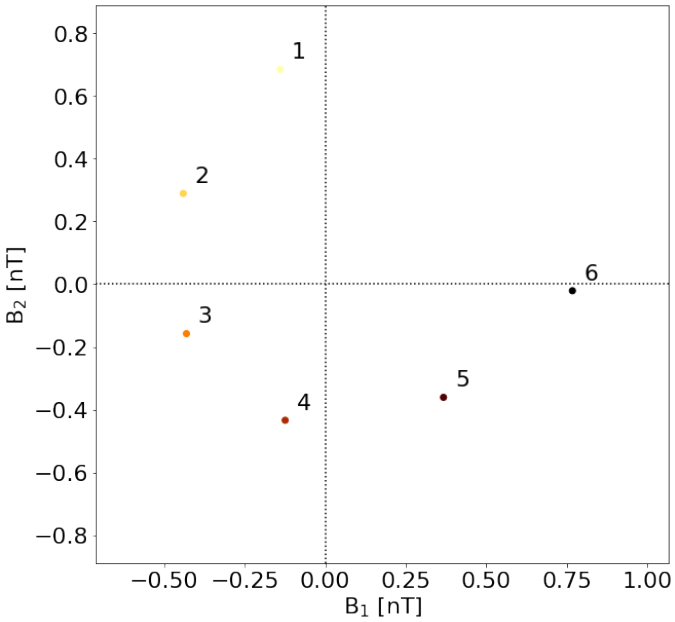

Fig. 7. Hodogram of the magnetic field components orthogonal to the wave vector **B** (assumed completely parallel to the magnetic field), at $x = -2R_M$ and $z = -0.4R_M$. Each point correspond to a different time-step, with a cadence of $0.5\omega^{-1}_{pi,sw} \sim 0.1\omega^{-1}_{pi,loc}$. Quantities are computed at at $t \sim 11 R_M/v_{sw,x}$.

outputs with a time step of $0.5\omega^{-1}_{pi,sw} \sim 0.1\omega^{-1}_{pi,loc}$ in order to well resolve the wave oscillation. Here, the *sw* and *loc* indices mean that the frequencies are computed in solar wind and locally averaged units, respectively. We observe narrow-band mode has a wave-vector $kd_{i,loc} \sim 14$ and an angular velocity $\omega \sim 0.5\omega_{ce,loc}$, where d_i is the ion inertial length and ω_{ce} is the electron cyclotron frequency. Quantities in local unities are obtained by averaging the density and the magnetic field in the region over which the dispersion relation is computed. The range of frequencies and features proper of the mode correspond well to whistler waves.

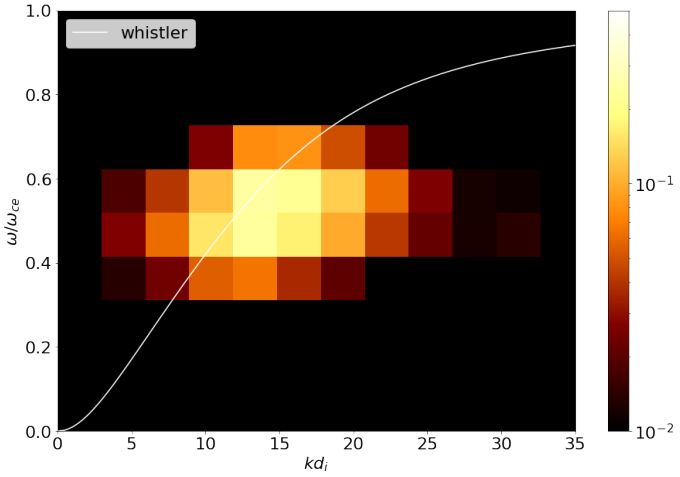

Fig. 8. Amplitude of the Fourier transform in both space and time of the observed waves compared with the theoretical dispersion relation for whistler waves (Eq. 1). Quantities computed at $t \sim 11 R_M/v_{sw,x}$.

In Fig. 8 where we draw the dispersion relation of the mode obtained by a Fourier transform in space and time. In this figure, we over-plot the dispersion relation for a whistler-mode wave propagating along the magnetic field in a cold plasma (Stix 1992; Omura et al. 2008):

$$c^2k^2 = \omega^2 + \frac{\omega\omega_{pe}^2}{\omega_{ce} - \omega} \tag{1}$$

We conclude that the observed mode is compatible with the whistler waves' dispersion relation.

In order to better understand the nature of these waves, we have investigated the electron anisotropy being electron temperature anisotropy a possible driver of whistler instability. In particular, the following condition is required (Kennel & Petschek 1966):

$$\frac{T_{e,\perp}}{T_{e,\parallel}} - 1 > \left(\frac{|\omega_{ce}|}{\omega} - 1\right)^{-1} \tag{2}$$

Fig. 9 shows the electron anisotropy (to which the wave contour is superimposed). In the figure the red regions correspond to those where the condition in Eq. 2 is met. We observe that the threshold in Eq. 2 is reached locally around the reconnection region and closer to the planet. From Fig. 9, it is also seen that far from the reconnection region and along the separatrices, where the waves propagate, the parallel electron temperature is higher than the perpendicular one. As a result the waves are likely to be generated by the electron temperature anisotropy in the reconnection region. Interestingly, we observe that $T_{e,\parallel} > T_{e,\perp}$ along the separatrices and further from the reconnection plane. Wondering about a possible nonlinear feedback of the generated whistler waves on a reduction of the electron temperature anisotropy, we compare the electron parallel thermal velocity

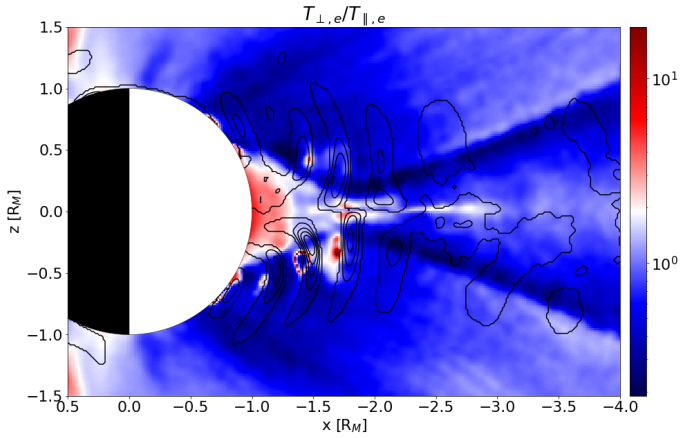

Fig. 9. Electron temperature anisotropy in the meridian plane, for $t \sim 11 R_M/v_{sw,x}$. Black lines are the contour plot of the waves, to indicate waves' location. Red regions indicate where the condition in Eq. 2 is met.

with the whistler wave phase velocity. We observe that they differ by about two orders of magnitude. For this reason, we exclude the possibility that the parallel temperature increase along the separatrices is due to wave-particle interactions with the observed whistler waves. Instead, it is rather likely due to other processes within the diffusion region, such as, e.g. electron parallel acceleration known to generate electron beams along the separatrices.

4. Discussion

In this study, we have presented two global numerical simulations of the Hermean magnetospheric environment. In particular, we have focused on magnetic reconnection at the magnetotail and its consequences on the energetic electron distribution. Moreover, around the diffusion region, waves at electron scales develop and propagate nearly parallel to the magnetic field.

First, we observe that magnetic reconnection in the magnetotail increases the electron temperature around the diffusion region. After reconnection onset, electrons below 1 keV are observed both in regions with open and closed magnetic field lines. Energetic electrons with energy above 1 KeV are instead only observed in regions with closed magnetic field lines since non trapped electrons exit the simulation domain.

Second, the simulation reveals the presence of narrow-band whistler-mode waves in the magnetotail. These waves originate at the nightside reconnection site and propagate parallel to the magnetic field. Electron anisotropy has been identified to be the source of these waves. Furthermore, the region where the waves develop and propagate is characterized by an inhomogeneous plasma, with density and magnetic field magnitude varying by almost an order of magnitude. This strongly supports the notion that the background magnetic inhomogeneity plays a pivotal role in the generation process of planetary whistler waves, in agreement with the simulations modeling Mercury's environment (Omura et al. 2008; Hikishima et al. 2009; Omura et al. 2015; Ozaki et al. 2023). The results shown in this work will be of crucial importance to interpret plasma waves observations by BepiColombo PWI instrument during the science phase.

It is worth discussing the possible role of the northward-shifted magnetic dipole of Mercury, observed from MESSENGER (Anderson et al. 2012), in the generation of the whistler waves we observe in the tail. In the specific numerical simulation reported in this paper, we do not use any shifted magnetic dipole moment. We have also run complementary numerical simulations that include the shift in Mercury's magnetic dipole moment. The same waves as those reported here are observed in those simulations that include a dipole offset. Therefore, the existence of these waves near the reconnection point is found to be a general feature common to all mini-magnetospheres, rather than being specific to Mercury. Therefore, the results reported in this work extend beyond the study of planet Mercury.

Whistler-mode chorus waves have been observed during the two flybys at Mercury by BepiColombo (Ozaki et al. 2023). As discussed in this paper, obtaining a comprehensive global map of chorus waves on Mercury holds significant importance in comprehending the energetic electron loss mechanisms. In particular, our results may provide an early example of the distribution of such waves in the magnetotail. The location of the waves is shown in Fig.10. Our results indicate that the waves propagate within low altitudes from the equatorial plane, at altitudes ranging from -1 to 1 R_M, and that they are spread almost symmetrically with respect to the magnetic equatorial plane even if a bit more distributed dawnside. Nonetheless, BepiColombo measurements show the presence of whistler waves on the dawn side of Mercury, while they still have to be observed in the magnetotail region. In this study, we have considered only a purely southward IMF. To achieve a more comprehensive distribution map of such waves, it might be beneficial to investigate in the future how the location and the amplitude of these waves could be influenced by the upstream solar wind properties, especially the IMF direction.

One of the characteristics of narrow-band whistler waves (*i.e.* chorus) from observations and theory is "chirping", consisting in the variation of the center frequency of the narrow-band wave as a function of time (Burtis & Helliwell 1969; Tsurutani & Smith 1974). In our simulations, however, this phenomenon is not observed. We do not know whether this is due to an absence of the phenomenon itself or to the total integration time of the simulation (because of computational reasons) not sufficient to let the chirping mechanism develop. Therefore we refer to the observed waves as narrow-band whistler waves. Nonetheless, also the BepiColombo observations did not show the finer structures of typical rising-tone elements in the time domain due to telemetry limitations (Ozaki et al. 2023).

It is crucial to emphasize that in this scenario, the scaling of the planet could impact the waves' location. This is primarily due to the proximity of the diffusion region to the planet, with the wavelength being comparable with the planet's radius size. Indeed, due to computational constraints it still remains necessary to reduce the scale separation between planet, ion, and electron scales. Reducing the ion-to-electron mass ratio and the plasma-to-cyclotron frequency ratio is a well-established technique in fully kinetic simulations. Previous studies (Bret & Dieckmann 2010; Le et al. 2013; Lavorenti et al. 2021, 2022, 2023) extensively discuss the effects of this approach.

Concerning the planet scaling, its influence on magnetic reconnection has already been discussed in Lavorenti et al. (2022, 2023). When the planet's radius is scaled down (here R_M=230 km and $R_{M,2}$=115 km, as opposed to the realistic radius of Mercury at about 2400 km), the diffusion regions in the tail, both for electrons and ions, moves closer to the planet's surface. As shown in Fig. 1, there is a moderate separation of the ion and electron diffusion regions from the planet. Consequently, the ion dynamics within the outflow will be influenced by this reduction in size, but such an effect should not be observed for electrons. In particular, the characteristics of high-energy electrons

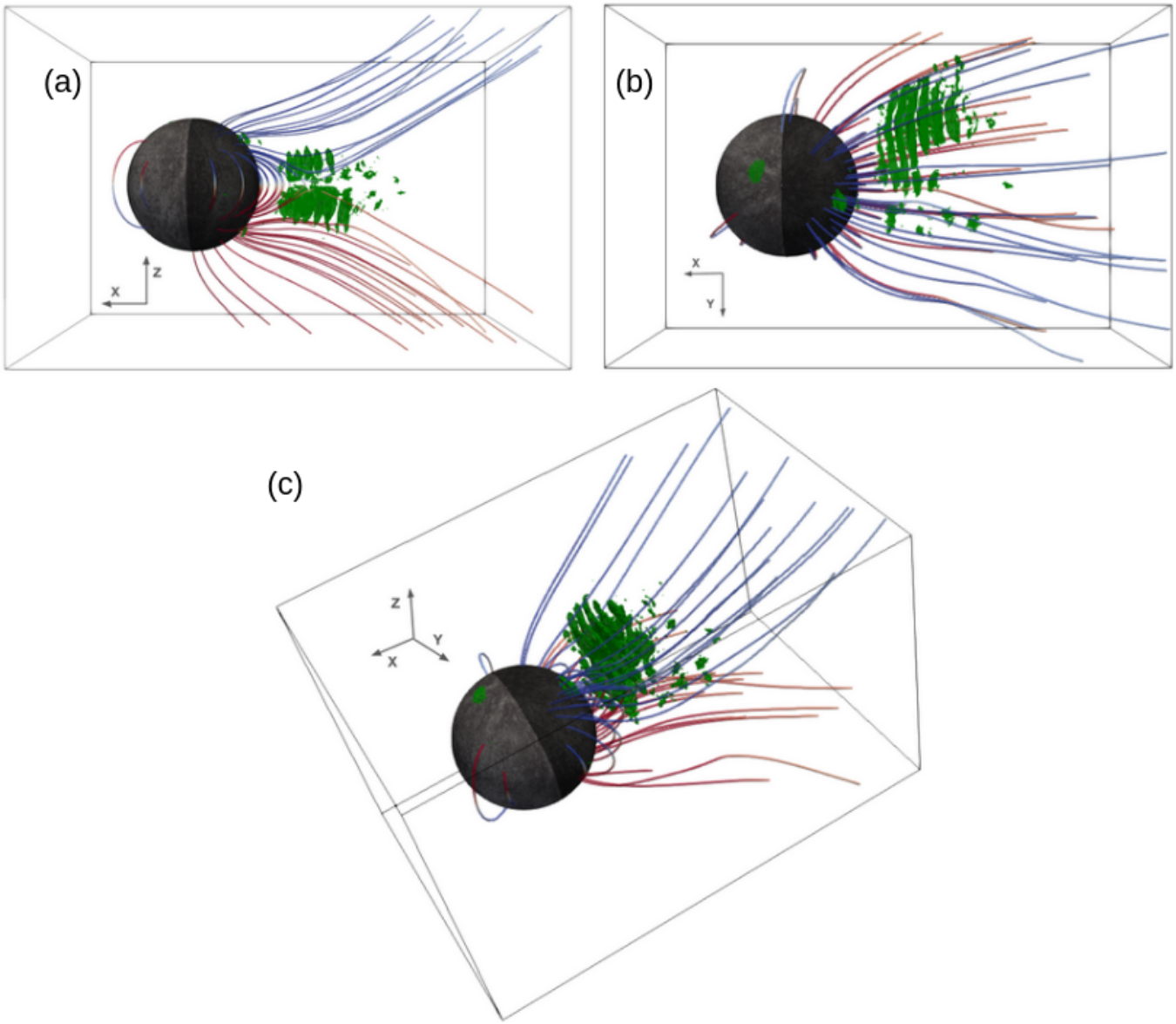

Fig. 10. Locations where the waves are observed at $t \sim 11 R_M / v_{sw,x}$. We show here the cells in *Run1* for which the parallel component of the electric field is above a threshold of 26 mV/m, from three different perspectives.

observed in our simulations as a result of magnetic reconnection will remain consistent when dealing with a planet of actual size. Finally, comparing the modes that are generated in *Run1* and *Run2*, we observe that the dispersion relation is not altered by scaling the planet.

5. Conclusions

We have presented the results of two global full-PIC numerical simulations of the Hermean magnetosphere addressing the development of magnetic reconnection and related dynamics at the magnetotail, in particular focusing on the study of narrow band whistler waves originating around the reconnection region. These waves, driven by electron temperature anisotropy, propagate parallel to the magnetic field with frequency $f \sim 0.5 f_{ce}$ and present both electromagnetic and electrostatic components. The possibility of studying these waves and their spatial distribution in the tail is of great importance for a better understanding of the electron dynamics in Mercury. Presently, the distinction in the spatio-temporal distribution of electron-driven chorus and whistler waves between Earth and Mercury remains unknown through observational means. Unraveling the distinctions between these two environments constitutes a forthcoming challenge, essential for stepping forward our comprehension of how solar wind shapes diverse planetary environments. To address this, the outcomes of the current study play a crucial role in designing and planning the forthcoming observations for the science phase subsequent to the final orbit insertion of BepiColombo in 2025.

Acknowledgements. This work was granted access to the HPC resources at TGCC under the allocations AP010412622 and A0100412428 made by GENCI via the DARI procedure. We acknowledge the Italian supercomputing center CINECA where the simulation has been performed under ISCRA grant. We acknowledge the support of CNES for the BepiColombo mission.

References

Aizawa, S., Griton, L., Fatemi, S., et al. 2021, Planetary and Space Science, 198, 105176
Allison, H. J., Shprits, Y. Y., Zhelavskaya, I. S., Wang, D., & Smirnov, A. G. 2021, Science Advances, 7, eabc0380
Anderson, B. J., Johnson, C. L., Korth, H., et al. 2012, Journal of Geophysical Research (Planets), 117, E00L12
Benkhoff, J., Murakami, G., Baumjohann, W., et al. 2021, Space Science Reviews, 217, 90
Benna, M., Anderson, B. J., Baker, D. N., et al. 2010, Icarus, 209, 3
Biskamp, D., Schwarz, E., & Drake, J. F. 1997, Physics of Plasmas, 4, 1002
Bret, A. & Dieckmann, M. E. 2010, Physics of Plasmas, 17, 032109
Burtis, W. J. & Helliwell, R. A. 1969, Journal of Geophysical Research, 74, 3002
Chen, Y., Tóth, G., Jia, X., et al. 2019, Journal of Geophysical Research (Space Physics), 124, 8954
Cuesta, M. E., Chhiber, R., Roy, S., et al. 2022, The Astrophysical Journal, 932, L11
Dibraccio, G. A., Slavin, J. A., Boardsen, S. A., et al. 2013, Journal of Geophysical Research (Space Physics), 118, 997
DiBraccio, G. A., Slavin, J. A., Boardsen, S. A., et al. 2013, Journal of Geophysical Research: Space Physics, 118, 997
DiBraccio, G. A., Slavin, J. A., Raines, J. M., et al. 2015, Geophysical Research Letters, 42, 9666
Dong, C., Wang, L., Hakim, A., et al. 2019, Geophysical Research Letters, 46, 11,584
Drake, J. F. & Kleva, R. G. 1991, Physical Review Letters, 66, 1458
Dungey, J. W. 1961, Physical Review Letters, 6, 47
Exner, W. 2021, PhD thesis, [object Object]
Exner, W., Heyner, D., Liuzzo, L., et al. 2018, Planetary and Space Science, 153, 89
Exner, W., Simon, S., Heyner, D., & Motschmann, U. 2020, Journal of Geophysical Research: Space Physics, 125, e2019JA027691
Fatemi, S., Poirier, N., Holmström, M., et al. 2018, Astronomy and Astrophysics, 614, A132
Fujimoto, M., Shinohara, I., & Kojima, H. 2011, Space Science Reviews, 160, 123
Fuselier, S. A., Vines, S. K., Burch, J. L., et al. 2017, Journal of Geophysical Research: Space Physics, 122, 5466
Glauert, S. A. & Horne, R. B. 2005, Journal of Geophysical Research: Space Physics, 110, 2004JA010851
Gurnett, D. A., Kurth, W. S., Scarf, F. L., & Poynter, R. L. 1986, Science, 233, 106
Gurnett, D. A., Shaw, R. R., Anderson, R. R., Kurth, W. S., & Scarf, F. L. 1979, Geophysical Research Letters, 6, 511
Hikishima, M., Yagitani, S., Omura, Y., & Nagano, I. 2009, Journal of Geophysical Research: Space Physics, 114, n/a
Horne, R. B., Thorne, R. M., Glauert, S. A., et al. 2008, Nature Physics, 4, 301
Horne, R. B., Thorne, R. M., Shprits, Y. Y., et al. 2005, Nature, 437, 227
Hua, M., Bortnik, J., Kellerman, A. C., Camporeale, E., & Ma, Q. 2023, Space Weather, 21, e2022SW003234
Hua, M., Bortnik, J., & Ma, Q. 2022, Geophysical Research Letters, 49, e2022GL099618
Imber, S. M., Slavin, J. A., Boardsen, S. A., et al. 2014, Journal of Geophysical Research (Space Physics), 119, 5613
Ip, W.-H. & Kopp, A. 2002, Journal of Geophysical Research: Space Physics, 107, SSH 4
James, M. K., Imber, S. M., Bunce, E. J., et al. 2017, Journal of Geophysical Research: Space Physics, 122, 7907
Jia, X., Slavin, J. A., Gombosi, T. I., et al. 2015, Journal of Geophysical Research (Space Physics), 120, 4763
Jia, X., Slavin, J. A., Poh, G., et al. 2019, Journal of Geophysical Research (Space Physics), 124, 229
Kabin, K. 2000, Icarus, 143, 397
Kallio, E. & Janhunen, P. 2003, Annales Geophysicae, 21, 2133
Kallio, E. & Janhunen, P. 2004, Advances in Space Research, 33, 2176
Kasaba, Y., Kojima, H., Moncuquet, M., et al. 2020, Space Science Reviews, 216, 65
Kennel, C. F. & Petschek, H. E. 1966, Journal of Geophysical Research, 71, 1
Khotyaintsev, Y. V., Graham, D. B., Norgren, C., & Vaivads, A. 2019, Frontiers in Astronomy and Space Sciences, 6, 70
Kurth, W. S. & Gurnett, D. A. 1991, Journal of Geophysical Research: Space Physics, 96, 18977
Lapenta, G., Schriver, D., Walker, R. J., et al. 2022, Journal of Geophysical Research: Space Physics, n/a, e2021JA030241
Lauben, D. S., Inan, U. S., Bell, T. F., et al. 1998, Geophysical Research Letters, 25, 2995
Lavorenti, F. 2023, Mercury particle precipitation using full-PIC global simulations
Lavorenti, F., Henri, P., Califano, F., Aizawa, S., & André, N. 2021, Astronomy and Astrophysics, 652, A20
Lavorenti, F., Henri, P., Califano, F., et al. 2022, Astronomy and Astrophysics, 664, A133
Lavorenti, F., Henri, Pierre, Califano, Francesco, et al. 2023, A&A, 674, A153
Le, A., Egedal, J., Ohia, O., et al. 2013, Physical Review Letters, 110, 135004
Le Contel, O., Roux, A., Jacquey, C., et al. 2009, Annales Geophysicae, 27, 2259
Liu, K., Gary, S. P., & Winske, D. 2011, Geophysical Research Letters, 38, n/a
Mandt, M. E., Denton, R. E., & Drake, J. F. 1994, Geophysical Research Letters, 21, 73
Markidis, S., Lapenta, G., & Rizwan-uddin. 2010, Mathematics and Computers in Simulation, 80, 1509
Milillo, A., Fujimoto, M., Murakami, G., et al. 2020, Space Science Reviews, 216, 93
Müller, J., Simon, S., Wang, Y.-C., et al. 2012, Icarus, 218, 666
Ness, N. F., Behannon, K. W., Lepping, R. P., & Whang, Y. C. 1976, Icarus, 28, 479
Ness, N. F., Behannon, K. W., Lepping, R. P., Whang, Y. C., & Schatten, K. H. 1974, Science, 185, 151
Nogi, T., Nakamura, S., & Omura, Y. 2020, Journal of Geophysical Research: Space Physics, 125, e2020JA027953
Oliven, M. N. & Gurnett, D. A. 1968, Journal of Geophysical Research, 73, 2355
Omura, Y., Katoh, Y., & Summers, D. 2008, Journal of Geophysical Research: Space Physics, 113, n/a
Omura, Y., Miyashita, Y., Yoshikawa, M., et al. 2015, Journal of Geophysical Research: Space Physics, 120, 9545
Ozaki, M., Yagitani, S., Kasaba, Y., et al. 2023, Nature Astronomy
Pantellini, F., Griton, L., & Varela, J. 2015, Planetary and Space Science, 112, 1
Poh, G., Slavin, J. A., Jia, X., et al. 2017, Geophysical Research Letters, 44, 678
Raines, J. M., DiBraccio, G. A., Cassidy, T. A., et al. 2015, Space Science Reviews, 192, 91
Russell, C. T., Baker, D. N., & Slavin, J. A. 1988, The magnetosphere of Mercury. (NTRS), 514–561
Sarantos, M., Killen, R. M., & Kim, D. 2007, Planetary and Space Science, 55, 1584
Scarf, F. L., Gurnett, D. A., & Kurth, W. S. 1979, Science, 204, 991
Scudder, J. & Daughton, W. 2008, Journal of Geophysical Research: Space Physics, 113, n/a
Siscoe, G. L., Ness, N. F., & Yeates, C. M. 1975, Journal of Geophysical Research, 80, 4359
Slavin, J. A. 2004, Advances in Space Research, 33, 1859
Slavin, J. A., Anderson, B. J., Baker, D. N., et al. 2012, Journal of Geophysical Research (Space Physics), 117, A01215
Slavin, J. A., Anderson, B. J., Zurbuchen, T. H., et al. 2009, Geophysical Research Letters, 36
Slavin, J. A., DiBraccio, G. A., Gershman, D. J., et al. 2014, Journal of Geophysical Research: Space Physics, 119, 8087
Slavin, J. A., Middleton, H. R., Raines, J. M., et al. 2019, Journal of Geophysical Research (Space Physics), 124, 6613
Solomon, S. C. & Anderson, B. J. 2018, in Mercury. The View after MESSENGER, ed. S. C. Solomon, L. R. Nittler, & B. J. Anderson, 1–29
Spreiter, J. R., Summers, A. L., & Alksne, A. Y. 1966, Planetary and Space Science, 14, 223
Stix, T. 1992, Waves in Plasmas
Summers, D., Ni, B., & Meredith, N. P. 2007, Journal of Geophysical Research: Space Physics, 112, n/a
Summers, D., Thorne, R. M., & Xiao, F. 1998, Journal of Geophysical Research: Space Physics, 103, 20487
Sun, W. J., Fu, S. Y., Slavin, J. A., et al. 2016, Journal of Geophysical Research (Space Physics), 121, 7590
Sundberg, T., Slavin, J. A., Boardsen, S. A., et al. 2012, Journal of Geophysical Research (Space Physics), 117, A00M03
Thorne, R. M., Li, W., Ni, B., et al. 2013, Nature, 504, 411
Trávníček, P., Hellinger, P., & Schriver, D. 2007, Geophysical Research Letters, 34, L05104
Trávníček, P. M., Hellinger, P., Schriver, D., et al. 2009, Geophysical Research Letters, 36, L07104
Trávníček, P. M., Schriver, D., Hellinger, P., et al. 2010, Icarus, 209, 11
Tsurutani, B. T. & Smith, E. J. 1974, Journal of Geophysical Research, 79, 118
Winslow, R. M., Anderson, B. J., Johnson, C. L., et al. 2013, Journal of Geophysical Research: Space Physics, 118, 2213
Woodfield, E. E., Glauert, S. A., Menietti, J. D., et al. 2019, Geophysical Research Letters, 46, 7191
Xiao, F., Yang, C., He, Z., et al. 2014, Journal of Geophysical Research: Space Physics, 119, 3325
Yagi, M., Seki, K., Matsumoto, Y., Delcourt, D. C., & Leblanc, F. 2010, Journal of Geophysical Research: Space Physics, 115
Yu, X., Yuan, Z., Li, H., et al. 2018, Geophysical Research Letters, 45, 8755

9.3 Behar et al (under review)

Astronomy & Astrophysics manuscript no. output
August 24, 2024

Impact of solar wind turbulence on a planetary bow shock

A global 3D simulation

E. Behar[1,2], F. Pucci[3], C. Simon Wedlund[4], P. Henri[1,5], G. Ballerini[6,7], L. Preisser[4], and F. Califano[7]

[1] Laboratoire Lagrange, Observatoire de la Côte d'Azur, Université Côte d'Azur, CNRS, Nice, France

[2] Swedish Institute of Space Physics, Kiruna, Sweden

[3] Institute for Plasma Science and Technology, National Research Council, CNR-ISTP, Bari, Italy
e-mail: francesco.pucci@istp.cnr.it

[4] Space Research Institute, Austrian Academy of Sciences, Graz, Austria

[5] LPC2E, CNRS, Université d'Orléans, CNES, Orléans, France

[6] LPP, CNRS/Sorbonne Université/Université Paris-Saclay/Observatoire de Paris/Ecole Polytechnique Institut Polytechnique de Paris, Palaiseau, France

[7] Dipartimento di Fisica "E. Fermi", Università di Pisa, Pisa, Italy

Received: ... ; accepted ...

ABSTRACT

Context. The interaction of the solar wind plasma with a magnetized planet generates a bow-shaped supercritical shock ahead of it. Over the past decades, near-Earth spacecraft observations have provided insights into the physics of the bow shock, suggesting that solar wind intrinsic turbulence influences the bow shock dynamics. On the other hand, theoretical studies, primarily based on global numerical simulations, have not yet investigated the global 3D interaction between a turbulent solar wind and a planetary magnetosphere. This paper addresses this gap for the first time by investigating the global dynamics of this interaction, providing new perspectives on the underlying physical processes.
Aims. We examine how the turbulent nature of the solar wind influences the 3D structure and dynamics of magnetized planetary environments like those of Mercury, Earth, or magnetized Earth-like exoplanets, using the newly developed numerical model *Menura*.
Methods. We use the hybrid Particle-In-Cell model *Menura* to conduct 3D simulations of the turbulent solar wind and its interaction with an Earth-like magnetized planet through global numerical simulations of the magnetosphere and its surroundings. *Menura* runs in parallel on GPUs, enabling efficient and self-consistent modelling of turbulence.
Results. By comparison with a case in which the solar wind is laminar, we show that solar wind turbulence globally influences the shape and dynamics of the bow shock, the magnetosheath structures, and the ion foreshock dynamics.
We show that a turbulent solar wind disrupts the coherence of foreshock fluctuations, induces large fluctuations on the quasi-perpendicular surface of the bow shock, facilitates the formation of bubble-like structures near the bow shock's nose, and modifies the properties of the magnetosheath region. None of these phenomena occur when comparing with the case in which the solar wind is laminar.
Conclusions. The turbulent nature of the solar wind impacts the 3D shape and dynamics of the bow shock, magnetosheath, and ion foreshock region. This influence should be taken into account when studying solar wind–planet interactions in both observations and simulations. We discuss the relevance of our findings for current and future missions launched into the heliosphere.

Key words. solar wind – turbulence – magnetosphere – Earth – plasmas

1. Introduction

The solar wind is a supersonic and super-Alfvénic plasma flow, mainly composed of energetic protons embedded in a large-scale magnetic field. It fills the interplanetary medium and directly interacts with planets, forming a magneto-environment around them. The main features of this environment are a supercritical collisionless bowshock, a turbulent magnetosheath and an induced elongated magnetosphere downstream of it (Parks et al. 2021; Sibeck & Murphy 2021; Southwood 2021). Depending on the value of θ_{Bn}, defined as the angle between the local shock normal and the upstream magnetic field's direction, the bow shock can be locally classified as quasi-parallel ($\theta_{Bn} < 45°$) or quasi-perpendicular ($\theta_{Bn} > 45°$), with θ_{Bn} values around 45° defining a so-called oblique geometry (Jones & Ellison 1991; Schwartz 1998). The existence of these two main shock geometries leads to different plasma kinetic dynamics around the bow-shock region (Burgess & Scholer 2015).

Solar wind-planet interaction has been extensively studied over the last decades using numerical simulations. The global

interaction of the solar wind and Earth-like magnetospheres has been investigated in the past by means of two-dimensional (2D) kinetic hybrid models, where ions are treated as individual kinetic macroparticles and electrons as a charge-neutralizing magnetohydrodynamic fluid. Pioneering hybrid modelling studies include those for curved collisionless shocks (Thomas & Winske 1990) and for Earth's magnetosphere models (Swift 1995), and have, for example, focused on the interaction of an interplanetary rotational discontinuity with Earth's magnetosphere (Lin et al. 1996). Later on, wave behaviour (Lin et al. 2001) and velocity distribution functions (Lin & Wang 2002) have been studied extensively in the magnetosheath region. A three-dimensional (3D) geometry has been used to reproduce the basic dynamics of the magnetosphere with the existence of a turbulent magnetosheath medium, ion foreshock and waves associated with different regions upstream of the magnetopause (Kallio & Janhunen 2003; Kallio & Janhunen 2004; Trávníček et al. 2007; Müller et al. 2011, 2012; von Alfthan et al. 2014; Modolo et al. 2016; Jarvinen et al. 2020; Aizawa et al. 2021; Aizawa et al. 2022; Kallio et al. 2022; Teubenbacher et al. 2024). Recently, global full kinetic Particle-In-Cell (PIC) simulations of the interaction between the solar wind and a magnetized planet have been performed in 2D (Peng et al. 2015) and 3D (Lavorenti et al. 2022; Lapenta et al. 2022; Lavorenti et al. 2023) to investigate the role of electron kinetics in the global interaction of the solar wind with a magnetized planet.

All such global models always take, for the sake of simplicity, the standpoint that the solar wind plasma dynamics is laminar. Nevertheless, the solar wind is turbulent, with relatively large amplitude, large-scale magnetic and density fluctuations driven by continuous large-scales energy injection from the Sun. Solar wind fluctuations span a large range of spatial and temporal scales (Bruno & Carbone 2013; Kiyani et al. 2015; Verscharen et al. 2019). It is expected that the turbulent solar wind may influence the shock dynamics, as predicted by basic theoretical models (Zank et al. 2002).

Observational studies have focused on the dynamics and turbulent nature of the solar wind and its connection to the bow shock, magnetosheath and magnetosphere dynamics (see, e.g., Rakhmanova et al. 2023, and references therein). In particular, observations have shown that geomagnetic activity depends on internal magnetospheric processes and solar wind conditions (D'Amicis et al. 2020; Guio & Pécseli 2021a,b). Complementary to observations, numerical studies of the interaction of solar wind turbulence with an interplanetary shock are very recent. Different with respect to global simulations, they have been performed in a 'local' sense, that is, looking at a relatively small portion of the shock interaction region, not taking into account the global curved nature of a planetary shock and using one wall of the simulation as a fully reflective boundary. These local hybrid PIC simulations have shown that turbulent fluctuations in the upstream region enhance particle acceleration at the shock front, leading to a diffusive spread of the particles in velocity space (Trotta et al. 2021). This result has been supported by observations of an increase in the magnetic helicity downstream of the shock as turbulent structures are compressed while transmitted across the quasi-perpendicular shock (Guo et al. 2021; Trotta et al. 2022). Local hybrid PIC simulations have also been used to study the interaction of multiple current sheets with a shock wave, discussing the implication of such interaction on particle acceleration in the downstream shock region (Nakanotani et al. 2021). Further hybrid PIC simulations have confirmed the role of upstream turbulence as a scattering agent to promote diffusive shock acceleration (Nakanotani et al. 2022). More recently, by coupling turbulent MHD fields and local quasi-perpendicular hybrid kinetic 3D simulations, Trotta et al. (2023) showed that turbulence increases fluctuations at the shock interface and the isotropization of the magnetic field spectra in the downstream region close to the bow shock.

However, none of the above studies have investigated the global response of a magnetised planet's magnetosphere to solar wind turbulence. The numerical model that we use in this study, namely *Menura*, has been specifically designed for this purpose. *Menura* can self-consistently model a fully-developed turbulent solar wind interacting with a planet (Behar et al. 2022) and was recently used by Behar, E. & Henri, P. (2023) to show in 2D that the turbulence of the solar wind significantly modifies the dynamics of the induced magnetosphere of comets.

Here, we present the results of the first 3D hybrid simulation of the interaction between a turbulent solar wind and the magnetosphere of a magnetised planet with a size approaching that of the Earth. For the first time, we show how the turbulent nature of the solar wind affects the global shape and dynamic of the bow shock, the fluctuations in the magnetosheath, and the ion foreshock region.

The paper is organized as follows. In Section 2, we describe the model and the parameters of the simulations conducted with *Menura*. Section 3 discusses the shape of the bow shock and its dynamics. We focused specifically on the ion foreshock and the structures locally created by the upstream turbulence as examples of kinetic effects captured by Menura on both quasi-parallel and quasi-perpendicular sides of the bow shock. We conclude and discuss the future perspectives that open up with this study in Sect. 4.

2. The model

We use the 3D hybrid kinetic particle-in-cell (PIC) model *Menura* to simulate the interaction of a turbulent solar wind with a planetary magnetosphere. A detailed code description is available in Behar et al. (2022), and an example of application in a reduced, so-called 2.5D geometry is described in Behar, E. & Henri, P. (2023). In this work, we use the 3D version of the code. *Menura* is a hybrid PIC model that provides a kinetic description of ion dynamics and employs a generalized Ohm's law coupled to a polytropic closure for the massless electrons. *Menura* uses the CAM scheme (or Current Advanced Method) (Matthews 1994), used routinely in PIC hybrid codes as well more recently in hybrid Eulerian Vlasov codes (Valentini et al. 2007).

Our study here is conducted in two successive steps. First, we perform a 3D simulation of solar wind decaying turbulence using periodic boundary conditions. This simulation follows the solar wind evolution until a quasi-stationary state is achieved and the turbulence is fully developed. Second, we use the last iteration step of the turbulent decay simulation as the initial condition of a new run in which we simulate the interaction of this turbulent solar wind with a compact magnetized planet (such as the Earth or Mercury). More details on treating boundary conditions for this second step are described in Behar et al. (2022) and Behar, E. & Henri, P. (2023). Additionally, a reference simulation is performed using laminar solar wind conditions to properly assess the effects of solar wind turbulence on the interaction with the planetary obstacle.

In both steps, the solar wind and planetary plasma dynamics equations are solved in the solar wind reference frame. Unlike the object-centred reference frame used in other models with similar scientific purposes (von Alfthan et al. 2014; Grandin

et al. 2023; Karimabadi et al. 2006), solving equations in the solar wind reference frame enables the introduction of a solar wind flow-aligned magnetic field that varies in time. This condition is necessary to inject a well-defined, fully developed, self-consistently generated turbulent flow that includes, for example, magnetic vortices.

In the following, we describe the initial conditions and parameters of these two successive simulations, which we named Sim 1 and Sim 2.1, and the reference laminar run, which we named Sim 2.2. Table 1 summarises the simulations' input parameters.

2.1. Decaying simulation of solar wind turbulence (Sim 1)

In this kinetic hybrid simulation, the solar wind consists of one ion species, i.e. protons, and massless neutralizing electrons. The simulation domain is a Cartesian box of equal size $L_{box} = L_X = L_Y = L_Z = 2000\ d_i$ in the three spatial directions, discretized in 400 cells in each direction with a spatial resolution of $\Delta x = 5d_i$, with d_i the solar wind proton inertial length. We populate each cell with 600 macroparticles to ensure a statistically satisfactory representation of the ion distribution function. The simulation's time step is $\Delta t = 0.5\ \Omega_{ci}^{-1}$, with Ω_{ci} the solar wind proton gyrofrequency. Consequently, these simulation parameters are such that ion scales are poorly resolved spatially and temporally. Such a resolution is imposed by computational constraints; however, in this study, we do not specifically focus on the dynamics at the ion and sub-ion scale but rather on phenomena just below the smallest MHD scales, approaching the ion kinetic scales, while enabling us to describe some kinetic features such as a supercritical bow shock and the associated reflected ions in the foreshock. The initial equilibrium condition is made of a solar wind plasma with homogeneous density and temperature, permeated by a homogeneous, oblique (to the solar wind flow) mean magnetic field B_0 (see Table 1). At equilibrium, the ratio of ion kinetic and magnetic pressures is $\beta_i = 0.5$ and the ion-to-electron temperature ratio is $T_i/T_e = 1$, resulting in $\beta = \beta_i + \beta_e = 1$. We impose an isothermal closure on electrons, corresponding to an adiabatic index $\gamma_e = 1$. We perturb this equilibrium with magnetic and velocity fluctuations at large scales. The initial velocity fluctuations are incompressible following $\nabla \cdot \mathbf{v} = 0$. The initial perturbation is made of sinusoidal fluctuations with a polarization orthogonal to both the mean field and the wavevector $\mathbf{k}$. The wavevectors are directed along the three Cartesian directions and all wavevectors within the range $[k_{min}, k_{max}] = [2\pi/L_{box}, 5{\cdot}2\pi/L_{box}]$ are populated. The phases are random and different for the velocity and magnetic fluctuations.

The magnetic field lines and the total charge current $|J|$ in the simulation box at the end of the decaying turbulence simulation are shown in Fig. 1a. The anisotropy in the magnetic field fluctuations is evident from the elongated shape of the current structures aligned parallel to the mean solar wind magnetic field.

The time evolution of the charge current fluctuations $J_{\rm rms}$, defined as its root mean square (RMS), is shown in Fig. 1b. The vertical dashed line indicates the time the decaying turbulence simulation is fully developed so that it can be injected later in the magnetised planet simulation. We identify it with the time when the RMS current saturates. At the end of this first simulation, the RMS value of the final perturbation is $\delta B/B_0 = 0.45$ and $\delta v/C_A = 0.33$, where δB and δv are the magnetic and velocity RMS values, B_0 is the background magnetic field and C_A is the background Alfvén speed in normalised units.

We have computed the parallel and perpendicular (to the mean solar wind magnetic field direction) spectra of magnetic and velocity fluctuations, shown in Fig. 1c. The magnetic field follows a power-law trend with a spectral slope consistent with the expected Kolmogorov decay of $-5/3$. At smaller scales, closer to one d_i, the spectral trend changes under the effect of both the numerical dissipation (hyper-resistivity) and dispersive and kinetic ion physics (Matteini et al. 2016).

The electric field and magnetic field as well as the plasma distribution function from the decaying turbulence simulation at time $t \simeq 650\,\Omega_{\rm ci}^{-1}$ are used to initialize the second simulation of our model (Sim 2.1).

2.2. Interaction between a magnetized planet and a solar wind turbulent dynamics (Sim 2.1)

In this second simulation, we model the interaction between a solar wind with fully developed turbulent dynamics, resulting from Sim 1, and a magnetized planet. The magnetised planet is modelled as a perfectly absorbing body on which entering ions are removed from the simulation, together with a permanent magnetic dipole, taken as an external magnetic field.

Since the computation is performed in the solar wind frame, the planet is moving in the simulation domain at the opposite of the solar wind speed. To maintain the planet at a fixed position in the simulation domain, we continuously shift the domain sideways (in the $+X$ direction). Consistently, the dipole field is recalculated each time the simulation box moves. In fact, our choice of reference frame requires adding an additional term in Faraday's law corresponding to a Lorentz transformation. To our knowledge, this is the first time a non-fixed reference frame has been used for this type of application. In the simulation box, the planet's centre is kept at coordinates $(X_{\rm P}, Y_{\rm P}, Z_{\rm P}) = (3L_{\rm box}/8, L_{\rm box}/2, L_{\rm box}/2) = (750, 1000, 1000)\ d_i$, with $L_{\rm box}$ the size of the box in any direction in units of d_i.

The dipole value is chosen by defining the value D_p as the position of the nose of the magnetopause normalized to the ion's inertial length. This parameter has proven to be an effective method for characterizing the magnetospheric structure as a function of dipole strength (Omidi et al. 2004; Karimabadi et al. 2014). In this work, to reduce the computational effort, we use $D_p = 200\,d_i$, a smaller value with respect to the real value at Earth ($D_{p,\rm Earth} \sim 640\,d_i$). As pointed out in Omidi et al. (2004), simulations with D_p greater than ~ 20, one order of magnitude smaller than the one we used, have Earth-like characteristics both on the dayside and in the magnetotail. The smaller size of the magnetosphere and magnetosheath reduces the transit time of the plasma inside the magnetosheath by a factor ~ 3 with respect to the Earth. This may affect the development of waves in the region, such as wave modes with a relatively low growth rate, as they may not have time to develop before reaching the magnetopause. However, this work is the first step in studying how turbulent solar wind globally affects the different large-scale frontiers in a planetary magneto-environment.

2.3. Interaction between a magnetized planet and a solar wind laminar dynamics (Sim 2.2)

To properly assess the impact of the turbulent nature of the solar wind on a magnetosphere, it is necessary to compare its effect to that of an upstream solar wind that would be laminar. For this purpose, we run a third reference simulation in which the planet interacts with a laminar solar wind. In this case, the planet moves into a homogeneous solar wind with plasma density and temperature equal to those chosen as the initial condition of Sim 1. The

Variable	Unit	Value	Description
Normalisation			
Density	n_0		Initial solar wind density
Magnetic field	B_0		Module of initial solar wind magnetic field
Time	$\Omega_{\rm ci}^{-1}$	$m_p c/eB_0$	Inverse of proton gyrofrequency
Speed	C_A	$B_0/\sqrt{4\pi n_0 m_p}$	Alfvén speed
Length	d_i	$C_A/\Omega_{\rm ci}$	Proton inertial length
Pressure	P_0	$n_0 m_p C_A^2$	Normalizing pressure
Solar wind parameters			
$n_{\rm sw}$	n_0	1.0	Solar wind proton density
$\mathbf{B}_{\rm sw}$	B_0	$\left(\frac{1}{\sqrt{2}}, \frac{1}{\sqrt{2}}, 0\right)$	Solar wind magnetic field vector
$\mathbf{U}_{\rm sw}$	C_A	$(-10, 0, 0)$	Solar wind velocity vector, planet's reference frame
T_i/T_e	-	1.0	Ratio of proton temperature to electron temperature
$\beta_{\rm sw} = \beta_i + \beta_e$	-	1.0	Solar wind plasma beta
γ_e	-	1.0	Electron adiabatic index
$C_{\rm s}$	C_A	1.4	Solar wind sound speed
$C_{\rm ms}$	C_A	1.7	Solar wind magnetosonic speed
$M_{\rm A}$	-	10	Bow shock Mach number
Turbulence			
$\delta B_0/B_0$	-	0.54	Initial magnetic field fluctuations
$\delta v_0/C_A$	-	0.54	Initial velocity fluctuations
Magnetized planet			
$(X_{\rm P}, Y_{\rm P}, Z_{\rm P})$	d_i	$\left(\frac{3L_{box}}{8}, \frac{L_{box}}{2}, \frac{L_{box}}{2}\right)$	Position of the planet's centre in simulation box
$\tau_{\rm dip}$	-	$(0, -1, 0)$	Dipole moment direction
$D_{\rm mp}$	d_i	200	Distance to the magnetopause from the planet's centre
Grid and numerics			
$\Delta X = \Delta Y = \Delta Z$	d_i	5.0	Grid resolution
Δt	$\Omega_{\rm ci}^{-1}$	0.5	Time resolution
$L_{box} = L_X = L_Y = L_Z$	d_i	2000	Box size in each spatial direction
$N_{\rm pcc}$	-	600	Number of particles per cell
$\eta_{\rm hyp}$	-	0.01	Numerical hyper-resistivity
Simulation names			
Sim 1			Decaying solar wind turbulence
Sim 2.1			Turbulent solar wind vs. planet
Sim 2.2			Laminar solar wind vs. planet

Table 1. Input parameters of the simulations performed: code normalizations, solar wind parameters for all runs, initial amplitude of turbulence in the decaying run, characteristics of the magnetized planet, grid and time resolution for all runs. m_p is the proton mass, c the speed of light in vacuum and e the elementary charge. Simulation parameters are typical of the solar wind (Owens et al. 2023), with n_0 and B_0 the initial solar wind density and magnetic field magnitude.

solar wind magnetic field is also homogeneous and equal to $\mathbf{B}_{\rm sw}$. All other simulation parameters, including planet parameters and spatial and temporal resolution, are identical to those of Sim 2.1.

3. Impact of a turbulent solar wind on a planetary bow shock

In the following, we compare the *turbulent* (Sim 2.1) and *laminar* (Sim 2.2) simulations to highlight the effects that the turbulent nature of the solar wind has on the magneto-environment of a planet. To compare the structure and dynamics of the solar wind, shock, and magnetosheath in the two simulations, we present maps of relevant quantities in three perpendicular planes intersecting the centre of the planet, located at coordinates $(X_{\rm P}, Y_{\rm P}, Z_{\rm P})$.

Figures 2, 3 and 4 present global maps of the plasma density, magnetic field magnitude and proton bulk speed, respectively: the left column (panels a, b, c) shows the laminar solar wind case results, whereas the right column (panels d, e, f) shows the turbulent solar wind case at the same simulation time $t = 250\,\Omega_{\rm ci}^{-1}$. Density is normalised to the solar wind proton density, the magnetic field to the solar wind magnetic field, and proton bulk speeds to the Alfvén speed (see Table 1). For both turbulent and laminar simulations, the bow shock, magnetosheath, and magnetopause regions can be clearly identified, with the quasi-parallel ($Y > 1400\,d_i$) and quasi-perpendicular ($Y < 800\,d_i$) sides of the shock having shapes and extents in good qualitative agreement with other global simulations (Turc et al. 2023). Closer to the planet, regions where ions are seen flowing within the magnetosphere of the planet take the shape of highly structured cones in 3D (see Fig. 2a in the X–Y plane at $Z = Z_{\rm P}$, with $Z_{\rm P}$ the position of the planet's centre), closely mimicking the Earth's plasma cusps. These "cusps" appear relatively less defined in the turbulent solar wind case, owing to the less homogeneous magnetosheath (Fig. 2b). The following sections provide a detailed description of how the turbulent nature of the solar wind shapes these boundaries and regions.

3.1. Shape of the bow shock

To facilitate comparisons of the shape of the bow shock in the absence or presence of turbulence in the solar wind, we built

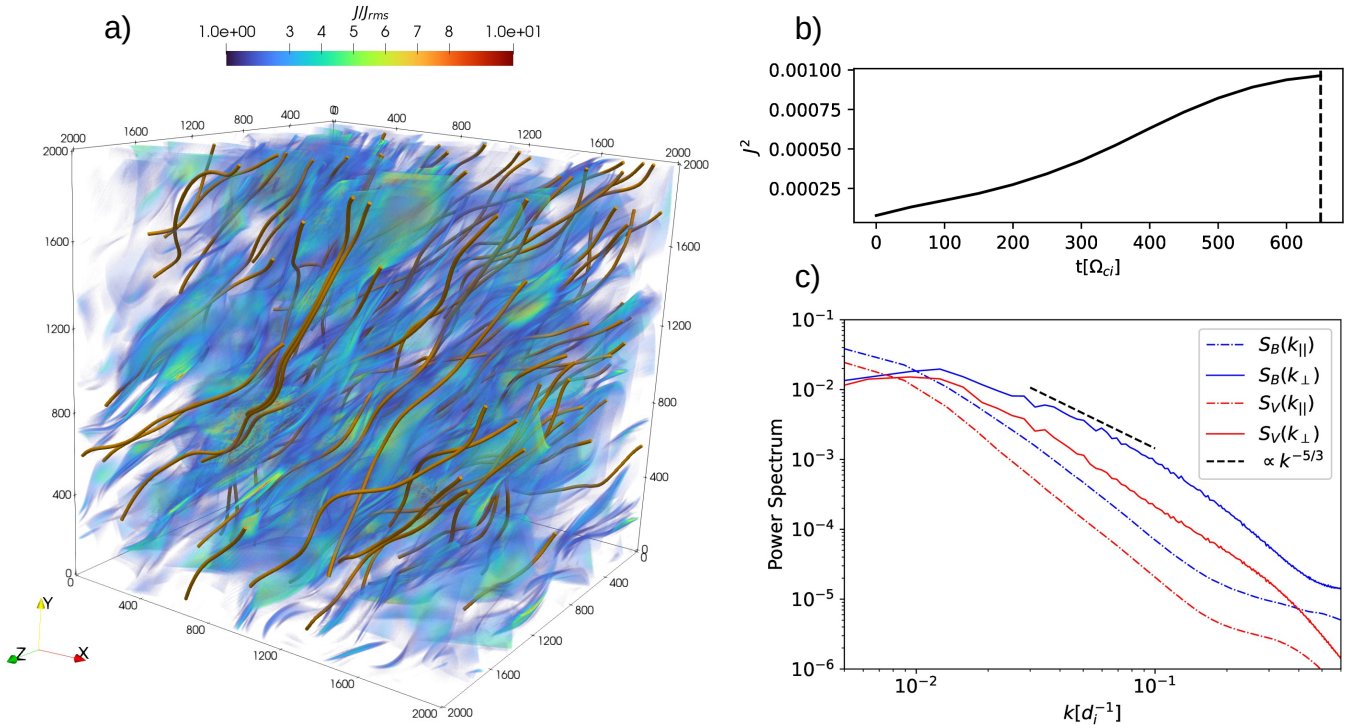

Fig. 1. Characteristics of the decaying simulation of solar wind turbulence (Sim 1). a) Current density normalized to its root mean square $J_{\rm rms}$ (colour map) and magnetic field lines (orange) in the full 3D plasma box. b) Box-averaged square current density J^2 as a function of time. The vertical dashed line marks the time of the snapshot ($t \simeq 650\,\Omega_{\rm ci}^{-1}$) used to initialize the solar wind turbulence in Sim 2.1. c) Power spectrum of magnetic and velocity field for parallel and perpendicular wavevectors.

a simple proxy of the 3D position of the shock surface saved at high temporal cadence during a numerical run. This proxy is defined using the plasma density: for each (Y, Z) coordinate, the position of the bow shock is estimated to be the first position along the X direction at which the density jumps above a value of $10^{1/4}$, i.e. about 1.8 times the solar wind background value, which is chosen as an intermediate value between the upstream solar wind and the downstream magnetosheath plasma.

The position of the shock in the laminar solar wind case (Sim 2.2) is shown in Fig. 2 by the thin solid black line within each plane. The same line is superimposed onto the results of the turbulent case (Sim 2.1) as a baseline for comparison between the laminar and turbulent solar wind-planet simulations. Moreover, the same bow shock position in the laminar case is superimposed onto the magnetic field maps (Fig. 3), showing how well it captures the sharp transition between the upstream solar wind magnetic field (in white) and the compressed downstream magnetic field and denser magnetosheath (in red). Similarly, this sharp transition is seen on the proton bulk speed maps (Fig. 4) where the solar wind (in white) is abruptly slowed down to subsonic speeds at and downstream of the shock (blue hues).

When observing the quasi-perpendicular region of the bow shock, the density maps in (Fig. 2a-f) show that the shock surface is inflated or deflated with respect to the laminar case when the impinging initial solar wind is turbulent. This feature is also confirmed by the magnetic field (Fig. 3) and the proton bulk speed maps (Fig. 4). These fluctuations of the quasi-perpendicular bow shock surface result from local inhomogeneities in the solar wind bulk dynamic pressure, which stem from the turbulent nature of the initial solar wind condition in Sim 2.1: turbulence causes certain regions to experience higher or lower values of solar wind dynamic pressure compared to the laminar case (Sim 2.2).

The difference between the bow shock's location in the two runs is most pronounced for the quasi-parallel shock. In the quasi-parallel shock region, the shock surface proxy does vary widely, as seen for $Y \gtrsim 1300\,d_i$ in Fig. 2a and at $Y \sim 1500\,d_i$ in the corresponding perpendicular plane in Fig. 2c, laminar case, but can capture the overall shape of the shock in this highly variable region. That said, the sharp and well-defined transition between the upstream and quasi-parallel downstream domains in the laminar case is mostly lost in the turbulent case due to fluctuations in the solar wind that locally change the magnetic field orientation with respect to the shock normal. In this way, the density variation proxy used for the laminar case cannot capture the highly variable quasi-parallel shock interface in the turbulent case. However, such a proxy remains useful to highlight how far turbulence changes the quasi-parallel shock location and shape.

In the density maps in Fig. 2, we observe that the compression downstream of the quasi-parallel shock is less pronounced in the turbulent case (Fig. 2d) and the structure of the bow shock is significantly more perturbed than in the laminar case (Fig. 2c,f). For $Y > 1600\,d_i$, it becomes difficult to identify the exact location of the quasi-parallel shock boundary (Fig. 2d).

These differences are clearly shown in Fig. 5 where the bow shock is visualized in 3D, setting a transparency threshold of $n_{th} = 10^{1/4} n_0$ on the plasma density. While in the laminar case (Fig. 5a), the shock boundary is mainly smooth over all the corresponding quasi-perpendicular surface, for the turbulent simulation (Fig. 5b) large fluctuations are presented over all the bow shock. The quasi-parallel region is more easily identified in the laminar case, where the fluctuations delimit a clear area around

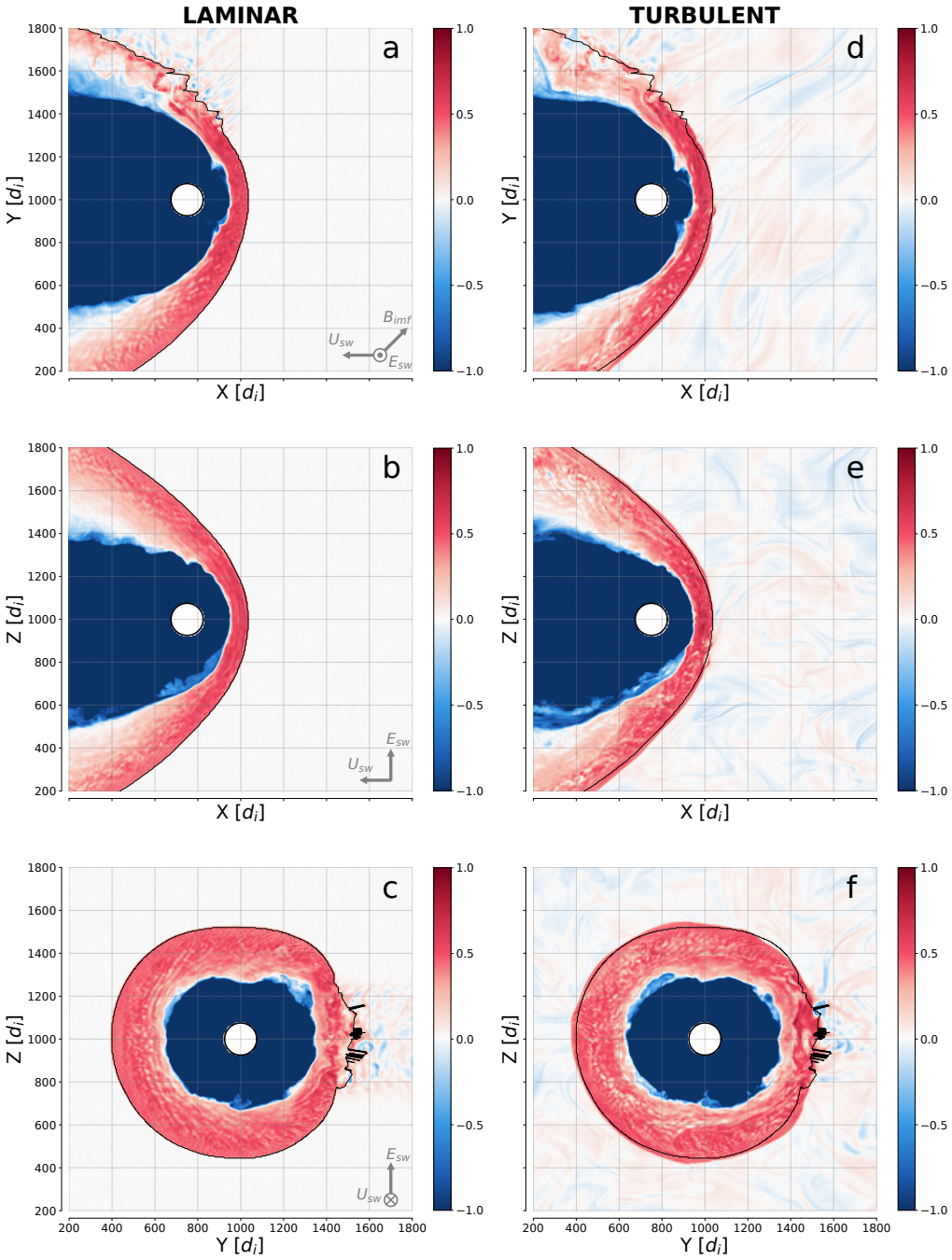

Fig. 2. Comparison of ion density in logarithmic scale between laminar (a-c) and turbulent (d-f) simulations at $t = 250\,\Omega_{ci}^{-1}$ for the same 2D planes intersecting the planet's centre. The initial solar wind magnetic field $\mathbf{B}_{sw}$ is contained in the X–Y plane (in a 45° angle). In the planet's reference frame, the $+Z$ direction contains the solar wind convection electric field $\mathbf{E}_{sw}$, whereas the solar wind bulk velocity $\mathbf{U}_{sw}$ is along $-X$, and given as indicators. The position of the bow shock based on a density threshold for the laminar simulation (left column) is shown for comparison as a black contour line for both simulations.

the north pole region that corresponds to the foot points from where magnetic field lines (in red) parallel to the local shock normal are emerging. In contrast, the corresponding quasi-parallel region is not well delimited for the turbulent case, and the magnetic field lines do not appear aligned as they are in the laminar case. This feature affects the dynamics of the ion foreshock, as discussed in more detail in Sect. 3.4.

3.2. Dynamics of the bow shock

As already described, the proxy of the bow shock position introduced in the previous section is computed during runtime and at high cadence. This enables high-resolution analysis of the bow shock shape and evolution forced by the solar wind dynamics. This analysis is shown in Fig. 6. To reduce the dimension of the problem, we first consider in Fig. 6a, b the cut $Y = Y_P$ of the bow shock surface. The time evolution of this 1D cut along z of the bow shock position is shown for both the laminar

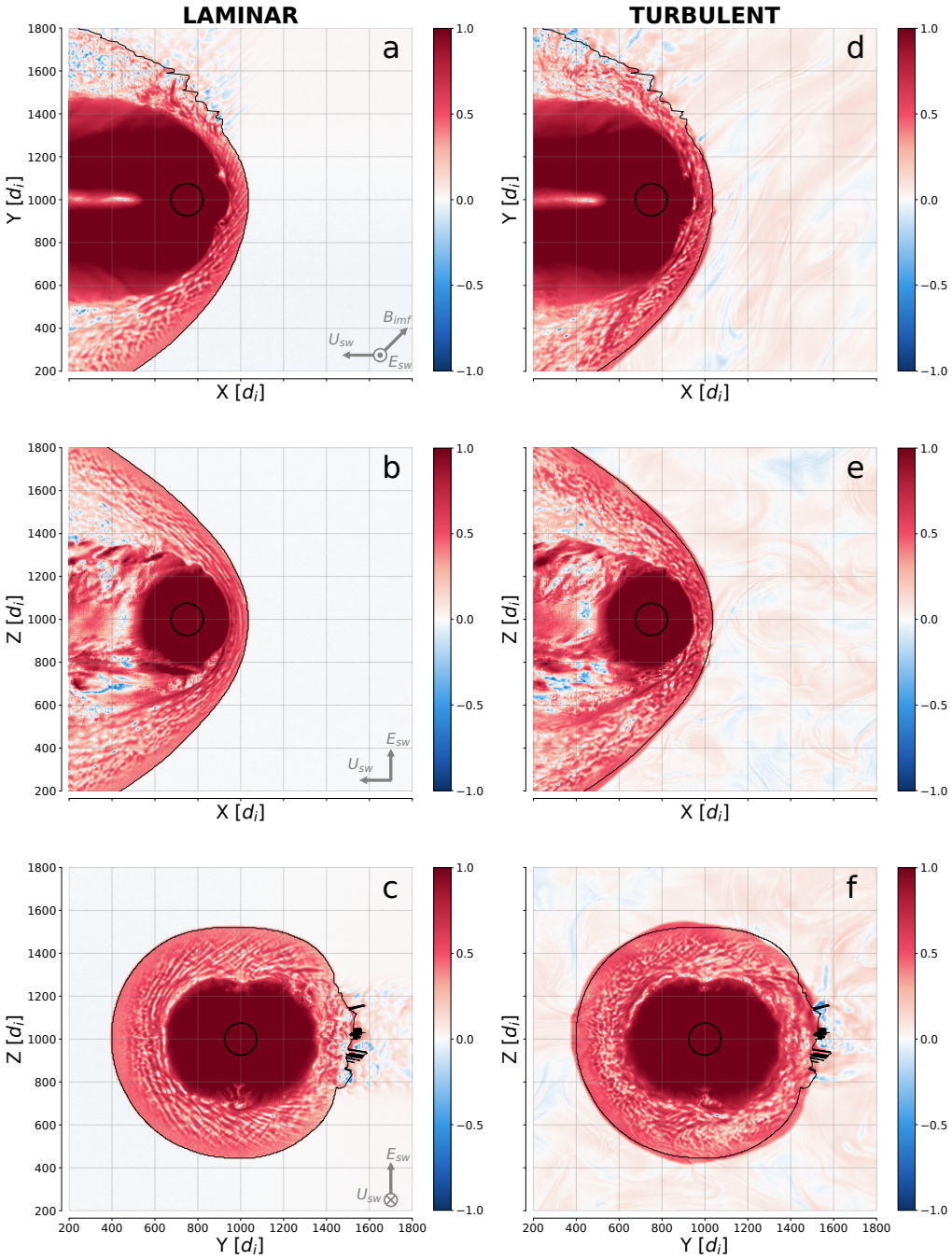

Fig. 3. Comparison of the magnetic field amplitude in logarithm scale between laminar and turbulent simulations at $t = 250\,\Omega_{ci}^{-1}$. Same format as in Fig. 2.

(Fig. 6a) and turbulent (Fig. 6b) solar wind dynamics. The bow shock position along the Sun-planet direction X with respect to its mean value over time, i.e., with respect to its time-averaged position, is shown in colour, with red (resp. blue) tones highlighting the times and positions at which the shock position is upstream (resp. downstream) of its average position. Using the same range of colours for the turbulent and laminar cases (the deviations from the average position are displayed between $-10\,d_i$ and $+10\,d_i$), we appreciate how the turbulence of the impinging solar wind induces much larger amplitude oscillations of the shock's surface. The variance of the values shown in Fig. 6a is $0.8\,d_i$, while a greater variance of $2.0\,d_i$ is found in the turbulent case.

Second, we illustrate the deformation of the bow shock in Fig. 6c, d by showing the planar projections of the full 3D shock surface position with respect to its time-averaged position at a given time $t = 250\,\Omega_{ci}^{-1}$, for both laminar (Fig. 6c) and turbulent (Fig. 6d) solar wind dynamics. This representation of the bow shock deformation is similar to that of the position of a vibrating tambourine skin under the drumming action of the impinging solar wind. We observe local and global oscillations of the shock position. In the laminar solar wind dynamics case, the bow shock deformation is first observed at the bow shock nose and subse-

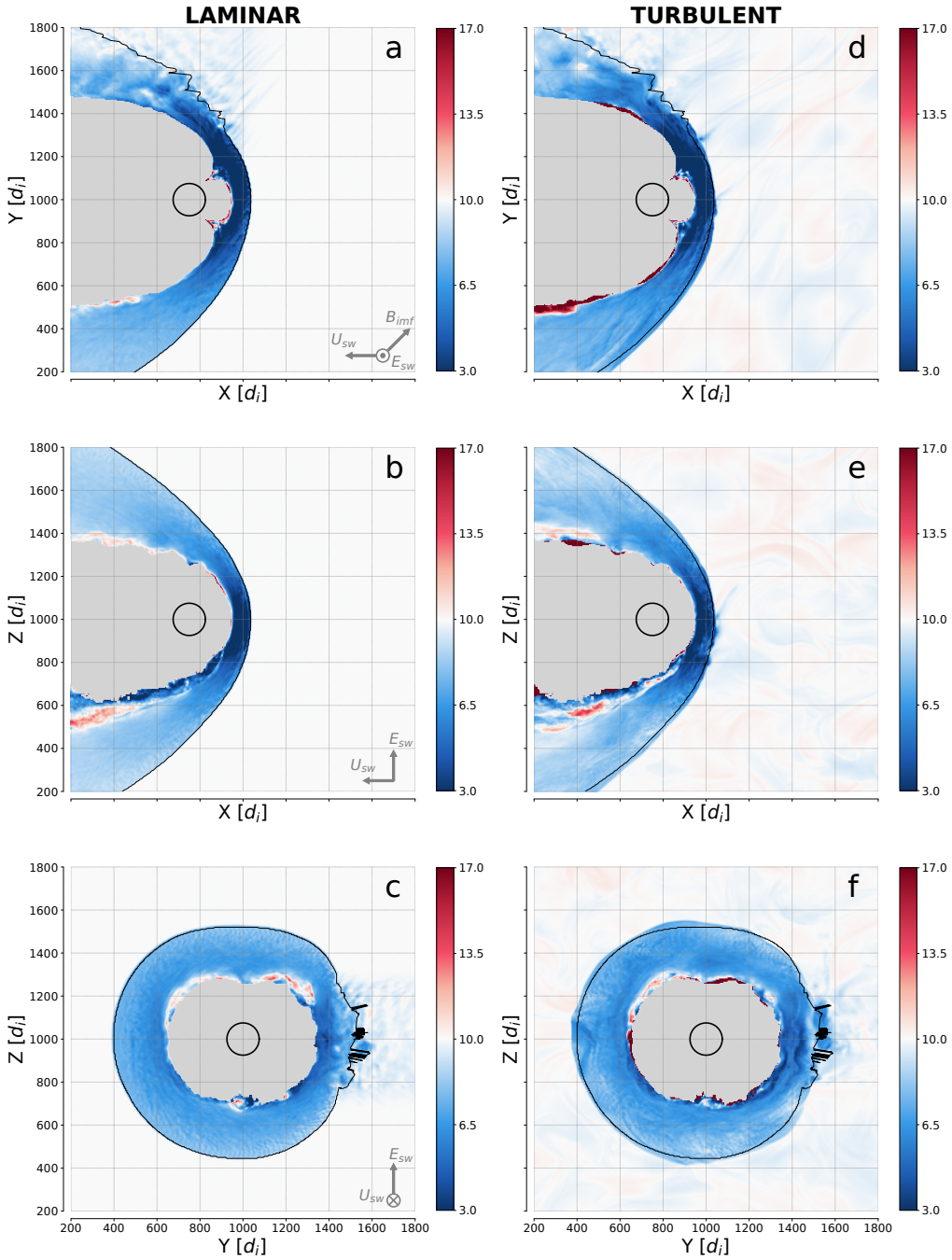

Fig. 4. Comparison of the proton bulk speed U_p between laminar (left column) and turbulent solar wind simulations (right column) at $t = 250\,\Omega_{ci}^{-1}$. Note that the colour scale is linear for clarity, unlike in Figs. 2 and 3. Same format as in Fig. 2, with colour bar in units of Alfvén speed C_A and white the input solar wind speed ($U_{sw} = 10\,C_A$). Note that the bulk speeds are expressed in the planet's reference frame here. Grey regions are those where the plasma density is smaller than $0.1n_0$.

quently propagates from the nose towards the flanks, along the surface of the shock, creating the "butterfly-shaped" propagating structures in the Z–t space observed in the top panels. In contrast, for the turbulent solar wind dynamics case, the bow shock deformation originates from multiple regions (not only the nose) depending on the solar wind dynamics and the local conditions at the shock. These deformations later propagate towards the flanks along the surface of the shock, generating an even more complex deformation pattern. This dynamics is reminiscent of the ubiquitous rippling observations at the Earth's quasi-parallel (Pollock et al. 2022), quasi-perpendicular (Moullard et al. 2006) and oblique (Gingell et al. 2017) bow shock.

The quasi-parallel shock region exhibits significant variability, regardless of the initial solar wind conditions imposed in the simulations; the oblique and quasi-perpendicular shock surface variations are strongly enhanced in the turbulent solar wind case, with amplitudes reaching $\pm 10 d_i$, whereas in the laminar case, maximum amplitudes are much weaker ($\pm 2 d_i$). Beyond this much greater motion of the shock surface, turbulence is also responsible for the peculiar dynamics observed in confined re-

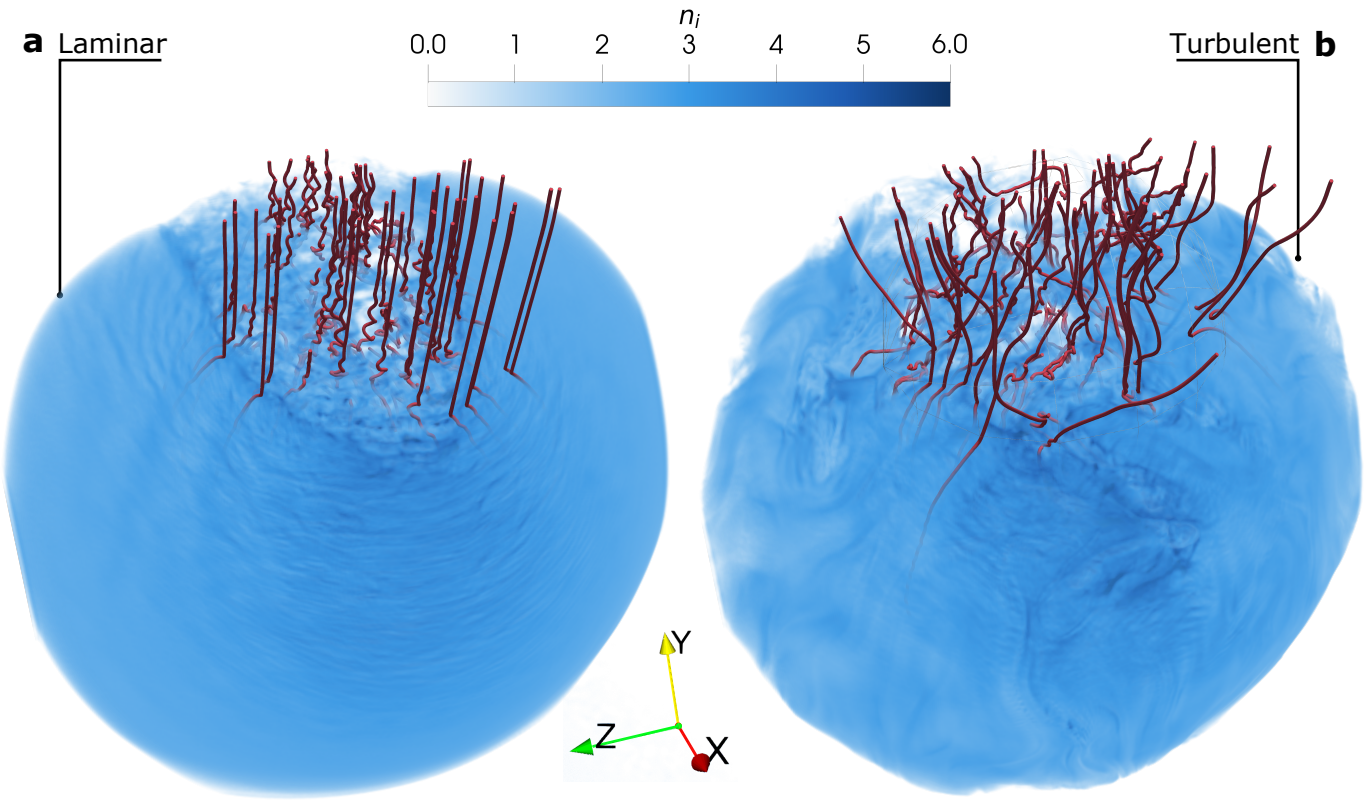

Fig. 5. 3D rendering of the bow shock for the a) laminar and b) turbulent solar wind cases. Ion density is represented in blue hues. A threshold density $n_{th} = 10^{1/4} n_0$ is applied, such that all regions in which $n_i < n_{th}$ are made transparent. A linear transparency profile is applied from $n_i = n_{th}$ to $n_i = 6n_0$, so low-density regions are more transparent than high-density ones. Upstream magnetic field lines crossing the ion foreshock regions are drawn in red.

gions of the shock front. At $t \sim 250\,\Omega_{ci}^{-1}$, close to the nose of the shock around $Z \sim 800\,d_i$, a small "spot" (circled in black in Fig. 6b) departing from the average shock position is seen on the time series for the turbulent simulation. This transient structure is located at the bow shock interface around coordinates $(1000, 800)\ d_i$ in panel e, corresponding to the X–Z plane in Figs. 2, 3 and 4 and propagates along the shock's surface and inside the magnetosheath (Fig. 6b). We show a zoom-in plot of this highly dynamic structure in Fig. 7, with density, magnetic field and bulk speeds, corresponding to a snapshot of the simulation when the structure has fully formed. It appears as a localised "bubble" of high-magnetic field, high-density plasma enclosing a much lower magnetic field and lower-density plasma. This suggests that, locally, a bubble of shocked solar wind plasma can impulsively penetrate inside the magnetosheath and start interacting with the local plasma there. Complexifying this picture, Fig. 7c also shows that the bulk speed inside this bubble is as low as its immediate surroundings with plasma already decelerated to magnetosheath-like speeds, whereas its density and magnetic field amplitude are closer to solar wind values. Although the analysis of this precise structure and others found in the quasi-perpendicular shock of the turbulent simulation is out of the scope of this study, it is interesting to notice that such signatures, characteristic of rippling and reformation processes which are usually found in quasi-parallel shocks, have also been seen in local hybrid simulations of plasma turbulence interacting with quasi-perpendicular shocks (Trotta et al. 2022).

3.3. Magnetosheath structure

As can be seen in Fig. 2 (plasma density), the thickness of the magnetosheath downstream of the quasi-parallel shock is smaller than downstream of the quasi-perpendicular shock for both laminar and turbulent solar wind conditions. This is consistent with THEMIS observations over a 5-year period (Dimmock & Nykyri 2013), which uncovered an asymmetry in the Earth's magnetosheath between the dawn and dusk regions due to the nominal Parker spiral geometry. When comparing the laminar and turbulent runs, this asymmetry persists.

In Figs. 2a,c and 3a,c for the laminar run (left column), the magnetosheath region also exhibits large fluctuations in density and magnetic field magnitude, which fill all of the magnetosheaths, as expected from observations (Narita et al. 2021). Fluctuations are more coherent in the quasi-perpendicular region compared with the quasi-parallel region, where this coherence is mostly lost, and fluctuations become larger in size and amplitude. In the turbulent case, some of that coherence is further lost, as can be observed when comparing both columns in Figs. 2 and 3. This is very similar to what has been seen in numerical simulations of solar wind-comet interactions when considering the turbulent nature of the solar wind (Behar, E. & Henri, P. 2023).

The additional loss of coherence in fluctuations in the quasi-perpendicular magnetosheath due to solar wind turbulence may be explained by the transmission of large-scale solar wind turbulence structures across the shock. These structures are observed clearly in some regions immediately downstream of the bow shock, e.g., around coordinates (400, 1100) d_i and

(1000, 400) d_i in the Y–Z plane in Figs. 2f, 3f and 4f. However, another possible explanation for the observed structures downstream of the quasi-perpendicular shock is the interaction of self-generated transients at the quasi-perpendicular shock, such as the high-density high-B-field "bubble" previously mentioned in Sect. 3.2 around $(X, Z) \approx (1000, 800)\, d_i$ in Figs. 2e, 3e and 4e.

For the quasi-parallel region, the presence of upstream solar wind turbulence increases the size and magnitude of the fluctuations in the magnetosheath, as can be seen for $Y \gtrsim 1300\, d_i$ in panel d, and for $Y \sim 1400\, d_i$ and $700 \lesssim Z \lesssim 1300\, d_i$ in panel f of Figs. 2 and 3. In this geometry, the fluctuations occurring on the downstream and upstream sides of the shock were already present in the laminar case, albeit in a less developed and intense manner (Figs. 2c and 3c). Disentangling the effects due solely to solar wind dynamics turbulence from those inherited from the basic laminar conditions will require a dedicated analysis, which is outside the scope of the present study. These aspects will be explored in future research.

Figure 4 shows how the plasma in the wake of the bow shock is slowed down to speeds significantly below the upstream solar wind bulk speed of $U_{\rm sw} = 10\, C_A$, with white marking the reference solar wind speed. In the quasi-perpendicular side of the magnetosheath in the laminar case (Fig. 4a), fluctuations in plasma speed provide a "baseline" level of the magnetosheath natural turbulence, with striations appearing perpendicular to the shock surface in the immediate wake of the shock front (as clearly seen in Fig 4c). In contrast, bulk plasma speed fluctuations are much increased for the turbulent case as compared to the laminar case, with large wavy structures developing almost parallel to the shock surface behind the terminator line (Fig. 4d) and superimposed to the natural turbulence of the magnetosheath (Fig. 4f). Deeper in the quasi-perpendicular magnetosheath, the plasma is further compressed and witnesses increased speed near the modelled magnetopause. In general, downstream of the quasi-perpendicular shock, the plasma velocity fluctuates much more in the turbulent case than in the laminar case, as especially seen in the flanks (Fig. 4f), with large defined structures possibly modulated by the global scale turbulence upstream of the shock.

In the quasi-parallel side of the magnetosheath, the conclusions already drawn for Figs. 2 and 3 hold: fluctuations in the ion foreshock region increase substantially, with a loss of coherence of the backstreaming ions that create the characteristic Ultra Low Frequency (ULF) waves populating the foreshock. Streams of low bulk speeds (in dark blue, Fig. 4d) appear upstream of the shock, corresponding to relatively low magnetic field intensities-low plasma densities.

While the solar wind mainly crosses the quasi-perpendicular part of the bow shock, some of it is actually reflected in the quasi-parallel part, forming the so-called ion foreshock region upstream of the quasi-parallel shock region. We now focus on this region.

3.4. Dynamics within the ion foreshock

In this section, we discuss the influence of the turbulent nature of the solar wind on ion foreshock. Because the bow shock is supercritical and collisionless, solar wind ions are expected to be reflected in the bow shock region quasi-parallel to the solar-wind magnetic field. This is well modelled in our kinetic hybrid simulations, and the resulting ion foreshock is observed upstream of the shock, for $Y > 1400\ d_i$ in panels a,d in Figs. 2, 3 and 4, as expected.

The solar wind ions reflected by the bow shock are seen in the ion velocity distribution functions (VDFs) shown in Fig. 8, both for the laminar and turbulent solar wind. The VDF is computed in a cubic box centred in $\mathbf{r}_{0,vdf}(x, y, z) = (860, 1620, 1020) d_i$ and having size $40d_i \times 40d_i \times 40d_i$. The box size is chosen to ensure enough statistics on the particle beam. Figure 8 displays the VDFs in a reference frame oriented as $\hat{\mathbf{e}}_{\parallel} = \mathbf{B}/|\mathbf{B}|$, $\hat{\mathbf{e}}_{\perp,1} = -\mathbf{V} \times \mathbf{B}/(|\mathbf{V} \times \mathbf{B}|)$, and $\hat{\mathbf{e}}_{\perp,2} = \hat{\mathbf{e}}_{\parallel} \times \hat{\mathbf{e}}_{\perp_1}$, where $\mathbf{B}$ and $\mathbf{V}$ are the local magnetic and ion velocity fields, i.e. their box-averaged value in the box where the VDF is computed. In both laminar and turbulent solar wind conditions, we observe the characteristic solar wind core population centred at the origin of the coordinates and a less populated beam moving on average in the $+\hat{\mathbf{e}}_{\parallel}$ direction, as indicated by the dashed blue line. The beam velocity is $v_{\rm beam} = -U_{\rm sw} = 10$ in Alfvén speed (code) units. The beam width is comparable in the two perpendicular directions and the VDF is thus close to gyrotropic (Fig. 8c,f). The two VDFs (in laminar and turbulent solar wind conditions) look quite similar in the selected location. However, the particle density in the beam corresponding to reflected particles is reduced in the turbulent case compared to the laminar one. We observed such a feature everywhere in the ion foreshock.

The presence of solar wind turbulence influences the spatial distribution of the reflected beam itself. Figure 9 shows its density N_b in the foreshock region for the two simulations. The plot is obtained using the following procedure. The VDF is computed in boxes of $40d_i \times 40d_i \times 40d_i$, forming a grid in the physical space. For each set of particles located inside one box, particles having a speed $v > 5C_A$, where C_A is the Alfvén speed in the pristine solar wind in our simulation, are used to compute the beam density. We observe that the fluctuations in the reflected beam density are much more pronounced in the turbulent (Fig. 9b) than in the laminar (Fig. 9a) case. We argue that this behaviour is due to two factors: in the turbulent case as compared with the laminar, i) the foreshock base region is more inhomogeneous (as shown in Fig. 5), and ii) the magnetic field line diffusion in the direction perpendicular to the mean magnetic field is enhanced. The combination of these two processes influences the transport of particle beams, resulting in a loss of coherence of the beam itself when moving away from the bow shock and a more patchy density distribution in the turbulent case.

To elucidate the global picture of this process, Fig. 5 shows a 3D rendering of magnetic field lines in the foreshock region. We observe that the laminar case's magnetic field lines appear to align with the direction of the solar-wind magnetic field. The field lines oscillate due to beam-induced waves in the foreshock, typical of the right-hand polarized ULF waves seen at Earth and arising from wave-particle interactions (Narita et al. 2004). In contrast, the field line topology appears much more complex in the turbulent case. The oscillations in the laminar case are observed only close to the shock base and disappear while moving away from it towards the solar wind. Moreover, in the turbulent case, some magnetic field lines crossing the foreshock region have footprints outside the quasi-parallel shock base. This implies that part of the plasma in the foreshock region comes from outside the foreshock where particle reflection has been less efficient. This complex magnetic topology results in the patchy distribution of the ion beam density in the foreshock region, as reported in Fig. 9b.

4. Conclusion

What is the impact of the turbulent nature of the solar wind on its interaction with a magnetized planet like the Earth or Mercury? How do the dynamics of solar wind turbulence affect the bow shock location and shape? How is the solar wind turbulence

itself modified by the bow shock crossing? What is the influence of the solar wind turbulence on the ion foreshock? To address these questions, we performed the first 3D global simulation of the interaction between a turbulent solar wind and a magnetized planet. We investigated the influence of turbulence on the bow shock shape and dynamics, the structure of the magnetosheath, and the ion foreshock.

Regarding the bow-shock dynamics, larger fluctuations in the shock's position are observed as compared to the laminar case. Additionally, we have shown that while in the laminar case the deformation of the bow shock outside of the quasi-parallel region originates solely at the nose of the shock, in the turbulent case deformations are triggered in multiple regions depending on solar wind dynamics and local conditions. These deformations propagate along the shock's surface towards the flanks, resulting in a more complex pattern. Consequently, the oscillations in the surfaces of oblique and quasi-perpendicular shocks are significantly amplified in turbulent solar wind conditions. Our study also shows that bubble-like plasma structures can form in the quasi-perpendicular shock area, where they start interacting with the local plasma in the magnetosheath. Further investigation into this phenomenon is deferred to future research.

The magnetosheath structure under laminar and turbulent solar wind conditions exhibits similar behaviour with a spatial asymmetry between the quasi-parallel and quasi-perpendicular sides of the shock in agreement with observational statistical studies (Dimmock & Nykyri 2013). The main effect of the turbulent solar wind dynamics on the magnetosheath is, on average, to diminish the coherence of the B-field and density fluctuations and enhance their amplitude, which is qualitatively consistent with the observed transmission through the bow shock of the turbulence inherited from the solar wind. In the ion bulk speeds, we also observed the appearance of structures almost parallel to the shock surface and superimposed to the perpendicular structures containing relatively larger ion speeds that populate the laminar case simulation. In the future, we aim at exploring in more detail how 3D solar wind structures are processed by the shock (following, e.g., Trotta et al. 2022) and investigate whether the relaxed equilibrium states, typical of the turbulent phenomenology, that are observed in the magnetosheath are locally generated or may originate from the solar wind (Pecora et al. 2023).

In the ion foreshock region, the presence of upstream turbulence influences the spatial properties of the reflected ion beam. Specifically, this ion beam in the turbulent case is more inhomogeneously distributed in space and extends less further upstream from the shock than in the laminar one due to the enhanced complexity of the magnetic field lines. Furthermore, we have shown that turbulence and beam-induced fluctuations in the foreshock region may exist for the solar wind turbulence level considered in our simulation. We may expect their presence and importance in the foreshock region to vary with the amplitude of the turbulence advected by the solar wind. A systematic study of the interplay between the two will require more simulations where the amplitude of the upstream solar wind turbulence is varied; this is also left for future work.

Menura's distinctive approach, reproducing the global interaction of a turbulent solar wind with compact objects, including planetary magnetospheres, induced or not, marks a significant advancement in our theoretical description of the near-Earth environment. Multi-satellite missions such as ESA/Cluster, NASA/Time History of Events and Macroscale Interactions during Substorms (THEMIS) or, more recently, the NASA/Magnetospheric Multiscale Mission (MMS), all continue to investigate with increasing temporal and spatial resolution the Earth's magnetosphere, magnetosheath and near-Earth solar wind and may benefit from numerical work such as that we presented here.

Further, Menura is a parallel code based on and running on GPUs. We expect that, in the future, due to increased computational power, simulation at the full Earth scale may become feasible. Meanwhile, planetary magnetospheres of smaller sizes may be studied with full-scale simulations. These upcoming simulations are timely, considering that the ESA-JAXA/BepiColombo mission will reach Mercury in December 2025. Additionally, due to the ease with which different temporally variable initial conditions can be imposed in Menura, future studies could also include modelling magnetic clouds (coming from Coronal Mass Ejections) and stream interaction regions.

Finally, numerical studies of global dynamics that consider kinetic effects, such as presented in this work, may also be relevant to many other astrophysical systems constituted by a compact object, with or without an intrinsic magnetic field, interacting with a non-laminar flow.

Acknowledgements. E. Behar acknowledges support from the Swedish National Research Council, Grant 2019-06289. This work was granted access to the HPC resources of IDRIS under the allocation 2021-AP010412309 made by GENCI. P.H. acknowledges support from CNES APR. This work was granted access to the HPC resources of IDRIS under the allocation 2024-AD010412990R1 made by GENCI. C. Simon Wedlund is funded by the Austrian Science Fund (FWF) 10.55776/P35954. L. Preisser was supported by the Austrian Science Fund (FWF): P 33285-N. F.P. acknowledges support from the National Research Council (CNR) Short Term Mobility (STM) 2023 program and from the Research Foundation – Flanders (FWO) Junior research project on fundamental research G020224N. We acknowledge the CINECA award under the ISCRA initiative, for the availability of high performance computing resources and support.

References

Aizawa, S., Griton, L., Fatemi, S., et al. 2021, Planetary and Space Science, 198, 105176
Aizawa, S., Persson, M., Menez, T., et al. 2022, Planet. Space Sci., 218, 105499
Behar, E., Fatemi, S., Henri, P., & Holmström, M. 2022, Ann. Geophys., 40, 281
Behar, E. & Henri, P. 2023, A&A, 671, A144
Bruno, R. & Carbone, V. 2013, Living Reviews in Solar Physics, 10, 2
Burgess, D. & Scholer, M. 2015, Collisionless Shocks in Space Plasmas
Dimmock, A. P. & Nykyri, K. 2013, Journal of Geophysical Research: Space Physics, 118, 4963
D'Amicis, R., Telloni, D., & Bruno, R. 2020, Frontiers in Physics, 8
Gingell, I., Schwartz, S. J., Burgess, D., et al. 2017, Journal of Geophysical Research (Space Physics), 122, 11,003
Grandin, M., Luttikhuis, T., Battarbee, M., et al. 2023, Journal of Space Weather and Space Climate, 13, 20
Guio, P. & Pécseli, H. L. 2021a, Frontiers in Astronomy and Space Sciences, 7
Guio, P. & Pécseli, H. L. 2021b, Frontiers in Astronomy and Space Sciences, 7, 107
Guo, F., Giacalone, J., & Zhao, L. 2021, Frontiers in Astronomy and Space Sciences, 8, 644354
Jarvinen, R., Alho, M., Kallio, E., & Pulkkinen, T. I. 2020, MNRAS, 491, 4147
Jones, F. C. & Ellison, D. C. 1991, Space Science Reviews, 58, 259
Kallio, E. & Janhunen, P. 2003, Annales Geophysicae, 21, 2133
Kallio, E. & Janhunen, P. 2004, Advances in Space Research, 33, 2176
Kallio, E., Jarvinen, R., Massetti, S., et al. 2022, Geophys. Res. Lett., 49, e2022GL101850
Karimabadi, H., Roytershteyn, V., Vu, H. X., et al. 2014, Physics of Plasmas, 21, 062308
Karimabadi, H., Vu, H. X., Krauss-Varban, D., & Omelchenko, Y. 2006, in Astronomical Society of the Pacific Conference Series, Vol. 359, Numerical Modeling of Space Plasma Flows, ed. G. P. Zank & N. V. Pogorelov, 257
Kiyani, K. H., Osman, K. T., & Chapman, S. C. 2015, Dissipation and heating in solar wind turbulence: from the macro to the micro and back again
Lapenta, G., Schriver, D., Walker, R. J., et al. 2022, Journal of Geophysical Research (Space Physics), 127, e30241
Lavorenti, F., Henri, P., Califano, F., et al. 2022, A&A, 664, A133
Lavorenti, F., Henri, P., Califano, F., et al. 2023, A&A, 674, A153

Lin, Y., Denton, R. E., Lee, L. C., & Chao, J. K. 2001, J. Geophys. Res., 106, 10691
Lin, Y., Swift, D. W., & Lee, L. C. 1996, Journal of Geophysical Research: Space Physics, 101, 27251
Lin, Y. & Wang, X. Y. 2002, Geophys. Res. Lett., 29, 1687
Matteini, L., Alexandrova, O., Chen, C. H. K., & Lacombe, C. 2016, Monthly Notices of the Royal Astronomical Society, 466, 945
Matthews, A. P. 1994, Journal of Computational Physics, 112, 102
Modolo, R., Hess, S., Mancini, M., et al. 2016, Journal of Geophysical Research (Space Physics), 121, 6378
Moullard, O., Burgess, D., Horbury, T. S., & Lucek, E. A. 2006, Journal of Geophysical Research (Space Physics), 111, A09113
Müller, J., Simon, S., Motschmann, U., et al. 2011, Computer Physics Communications, 182, 946
Müller, J., Simon, S., Wang, Y.-C., et al. 2012, Icarus, 218, 666
Nakanotani, M., Zank, G., & Zhao, L.-L. 2021, The Astrophysical Journal, 922, 219
Nakanotani, M., Zank, G., & Zhao, L.-L. 2022, The Astrophysical Journal, 926, 109
Narita, Y., Glassmeier, K.-H., Schäfer, S., et al. 2004, Annales Geophysicae, 22, 2315
Narita, Y., Plaschke, F., & Vörös, Z. 2021, The Magnetosheath (American Geophysical Union (AGU)), 137–152
Omidi, N., Blanco-Cano, X., Russell, C., & Karimabadi, H. 2004, Advances in Space Research, 33, 1996
Owens, M. J., Lockwood, M., Barnard, L. A., et al. 2023, Sol. Phys., 298, 111
Parks, G. K., Lee, E., Yang, Z. W., et al. 2021, Solar Wind Interaction with Earth's Bow Shock (American Geophysical Union (AGU)), 123–135
Pecora, F., Yang, Y., Chasapis, A., et al. 2023, arXiv preprint arXiv:2302.00634
Peng, I. B., Markidis, S., Laure, E., et al. 2015, Physics of Plasmas, 22, 092109
Pollock, C. J., Chen, L. J., Schwartz, S. J., et al. 2022, Physics of Plasmas, 29, 112902
Rakhmanova, L., Riazantseva, M., Zastenker, G., & Yermolaev, Y. 2023, Frontiers in Astronomy and Space Sciences, 10, 47
Schwartz, S. J. 1998, ISSI Scientific Reports Series, 1, 249
Sibeck, D. G. & Murphy, K. R. 2021, Large-Scale Structure and Dynamics of the Magnetosphere (American Geophysical Union (AGU)), 15–36
Southwood, D. J. 2021, A Brief History of the Magnetosphere (American Geophysical Union (AGU)), 1–13
Swift, D. W. 1995, Geophys. Res. Lett., 22, 311
Teubenbacher, D., Exner, W., Feyerabend, M., et al. 2024, A&A, 681, A98
Thomas, V. A. & Winske, D. 1990, Geophysical Research Letters, 17, 1247
Trávníček, P., Hellinger, P., & Schriver, D. 2007, Geophys. Res. Lett., 34, L05104
Trotta, D., Pecora, F., Settino, A., et al. 2022, The Astrophysical Journal, 933, 167
Trotta, D., Pezzi, O., Burgess, D., et al. 2023, MNRAS, 525, 1856
Trotta, D., Valentini, F., Burgess, D., & Servidio, S. 2021, Proceedings of the National Academy of Sciences, 118, e2026764118
Turc, L., Roberts, O. W., Verscharen, D., et al. 2023, Nature Physics, 19, 78
Valentini, F., Trávníček, P., Califano, F., Hellinger, P., & Mangeney, A. 2007, Journal of Computational Physics, 225, 753
Verscharen, D., Klein, K. G., & Maruca, B. A. 2019, Living Reviews in Solar Physics, 16, 5
von Alfthan, S., Pokhotelov, D., Kempf, Y., et al. 2014, Journal of Atmospheric and Solar-Terrestrial Physics, 120, 24
Zank, G. P., Zhou, Y., Matthaeus, W. H., & Rice, W. 2002, Physics of Fluids, 14, 3766

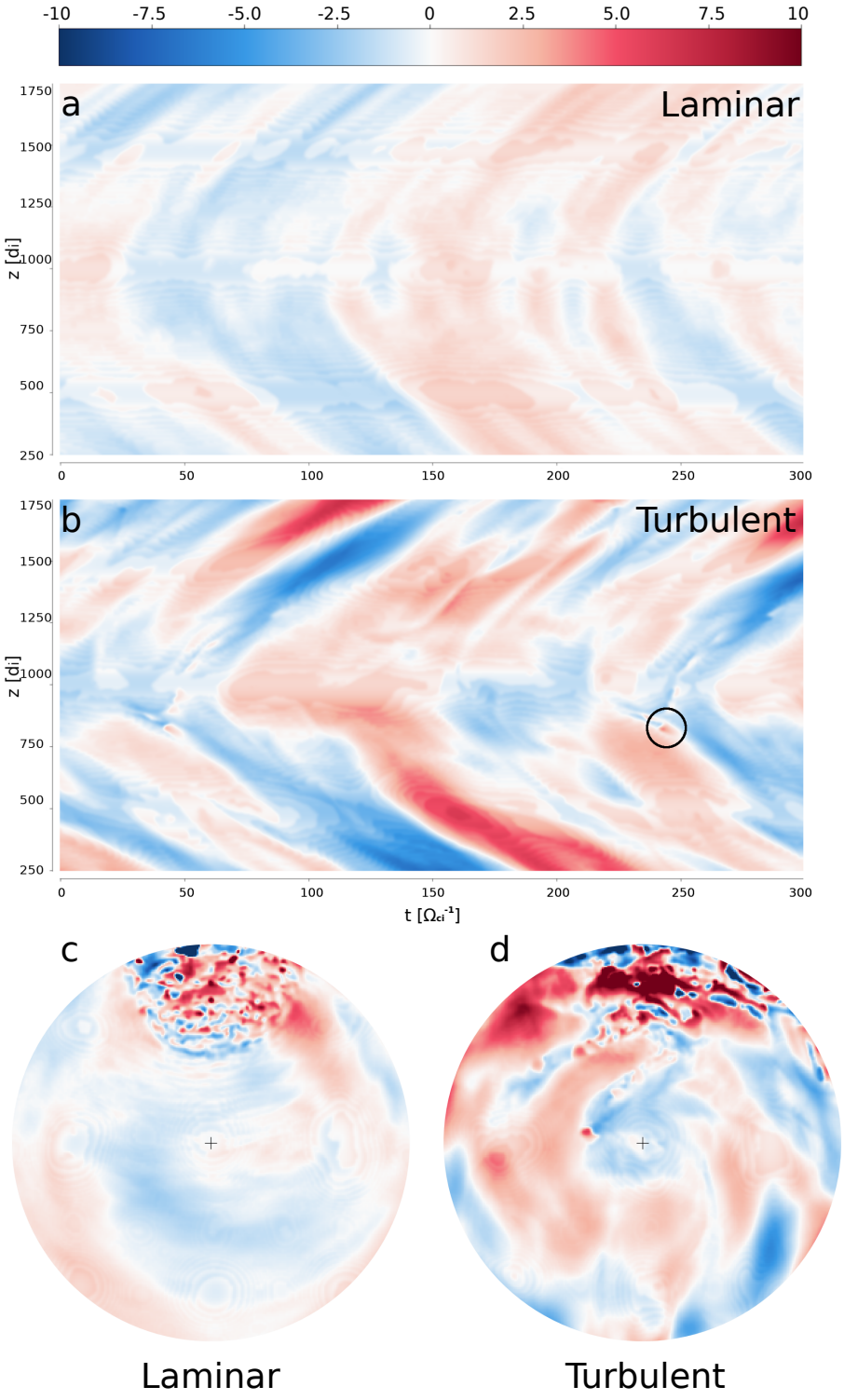

Fig. 6. Temporal evolution of the Bow shock position at each time step t for the coordinates (Y_P, Z) for the laminar (a) and turbulent (b) initial conditions. The corresponding planar projections (c,d) of the full 3D shock surface with respect to its time-averaged position at $t = 250\,\Omega_{ci}^{-1}$. The colour code provides the deviation from the overall time-averaged position in d_i. The black circle points to the "bubble" appearing around $(1000, 800)$ d_i in Figs. 2e, 3e and 4e and discussed in Fig. 7.

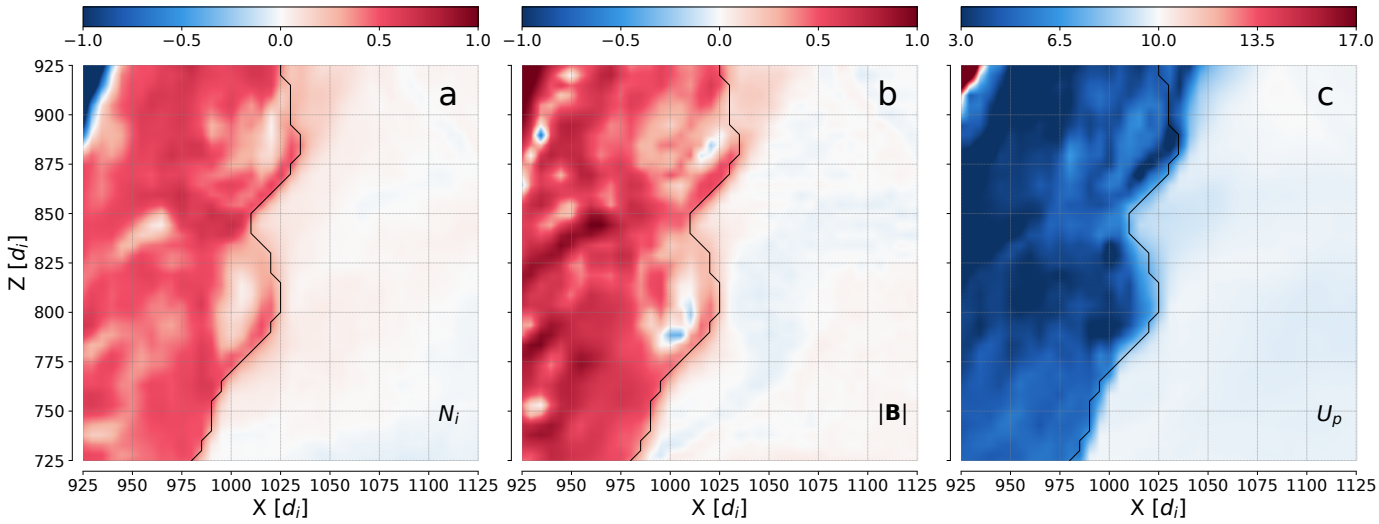

Fig. 7. Transient structure along the bow shock's location in the X–Z plane of the turbulent simulation at $t = 250\,\Omega_{ci}^{-1}$. (a): ion density N_i (logarithmic scale, in units of n_0), (b): total magnetic field intensity $|\mathbf{B}|$ (logarithmic scale, in units of B_0) and (c) proton bulk speed U_p (linear scale, in units of C_A, in the shock's reference frame).

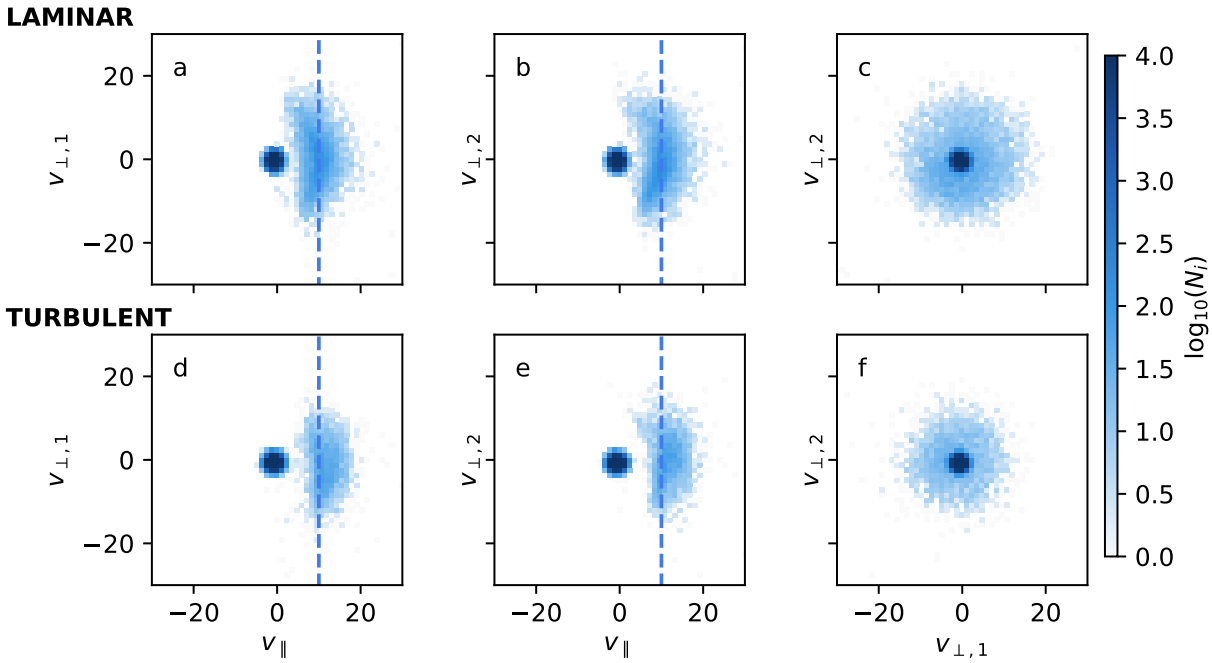

Fig. 8. Ion velocity distribution function (VDF) for the laminar (panels a-c) and turbulent case (panels d-f) in logarithmic scale. The VDF is plotted in a reference frame aligned with the local magnetic field and moving with the solar wind. The plots show the number of macroparticles integrated in the out-of-plane direction. The blue dashed line corresponds to the opposite of the solar wind speed in the planet reference frame.

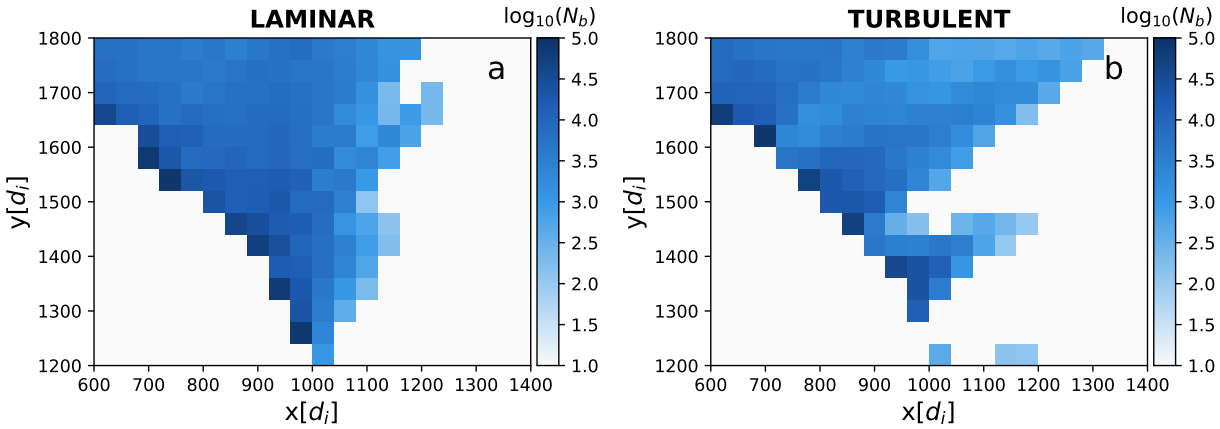

Fig. 9. Ion beam density N_b in the foreshock region for a) laminar and b) turbulent solar wind dynamics conditions. The colour bar is in logarithmic scale; N_b<10 in white regions.

Appendix

A Table of database crossings

Here we include the list of crossings of the database discussed in Chapter 5. For each crossing, the following data are added (in order here for each column):

- The date;
- The beginning time of the crossing;
- The end time of the crossing;
- The type of hodogram of the magnetic field in the tangential plane, selected as explained in Section 5.3;
- The normal obtained using the GF2 (introduced in Section 3.4.1) tool using the magnetic field data, averaged in the time interval;
- The normal obtained using the GF2 tool using the ion mass flux data, averaged in the time interval;
- The dimensionality index defined in Eq. 3.8 (Rezeau et al., 2018);
- The dimensionality index defined in Eq. 3.17 (Ballerini et al., 2024b);
- The non-gyrotropy index defined in Eq. 4.15 (Aunai et al., 2013a);
- The non-gyrotropy index defined in Eq. 4.16 (Ballerini et al., 2024b);
- The estimated length of the magnetopause;
- The estimated averaged ion Larmor radius (rho) of the magnetopause;
- The estimated averaged ion inertial length of the magnetopause;

Date	Time start	Time end	Hodogram	mean normal (B)	mean normal (ions)	D1	D1 GB	DAunai	Dperp	L [km]	rho [km]	di [km]
02/09/2015	15:26:26.4	15:26:29.6	Other	[-0.86,-0.17, 0.48]	[0.75,0.31, -0.58]	0.90	0.81	0.04	0.04	540.46	24.76	41.08
02/09/2015	16:08:28.8	16:08:35.5	Other	[0.52,0.85, -0.06]	[-0.46,-0.89, -0.04]	0.95	0.86	0.02	0.02	477.99	55.33	67.22
02/09/2015	17:34:25.8	17:34:32.6	Other	[-0.92,-0.33, 0.22]	[-0.82,-0.56, 0.13]	0.91	0.80	0.06	0.11	720.15	171.38	125.63
02/09/2015	17:36:10.5	17:36:15.0	Linear	[0.01,1.00, -0.04]	[-0.28,-0.96, -0.03]	0.93	0.85	0.03	0.05	802.39	224.93	61.26
09/09/2015	12:37:50.5	12:37:58.5	Linear	[0.73,0.56, -0.39]	[0.67,0.65, -0.36]	0.95	0.81	0.04	0.06	362.32	131.39	82.85
09/09/2015	14:37:35.5	14:37:38.5	Linear	[0.87,0.17, -0.46]	[-0.61,-0.33, 0.72]	0.91	0.86	0.04	0.05	419.84	113.67	89.93
09/09/2015	15:51:14.0	15:51:18.0	Circular	[0.99,0.02, 0.12]	[-0.95,-0.26, -0.17]	0.90	0.80	0.02	0.04	718.07	135.91	85.68
09/09/2015	16:11:27.0	16:11:32.5	Linear	[0.83,0.53, -0.18]	[-0.77,-0.62, 0.15]	0.94	0.80	0.04	0.06	484.99	54.21	76.24
15/09/2015	13:06:20.0	13:06:23.5	Linear	[-0.87,-0.49, -0.05]	[-0.76,-0.64, 0.08]	0.95	0.85	0.03	0.02	558.94	259.19	66.06
15/09/2015	13:06:31.0	13:06:42.0	Other	[0.66,0.73, -0.18]	[0.81,0.56, -0.18]	0.96	0.84	0.04	0.04	443.87	81.45	87.71
15/09/2015	13:06:43.1	13:06:46.2	Other	[0.97,0.23, -0.11]	[-0.78,-0.62, -0.12]	0.90	0.85	0.04	0.06	474.53	111.26	79.14
19/09/2015	09:05:29.0	09:05:35.0	Other	[-0.83,-0.06, 0.56]	[-0.83,-0.10, 0.55]	0.97	0.86	0.04	0.07	416.80	69.70	97.99
19/09/2015	09:08:45.1	09:08:50.8	Linear	[-0.84,-0.53, 0.11]	[0.87,0.49, 0.09]	0.95	0.80	0.05	0.06	396.80	62.81	98.75
19/09/2015	09:09:35.0	09:09:40.0	Other	[0.57,0.75, -0.33]	[0.56,0.67, -0.49]	0.93	0.80	0.04	0.05	444.23	81.78	45.41
19/09/2015	09:09:49.0	09:09:53.0	Other	[-0.80,-0.59, 0.10]	[-0.77,-0.64, 0.08]	0.94	0.86	0.10	0.09	393.99	79.01	103.64
19/09/2015	09:27:12.0	09:27:22.0	Other	[0.85,0.50, -0.16]	[-0.79,-0.60, 0.14]	0.93	0.86	0.07	0.10	374.95	56.42	48.64
19/10/2015	09:51:18.0	09:51:21.2	Radial	[0.92,-0.13, -0.36]	[0.72,-0.47, -0.51]	0.90	0.84	0.05	0.06	798.47	200.57	71.12
19/09/2015	10:46:50.0	10:46:54.5	Circular	[-0.73,-0.68, 0.04]	[-0.55,-0.75, 0.36]	0.95	0.87	0.06	0.06	475.16	58.15	78.39
22/09/2015	07:54:41.5	07:54:44.6	Other	[-0.80,0.19, 0.57]	[0.56,-0.39, -0.73]	0.92	0.81	0.04	0.07	498.84	73.41	69.98
25/09/2015	09:39:49.5	09:39:55.0	Other	[-0.89,0.04, 0.45]	[0.92,0.05, -0.39]	0.91	0.81	0.04	0.08	526.53	144.79	71.38
25/09/2015	09:43:05.2	09:43:08.5	Radial	[0.95,0.25, -0.17]	[0.95,0.27, -0.17]	0.97	0.87	0.06	0.10	533.43	78.17	114.55
30/09/2015	10:19:01.5	10:19:05.5	Radial	[-0.88,-0.40, 0.23]	[0.91,0.19, -0.37]	0.95	0.86	0.03	0.05	372.10	61.56	108.40
01/10/2015	18:10:25.0	18:10:29.0	Other	[0.84,0.51, -0.19]	[-0.66,-0.66, 0.35]	0.96	0.90	0.03	0.05	338.07	120.98	122.88
02/10/2015	07:53:37.0	07:53:43.0	Other	[0.66,0.61, -0.44]	[0.78,0.48, -0.39]	0.90	0.84	0.08	0.14	476.08	89.12	90.80
03/10/2015	15:34:54.6	15:35:00.0	Radial	[0.94,0.25, -0.24]	[-0.90,-0.36, 0.24]	0.93	0.85	0.06	0.05	614.47	115.84	97.15
06/10/2015	15:22:04.0	15:22:14.0	Other	[0.85,0.52, -0.13]	[-0.76,-0.62, 0.21]	0.92	0.83	0.04	0.05	597.79	93.50	75.38
06/10/2015	15:23:51.5	15:23:56.5	Linear	[0.69,0.71, -0.14]	[-0.52,-0.73, 0.44]	0.93	0.87	0.09	0.19	580.31	91.20	89.05
16/10/2015	10:55:21.0	10:55:27.3	Circular	[0.63,0.74, -0.25]	[0.76,0.50, -0.42]	0.96	0.85	0.06	0.05	417.06	86.98	105.79
16/10/2015	11:10:18.0	11:10:25.0	Linear	[-0.95,-0.09, 0.30]	[0.86,0.21, -0.46]	0.95	0.85	0.05	0.04	493.93	71.87	58.41
16/10/2015	13:05:42.6	13:05:47.0	Linear	[0.89,0.12, -0.43]	[-0.92,0.03, 0.40]	0.96	0.89	0.08	0.12	382.11	119.75	124.97
16/10/2015	13:40:33.0	13:40:37.5	Other	[-0.34,-0.93, 0.15]	[0.78,0.50, -0.37]	0.92	0.83	0.05	0.07	509.36	121.05	123.21
16/10/2015	13:40:43.1	13:40:46.3	Other	[0.94,0.18, -0.30]	[-0.92,-0.27, 0.29]	0.97	0.89	0.05	0.09	392.25	103.62	159.72
16/10/2015	13:40:53.5	13:41:00.3	Linear	[0.64,0.73, -0.25]	[-0.78,-0.61, 0.12]	0.94	0.84	0.06	0.10	418.53	103.80	103.38
23/10/2015	08:06:48.0	08:06:58.0	Radial	[0.89,0.39, -0.23]	[-0.78,0.50, 0.37]	0.96	0.88	0.05	0.08	420.19	86.49	82.74
23/10/2015	08:20:56.5	08:21:01.5	Linear	[-0.89,-0.42, 0.19]	[0.96,0.21, 0.19]	0.96	0.88	0.04	0.04	737.80	86.91	83.50
30/10/2015	05:15:45.0	05:15:49.0	Other	[-0.96,0.00, 0.28]	[-1.00,0.08, 0.05]	0.94	0.87	0.07	0.10	366.24	81.67	47.35
09/11/2015	03:34:29.8	03:34:35.5	Other	[-0.85,-0.51, 0.14]	[-0.81,-0.25, 0.53]	0.91	0.87	0.02	0.02	389.01	117.28	65.03

Date	Time start	Time end	Hodogram	mean normal (B)	mean normal (ions)	D1	D1 GB	DAunai	Dperp	L [km]	rho [km]	di [km]
10/11/2015	02:13:13.7	02:13:18.1	Other	[0.94,0.28, -0.21]	[0.93,0.05, -0.37]	0.90	0.83	0.05	0.06	589.60	84.28	82.72
13/11/2015	04:02:34.9	04:02:51.0	Other	[0.91,0.25, -0.33]	[0.36,-0.40, 0.84]	0.94	0.87	0.06	0.09	390.81	78.03	71.24
13/11/2015	04:46:35.0	04:46:52.0	Other	[-0.96,-0.12, 0.24]	[-0.53,-0.63, 0.57]	0.93	0.80	0.06	0.07	323.76	51.80	84.45
17/11/2015	02:14:04.5	02:14:17.0	Linear	[-0.98,0.07, 0.19]	[-0.97,0.23, 0.07]	0.95	0.81	0.12	0.08	415.16	58.26	95.51
17/11/2015	14:39:10.5	14:39:13.7	Linear	[0.87,-0.48, -0.15]	[-0.77,0.20, 0.61]	0.95	0.85	0.06	0.09	504.87	56.04	61.41
18/11/2015	02:11:36.3	02:11:43.0	Linear	[0.97,0.25, 0.03]	[-0.93,-0.37, 0.02]	0.90	0.83	0.05	0.03	451.57	43.35	94.81
24/11/2015	03:38:25.0	03:38:30.0	Other	[-0.97,-0.02, 0.24]	[0.01,0.48, 0.87]	0.99	0.94	0.04	0.04	469.96	37.08	88.07
24/11/2015	07:08:05.0	07:08:15.0	Other	[-0.96,0.04, 0.28]	[0.96,0.14, 0.24]	0.95	0.85	0.02	0.05	474.47	63.88	75.87
24/11/2015	11:32:16.0	11:32:22.0	Linear	[0.89,0.41, -0.21]	[-0.88,-0.37, 0.28]	0.97	0.87	0.05	0.08	513.64	75.86	53.58
24/11/2015	12:00:37.0	12:00:41.5	Other	[0.69,-0.58, -0.44]	[-0.64,0.59, 0.49]	0.93	0.85	0.05	0.07	386.38	63.62	148.11
25/11/2015	13:04:06.0	13:04:21.0	Other	[0.96,0.00, -0.27]	[-0.97,-0.07, 0.25]	0.92	0.81	0.02	0.02	325.10	37.44	92.24
25/11/2015	13:05:54.0	13:05:59.5	Other	[0.91,0.40, -0.14]	[-0.92,-0.40, -0.01]	0.92	0.86	0.04	0.05	321.65	37.11	95.96
26/11/2015	13:20:30.0	13:20:33.0	Other	[-0.54,-0.79, 0.28]	[0.60,0.79, -0.12]	0.94	0.85	0.08	0.09	366.25	39.20	63.37
01/12/2015	12:34:44.5	12:34:48.0	Other	[0.89,0.10, -0.45]	[0.95,0.23, -0.20]	0.97	0.91	0.05	0.05	546.50	100.35	93.64
01/12/2015	12:49:19.0	12:49:29.0	Other	[-0.94,-0.34, 0.09]	[-0.96,-0.28, 0.07]	0.96	0.91	0.06	0.08	411.65	68.35	93.13
04/12/2015	02:06:46.9	02:06:54.0	Linear	[-0.95,0.04, 0.32]	[-0.91,-0.17, 0.37]	0.94	0.85	0.06	0.11	422.64	48.92	94.46
06/12/2015	23:38:29.4	23:38:33.0	Other	[0.84,-0.44, -0.32]	[0.77,-0.48, -0.41]	0.96	0.89	0.11	0.16	442.53	76.13	137.16
06/12/2015	23:45:27.3	23:45:37.0	Linear	[0.91,-0.24, -0.33]	[-0.91,0.19, 0.36]	0.93	0.84	0.09	0.14	374.97	69.82	67.08
07/12/2015	00:30:40.0	00:30:45.0	Other	[-0.93,0.15, 0.33]	[0.89,-0.20, -0.40]	0.98	0.93	0.13	0.17	424.81	45.01	86.50
08/12/2015	09:39:00.5	09:39:08.5	Linear	[0.88,-0.21, -0.43]	[-0.70,-0.39, 0.60]	0.90	0.81	0.07	0.09	399.40	119.43	94.04
08/12/2015	11:29:17.9	11:29:25.0	Other	[0.93,0.14, -0.33]	[-1.00,0.05, 0.08]	0.94	0.83	0.07	0.08	297.31	84.35	78.01
09/12/2015	11:38:27.0	11:38:31.0	Linear	[0.91,0.26, -0.32]	[0.96,0.25, 0.12]	0.96	0.87	0.07	0.11	522.61	41.44	86.47
10/12/2015	11:36:13.0	11:36:17.5	Linear	[0.93,0.12, -0.35]	[0.73,-0.36, -0.58]	0.92	0.83	0.05	0.02	382.49	63.65	83.08
11/12/2015	12:16:46.5	12:16:52.5	Other	[0.91,0.03, -0.41]	[-0.88,-0.46, -0.08]	0.90	0.82	0.07	0.11	423.74	213.27	80.68
11/12/2015	23:59:58.5	00:00:05.5	Other	[-0.81,0.43, 0.39]	[-0.61,0.32, 0.72]	0.97	0.88	0.04	0.04	499.77	109.18	76.23
12/12/2015	00:00:32.0	00:00:36.5	Linear	[-0.97,-0.22, 0.12]	[0.93,0.10, 0.36]	0.92	0.82	0.06	0.11	413.74	127.65	90.68
12/12/2015	00:02:00.3	00:02:07.5	Other	[0.52,-0.83, -0.21]	[-0.20,0.50, 0.84]	0.91	0.83	0.04	0.05	702.77	86.74	88.21
12/12/2015	00:12:27.3	00:12:30.8	Linear	[-0.96,-0.27, -0.05]	[0.93,0.37, 0.04]	0.95	0.89	0.06	0.08	506.04	171.30	90.08
13/12/2015	00:28:01.0	00:28:08.0	Other	[0.97,-0.04, -0.26]	[0.92,0.05, -0.38]	0.96	0.88	0.07	0.03	465.88	79.46	104.27
13/12/2015	10:31:22.0	10:31:26.5	Other	[-0.95,-0.26, 0.16]	[-0.84,0.23, 0.49]	0.97	0.90	0.08	0.09	424.92	113.21	118.44
18/12/2015	00:09:59.0	00:10:11.0	Linear	[0.92,-0.29, -0.27]	[0.75,-0.46, -0.48]	0.95	0.85	0.04	0.04	334.72	79.74	87.63
18/12/2015	07:54:19.0	07:54:23.8	Radial	[0.92,0.22, -0.32]	[-0.77,0.22, 0.59]	0.94	0.85	0.05	0.07	326.44	140.58	77.06
18/12/2015	07:54:49.0	07:54:59.0	Linear	[-0.86,0.05, 0.52]	[-0.73,0.37, 0.57]	0.92	0.83	0.04	0.07	376.88	97.05	73.54
18/12/2015	09:10:43.0	09:10:51.0	Linear	[0.99,-0.00, -0.10]	[0.94,-0.29, -0.17]	0.97	0.90	0.02	0.02	403.07	106.88	61.42
27/12/2015	09:53:34.0	09:53:44.5	Other	[0.87,-0.20, -0.45]	[-0.77,0.33, 0.55]	0.93	0.88	0.04	0.03	386.42	98.79	60.64
27/12/2015	21:30:58.0	21:31:05.0	Other	[-0.87,0.42, 0.26]	[-0.72,0.37, 0.58]	0.97	0.92	0.05	0.09	593.77	68.18	42.85
28/12/2015	09:53:49.0	09:53:54.0	Linear	[0.85,0.50, 0.14]	[0.89,0.45, 0.10]	0.99	0.94	0.03	0.04	621.19	60.53	100.77

Date	Time start	Time end	Hodogram	mean normal (B)	mean normal (ions)	D1	D1 GB	DAunai	Dperp	L [km]	rho [km]	di [km]
28/12/2015	10:44:55.0	10:45:02.0	Other	[-0.97,-0.04, 0.23]	[0.99,0.04, -0.12]	0.91	0.82	0.04	0.06	497.95	70.29	73.10
28/12/2015	22:12:02.0	22:12:09.0	Linear	[-0.82,0.47, 0.33]	[-0.75,0.60, 0.28]	0.98	0.90	0.07	0.07	379.14	142.06	97.85
29/12/2015	05:38:25.0	05:38:31.0	Linear	[0.89,-0.26, -0.38]	[0.95,0.01, -0.33]	0.95	0.87	0.05	0.08	431.69	85.34	124.16
29/12/2015	06:05:19.0	06:05:23.0	Linear	[0.83,-0.35, -0.43]	[-0.61,-0.62, -0.50]	0.90	0.83	0.04	0.07	569.43	182.15	75.40
01/01/2016	21:34:30.0	21:34:37.0	Other	[-0.89,0.38, 0.27]	[0.95,-0.25, -0.21]	0.92	0.84	0.03	0.05	508.05	55.25	80.10
03/01/2016	08:16:38.0	08:16:42.0	Linear	[0.92,-0.21, -0.33]	[0.83,-0.30, -0.47]	0.96	0.91	0.05	0.04	412.33	55.20	96.24
03/01/2016	22:10:59.0	22:11:13.0	Linear	[0.62,-0.69, -0.38]	[-0.58,0.58, 0.58]	0.94	0.84	0.04	0.06	371.78	60.54	84.27
04/01/2016	01:34:14.0	01:34:20.0	Other	[0.97,-0.09, -0.23]	[-0.93,0.24, 0.26]	0.97	0.89	0.07	0.06	443.24	124.52	89.29
04/01/2016	08:47:06.8	08:47:12.0	Other	[0.88,-0.32, -0.34]	[0.65,-0.15, -0.74]	0.90	0.83	0.05	0.08	410.38	45.51	89.16
04/01/2016	22:40:32.0	22:40:40.0	Radial	[0.95,-0.26, -0.16]	[0.92,-0.38, -0.13]	0.94	0.82	0.04	0.05	397.30	41.77	93.49
04/01/2016	23:02:15.0	23:02:25.0	Other	[-0.66,0.66, 0.37]	[0.68,-0.66, -0.33]	0.97	0.88	0.08	0.07	406.55	50.50	73.98
10/01/2016	09:12:07.5	09:12:11.0	Circular	[0.70,-0.60, -0.39]	[0.59,-0.72, -0.36]	0.92	0.84	0.08	0.08	417.45	54.97	65.86
10/01/2016	09:15:39.0	09:15:42.2	Radial	[0.91,0.42, 0.08]	[0.92,0.39, -0.07]	0.92	0.88	0.05	0.05	674.44	61.91	177.41
10/01/2016	22:10:00.0	22:10:09.0	Linear	[-0.62,0.72, 0.31]	[0.61,-0.65, -0.45]	0.98	0.89	0.09	0.09	333.15	96.16	104.38
12/01/2016	21:53:46.0	21:53:50.0	Linear	[-0.89,0.38, 0.25]	[-0.86,0.45, 0.24]	0.96	0.90	0.07	0.11	359.88	64.00	85.59
17/01/2016	22:35:41.0	22:35:54.0	Linear	[-0.86,0.45, 0.24]	[-0.83,0.49, 0.25]	0.94	0.86	0.04	0.04	419.99	59.37	66.28
23/01/2016	22:17:09.0	22:17:14.0	Radial	[0.86,-0.49, -0.11]	[-0.46,-0.65, 0.61]	0.96	0.87	0.04	0.02	475.70	87.64	70.53
24/01/2016	04:30:50.0	04:30:59.0	Other	[0.70,-0.52, -0.49]	[0.84,-0.52, -0.15]	0.94	0.82	0.07	0.10	396.33	55.74	83.09
24/01/2016	06:57:36.5	06:57:44.0	Radial	[0.85,-0.28, -0.45]	[-0.92,0.13, -0.38]	0.90	0.82	0.05	0.06	371.02	41.14	96.57
27/01/2016	22:11:14.0	22:11:19.0	Other	[0.76,-0.63, -0.16]	[-0.78,0.58, 0.23]	0.93	0.84	0.12	0.17	392.19	62.25	112.02
28/01/2016	05:59:52.0	06:00:01.0	Linear	[0.84,-0.54, 0.03]	[0.94,-0.27, -0.20]	0.97	0.85	0.08	0.10	382.31	41.71	97.81
30/01/2016	00:25:00.0	00:25:04.5	Linear	[-0.25,0.76, 0.60]	[0.73,-0.63, -0.26]	0.91	0.82	0.05	0.07	493.28	134.94	68.82
30/01/2016	01:03:02.0	01:03:05.0	Other	[0.86,-0.34, -0.39]	[-0.82,0.47, 0.33]	0.96	0.86	0.05	0.07	579.67	72.23	69.66
14/02/2016	03:45:09.0	03:45:17.0	Radial	[0.94,-0.29, -0.20]	[0.96,-0.15, -0.23]	0.92	0.89	0.04	0.06	412.34	42.81	79.85
21/02/2016	21:01:32.0	21:01:37.0	Radial	[0.54,-0.77, -0.34]	[0.59,-0.64, -0.49]	0.97	0.90	0.07	0.04	479.20	64.38	90.18
21/02/2016	21:03:44.0	21:03:51.0	Radial	[0.63,-0.53, -0.56]	[-0.49,0.57, 0.66]	0.96	0.92	0.06	0.07	457.16	120.10	74.54
05/03/2016	23:01:34.0	23:01:38.0	Radial	[0.83,-0.51, 0.23]	[-0.32,0.89, -0.32]	0.97	0.89	0.08	0.07	428.35	66.19	80.91
16/10/2016	17:54:58.5	17:55:03.0	Other	[0.84,0.54, 0.11]	[-0.56,-0.76, -0.31]	0.97	0.94	0.06	0.09	595.98	217.74	86.60
02/11/2016	09:36:20.0	09:36:29.5	Linear	[-0.90,-0.32, 0.30]	[-0.97,-0.00, 0.25]	0.96	0.89	0.04	0.05	312.03	84.03	64.86
03/11/2016	16:57:57.0	16:58:03.0	Other	[-0.81,-0.59, 0.00]	[-0.82,-0.57, -0.02]	0.99	0.94	0.08	0.07	401.43	61.18	70.95
06/11/2016	08:40:06.0	08:40:14.5	Other	[0.88,0.15, -0.44]	[-0.73,-0.18, 0.65]	0.90	0.80	0.05	0.06	378.07	54.48	81.36
06/11/2016	08:41:01.0	08:41:06.0	Other	[-0.86,-0.31, 0.40]	[0.54,-0.52, 0.66]	0.93	0.83	0.10	0.09	613.63	64.07	74.70
06/11/2016	08:42:46.0	08:42:49.0	Other	[-0.96,-0.01, 0.29]	[0.84,0.28, -0.47]	0.97	0.90	0.08	0.12	447.86	45.58	94.86
06/11/2016	08:55:52.0	08:55:56.0	Other	[0.90,0.26, -0.36]	[-0.61,-0.44, 0.67]	0.98	0.91	0.11	0.07	487.82	49.99	56.20
06/11/2016	16:12:17.0	16:12:20.5	Other	[-0.97,-0.08, 0.23]	[0.89,0.17, 0.43]	0.94	0.84	0.07	0.09	458.70	70.91	130.48
12/11/2016	18:44:44.1	18:44:48.2	Linear	[-0.61,-0.79, -0.05]	[-0.81,0.53, -0.27]	0.91	0.82	0.02	0.03	481.73	81.11	91.03
15/11/2016	09:15:11.0	09:15:14.0	Linear	[-0.75,-0.49, 0.44]	[0.68,0.44, -0.59]	0.91	0.87	0.06	0.11	586.96	71.45	95.23

Date	Time start	Time end	Hodogram	mean normal (B)	mean normal (ions)	D1	D1 GB	DAunai	Dperp	L [km]	rho [km]	di [km]
21/11/2016	07:48:02.0	07:48:05.0	Radial	[-0.94,-0.08, 0.33]	[-0.62,-0.43, 0.66]	0.98	0.90	0.09	0.07	653.10	40.82	86.09
23/11/2016	07:09:01.0	07:09:05.5	Other	[0.85,0.42, -0.33]	[-0.82,-0.54, 0.17]	0.96	0.90	0.07	0.07	631.87	58.16	131.49
23/11/2016	16:47:55.0	16:48:00.0	Radial	[-0.67,-0.75, -0.01]	[-0.38,-0.82, -0.43]	0.96	0.85	0.04	0.06	699.39	64.00	68.17
23/11/2016	17:10:41.0	17:10:45.5	Other	[-0.88,-0.47, -0.04]	[0.08,-0.40, -0.91]	0.97	0.91	0.06	0.09	694.67	85.89	78.33
23/11/2016	17:54:24.0	17:54:32.5	Linear	[0.67,0.74, -0.08]	[0.40,0.82, 0.41]	0.95	0.88	0.05	0.05	439.20	94.47	68.66
23/11/2016	17:55:06.0	17:55:10.0	Linear	[0.96,0.27, -0.09]	[0.78,0.45, 0.43]	0.90	0.84	0.07	0.11	833.18	102.52	117.35
25/11/2016	08:03:22.0	08:03:30.0	Linear	[0.92,0.16, -0.37]	[0.43,0.31, -0.85]	0.97	0.92	0.07	0.13	354.10	106.44	143.56
25/11/2016	10:30:34.0	10:30:44.0	Other	[0.80,0.51, -0.31]	[-0.81,-0.13, 0.57]	0.95	0.88	0.06	0.10	500.04	105.56	154.38
26/11/2016	16:20:58.3	16:21:02.2	Linear	[-0.84,0.19, 0.51]	[0.05,-0.22, -0.97]	0.91	0.84	0.09	0.16	668.55	39.69	84.54
28/11/2016	14:30:01.0	14:30:05.0	Linear	[-0.93,-0.35, 0.12]	[-0.89,-0.01, 0.46]	0.98	0.92	0.05	0.07	484.60	138.36	88.99
30/11/2016	10:20:04.0	10:20:07.0	Radial	[0.91,-0.38, -0.19]	[-0.94,-0.11, -0.32]	0.96	0.87	0.04	0.06	452.62	62.73	95.96
30/11/2016	12:55:43.0	12:55:47.5	Other	[-0.97,-0.19, 0.15]	[0.72,0.02, -0.69]	0.95	0.81	0.04	0.04	411.47	98.06	112.25
30/11/2016	13:06:55.9	13:07:07.0	Other	[-0.97,-0.19, 0.11]	[0.91,0.41, -0.04]	0.92	0.81	0.04	0.06	409.88	83.58	121.10
02/12/2016	07:14:25.0	07:14:29.0	Other	[-0.77,0.60, 0.21]	[0.96,-0.29, -0.04]	0.96	0.86	0.06	0.07	450.63	55.89	99.91
02/12/2016	15:56:13.0	15:56:17.0	Linear	[0.84,0.54, -0.02]	[0.97,0.22, -0.12]	0.99	0.94	0.13	0.14	472.67	49.02	78.21
12/12/2016	16:15:44.0	16:15:49.0	Other	[0.36,0.91, 0.19]	[0.36,0.91, 0.19]	0.90	0.80	0.04	0.07	567.04	64.49	86.70
22/12/2016	14:14:02.0	14:14:06.0	Radial	[0.81,0.57, 0.16]	[0.94,0.17, -0.30]	0.94	0.86	0.05	0.08	493.29	64.59	118.26
22/12/2016	14:29:36.7	14:29:44.5	Radial	[-0.97,-0.18, 0.15]	[0.83,-0.46, 0.31]	0.93	0.80	0.11	0.06	443.20	69.08	145.09
30/12/2016	04:09:49.0	04:09:58.1	Linear	[-0.97,0.16, 0.16]	[-1.00,0.06, 0.03]	0.95	0.84	0.06	0.06	440.08	86.69	65.72
30/12/2016	06:43:29.0	06:43:36.0	Other	[-0.98,0.13, 0.11]	[0.96,-0.04, 0.28]	0.97	0.90	0.05	0.09	421.54	149.91	71.76
07/01/2017	13:48:18.5	13:48:22.8	Radial	[0.07,0.98, 0.21]	[-0.49,-0.85, -0.21]	0.96	0.89	0.05	0.08	675.72	172.50	87.81
18/01/2017	00:04:26.0	00:04:32.0	Linear	[-0.97,0.19, 0.16]	[-0.89,0.14, 0.44]	0.95	0.90	0.04	0.08	440.84	33.57	68.06
21/01/2017	11:14:19.0	11:14:25.0	Other	[0.99,-0.14, -0.07]	[-0.43,-0.08, 0.90]	0.97	0.91	0.11	0.17	500.89	79.27	67.05
24/01/2017	04:36:49.0	04:37:02.0	Radial	[0.98,0.15, -0.10]	[0.91,0.24, -0.33]	0.93	0.85	0.05	0.04	439.19	84.09	98.57
24/01/2017	04:49:24.0	04:49:30.0	Linear	[-0.94,0.33, -0.01]	[-0.82,0.57, 0.03]	0.91	0.85	0.07	0.10	415.01	101.38	161.74
27/01/2017	23:50:23.0	23:50:29.5	Linear	[0.91,-0.31, -0.28]	[-0.78,0.10, 0.62]	0.94	0.87	0.05	0.07	565.04	71.77	106.55
28/01/2017	00:34:05.5	00:34:09.5	Linear	[0.75,-0.60, -0.29]	[-0.76,0.54, 0.37]	0.99	0.95	0.12	0.16	594.64	105.40	91.73
28/01/2017	10:55:37.0	10:55:40.5	Linear	[0.98,0.21, 0.02]	[0.46,0.59, 0.66]	0.97	0.89	0.06	0.08	474.16	84.53	67.98
28/01/2017	10:56:50.5	10:56:55.0	Other	[-0.97,-0.13, -0.18]	[0.53,0.62, 0.58]	0.96	0.90	0.06	0.10	479.41	96.28	87.21
29/01/2017	00:35:10.0	00:35:17.0	Other	[0.78,-0.59, -0.22]	[-0.82,0.50, 0.29]	0.98	0.91	0.06	0.08	431.17	78.36	87.86
29/01/2017	00:47:26.0	00:47:30.0	Linear	[0.98,-0.20, 0.01]	[0.71,-0.60, -0.36]	0.97	0.91	0.04	0.03	557.64	60.25	69.03
29/01/2017	08:37:49.0	08:37:57.0	Linear	[0.98,-0.17, -0.13]	[-0.61,-0.49, 0.62]	0.92	0.84	0.04	0.04	502.70	134.15	114.51
31/01/2017	12:00:45.0	12:00:55.0	Radial	[-0.94,0.25, -0.22]	[-0.37,-0.05, 0.93]	0.92	0.81	0.05	0.06	399.39	67.74	81.40
05/02/2017	11:28:56.5	11:29:09.0	Other	[-0.86,0.50, -0.04]	[-0.86,0.45, -0.23]	0.92	0.84	0.08	0.07	468.27	83.82	67.73
07/12/2017	03:00:55.0	03:01:01.5	Radial	[0.87,-0.49, 0.00]	[0.51,-0.51, 0.70]	0.91	0.83	0.08	0.05	536.52	70.41	78.14

List of Figures

List of Tables

Bibliography

Allison, H. J., Shprits, Y. Y., Zhelavskaya, I. S., Wang, D., and Smirnov, A. G. (2021). Gyroresonant wave-particle interactions with chorus waves during extreme depletions of plasma density in the Van Allen radiation belts. *Science Advances*, 7(5):eabc0380.

Anderson, B. J., Johnson, C. L., Korth, H., Winslow, R. M., Borovsky, J. E., Purucker, M. E., Slavin, J. A., Solomon, S. C., Zuber, M. T., and McNutt, Ralph L., J. (2012). Low-degree structure in Mercury's planetary magnetic field. *Journal of Geophysical Research (Planets)*, 117:E00L12.

Andrews, G. B., Zurbuchen, T. H., Mauk, B. H., Malcom, H., Fisk, L. A., Gloeckler, G., Ho, G. C., Kelley, J. S., Koehn, P. L., LeFevere, T. W., Livi, S. S., Lundgren, R. A., and Raines, J. M. (2007). The energetic particle and plasma spectrometer instrument on the MESSENGER spacecraft. *Space Science Reviews*, 131(1):523–556.

Arró, G., Califano, F., and Lapenta, G. (2022). Spectral properties and energy transfer at kinetic scales in collisionless plasma turbulence. *Astronomy and Astrophysics*, 668:A33.

Aunai, N., Hesse, M., and Kuznetsova, M. (2013a). Electron nongyrotropy in the context of collisionless magnetic reconnection. *Physics of Plasmas*, 20(9):092903.

Aunai, N., Hesse, M., and Kuznetsova, M. (2013b). Electron nongyrotropy in the context of collisionless magnetic reconnection. *Physics of Plasmas*, 20(9):092903.

Aunai, N., Hesse, M., Lavraud, B., Dargent, J., and Smets, R. (2016). Orientation of the X-line in asymmetric magnetic reconnection. *Journal of Plasma Physics*, 82(4):535820401.

Aunai, N., Retin, A., Belmont, G., Smets, R., Lavraud, B., and Vaivads, A. (2011). The proton pressure tensor as a new proxy of the proton decoupling region in collisionless magnetic reconnection. *Annales Geophysicae*, 29(9):1571–1579.

Aunai, N., Smets, R., Ciardi, A., Deegan, P., Jeandet, A., Payet, T., Guyot, N., and Darrieumerlou, L. (2024). Phare: Parallel hybrid particle-in-cell code with patch-based adaptive mesh refinement. *Computer Physics Communications*, 295:108966.

Bagenal, F. (2013). Planetary Magnetospheres. In Oswalt, T. D., French, L. M., and Kalas, P., editors, *Planets, Stars and Stellar Systems*, pages 251–307. Springer Netherlands, Dordrecht.

Baker, D. N., Riesberg, L., Pankratz, C. K., Panneton, R. S., Giles, B. L., Wilder, F. D., and Ergun, R. E. (2016). Magnetospheric Multiscale Instrument Suite Operations and Data System. *Space Science Reviews*, 199(1-4):545–575.

Balikhin, M. A., Boynton, R. J., Walker, S. N., Borovsky, J. E., Billings, S. A., and Wei, H. L. (2011). Using the NARMAX approach to model the evolution of energetic electrons fluxes at geostationary orbit: NARMAX MODELLING OF RADIATION BELT ELECTRON FLUXES. *Geophysical Research Letters*, 38(18):n/a–n/a.

Ballerini, G., Lavorenti, F., Califano, F., and Henri, P. (2024a). Whistler-mode waves in the tail of mercury's magnetosphere: A numerical study. *Astronomy & Astrophysics*.

Ballerini, G., Rezeau, L., Belmont, G., and Califano, F. (2024b). Role of flr effects in magnetopause equilibrium. *Journal of Plasma Physics*, accepted.

Baumjohann, W., Matsuoka, A., Glassmeier, K. H., Russell, C. T., Nagai, T., Hoshino, M., Nakagawa, T., Balogh, A., Slavin, J. A., Nakamura, R., and Magnes, W. (2006). The magnetosphere of Mercury and its solar wind environment: Open issues and scientific questions. *Advances in Space Research*, 38(4):604–609.

Baumjohann, W. and Treumann, R. A. (1996). *Basic Space Plasma Physics*. PUBLISHED BY IMPERIAL COLLEGE PRESS AND DISTRIBUTED BY WORLD SCIENTIFIC PUBLISHING CO.

Behar, E., Fatemi, S., Henri, P., and Holmström, M. (2022). *Menura*: a code for simulating the interaction between a turbulent solar wind and solar system bodies. *Ann. Geophys.*, 40(3):281–297.

Behar, E., Pucci, F., Simon Wedlund, C., Henri, P., Ballerini, G., Preisser, L., and Califano, F. (2024). Impact of solar wind turbulence on the earth's bow shock. a global 3d simulation. *Astronomy and Astrophysics*, to be submitted.

Behar, E. and Henri, P. (2023). Interaction between the turbulent solar wind and a planetary magnetosphere: A 2d comet example. *A&A*, 671:A144.

Belmont, G., Aunai, N., and Smets, R. (2012). Kinetic equilibrium for an asymmetric tangential layer. *Physics of Plasmas*, 19(2):022108.

Belmont, G., Grappin, R., Mottez, F., Pantellini, F., and Pelletier, G. (2014). *Collisionless plasmas in astrophysics*. Wiley.

Belmont, G. and Rezeau, L. (1987). Finite Larmor radius effects: the two-fluid approach. *Annales Geophysicae*, pages vol. 5, no2, pp. 59–69.

Belmont, G., Rezeau, L., Riconda, C., and Zaslavsky, A. (2019). *Introduction to plasma physics*. ISTE Press.

Benkhoff, J., Murakami, G., Baumjohann, W., Besse, S., Bunce, E., Casale, M., Cremosese, G., Glassmeier, K. H., Hayakawa, H., Heyner, D., Hiesinger, H., Huovelin, J., Hussmann, H., Iafolla, V., Iess, L., Kasaba, Y., Kobayashi, M., Milillo, A., Mitrofanov, I. G., Montagnon, E., Novara, M., Orsini, S., Quemerais, E., Reininghaus, U., Saito, Y., Santoli, F., Stramaccioni, D., Sutherland, O., Thomas, N., Yoshikawa, I., and Zender, J. (2021). BepiColombo - Mission Overview and Science Goals. *Space Science Reviews*, 217(8):90.

Berchem, J. and Russell, C. T. (1982a). Magnetic field rotation through the magnetopause: ISEE 1 and 2 observations. *Journal of Geophysical Research: Space Physics*, 87(A10):8139–8148.

Berchem, J. and Russell, C. T. (1982b). The thickness of the magnetopause current layer: ISEE 1 and 2 observations. *Journal of Geophysical Research: Space Physics*, 87(A4):2108–2114.

Biermann, L. (1957). Solar corpuscular radiation and the interplanetary gas. *The Observatory*, 77:109–110. ADS Bibcode: 1957Obs....77..109B.

Biermann, L. and Schluter, A. (1951). Cosmic Radiation and Cosmic Magnetic Fields. II. Origin of Cosmic Magnetic Fields. *Physical Review*, 82(6):863–868.

Birdsall, C. K. and Langdon, A. B. (1991). *Plasma Physics via Computer Simulation*. CRC Press.

Birkeland, K. (1901). Rsultats des rescherches magnthiques faites par lexpdition Norvgienne de 18991900. *Archives des Sciences Physiques et Naturelles*, pages 565–586.

Biskamp, D., Schwarz, E., and Drake, J. F. (1997). Two-fluid theory of collisionless magnetic reconnection. *Physics of Plasmas*, 4(4):1002–1009.

Boardsen, S. A., Eastman, T. E., Sotirelis, T., and Green, J. L. (2000). An empirical model of the highlatitude magnetopause. *Journal of Geophysical Research: Space Physics*, 105(A10):23193–23219.

Borovsky, J. E. and Valdivia, J. A. (2018). The Earths Magnetosphere: A Systems Science Overview and Assessment. *Surveys in Geophysics*, 39(5):817–859.

Braginskii, S. I. (1965). Transport Processes in a Plasma. *Reviews of Plasma Physics*, 1:205. ADS Bibcode: 1965RvPP....1..205B.

Bret, A. and Dieckmann, M. E. (2010). How large can the electron to proton mass ratio be in particle-in-cell simulations of unstable systems? *Physics of Plasmas*, 17(3):032109.

Bridge, H. S., Dilworth, C., Lazarus, A. J., Lyon, E. F., Rossi, B., and Scherb, F. (1962). Direct Observations of the Interplanetary Plasma. *Journal of the Physical Society of Japan Supplement*, 17:553. ADS Bibcode: 1962JPSJS..17B.553B.

Burch, J. L., Moore, T. E., Torbert, R. B., and Giles, B. L. (2016). Magnetospheric Multiscale Overview and Science Objectives. *Space Science Reviews*, 199(1-4):5–21.

Burch, J. L. and Phan, T. D. (2016a). Magnetic reconnection at the dayside magnetopause: Advances with mms. *Geophysical Research Letters*, 43(16):8327–8338.

Burch, J. L. and Phan, T. D. (2016b). Magnetic reconnection at the dayside magnetopause: Advances with MMS. *Geophysical Research Letters*, 43(16):8327–8338.

Burgess, D. and Scholer, M. (2015). *Collisionless Shocks in Space Plasmas*. Cambridge University Press.

Burtis, W. and Helliwell, R. (1976). Magnetospheric chorus: Occurrence patterns and normalized frequency. *Planetary and Space Science*, 24(11):1007–1024.

Burtis, W. J. and Helliwell, R. A. (1969). Banded chorus-A new type of VLF radiation observed in the magnetosphere by OGO 1 and OGO 3. *Journal of Geophysical Research*, 74(11):3002–3010.

Cahill, L. J. and Amazeen, P. G. (1963). The boundary of the geomagnetic field. *Journal of Geophysical Research*, 68(7):1835–1843.

Case, N. A. and Wild, J. A. (2013). The location of the Earth's magnetopause: A comparison of modeled position and in situ Cluster data. *Journal of Geophysical Research: Space Physics*, 118(10):6127–6135.

Cassak, P. A. and Fuselier, S. A. (2016). Reconnection at earths dayside magnetopause. In *Magnetic Reconnection*, volume 427, pages 213–276. Springer International Publishing. Series Title: Astrophysics and Space Science Library.

Chanteur, G. (1998). Spatial interpolation for four spacecraft: Theory. *ISSI Scientific Reports Series*, 1:349–370. ADS Bibcode: 1998ISSIR...1..349C.

Chanteur, G. and Mottez, F. (1993). Geometrical tools for cluster data analysis. In *Spatio-temporal analysis for resolving plasma turbulence (START)*, ESA WWP 47, pages 341–344.

Chapman, S. (1917). On the Times of Sudden Commencement of Magnetic Storms. *Proceedings of the Physical Society of London*, 30(1):205–214.

Chapman, S. and Ferraro, V. C. A. (1930). A New Theory of Magnetic Storms. *Nature*, 126(3169):129–130.

Chapman, S. and Ferraro, V. C. A. (1933). A new theory of magnetic storms. *Terrestrial Magnetism and Atmospheric Electricity*, 38(2):79–96.

Chapman, S. and Ferraro, V. C. A. (1940). The theory of the first phase of a geomagnetic storm. *Terrestrial Magnetism and Atmospheric Electricity*, 45(3):245–268.

Chew, G., Goldberger, M., and Low, F. (1956). The boltzmann equation an d the one-fluid hydromagnetic equations in the absence of particle collisions. *Proceedings of the Royal Society of London. Series A. Mathematical and Physical Sciences*, 236(1204):112–118.

Chou, Y.-C. and Hau, L.-N. (2012-08). A statistical study of magnetopause structures: Tangential versus rotational discontinuities: THE STRUCTURE OF MAGNETOPAUSE CURRENT. *Journal of Geophysical Research: Space Physics*, 117:n/a–n/a.

Christon, S. P. (1987). A comparison of the Mercury and Earth magnetospheres: Electron measurements and substorm time scales. *Icarus*, 71(3):448–471.

Chust, T. and Belmont, G. (2006). Closure of fluid equations in collisionless magnetoplasmas. *Physics of Plasmas*, 13(1):012506.

Cowley, S. W. H. (1995). The Earth's magnetosphere: A brief beginner's guide. *Eos, Transactions American Geophysical Union*, 76(51):525–529.

Cramer, N. F. (2001). *The Physics of Alfvn Waves*. John Wiley and Sons, Ltd.

Cranmer, S. R., Gibson, S. E., and Riley, P. (2017). Origins of the Ambient Solar Wind: Implications for Space Weather. *Space Science Reviews*, 212(3-4):1345–1384.

Dakeyo, J.-B., Maksimovic, M., Dmoulin, P., Halekas, J., and Stevens, M. L. (2022). Statistical analysis of the radial evolution of the solar winds between 0.1 and 1 au and their semiempirical isopoly fluid modeling. *The Astrophysical Journal*, 940(2):130.

Dargent, J., Aunai, N., Lavraud, B., ToledoRedondo, S., Shay, M. A., Cassak, P. A., and Malakit, K. (2017). Kinetic simulation of asymmetric magnetic reconnection with cold ions. *Journal of Geophysical Research: Space Physics*, 122(5):5290–5306.

Davis, L. and Williamson, J. (1962). Summary of early results from Explorer 12. *Transactions of the American Geophysical Union*, IG Bulletin(58).

De Hoffmann, F. and Teller, E. (1950). Magneto-Hydrodynamic Shocks. *Physical Review*, 80(4):692–703.

De Keyser, J. (2008). Empirical reconstruction. *ISSI Scientific Reports Series*, 8, 9198.

Deca, J., Divin, A., Henri, P., Eriksson, A., Markidis, S., Olshevsky, V., and Horányi, M. (2017). Electron and Ion Dynamics of the Solar Wind Interaction with a Weakly Outgassing Comet. *Phys. Rev. Lett.*, 118(20):205101.

Denton, R. E., Sonnerup, B. U. O., Russell, C. T., Hasegawa, H., Phan, T., Strangeway, R. J., Giles, B. L., Ergun, R. E., Lindqvist, P., Torbert, R. B., Burch, J. L., and Vines, S. K. (2018). Determining $\boldsymbol{L}$ $\boldsymbol{M}$ $\boldsymbol{N}$ Current Sheet Coordinates at the Magnetopause From Magnetospheric Multiscale Data. *Journal of Geophysical Research: Space Physics*, 123(3):2274–2295.

Denton, R. E., Sonnerup, B. U. ., Hasegawa, H., Phan, T. D., Russell, C. T., Strangeway, R. J., Giles, B. L., Gershman, D., and Torbert, R. B. (2016). Motion of the MMS spacecraft relative to the magnetic reconnection structure observed on 16 October 2015 at 1307 UT. *Geophysical Research Letters*, 43(11):5589–5596.

Dibraccio, G. A., Slavin, J. A., Boardsen, S. A., Anderson, B. J., Korth, H., Zurbuchen, T. H., Raines, J. M., Baker, D. N., McNutt, R. L., and Solomon, S. C. (2013). MESSENGER observations of magnetopause structure and dynamics at Mercury. *Journal of Geophysical Research (Space Physics)*, 118(3):997–1008.

DiBraccio, G. A., Slavin, J. A., Raines, J. M., Gershman, D. J., Tracy, P. J., Boardsen, S. A., Zurbuchen, T. H., Anderson, B. J., Korth, H., McNutt, R. L., and Solomon, S. C. (2015). First observations of Mercury's plasma mantle by MESSENGER. *Geophysical Research Letters*, 42(22):9666–9675.

Dorville, N., Belmont, G., Aunai, N., Dargent, J., and Rezeau, L. (2015a). Asymmetric kinetic equilibria: Generalization of the BAS model for rotating magnetic profile and non-zero electric field. *Physics of Plasmas*, 22(9):092904.

Dorville, N., Belmont, G., Rezeau, L., Grappin, R., and Retin, A. (2014). Rotational/compressional nature of the magnetopause: Application of the BV technique on a magnetopause case study. *Journal of Geophysical Research: Space Physics*, 119(3):1898–1908.

Dorville, N., Haaland, S., Anekallu, C., Belmont, G., and Rezeau, L. (2015b). Magnetopause orientation: Comparison between generic residue analysis and BV method: GRA/BV COMPARISON. *Journal of Geophysical Research: Space Physics*, 120(5):3366–3379.

Drake, J. F. and Kleva, R. G. (1991). Collisionless reconnection and the sawtooth crash. *Physical Review Letters*, 66(11):1458–1461.

Dungey, J. W. (1955). *Electrodynamics of the Outer Atmosphere*. Pennsylvania State University. Conference Name: Physics of the Ionosphere Pages: 229 ADS Bibcode: 1955phio.conf..229D.

Dungey, J. W. (1961). Interplanetary Magnetic Field and the Auroral Zones. *Physical Review Letters*, 6(2):47–48.

Eastman, T. E., Hones, E. W., Bame, S. J., and Asbridge, J. R. (1976). The magnetospheric boundary layer: Site of plasma, momentum and energy transfer from the magnetosheath into the magnetosphere. *Geophysical Research Letters*, 3(11):685–688.

Ergun, R. E., Tucker, S., Westfall, J., Goodrich, K. A., Malaspina, D. M., Summers, D., Wallace, J., Karlsson, M., Mack, J., Brennan, N., Pyke, B., Withnell, P., Torbert, R., Macri, J., Rau, D., Dors, I., Needell, J., Lindqvist, P.-A., Olsson, G., and Cully, C. M. (2016). The Axial Double Probe and Fields Signal Processing for the MMS Mission. *Space Science Reviews*, 199(1-4):167–188.

Escoubet, C., Fehringer, M., and Goldstein, M. (2001). Introduction The Cluster mission. *Annales Geophysicae*, 19(10-12).

Escoubet, C., Schmidt, R., and Goldstein, M. (1997). Cluster - Science and mission overview. *Space Science Reviews*, 79(1/2):11–32.

Exner, W. (2021). *Modeling of Mercury's Magnetosphere Under Different Solar Wind Conditions*. PhD thesis, [object Object].

Faganello, M., Califano, F., Pegoraro, F., and Retin, A. (2014). Kelvin-Helmholtz vortices and double mid-latitude reconnection at the Earth's magnetopause: Comparison between observations and simulations. *EPL (Europhysics Letters)*, 107(1):19001.

Farris, M. H. and Russell, C. T. (1994). Determining the standoff distance of the bow shock: Mach number dependence and use of models. *Journal of Geophysical Research: Space Physics*, 99:17681–17689.

Fatemi, S., Poppe, A. R., Delory, G. T., and Farrell, W. M. (2017). AMITIS: A 3d GPU-based hybrid-PIC model for space and plasma physics. *Journal of Physics: Conference Series*, 837:012017.

Ferraro, V. C. A. (1952). On the theory of the first phase of a geomagnetic storm: A new illustrative calculation based on an idealised (plane not cylindrical) model field distribution. *Journal of Geophysical Research*, 57(1):15–49.

Franci, L., Landi, S., Matteini, L., Verdini, A., and Hellinger, P. (2015). HIGH-RESOLUTION HYBRID SIMULATIONS OF KINETIC PLASMA TURBULENCE AT PROTON SCALES. *The Astrophysical Journal*, 812(1):21.

Freeman, J. W., Van Allen, J. A., and Cahill, L. J. (1963). Explorer 12 observations of the magnetospheric boundary and the associated solar plasma on September 13, 1961. *Journal of Geophysical Research*, 68(8):2121–2130.

Friedman, J. H. (2001-10-01). Greedy function approximation: A gradient boosting machine. *The Annals of Statistics*, 29(5).

Fryxell, B., Olson, K., Ricker, P., Timmes, F. X., Zingale, M., Lamb, D. Q., MacNeice, P., Rosner, R., Truran, J. W., and Tufo, H. (2000). FLASH: An adaptive mesh hydrodynamics code for modeling astrophysical thermonuclear flashes. *The Astrophysical Journal Supplement Series*, 131(1):273–334.

Fujimoto, M., Shinohara, I., and Kojima, H. (2011). Reconnection and Waves: A Review with a Perspective. *Space Science Reviews*, 160(1-4):123–143.

Fuselier, S. A. (2021). Dayside Magnetopause Processes. In Maggiolo, R., Andr, N., Hasegawa, H., Welling, D. T., Zhang, Y., and Paxton, L. J., editors, *Geophysical Monograph Series*, pages 153–161. Wiley, 1 edition.

Fuselier, S. A., Petrinec, S. M., Trattner, K. J., and Lavraud, B. (2014). Magnetic field topology for northward IMF reconnection: Ion observations. *Journal of Geophysical Research: Space Physics*, 119(11):9051–9071.

Fuselier, S. A., Vines, S. K., Burch, J. L., Petrinec, S. M., Trattner, K. J., Cassak, P. A., Chen, L., Ergun, R. E., Eriksson, S., Giles, B. L., Graham, D. B., Khotyaintsev, Y. V., Lavraud, B., Lewis, W. S., Mukherjee, J., Norgren, C., Phan, T., Russell, C. T., Strangeway, R. J., Torbert, R. B., and Webster, J. M. (2017). Largescale characteristics of reconnection diffusion regions and associated magnetopause crossings observed by MMS. *Journal of Geophysical Research: Space Physics*, 122(5):5466–5486.

Genestreti, K. J., Nakamura, T. K. M., Nakamura, R., Denton, R. E., Torbert, R. B., Burch, J. L., Plaschke, F., Fuselier, S. A., Ergun, R. E., Giles, B. L., and Russell, C. T. (2018). How Accurately Can We Measure the Reconnection Rate $\boldsymbol{E}_{\boldsymbol{m}}$ for the MMS Diffusion Region Event of 11 July 2017? *Journal of Geophysical Research: Space Physics*, 123(11):9130–9149.

Glauert, S. A. and Horne, R. B. (2005). Calculation of pitch angle and energy diffusion coefficients with the PADIE code. *Journal of Geophysical Research: Space Physics*, 110(A4):2004JA010851.

Goldstein, H. (1950). *Classical mechanics*. Addison-Wesley, student ed edition. OCLC: 917197621.

Goldston, R. J. and Rutherford, P. H. (2003). *Introduction to plasma physics*. Inst. of Physics Publ., Bristol, reprinted edition.

Groelj, D., Mallet, A., Loureiro, N. F., and Jenko, F. (2018). Fully kinetic simulation of 3d kinetic alfvn turbulence. *Physical Review Letters*, 120(10):105101.

Gurnett, D. A., Kurth, W. S., Scarf, F. L., and Poynter, R. L. (1986). First Plasma Wave Observations at Uranus. *Science*, 233(4759):106–109.

Gurnett, D. A., Shaw, R. R., Anderson, R. R., Kurth, W. S., and Scarf, F. L. (1979). Whistlers observed by Voyager 1: Detection of lightning on Jupiter. *Geophysical Research Letters*, 6(6):511–514.

Haaland, S., Hasegawa, H., Paschmann, G., Sonnerup, B., and Dunlop, M. (2021). 20 Years of Cluster Observations: The Magnetopause. *Journal of Geophysical Research: Space Physics*, 126(8):e2021JA029362.

Haaland, S., Paschmann, G., Oieroset, M., Phan, T., Hasegawa, H., Fuselier, S. A., Constantinescu, V., Eriksson, S., Trattner, K. J., Fadanelli, S., Tenfjord, P., Lavraud, B., Norgren, C., Eastwood, J. P., Hietala, H., and Burch, J. (2020). Characteristics of the Flank Magnetopause: MMS Results. *Journal of Geophysical Research: Space Physics*, 125(3):e2019JA027623.

Haaland, S., Reistad, J., Tenfjord, P., Gjerloev, J., Maes, L., DeKeyser, J., Maggiolo, R., Anekallu, C., and Dorville, N. (2014). Characteristics of the flank magnetopause: Cluster observations. *Journal of Geophysical Research: Space Physics*, 119(11):9019–9037.

Haaland, S. E., Sonnerup, B. U. O., Dunlop, M. W., Balogh, A., Georgescu, E., Hasegawa, H., Klecker, B., Paschmann, G., Puhl-Quinn, P., Rème, H., Vaith, H., and Vaivads, A. (2004). Four-spacecraft determination of magnetopause orientation, motion and thickness: comparison with results from single-spacecraft methods. *Annales Geophysicae*, 22(4):1347–1365.

Harris, E. G. (1962). On a plasma sheath separating regions of oppositely directed magnetic field. *Il Nuovo Cimento*, 23(1):115–121.

Harvey, C. (1998). Spatial gradients and the volumetric tensor. In *Analysis Methods for Multi-Spacecraft Data*, Int. Space Sci. Inst., Bern,, pages 307–322.

Hasegawa, A. and Uberoi, C. (1982). *The Alfvn wave*. Oak Ridge, TN (USA): U.S. Department of Energy Technical Information Center.

Hasegawa, H. (2012). Structure and Dynamics of the Magnetopause and Its Boundary Layers. *Monographs on Environment, Earth and Planets*, 1(2):71–119.

Hasegawa, H., Sonnerup, B. U. ., Klecker, B., Paschmann, G., Dunlop, M. W., and Rme, H. (2005). Optimal reconstruction of magnetopause structures from Cluster data. *Annales Geophysicae*, 23(3):973–982.

Heppner, J. P., Ness, N. F., Scearce, C. S., and Skillman, T. L. (1963). Explorer 10 magnetic field measurements. *Journal of Geophysical Research*, 68(1):1–46.

Hesse, M., Aunai, N., Sibeck, D., and Birn, J. (2014). On the electron diffusion region in planar, asymmetric, systems. *Geophysical Research Letters*, 41(24):8673–8680.

Hesse, M. and Cassak, P. A. (2020). Magnetic Reconnection in the Space Sciences: Past, Present, and Future. *Journal of Geophysical Research: Space Physics*, 125(2):e2018JA025935.

Hesse, M., Neukirch, T., Schindler, K., Kuznetsova, M., and Zenitani, S. (2011). The Diffusion Region in Collisionless Magnetic Reconnection. *Space Science Reviews*, 160(1-4):3–23.

Hockney, R. and Eastwood, J. (2021). *Computer Simulation Using Particles*. CRC Press, 0 edition.

Hodgson, R. (1859). On a curious appearance seen in the Sun. *Monthly Notices of the Royal Astronomical Society*, 20(1):15–16.

Horne, R. B., Thorne, R. M., Glauert, S. A., Douglas Menietti, J., Shprits, Y. Y., and Gurnett, D. A. (2008). Gyro-resonant electron acceleration at Jupiter. *Nature Physics*, 4(4):301–304.

Horne, R. B., Thorne, R. M., Shprits, Y. Y., Meredith, N. P., Glauert, S. A., Smith, A. J., Kanekal, S. G., Baker, D. N., Engebretson, M. J., Posch, J. L., Spasojevic, M., Inan, U. S., Pickett, J. S., and Decreau, P. M. E. (2005). Wave acceleration of electrons in the Van Allen radiation belts. *Nature*, 437(7056):227–230.

Hua, M., Bortnik, J., Kellerman, A. C., Camporeale, E., and Ma, Q. (2023). Ensemble Modeling of Radiation Belt Electron Acceleration by Chorus Waves: Dependence on Key Input Parameters. *Space Weather*, 21(3):e2022SW003234.

Hua, M., Bortnik, J., and Ma, Q. (2022). Upper Limit of Outer Radiation Belt Electron Acceleration Driven by WhistlerMode Chorus Waves. *Geophysical Research Letters*, 49(15):e2022GL099618.

Hudson, P. (1971). Rotational discontinuities in an anisotropic plasma. *Planetary and Space Science*, 19(12):1693–1699.

Imber, S. M., Slavin, J. A., Boardsen, S. A., Anderson, B. J., Korth, H., McNutt, R. L., and Solomon, S. C. (2014). MESSENGER observations of large dayside flux transfer events: Do they drive Mercury's substorm cycle? *Journal of Geophysical Research (Space Physics)*, 119(7):5613–5623.

Ip, W.-H. and Kopp, A. (2002). Mhd simulations of the solar wind interaction with mercury. *Journal of Geophysical Research: Space Physics*, 107(A11):SSH 4–1–SSH 4–8.

James, M. K., Imber, S. M., Bunce, E. J., Yeoman, T. K., Lockwood, M., Owens, M. J., and Slavin, J. A. (2017). Interplanetary magnetic field properties and variability near mercury's orbit. *Journal of Geophysical Research: Space Physics*, 122(8):7907–7924.

Jeffrey, A. and Taniuti, T. (1964). *Non-linear Wave Propagation: With Applications to Physics and Magnetohydrodynamics (Mathematics in science and engineering ; v. 9)*. Academic Press.

Johnson, C. L., Philpott, L. C., Anderson, B. J., Korth, H., Hauck, S. A., Heyner, D., Phillips, R. J., Winslow, R. M., and Solomon, S. C. (2016). MESSENGER observations of induced magnetic fields in Mercury's core. *Geophysical Research Letters*, 43(6):2436–2444.

Kajdi, P., Alexandrova, O., Maksimovic, M., Lacombe, C., and Fazakerley, A. N. (2016). SUPRATHERMAL ELECTRON STRAHL WIDTHS IN THE PRESENCE OF NARROW-BAND WHISTLER WAVES IN THE SOLAR WIND. *The Astrophysical Journal*, 833(2):172.

Kallio, E. and Janhunen, P. (2003). Modelling the solar wind interaction with Mercury by a quasi-neutral hybrid model. *Annales Geophysicae*, 21(11):2133–2145.

Kallio, E. and Janhunen, P. (2004). The response of the Hermean magnetosphere to the interplanetary magnetic field. *Advances in Space Research*, 33(12):2176–2181.

Karimabadi, H., Daughton, W., and Scudder, J. (2007). Multiscale structure of the electron diffusion region. *Geophysical Research Letters*, 34(13):2007GL030306.

Karimabadi, H., Roytershteyn, V., Vu, H. X., Omelchenko, Y. A., Scudder, J., Daughton, W., Dimmock, A., Nykyri, K., Wan, M., Sibeck, D., Tatineni, M., Majumdar, A., Loring, B., and Geveci, B. (2014). The link between shocks, turbulence, and magnetic reconnection in collisionless plasmas. *Physics of Plasmas*, 21(6):062308.

Kasaba, Y., Kojima, H., Moncuquet, M., Wahlund, J.-E., Yagitani, S., Sahraoui, F., Henri, P., Karlsson, T., Kasahara, Y., Kumamoto, A., Ishisaka, K., Issautier, K., Wattieaux, G., Imachi, T., Matsuda, S., Lichtenberger, J., and Usui, H. (2020). Plasma wave investigation (PWI) aboard BepiColombo mio on the trip to the first measurement of electric fields, electromagnetic waves, and radio waves around mercury. *Space Science Reviews*, 216(4):65.

Kennel, C. F. and Petschek, H. E. (1966). Limit on stably trapped particle fluxes. *Journal of Geophysical Research*, 71(1):1–28.

Khotyaintsev, Y. V., Graham, D. B., Norgren, C., and Vaivads, A. (2019). Collisionless Magnetic Reconnection and Waves: Progress Review. *Frontiers in Astronomy and Space Sciences*, 6:70.

King, J. H. and Papitashvili, N. E. (2005). Solar wind spatial scales in and comparisons of hourly wind and ACE plasma and magnetic field data. *Journal of Geophysical Research: Space Physics*, 110:2004JA010649.

Kivelson, M. G. and Bagenal, F. (2014). Planetary Magnetospheres. In *Encyclopedia of the Solar System*, pages 137–157. Elsevier.

Kivelson, M. G. and Russell, C. T., editors (1995). *Introduction to space physics*. Cambridge University Press. OCLC: 1124679918.

Klimontovich, I. L. (1982). *Kinetic theory of nonideal gases and nonideal plasmas*. Number v. 105 in International series in natural philosophy. Pergamon Press, Oxford ; New York, 1st ed edition.

Krall, N. A., Trivelpiece, A. W., and Gross, R. A. (1973). Principles of Plasma Physics. *American Journal of Physics*, 41(12):1380–1381.

Kurth, W. S. and Gurnett, D. A. (1991). Plasma waves in planetary magnetospheres. *Journal of Geophysical Research: Space Physics*, 96(S01):18977–18991.

Landau, L. D. and Lifshitz, E. M. (1975). *The classical theory of fields*. Number 2 in Course of theoretical physics / L. D. Landau and E. M. Lifshitz. Elsevier Butterworth Heinemann, 4. rev. engl. ed., repr edition.

Landau, L. D. and Lifshitz, E. M. (1976). *Mechanics*. Number v. 1 in Course of theoretical physics. Pergamon Press, 3d edition.

Landau, L. D. and Lifshitz, E. M. (1987). *Fluid mechanics*. Pergamon Press.

Lapenta, G., Pucci, F., Goldman, M. V., and Newman, D. L. (2020). Local Regimes of Turbulence in 3D Magnetic Reconnection. *apj*, 888(2):104.

Lapenta, G., Schriver, D., Walker, R. J., Berchem, J., El Alaoui, M., Echterling, N. F., and Travnicek, P. (2022). Do we need to study the electrons kinetically to properly model a planetary magnetosphere: the case of mercury. *Journal of Geophysical Research: Space Physics*, n/a(n/a):e2021JA030241.

Lauben, D. S., Inan, U. S., Bell, T. F., Kirchner, D. L., Hospodarsky, G. B., and Pickett, J. S. (1998). VLF chorus emissions observed by Polar during the January 10, 1997, magnetic cloud. *Geophysical Research Letters*, 25(15):2995–2998.

Lavorenti, F. (2023). Mercury particle precipitation using full-PIC global simulations.

Lavorenti, F., Henri, P., Califano, F., Deca, J., Aizawa, S., André, N., and Benkhoff, J. (2022). Electron dynamics in small magnetospheres. Insights from global, fully kinetic plasma simulations of the planet Mercury. *Astronomy and Astrophysics*, 664:A133.

Lavorenti, F., Henri, Pierre, Califano, Francesco, Deca, Jan, Lindsay, Simon, Aizawa, Sae, and Benkhoff, Johannes (2023). Solar-wind electron precipitation on weakly magnetized bodies: The planet mercury. *A&A*, 674:A153.

Le, A., Egedal, J., Ohia, O., Daughton, W., Karimabadi, H., and Lukin, V. S. (2013). Regimes of the Electron Diffusion Region in Magnetic Reconnection. *Physical Review Letters*, 110(13):135004.

Le Contel, O., Roux, A., Jacquey, C., Robert, P., Berthomier, M., Chust, T., Grison, B., Angelopoulos, V., Sibeck, D., Chaston, C. C., Cully, C. M., Ergun, B., Glassmeier, K.-H., Auster, U., McFadden, J., Carlson, C., Larson, D., Bonnell, J. W., Mende, S., Russell, C. T., Donovan, E., Mann, I., and Singer, H. (2009). Quasi-parallel whistler mode waves observed by THEMIS during near-earth dipolarizations. *Annales Geophysicae*, 27(6):2259–2275.

Lindqvist, P.-A., Olsson, G., Torbert, R. B., King, B., Granoff, M., Rau, D., Needell, G., Turco, S., Dors, I., Beckman, P., Macri, J., Frost, C., Salwen, J., Eriksson, A., hln, L., Khotyaintsev, Y. V., Porter, J., Lappalainen, K., Ergun, R. E., Wermeer, W., and Tucker, S. (2016). The Spin-Plane Double Probe Electric Field Instrument for MMS. *Space Science Reviews*, 199(1-4):137–165.

Liu, K., Gary, S. P., and Winske, D. (2011). Excitation of banded whistler waves in the magnetosphere: EXCITATION OF BANDED WHISTLERS. *Geophysical Research Letters*, 38(14):n/a–n/a.

Liu, Y., Hesse, M., Cassak, P. A., Shay, M. A., Wang, S., and Chen, L. (2018). On the collisionless asymmetric magnetic reconnection rate. *Geophysical Research Letters*, 45(8):3311–3318.

Lukin, A. S., Artemyev, A. V., Petrukovich, A. A., Angelopoulos, V., Runov, A., Wang, C., and Yushkov, E. V. (2019). Spatial scales and plasma properties of the distant magnetopause: Evidence for selective ion and electron transport. *Journal of Geophysical Research: Space Physics*, 124(7):5027–5041.

Mandt, M. E., Denton, R. E., and Drake, J. F. (1994). Transition to whistler mediated magnetic reconnection. *Geophysical Research Letters*, 21(1):73–76.

Markidis, S., Lapenta, G., and Rizwan-uddin (2010). Multi-scale simulations of plasma with IPIC3D. *Mathematics and Computers in Simulation*, 80:1509–1519.

Maron, J. L., Mac Low, M., and Oishi, J. S. (2008). A constrainedtransport magnetohydrodynamics algorithm with nearspectral resolution. *The Astrophysical Journal*, 677(1):520–529.

Matthews, A. P. (1994). Current advance method and cyclic leapfrog for 2d multispecies hybrid plasma simulations. *Journal of Computational Physics*, 112(1):102–116.

Michotte de Welle, B. (2024). *Statistical Study of the Global Constraints Governing Magnetic Reconnection at the Earth's Magnetopause*. PhD thesis, These de doctorat de l'Université Paris-Saclay.

Michotte De Welle, B., Aunai, N., Nguyen, G., Lavraud, B., Gnot, V., Jeandet, A., and Smets, R. (2022). Global ThreeDimensional Draping of Magnetic Field Lines in Earths Magnetosheath From InSitu Spacecraft Measurements. *Journal of Geophysical Research: Space Physics*, 127(12):e2022JA030996.

Mignone, A., Zanni, C., Tzeferacos, P., van Straalen, B., Colella, P., and Bodo, G. (2012). The PLUTO code for adaptive mesh computations in astrophysical fluid dynamics. *The Astrophysical Journal Supplement Series*, 198:7. Publisher: IOP ADS Bibcode: 2012ApJS..198....7M.

Milillo, A., Fujimoto, M., Murakami, G., Benkhoff, J., Zender, J., Aizawa, S., Dósa, M., Griton, L., Heyner, D., Ho, G., Imber, S. M., Jia, X., Karlsson, T., Killen, R. M., Laurenza, M., Lindsay, S. T., McKenna-Lawlor, S., Mura, A., Raines, J. M., Rothery, D. A., André, N., Baumjohann, W., Berezhnoy, A., Bourdin, P. A., Bunce, E. J., Califano, F., Deca, J., deÂ la Fuente, S., Dong, C., Grava, C., Fatemi, S., Henri, P., Ivanovski, S. L., Jackson, B. V., James, M., Kallio, E., Kasaba, Y., Kilpua, E., Kobayashi, M., Langlais, B., Leblanc, F., Lhotka, C., Mangano, V., Martindale, A., Massetti, S., Masters, A., Morooka, M., Narita, Y., Oliveira, J. S., Odstrcil, D., Orsini, S., Pelizzo, M. G., Plainaki, C., Plaschke, F., Sahraoui, F., Seki, K., Slavin, J. A., Vainio, R., Wurz, P., Barabash, S., Carr, C. M., Delcourt, D., Glassmeier, K. H., Grande, M., Hirahara, M., Huovelin, J., Korablev, O., Kojima, H., Lichtenegger, H., Livi, S., Matsuoka, A., Moissl, R., Moncuquet, M., Muinonen, K., Quèmerais, E., Saito, Y., Yagitani, S., Yoshikawa, I., and Wahlund, J. E. (2020). Investigating Mercury's Environment with the Two-Spacecraft BepiColombo Mission. *Space Science Reviews*, 216(5):93.

Mller, J., Simon, S., Motschmann, U., Schle, J., Glassmeier, K.-H., and Pringle, G. J. (2011). A.i.k.e.f.: Adaptive hybrid model for space plasma simulations. *Computer Physics Communications*, 182:946–966. ADS Bibcode: 2011CoPhC.182..946M.

Ness, N. F., Behannon, K. W., Lepping, R. P., and Whang, Y. C. (1976). Observations of Mercury's Magnetic Field. *Icarus*, 28(4):479–488.

Ness, N. F., Behannon, K. W., Lepping, R. P., Whang, Y. C., and Schatten, K. H. (1974). Magnetic field observations near mercury: Preliminary results from mariner 10. *Science*, 185(4146):151–160.

Ness, N. F., Behannon, K. W., Lepping, R. P., Whang, Y. C., and Schatten, K. H. (1974). Magnetic Field Observations near Mercury: Preliminary Results from Mariner 10. *Science*, 185(4146):151–160.

Nguyen, G., Aunai, N., Michotte De Welle, B., Jeandet, A., Lavraud, B., and Fontaine, D. (2022a). Massive multimission statistical study and analytical modeling of the earth's magnetopause: 1. a gradient boosting based automatic detection of nearearth regions. *Journal of Geophysical Research: Space Physics*, 127(1):e2021JA029773.

Nguyen, G., Aunai, N., Michotte De Welle, B., Jeandet, A., Lavraud, B., and Fontaine, D. (2022b). Massive MultiMission Statistical Study and Analytical Modeling of the Earth's Magnetopause: 2. Shape and Location. *Journal of Geophysical Research: Space Physics*, 127(1):e2021JA029774.

Nmeek, Z., afrnkov, J., and imnek, J. (2020). An examination of the magnetopause position and shape based upon new observations. In Zong, Q., Escoubet, P., Sibeck, D., Le, G., and Zhang, H., editors, *Geophysical Monograph Series*, pages 135–151. Wiley, 1 edition.

Ogilvie, K. W., Scudder, J. D., Hartle, R. E., Siscoe, G. L., Bridge, H. S., Lazarus, A. J., Asbridge, J. R., Bame, S. J., and Yeates, C. M. (1974). Observations at Mercury Encounter by the Plasma Science Experiment on Mariner 10. *Science*, 185(4146):145–151.

Ogilvie, K. W., Scudder, J. D., Vasyliunas, V. M., Hartle, R. E., and Siscoe, G. L. (1977). Observations at the planet Mercury by the Plasma Electron Experiment: Mariner 10. *Journal Geophysical Research*, 82(13):1807.

Oliven, M. N. and Gurnett, D. A. (1968). Microburst phenomena: 3. An association between microbursts and VLF chorus. *Journal of Geophysical Research*, 73(7):2355–2362.

Omidi, N., Blanco-Cano, X., Russell, C., and Karimabadi, H. (2004). Dipolar magnetospheres and their characterization as a function of magnetic moment. *Advances in Space Research*, 33(11):1996–2003.

Omura, Y., Katoh, Y., and Summers, D. (2008). Theory and simulation of the generation of whistler-mode chorus: GENERATION PROCESS OF CHORUS EMISSIONS. *Journal of Geophysical Research: Space Physics*, 113(A4):n/a–n/a.

Omura, Y., Miyashita, Y., Yoshikawa, M., Summers, D., Hikishima, M., Ebihara, Y., and Kubota, Y. (2015). Formation process of relativistic electron flux through interaction with chorus emissions in the Earth's inner magnetosphere. *Journal of Geophysical Research: Space Physics*, 120(11):9545–9562.

Opher, M., Drake, J. F., Swisdak, M., Schoeffler, K. M., Richardson, J. D., Decker, R. B., and Toth, G. (2011). IS THE MAGNETIC FIELD IN THE HELIOSHEATH LAMINAR OR A TURBULENT SEA OF BUBBLES? *The Astrophysical Journal*, 734(1):71.

Otto, A. (2005). *The Magnetosphere*, pages 133–192. Springer Berlin Heidelberg, Berlin, Heidelberg.

Ozaki, M., Yagitani, S., Kasaba, Y., Kasahara, Y., Matsuda, S., Omura, Y., Hikishima, M., Sahraoui, F., Mirioni, L., Chanteur, G., Kurita, S., Nakazawa, S., and Murakami, G. (2023). Whistler-mode waves in Mercurys magnetosphere observed by BepiColombo/Mio. *Nature Astronomy*.

Pagel, C., Gary, S. P., De Koning, C. A., Skoug, R. M., and Steinberg, J. T. (2007). Scattering of suprathermal electrons in the solar wind: ACE observations. *Journal of Geophysical Research: Space Physics*, 112:2006JA011967.

Panov, E. V., Artemyev, A. V., Nakamura, R., and Baumjohann, W. (2011). Two types of tangential magnetopause current sheets: Cluster observations and theory: TANGENTIAL MAGNETOPAUSE STRUCTURE. *Journal of Geophysical Research: Space Physics*, 116(A12):n/a–n/a.

Panov, E. V., Bchner, J., Frnz, M., Korth, A., Savin, S. P., Rme, H., and Fornaon, K. (2008). Highlatitude earth's magnetopause outside the cusp: Cluster observations. *Journal of Geophysical Research: Space Physics*, 113:2006JA012123.

Parker, E. N. (1956). On the geomagnetic storm effect. *Journal of Geophysical Research*, 61(4):625–637.

Parker, E. N. (1958). Dynamics of the Interplanetary Gas and Magnetic Fields. *The Astrophysical Journal*, 128:664.

Paschmann, G. and Daly, P. W. (1998). Analysis Methods for Multi-Spacecraft Data. ISSI Scientific Reports Series SR-001, ESA/ISSI, Vol. 1. ISBN 1608-280X, 1998. *ISSI Scientific Reports Series*, 1. ADS Bibcode: 1998ISSIR...1.....P.

Paschmann, G., Haaland, S., Sonnerup, B. U. ., Hasegawa, H., Georgescu, E., Klecker, B., Phan, T. D., Rme, H., and Vaivads, A. (2005a). Characteristics of the near-tail dawn magnetopause and boundary layer. *Annales Geophysicae*, 23(4):1481–1497.

Paschmann, G., Haaland, S. E., Phan, T. D., Sonnerup, B. U. O., Burch, J. L., Torbert, R. B., Gershman, D. J., Dorelli, J. C., Giles, B. L., Pollock, C., Saito, Y., Lavraud, B., Russell, C. T., Strangeway, R. J., Baumjohann, W., and Fuselier, S. A. (2018). Large Scale Survey of the Structure of the Dayside Magnetopause by MMS. *Journal of Geophysical Research: Space Physics*, 123(3):2018–2033.

Paschmann, G., Schwartz, S. J., Escoubet, C. P., and Haaland, S., editors (2005b). *Outer Magnetospheric Boundaries: Cluster Results*, volume 20 of *Space Sciences Series of ISSI*. Springer Netherlands, Dordrecht.

Paschmann, G., Sonnerup, B. U. ., Papamastorakis, I., Sckopke, N., Haerendel, G., Bame, S. J., Asbridge, J. R., Gosling, J. T., Russell, C. T., and Elphic, R. C. (1979). Plasma acceleration at the Earth's magnetopause: evidence for reconnection. *Nature*, 282(5736):243–246.

Passot, T. and Sulem, P. L. (2006). A fluid model with finite Larmor radius effects for mirror mode dynamics. *Journal of Geophysical Research: Space Physics*, 111(A4):2005JA011425.

Phan, T. D. and Paschmann, G. (1996). Lowlatitude dayside magnetopause and boundary layer for high magnetic shear: 1. Structure and motion. *Journal of Geophysical Research: Space Physics*, 101(A4):7801–7815.

Phan, T. D., Shay, M. A., Gosling, J. T., Fujimoto, M., Drake, J. F., Paschmann, G., Oieroset, M., Eastwood, J. P., and Angelopoulos, V. (2013). Electron bulk heating in magnetic reconnection at Earth's magnetopause: Dependence on the inflow Alfvn speed and magnetic shear. *Geophysical Research Letters*, 40(17):4475–4480.

Phan, T. D., Shay, M. A., Haggerty, C. C., Gosling, J. T., Eastwood, J. P., Fujimoto, M., Malakit, K., Mozer, F. S., Cassak, P. A., Oieroset, M., and Angelopoulos, V. (2016). Ion Larmor radius effects near a reconnection X line at the magnetopause: THEMIS observations and simulation comparison. *Geophysical Research Letters*, 43(17):8844–8852.

Poh, G., Slavin, J. A., Jia, X., Raines, J. M., Imber, S. M., Sun, W.-J., Gershman, D. J., DiBraccio, G. A., Genestreti, K. J., and Smith, A. W. (2017). Mercury's cross-tail current sheet: Structure, x-line location and stress balance. *Geophysical Research Letters*, 44(2):678–686.

Pollock, C., Moore, T., Jacques, A., Burch, J., Gliese, U., Saito, Y., Omoto, T., Avanov, L., Barrie, A., Coffey, V., Dorelli, J., Gershman, D., Giles, B., Rosnack, T., Salo, C., Yokota, S., Adrian, M., Aoustin, C., Auletti, C., Aung, S., Bigio, V., Cao, N., Chandler, M., Chornay, D., Christian, K., Clark, G., Collinson, G., Corris, T., De Los Santos, A., Devlin, R., Diaz, T., Dickerson, T., Dickson, C., Diekmann, A., Diggs, F., Duncan, C., Figueroa-Vinas, A., Firman, C., Freeman, M., Galassi, N., Garcia, K., Goodhart, G., Guererro, D., Hageman, J., Hanley, J., Hemminger, E., Holland, M., Hutchins, M., James, T., Jones, W., Kreisler, S., Kujawski, J., Lavu, V., Lobell, J., LeCompte, E., Lukemire, A., MacDonald, E., Mariano, A.,

Mukai, T., Narayanan, K., Nguyan, Q., Onizuka, M., Paterson, W., Persyn, S., Piepgrass, B., Cheney, F., Rager, A., Raghuram, T., Ramil, A., Reichenthal, L., Rodriguez, H., Rouzaud, J., Rucker, A., Saito, Y., Samara, M., Sauvaud, J.-A., Schuster, D., Shappirio, M., Shelton, K., Sher, D., Smith, D., Smith, K., Smith, S., Steinfeld, D., Szymkiewicz, R., Tanimoto, K., Taylor, J., Tucker, C., Tull, K., Uhl, A., Vloet, J., Walpole, P., Weidner, S., White, D., Winkert, G., Yeh, P.-S., and Zeuch, M. (2016). Fast plasma investigation for magnetospheric multiscale. *Space Science Reviews*, 199(1):331–406.

Pritchett, P. L. and Mozer, F. S. (2009). Asymmetric magnetic reconnection in the presence of a guide field. *Journal of Geophysical Research: Space Physics*, 114:2009JA014343.

Pu, Z. and Kivelson, M. G. (1983). Kelvin:helmholtz instability at the magnetopause: Solution for compressible plasmas. *Journal of Geophysical Research: Space Physics*, 88:841–852.

Pucci, F., Matthaeus, W. H., Chasapis, A., Servidio, S., Sorriso-Valvo, L., Olshevsky, V., Newman, D. L., Goldman, M. V., and Lapenta, G. (2018). Generation of Turbulence in Colliding Reconnection Jets. *apj*, 867(1):10.

Raines, J. M., DiBraccio, G. A., Cassidy, T. A., Delcourt, D. C., Fujimoto, M., Jia, X., Mangano, V., Milillo, A., Sarantos, M., Slavin, J. A., and Wurz, P. (2015). Plasma Sources in Planetary Magnetospheres: Mercury. *Space Science Reviews*, 192(1-4):91–144.

Rezeau, L., Belmont, G., Manuzzo, R., Aunai, N., and Dargent, J. (2018). Analyzing the magnetopause internal structure: New possibilities offered by mms tested in a case study. *Journal of Geophysical Research: Space Physics*, 123.

Russell, C. and Elphic, R. (1978). Initial ISEE magnetometer results: magnetopause observations. *Space Science Reviews*, 22(6).

Russell, C. T., Anderson, B. J., Baumjohann, W., Bromund, K. R., Dearborn, D., Fischer, D., Le, G., Leinweber, H. K., Leneman, D., Magnes, W., Means, J. D., Moldwin, M. B., Nakamura, R., Pierce, D., Plaschke, F., Rowe, K. M., Slavin, J. A., Strangeway, R. J., Torbert, R., Hagen, C., Jernej, I., Valavanoglou, A., and Richter, I. (2016). The magnetospheric multiscale magnetometers. *Space Science Reviews*, 199(1):189–256.

Russell, C. T., Baker, D. N., and Slavin, J. A. (1988). *The magnetosphere of Mercury.* NTRS.

Russell, C. T., Mellott, M. M., Smith, E. J., and King, J. H. (1983). Multiple spacecraft observations of interplanetary shocks: Four spacecraft determination of shock normals. *Journal of Geophysical Research: Space Physics*, 88:4739–4748.

Sabine, E. (1851). V. On periodical laws discoverable in the mean effects of the larger magnetic disturbances. *Philosophical Transactions of the Royal Society of London*, 141:123–139.

Sabine, E. (1852). VIII. On periodical laws discoverable in the mean effects of the larger magnetic disturbance.No. II. *Philosophical Transactions of the Royal Society of London*, 142:103–124.

Safrankova, J., Nemecek, Z., Dusk, S., Prech, L., Sibeck, D. G., and Borodkova, N. N. (2002). The magnetopause shape and location: a comparison of the Interball and Geotail observations with models. *Annales Geophysicae*, 20(3):301–309.

Sarantos, M., Killen, R. M., and Kim, D. (2007). Predicting the long-term solar wind ion-sputtering source at Mercury. *Planetary and Space Science*, 55(11):1584–1595.

Scarf, F. L., Gurnett, D. A., and Kurth, W. S. (1979). Jupiter Plasma Wave Observations: An Initial Voyager 1 Overview. *Science*, 204(4396):991–995.

Schrijver, C. J. and Siscoe, G. L. (2009). *Heliophysics: Plasma Physics of the Local Cosmos.* Cambridge University Press, Cambridge. OCLC: 889952516.

Schwenn, R. and Marsch, E. (1990). *Physics of the Inner Heliosphere I. Large-Scale Phenomena.* Springer-Verlag. Publication Title: Physics of the Inner Heliosphere I ADS Bibcode: 1990pihl.book.....S.

Schwenn, R. and Marsch, E. (1991). *Physics of the inner heliosphere.* Springer-Verlag, Berlin. OCLC: 681182291.

Scudder, J. and Daughton, W. (2008a). illuminating electron diffusion regions of collisionless magnetic reconnection using electron agyrotropy. *Journal of Geophysical Research: Space Physics*, 113:2008JA013035.

Scudder, J. and Daughton, W. (2008b). Illuminating electron diffusion regions of collisionless magnetic reconnection using electron agyrotropy: ELECTRON DIFFUSION REGION AND AGYROTROPY. *Journal of Geophysical Research: Space Physics*, 113(A6):n/a–n/a.

Scudder, J. D., Holdaway, R. D., Daughton, W. S., Karimabadi, H., Roytershteyn, V., Russell, C. T., and Lopez, J. Y. (2012). First resolved observations of the demagnetized electron-diffusion region of an astrophysical magnetic-reconnection site. *Physical Review Letters*, 108(22):225005.

Shay, M. A. and Drake, J. F. (1998). The role of electron dissipation on the rate of collisionless magnetic reconnection. *grl*, 25(20):3759–3762.

Shi, Q. Q., Shen, C., Pu, Z. Y., Dunlop, M. W., Zong, Q.-G., Zhang, H., Xiao, C. J., Liu, Z. X., and Balogh, A. (2005). Dimensional analysis of observed structures using multipoint magnetic field measurements: Application to cluster: STRUCTURE DIMENSIONALITY DETERMINATION. *Geophysical Research Letters*, 32(12):n/a–n/a.

Shi, Q. Q., Tian, A. M., Bai, S. C., Hasegawa, H., Degeling, A. W., Pu, Z. Y., Dunlop, M., Guo, R. L., Yao, S. T., Zong, Q.-G., Wei, Y., Zhou, X.-Z., Fu, S. Y., and Liu, Z. Q. (2019). Dimensionality, Coordinate System and Reference Frame for Analysis of In-Situ Space Plasma and Field Data. *Space Science Reviews*, 215(4):35.

Shue, J., Chao, J. K., Fu, H. C., Russell, C. T., Song, P., Khurana, K. K., and Singer, H. J. (1997). A new functional form to study the solar wind control of the magnetopause size and shape. *Journal of Geophysical Research: Space Physics*, 102(A5):9497–9511.

Shue, J., Song, P., Russell, C. T., Steinberg, J. T., Chao, J. K., Zastenker, G., Vaisberg, O. L., Kokubun, S., Singer, H. J., Detman, T. R., and Kawano, H. (1998). Magnetopause location under extreme solar wind conditions. *Journal of Geophysical Research: Space Physics*, 103(A8):17691–17700.

Sibeck, D., Lopez, R., and Roelof, E. (1991). Solar wind control of the magnetopause shape, location, and motion. *Journal of Geophysical Research: Space Physics*, 96(A4):5489–5495.

Siscoe, G. L., Ness, N. F., and Yeates, C. M. (1975). Substorms on Mercury? *Journal of Geophysical Research*, 80(31):4359.

Slavin, J. A. (2004). Mercury's magnetosphere. *Advances in Space Research*, 33(11):1859–1874.

Slavin, J. A., Anderson, B. J., Baker, D. N., Benna, M., Boardsen, S. A., Gold, R. E., Ho, G. C., Imber, S. M., Korth, H., Krimigis, S. M., McNutt, Ralph L., J., Raines, J. M., Sarantos, M., Schriver, D., Solomon, S. C., Trávníček, P., and Zurbuchen, T. H. (2012). MESSENGER and Mariner 10 flyby observations of magnetotail structure and dynamics at Mercury. *Journal of Geophysical Research (Space Physics)*, 117(A1):A01215.

Slavin, J. A., Anderson, B. J., Zurbuchen, T. H., Baker, D. N., Krimigis, S. M., Acua, M. H., Benna, M., Boardsen, S. A., Gloeckler, G., Gold, R. E., Ho, G. C., Korth, H., McNutt Jr., R. L., Raines, J. M., Sarantos, M., Schriver, D., Solomon, S. C., and Trvnek, P. (2009). Messenger observations of mercury's magnetosphere during northward imf. *Geophysical Research Letters*, 36(2).

Slavin, J. A., DiBraccio, G. A., Gershman, D. J., Imber, S. M., Poh, G. K., Raines, J. M., Zurbuchen, T. H., Jia, X., Baker, D. N., Glassmeier, K.-H., Livi, S. A., Boardsen, S. A., Cassidy, T. A., Sarantos, M., Sundberg, T., Masters, A., Johnson, C. L., Winslow, R. M., Anderson, B. J., Korth, H., McNutt Jr., R. L., and Solomon, S. C. (2014). MESSENGER observations of Mercury's dayside magnetosphere under extreme solar wind conditions. *Journal of Geophysical Research: Space Physics*, 119(10):8087–8116.

Slavin, J. A. and Holzer, R. E. (1981). Solar wind flow about the terrestrial planets 1. Modeling bow shock position and shape. *Journal of Geophysical Research: Space Physics*, 86(A13):11401–11418.

Slavin, J. A., Middleton, H. R., Raines, J. M., Jia, X., Zhong, J., Sun, W. J., Livi, S., Imber, S. M., Poh, G. K., Akhavan-Tafti, M., Jasinski, J. Â. M., DiBraccio, G. A., Dong, C., Dewey, R. M., and Mays, M. L. (2019). MESSENGER Observations of Disappearing Dayside Magnetosphere Events at Mercury. *Journal of Geophysical Research (Space Physics)*, 124(8):6613–6635.

Smith, E. J. (1962). A comparison of Explorer VI and Explorer X magnetometer data. *Journal of Geophysical Research*, 67(5):2045–2049.

Smith, E. J., Coleman, P. J., Judge, D. L., and Sonett, C. P. (1960). Characteristics of the extraterrestrial current system: Explorer VI and Pioneer V. *Journal of Geophysical Research*, 65(6):1858–1861.

Solomon, S. C., Nittler, L. R., and Anderson, B. J. (2018). *Mercury: The View after MESSENGER*. Cambridge University Press.

Sonett, C. P., Judge, D. L., and Kelso, J. M. (1959). Evidence concerning instabilities of the distant geomagnetic field: Pioneer I. *Journal of Geophysical Research*, 64(8):941–943.

Sonett, C. P., Judge, D. L., Sims, A. R., and Kelso, J. M. (1960). A radial rocket survey of the distant geomagnetic field. *Journal of Geophysical Research*, 65(1):55–68.

Sonnerup, B. and Scheible, M. (1998). Minimum and maximum variance analysis. In *Analysis Methods for Multi- Spacecraft Data*, pages pp. 185–220. Int. Space Sci. Inst./Eur. Space Agency, Bern/Paris.

Sonnerup, B. U. O. and Ledley, B. G. (1974). Magnetopause rotational forms. *Journal of Geophysical Research*, 79(28):4309–4314.

Sonnerup, B. U. . and Cahill, L. J. (1967). Magnetopause structure and attitude from Explorer 12 observations. *Journal of Geophysical Research*, 72(1):171.

Sonnerup, B. U. ., Haaland, S., Paschmann, G., Dunlop, M. W., Rme, H., and Balogh, A. (2006). Orientation and motion of a plasma discontinuity from singlespacecraft measurements: Generic residue analysis of Cluster data. *Journal of Geophysical Research: Space Physics*, 111(A5):2005JA011538.

Spreiter, J. R. (1976). Magnetohydrodynamic and gasdynamic aspects of solar-wind flow around terrestrial planets: A critical review. *NASA. Goddard Space Flight Center Solar-Wind Interaction with the Planets Mercury, Venus, and Mars.*

Spreiter, J. R., Summers, A. L., and Alksne, A. Y. (1966a). Hydromagnetic flow around the magnetosphere. *Planetary and Space Science*, 14(3):223–253.

Spreiter, J. R., Summers, A. L., and Alksne, A. Y. (1966b). Hydromagnetic flow around the magnetosphere. *Planetary and Space Science*, 14(3):223–253.

Stewart, B. (1861). XXII. On the great magnetic disturbance which extended from August 28 to September 7, 1859, as recorded by photography at the Kew Observatory. *Philosophical Transactions of the Royal Society of London*, 151:423–430.

Stix, T. (1992). *Waves in Plasmas*. American Institute of Physics.

Stormer, C. (1918). La Theorie Corpusculaire des Aurores Boreales. *L'astronomie*, 32:153–159.

Summers, D., Ni, B., and Meredith, N. P. (2007). Timescales for radiation belt electron acceleration and loss due to resonant wave-particle interactions: 2. Evaluation for VLF chorus, ELF hiss, and electromagnetic ion cyclotron waves: RADIATION BELT ELECTRON TIMESCALES. *Journal of Geophysical Research: Space Physics*, 112(A4):n/a–n/a.

Summers, D., Thorne, R. M., and Xiao, F. (1998). Relativistic theory of waveparticle resonant diffusion with application to electron acceleration in the magnetosphere. *Journal of Geophysical Research: Space Physics*, 103(A9):20487–20500.

Sun, J., Wang, X., Lu, Q., Zhang, B., Hu, Z., Liu, J., Hu, H., and Yang, H. (2023). Excitation and propagation of magnetosonic waves in the earth's dipole magnetic field: 3d PIC simulation. *Journal of Geophysical Research: Space Physics*, 128(9):e2023JA031311.

Sun, W., Dewey, R. M., Aizawa, S., Huang, J., Slavin, J. A., Fu, S., Wei, Y., and Bowers, C. F. (2022). Review of Mercury's dynamic magnetosphere: Post-MESSENGER era and comparative magnetospheres. *Science China Earth Sciences*, 65(1):25–74.

Sun, W. J., Fu, S. Y., Slavin, J. A., Raines, J. M., Zong, Q. G., Poh, G. K., and Zurbuchen, T. H. (2016). Spatial distribution of Mercury's flux ropes and reconnection fronts: MESSENGER observations. *Journal of Geophysical Research (Space Physics)*, 121(8):7590–7607.

Sundberg, T., Slavin, J. A., Boardsen, S. A., Anderson, B. J., Korth, H., Ho, G. C., Schriver, D., Uritsky, V. M., Zurbuchen, T. H., Raines, J. M., Baker, D. N., Krimigis, S. M., McNutt, Ralph L., J., and Solomon, S. C. (2012). MESSENGER observations of dipolarization events in Mercury's magnetotail. *Journal of Geophysical Research (Space Physics)*, 117:A00M03.

Tang, B., Zank, G. P., and Kolobov, V. I. (2020). Numerical modeling of suprathermal electron transport in the solar wind: Effects of whistler turbulence. *The Astrophysical Journal*, 892(2):95.

Teng, S., Wu, Y., Harada, Y., Bortnik, J., Zonca, F., Chen, L., and Tao, X. (2023). Whistler-mode chorus waves at mars. *Nature Communications*, 14(1):3142.

Thorne, R. M., Li, W., Ni, B., Ma, Q., Bortnik, J., Chen, L., Baker, D. N., Spence, H. E., Reeves, G. D., Henderson, M. G., Kletzing, C. A., Kurth, W. S., Hospodarsky, G. B., Blake, J. B., Fennell, J. F., Claudepierre, S. G., and Kanekal, S. G. (2013). Rapid local acceleration of relativistic radiation-belt electrons by magnetospheric chorus. *Nature*, 504(7480):411–414.

Torbert, R. B., Burch, J. L., Giles, B. L., Gershman, D., Pollock, C. J., Dorelli, J., Avanov, L., Argall, M. R., Shuster, J., Strangeway, R. J., Russell, C. T., Ergun, R. E., Wilder, F. D., Goodrich, K., Faith, H. A., Farrugia, C. J., Lindqvist, P., Phan, T., Khotyaintsev, Y., Moore, T. E., Marklund, G., Daughton, W., Magnes, W., Kletzing, C. A., and Bounds, S. (2016). Estimates of terms in Ohm's law during an encounter with an electron diffusion region. *Geophysical Research Letters*, 43(12):5918–5925.

Torbert, R. B., Burch, J. L., Phan, T. D., Hesse, M., Argall, M. R., Shuster, J., Ergun, R. E., Alm, L., Nakamura, R., Genestreti, K. J., Gershman, D. J., Paterson, W. R., Turner, D. L., Cohen, I., Giles, B. L., Pollock, C. J., Wang, S., Chen, L.-J., Stawarz, J. E., Eastwood, J. P., Hwang, K. J., Farrugia, C., Dors, I., Vaith, H., Mouikis, C., Ardakani, A., Mauk, B. H., Fuselier, S. A., Russell, C. T., Strangeway, R. J., Moore, T. E., Drake, J. F., Shay, M. A., Khotyaintsev, Y. V., Lindqvist, P.-A., Baumjohann, W., Wilder, F. D., Ahmadi, N., Dorelli, J. C., Avanov, L. A., Oka, M., Baker, D. N., Fennell, J. F., Blake, J. B., Jaynes, A. N., Le Contel, O., Petrinec, S. M., Lavraud, B., and Saito, Y. (2018). Electron-scale dynamics of the diffusion region during symmetric magnetic reconnection in space. *Science*, 362(6421):1391–1395.

Trávníček, P., Hellinger, P., and Schriver, D. (2007). Structure of Mercury's magnetosphere for different pressure of the solar wind: Three dimensional hybrid simulations. *Geophysical Research Letters*, 34(5):L05104.

Trávníček, P. M., Hellinger, P., Schriver, D., Herčík, D., Slavin, J. A., and Anderson, B. J. (2009). Kinetic instabilities in Mercury's magnetosphere: Three-dimensional simulation results. *Geophysical Research Letters*, 36(7):L07104.

Trávníček, P. M., Schriver, D., Hellinger, P., Herčík, D., Anderson, B. J., Sarantos, M., and Slavin, J. A. (2010). Mercury's magnetosphere-solar wind interaction for northward and southward interplanetary magnetic field: Hybrid simulation results. *Icarus*, 209(1):11–22.

Tsurutani, B. T. and Smith, E. J. (1974). Postmidnight chorus: A substorm phenomenon. *Journal of Geophysical Research*, 79(1):118–127.

Tsyganenko, N. (1989). A magnetospheric magnetic field model with a warped tail current sheet. *Planetary and Space Science*, 37(1):5–20.

Valentini, F., Trvnek, P., Califano, F., Hellinger, P., and Mangeney, A. (2007). A hybrid-vlasov model based on the current advance method for the simulation of collisionless magnetized plasma. *Journal of Computational Physics*, 225(1):753–770.

Van Der Holst, B. and Keppens, R. (2007). Hybrid block-AMR in cartesian and curvilinear coordinates: MHD applications. *Journal of Computational Physics*, 226(1):925–946.

Verscharen, D., Klein, K. G., and Maruca, B. A. (2019). The multi-scale nature of the solar wind. *Living Reviews in Solar Physics*, 16(1):5.

Verscharen, D., Parashar, T. N., Gary, S. P., and Klein, K. G. (2020). Dependence of kinetic plasma waves on ion-to-electron mass ratio and light-to-Alfvén speed ratio. *mnras*, 494(2):2905–2911.

Viall, N. M. and Borovsky, J. E. (2020). Nine Outstanding Questions of Solar Wind Physics. *Journal of Geophysical Research: Space Physics*, 125(7):e2018JA026005.

Vlasov, A. A. (1968). THE VIBRATIONAL PROPERTIES OF AN ELECTRON GAS. *Soviet Physics Uspekhi*, 10(6):721–733.

Vocks, C. and Mann, G. (2003). Generation of suprathermal electrons by resonant waveparticle interaction in the solar corona and wind. *The Astrophysical Journal*, 593(2):1134–1145.

Webster, J. M., Burch, J. L., Reiff, P. H., Daou, A. G., Genestreti, K. J., Graham, D. B., Torbert, R. B., Ergun, R. E., Sazykin, S. Y., Marshall, A., Allen, R. C., Chen, L., Wang, S., Phan, T. D., Giles, B. L., Moore, T. E., Fuselier, S. A., Cozzani, G., Russell, C. T., Eriksson, S., Rager, A. C., Broll, J. M., Goodrich, K., and Wilder, F. (2018). Magnetospheric

Multiscale Dayside Reconnection Electron Diffusion Region Events. *Journal of Geophysical Research: Space Physics*, 123(6):4858–4878.

Winslow, R. M., Anderson, B. J., Johnson, C. L., Slavin, J. A., Korth, H., Purucker, M. E., Baker, D. N., and Solomon, S. C. (2013). Mercury's magnetopause and bow shock from MESSENGER Magnetometer observations. *Journal of Geophysical Research: Space Physics*, 118(5):2213–2227.

Wolfe, J. H., Mihalov, J. D., Collard, H. R., McKibbin, D. D., Frank, L. A., and Intriligator, D. S. (1974). Pioneer 10 observations of the solar wind interaction with jupiter. *Journal of Geophysical Research*, 79(25):3489–3500.

Woodfield, E. E., Glauert, S. A., Menietti, J. D., Averkamp, T. F., Horne, R. B., and Shprits, Y. Y. (2019). Rapid Electron Acceleration in LowDensity Regions of Saturn's Radiation Belt by Whistler Mode Chorus Waves. *Geophysical Research Letters*, 46(13):7191–7198.

Xiao, F., Yang, C., He, Z., Su, Z., Zhou, Q., He, Y., Kletzing, C. A., Kurth, W. S., Hospodarsky, G. B., Spence, H. E., Reeves, G. D., Funsten, H. O., Blake, J. B., Baker, D. N., and Wygant, J. R. (2014). Chorus acceleration of radiation belt relativistic electrons during March 2013 geomagnetic storm. *Journal of Geophysical Research: Space Physics*, 119(5):3325–3332.

Yamada, M., Kulsrud, R., and Ji, H. (2010). Magnetic reconnection. *Reviews of Modern Physics*, 82(1):603–664.

Yamamoto, T. (1988). On the temporal fluctuations of pulsating auroral luminosity. *Journal of Geophysical Research: Space Physics*, 93(A2):897–911.

Yu, X., Yuan, Z., Li, H., Huang, S., Wang, D., Yao, F., Funsten, H. O., and Wygant, J. R. (2018). Response of Banded Whistler Mode Waves to the Enhancement of Solar Wind Dynamic Pressure in the Inner Earth's Magnetosphere. *Geophysical Research Letters*, 45(17):8755–8763.

Zhong, J., Shue, J. H., Wei, Y., Slavin, J. A., Zhang, H., Rong, Z. J., Chai, L. H., and Wan, W. X. (2020). Effects of Orbital Eccentricity and IMF Cone Angle on the Dimensions of Mercury's Magnetosphere. *The Astrophysical Journal*, 892(1):2.

Zhong, J., Wan, W. X., Wei, Y., Slavin, J. A., Raines, J. M., Rong, Z. J., Chai, L. H., and Han, X. H. (2015). Compressibility of Mercury's dayside magnetosphere. *Geophysical Research Letters*, 42(23):10,135–10,139.